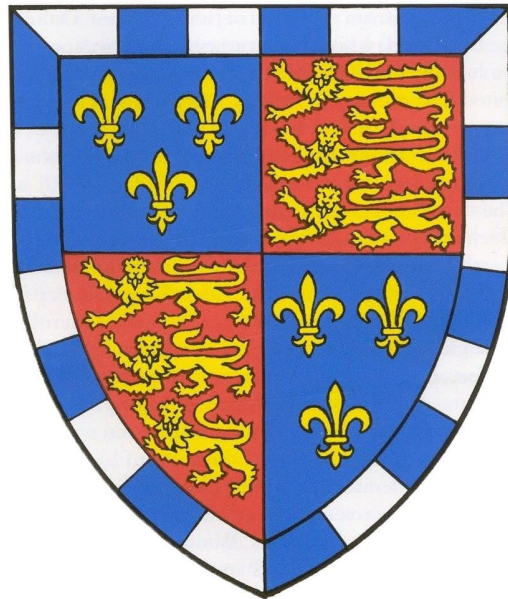


Investigating the surface hydrology of Antarctic ice shelves using remote sensing and machine learning



Rebecca Lauren Dell

Scott Polar Research Institute
University of Cambridge

This dissertation is submitted for the degree of Doctor of
Philosophy

Christ's College

June 2021

*For Nan, I promise to love unconditionally, and to always
pursue happiness.*

Declaration

I hereby declare that except where specific reference is made to the work of others, the contents of this dissertation are original and have not been submitted in whole or in part for consideration for any other degree or qualification in this, or any other university. This dissertation is my own work and contains nothing which is the outcome of work done in collaboration with others, except as specified in the text and Acknowledgements. This dissertation does not exceed the length limits prescribed by the Degree Committee for the Faculty of Earth Sciences and Geography.

Rebecca Dell

June 2021

Investigating the surface hydrology of Antarctic ice shelves using remote sensing and machine learning

Rebecca Lauren Dell

Surface meltwater is widespread across many of Antarctica's ice shelves and can contribute towards ice-shelf instability and potential collapse via hydrofracture or militate against potential ice-shelf instabilities by forming drainage systems that export surface meltwater off the ice-shelf edge. It is crucial, therefore, that water area and volume on Antarctic ice shelves are accurately quantified, and that the ways in which water is stored and transferred across ice-shelf surfaces are understood. This is because the partial or complete removal of ice-shelf areas that actively buttress upstream, grounded ice can lead to increased grounded ice contributions to global mean sea levels. Studying these meltwater systems through fieldwork is time consuming, expensive, and limits the spatial and temporal scale of the study. However, by utilising satellite imagery combined with machine learning methods, vast amounts of data can be processed quickly and cheaply, enabling ice-shelf hydrology to be studied on much greater spatial and temporal scales. This thesis develops novel remote sensing and machine learning methods to identify and track spatial and temporal trends in surface meltwater on Antarctic ice shelves. The first method utilises a normalised difference water index adapted for ice ($NDWI_{ice}$) threshold to track the changing volume and geometry of surface meltwater systems on the Nivlisen Ice Shelf for the 2016/2017 melt season in both Landsat 8 and Sentinel-2 imagery. Results presented for the Nivlisen Ice Shelf show the importance of two linear meltwater systems, which hold 63% of the total meltwater volume at the peak of the melt season. The second method uses machine learning to develop a supervised classifier capable of identifying slush (i.e. saturated firn) and ponded meltwater across all Antarctic ice

shelves using Landsat 8 imagery. This classifier is validated by four experts, returning accuracies of 84% for ponded water and 82% for slush, before being applied to the Roi Baudouin Ice Shelf as a case study. Between 2013 and 2020, on average, 64% of the meltwater identified on the Roi Baudouin Ice Shelf is classified as slush. The classifier is then applied across eight Antarctic Peninsula ice shelves for the full Landsat 8 record (2013 to 2021). The resulting dataset revealed high total surface meltwater extents in the 2017/2018 and 2019/2020 melt seasons across much of the west Antarctic Peninsula, and high total surface meltwater extents in 2016/2017 and 2019/2020 across much of the east Antarctic Peninsula. Overall, the methods presented in this thesis provide tools capable of utilising large quantities of remotely sensed data to accurately map all surface meltwater on Antarctic Ice Shelves. Amongst the results presented, a novel dataset showing the extent of slush across the Antarctic Peninsula shows that a large proportion of the total surface meltwater extent on ice shelves is often occupied by slush. This highlights the need for slush to be considered in future surface mass balance models.

Acknowledgements

Over the past four years I have had the pleasure of working with a dream team of supervisors. I would like to thank Ian Willis, for providing me with this PhD opportunity, for his constant academic support, and for making me feel welcome and settled in Cambridge from the day I arrived. I would also like to thank Neil Arnold, for having the patience to teach me to code, and for the many times I have chaotically entered his office, in need of advice. Special thanks also go to Alison Banwell, for being a female role model in glaciology, for constantly keeping me up to date with the current literature, and for giving me the opportunity to live and work in Boulder for a month. My thanks also go to Hamish Pritchard and the British Antarctic Survey, for being my CASE supervisor and sponsor respectively. Hamish always made me consider my work from a different angle, which has undoubtedly made me a better scientist. Beyond my supervisory team, I am grateful to Ruthie Halberstadt, Mahsa Mousavvi, Allen Pope, Stef Lhermitte, Bert Wouters, Andrew Orr, and Jennifer Arthur for the numerous useful discussions that we have had over the years. Thanks must also go to the Natural Environment Research Council, for funding this PhD (Grant no. NE/L002507/1).

My time as a PhD student has been shaped as a whole by my experiences at the Scott Polar Research Institute. The time I have spent working alongside Andrew, Samuel, Tom, Rob, and Karla has been endlessly entertaining, both in and out of the office. I owe it to each and every one of them for keeping me sane, even throughout a global pandemic, and I am confident that we will be in contact for many years to come. However, Scott Polar has been more than just a space for research to me. From the coffee and tea breaks, announced by the ring of the Terra Nova Bell, to the Christmas Concerts, and the meals out after evening seminars, every moment is one I will forever treasure. Special thanks go to Fiona, Rebecca, Helen, Maria, Naomi, Frankie, Alice and Morgan for the company they have all provided during coffee and tea breaks.

Beyond the hours that I spent working on my PhD, I spent much of my remaining time training with Cambridge University Boat Club, where I have made lifelong friends,

learnt some major life lessons, and let out any steam when other parts of my life seemed to not be going to plan! There are too many people who have impacted my time at the Boat Club to list, but special thanks go to Patrick Ryan, for coaching me for four solid years and for always allowing me to prioritise my academic commitments. Special thanks also go to Angela, Juli, Abba, Tricia, Adriana, Alice, Laura, Kate, Rhiannon, and Anouschka, for their unwavering belief in me and for their support through all of the ups and downs that the past four years have brought. I would also like to thank Sarah, Bronya, Elena, and Alex, for helping me to stay young and fun even when I feel like life is moving too quickly. Finally, I would like to acknowledge the three Blondie crews that I have had the privilege of training and racing with. God damn bloody O*ford.

2019	2020	2021
Cox: Catriona Bishop	Cox: Angela Harper	Cox: Angela Harper
Str: Fanny Belais	Str: Becky Dell	Str: Becky Dell
7: Sally O'Brien	7: Gemma King / Laura Foster	7: Kasia Pilch
6: Becky Dell	6: Rebecca Smith	6: Jo Matthews
5: Anouschka Fenley	5: Adriana Perez Rotondo	5: Gemma King
4: Abba Parker	4: Jo Matthews / Anna Harrison	4: Rhiannon Mulligan
3: Adriana Perez Rotondo	3: Gloria Jansen	3: Alex Riddell-Webster
2: Emma Andrews	2: Elena Von Muller	2: Elena Von Muller
Bow: Charlotte Jackson	Bow: Catherine King	Bow: Catherine King

Life can't be all work no play, and I would like to thank The HENS (Ella, Charlotte, Jo, and Amy) for being friends of a lifetime, and for creating memories with me that have

somehow made movie scenes look uneventful. From weekend breaks in Prague, to 'fly and flop' holidays in Spain, I am lucky to have friends that allow me to escape from the Cambridge Bubble, and who constantly refill my prosecco glass until the sun comes up. I would also thank Ella, for putting up with me for a month during our trip to Norway. There is no one I would rather scramble up mountains with on a caffeine deficit.

Throughout my PhD I have also had some incredible housemates who have supported me endlessly, particularly throughout Covid-19. I would like to thank Ollie, Charli, and Henry for endless hours of fun, themed dinners, and sofa chats. Special thanks also go to Mary and Colin, for their support over the past year. I have particularly enjoyed our strong G&Ts and fish and chip suppers!

Finally, I would like to thank my family; without their unwavering support, not only over the past four years, but throughout my entire life, I would never have come this far. In the last year, we lost Nan, who had been with me every step of the way so far in life. I will forever treasure the memories we made together. Thank you for being the kindest woman I have ever known, I hope I make you proud.

Table of contents

<i>Investigating the surface hydrology of Antarctic ice shelves using remote sensing and machine learning</i>	<i>i</i>
<i>Declaration</i>	<i>iv</i>
<i>Investigating the surface hydrology of Antarctic ice shelves using remote sensing and machine learning</i>	<i>vi</i>
<i>Acknowledgements</i>	<i>viii</i>
<i>Table of contents</i>	<i>xi</i>
<i>List of figures</i>	<i>xv</i>
<i>List of tables</i>	<i>xviii</i>
<i>List of nomenclature</i>	<i>xix</i>
Roman symbols	<i>xix</i>
Acronyms / abbreviations	<i>xix</i>
<i>Chapter 1 Introduction</i>	<i>1</i>
1.1 Thesis motivation	<i>1</i>
1.2 Aims and objectives	<i>4</i>
1.3 Thesis structure	<i>4</i>
1.4 Publications from this thesis	<i>5</i>
<i>Chapter 2 Literature Review</i>	<i>7</i>
2.1 Antarctic ice shelves	<i>7</i>
2.1.1 Controls on ice-shelf surface melt.....	<i>11</i>
2.1.2 Surface meltwater storage	<i>15</i>
2.1.2.1 Slush.....	<i>16</i>
2.1.2.2 Surface lakes	<i>16</i>
2.1.2.3 Surface streams and rivers.....	<i>19</i>
2.1.3 Potential impact of increased future surface melting	<i>20</i>
2.2 Remote sensing.....	<i>23</i>
2.2.1 Landsat 8	<i>24</i>
2.2.2 Sentinel-2.....	<i>26</i>
2.2.3 Methods for lake area quantification	<i>27</i>
2.2.4 Methods for lake depth quantification	<i>28</i>
2.2.5 Methods for lake tracking.....	<i>29</i>
2.3 Machine learning methods.....	<i>30</i>
2.3.1 Random Forest Classifiers.....	<i>31</i>
<i>Chapter 3 Results I: Lateral meltwater transfer across an Antarctic ice shelf</i>	<i>33</i>

Abstract.....	33
3.1 Introduction	34
3.2. Study area	38
3.3 Methods	38
3.3.1 Images and pre-processing	40
3.3.1.1 Landsat 8.....	40
3.3.1.2 Sentinel-2	42
3.3.2 Delineating water body areas	43
3.3.3 Water body depth calculations.....	44
3.3.4 Classifying water body types	46
3.3.5 Tracking water bodies.....	47
3.3.6 Digital elevation model.....	48
3.3.7 Regional climate simulation	48
3.4 Results.....	50
3.4.1 Spatial extent and distribution of surface water bodies	50
3.4.2 Tracking results	52
3.4.2.1 Total area and volume of tracked surface water bodies.....	52
3.4.2.2 Tracking individual water bodies	54
3.4.2.3 Identifying individual lake freeze-through and drainage events.....	59
3.5 Discussion	60
3.5.1 Spatial and temporal distribution of surface meltwater bodies	60
3.5.2 Loss of water volume from circular surface water bodies.....	64
3.5.3 Potential implications for ice-shelf stability	65
3.6 Conclusions	66
<i>Chapter 4 Results II: Supervised classification of ponded water and slush on</i> <i>Antarctic ice shelves using Landsat 8 imagery.....</i>	<i>68</i>
Abstract.....	69
4.1 Introduction	69
4.2 Materials and Methods	72
4.2.1 Study areas.....	72
4.2.2 Methods	74
4.2.2.1 Scene selection and pre-processing.....	74
4.2.2.2 Training data generation and supervised classification	76
4.2.2.3 Validation	77
4.2.2.4 Application on the Roi Baudouin Ice Shelf.....	78
4.3 Results.....	79

4.3.1 Classifier accuracy.....	79
4.3.2 Relative importance of input bands	83
4.3.3 Application to Roi Baudouin Ice Shelf.....	84
4.4 Discussion	89
4.4.1 Classifier accuracy.....	89
4.4.2 Comparison to NDWI _{ice}	91
4.4.3 Evolution of ponded water and slush over the Roi Baudouin Ice Shelf	93
4.4.4 Errors arising from cloud and cloud shadows.....	95
4.5 Conclusions	98
<i>Chapter 5 Results III: Mapping ponded water and slush extent across Antarctic Peninsula ice shelves, 2013 to 2021</i>	
<i>99</i>	
5.1 Introduction	99
5.2 Study Areas	100
5.3 Data and Methods	103
5.3.1 Cloud Post-Processing	104
5.4 Results.....	105
5.4.1. Temporal variability in total surface meltwater extent.....	105
5.4.2 Temporal variability in ponded water and slush extent.....	106
5.4.3 Spatial patterns in the total surface meltwater extent, total ponded meltwater extent, and total slush extent	107
5.4.4 Wilkins Ice Shelf.....	113
5.4.5 Bach Ice Shelf.....	117
5.4.6 North George VI Ice Shelf.....	122
5.5 Discussion	127
5.5.1 Inter-annual variability in total surface meltwater extent across the Antarctic Peninsula	127
5.5.2 Variability in ponded water and slush extent across the Antarctic Peninsula.....	128
5.5.3. Spatial patterns in ponded water and slush extent across the Antarctic Peninsula.....	129
5.5.4. Potential climate drivers of inter-annual surface meltwater variability across the Antarctic Peninsula	130
5.5.4.1 West Antarctic Peninsula.....	130
5.5.4.2 Northeast Antarctic Peninsula	131
5.5.5. Site-specific variability in surface meltwater extent across Wilkins, Bach, and north George VI ice shelves	132
5.5.5.1 Wilkins Ice Shelf	133
5.5.5.2 Bach Ice Shelf	135

5.5.5.3 North George VI Ice Shelf	137
5.6 Conclusions	139
<i>Chapter 6 Sythesis and Conclusions</i>	141
6.1 Objective 1 - Develop a semi-automated method capable of tracking the formation of surface meltwater systems	142
6.1.1 Key findings from this study	142
6.1.2 Directions for future research.....	143
6.2Objective 2 - Train and validate a Random Forest Classifier capable of detecting slush and ponded water across all Antarctic ice shelves	144
6.2.1 Key findings from this study	144
6.2.2 Directions for future research.....	145
6.3 Objective 3 - Map the extent of ponded water and slush across all ice shelves on the Antarctic Peninsula between 2013 and 2021	147
6.3.1 Key findings from this study	147
6.3.2 Directions for future research.....	148
6.4 Conclusions	149
<i>References</i>	151
<i>Appendix A</i>	171
<i>Appendix B</i>	176
<i>Appendix C</i>	181

List of figures

2.1 Conceptual diagram showing firn air depletion, from Kuipers Munneke et al. (2014)	9
2.2 Examples of surface meltwater drainage systems across various Antarctic ice shelves, from Kingslake et al. (2017)	12
2.3 Air temperatures across the Antarctic Peninsula from 1979-2014, from Tuner et al. (2016)	13
2.4 Results of a simulation to show a chain reaction of lake drainage events on the Larsen B Ice Shelf, from Banwell et al. (2013)	18
2.5 130 m wide waterfall exporting surface melt off the Nansen Ice Shelf, from Bell et al. (2017).	20
2.6 A Venn diagram conceptualising the three factors that govern the degree to which ice shelves control the Antarctic Ice Sheet’s response to atmospheric warming, from Lai et al. (2020).	22
2.7 A basic machine learning model, from Wang et al. (2009).	30
3.1 Study area map	39
3.2 Workflow diagram for FASTISh	41
3.3 Solidity thresholds applied to water bodies identified on the Nivlisen Ice Shelf	49
3.4 REMA DEM data for the Nivlisen Ice Shelf	50
3.5 Base images, area masks, and depth masks for five of the 11 dates studied in the 2016–2017 melt season on Nivlisen Ice Shelf	55
3.6 Maximum extent of all identified water bodies on the Nivlisen Ice Shelf for the 2016– 2017 melt season	56
3.7 Time-series of the total area and volume held in each water body category over the 2016–2017 melt season on the Nivlisen Ice Shelf.....	57
3.8 Time-series of the area and volume of the WS and ES on the Nivlisen Ice Shelf ..	57

3.9 Elevation profiles for the ES and WS on the Nivlisen Ice Shelf	58
3.10 Meteorological context of circular lake loss events on the Nivlisen Ice Shelf	61
3.11 Comparison of optical imagery and radar imagery on 26 January 2017 for Nivlisen Ice Shelf	63
4.1 Study area map	73
4.2 Workflow detailing the pre-processing, training, validation, and application steps for the supervised classifier	75
4.3 An example workflow for the k-means clustering algorithm over the Nivlisen Ice Shelf.....	77
4.4 Preliminary outputs from the supervised classifier, as applied to six Landsat 8 validation images	80
4.5 Scaled areas of ponded water and slush on the Roi Baudouin Ice Shelf from 2013/14 to 2019/20	86
4.6 15-day melt products for the 2016/2017 melt season across the Roi Baudouin Ice Shelf	87
4.7 Maximum melt extent plots for each melt season on the Roi Baudouin Ice Shelf ...	88
4.8 Outputs from the supervised classifier and from NDWI _{ice} thresholding applied to sections of Shackleton Ice Shelf, Nansen Ice Shelf ,and George VI Ice Shelf	92
4.9 Heatmap for ponded water, slush, and both ponded water slush on the Roi Baudouin Ice Shelf	97
5.1 Study area figure	102
5.2 Total time-series data for the nine Antarctic Peninsula ice shelves investigated	108-109
5.3 Scaled ponded water and slush time-series data for each of the nine Antarctic Peninsula ice shelves studied	110-111
5.4 Maximum surface meltwater extent products for each ice shelf.....	112-113

5.5 Maximum surface meltwater extents across the Wilkins Ice Shelf from 2013/2014 to 2020/2021	114-115
5.6 15-day surface meltwater products for the 2019/2020 melt season across the Wilkins Ice Shelf	116-117
5.7 Maximum surface meltwater extents across the Bach Ice Shelf from 2013/2014 to 2020/2021.....	119-120
5.8 15-day surface meltwater products for the 2017/2018 melt season across the Bach Ice Shelf.....	121 -122
5.9 Maximum surface meltwater extents across the north George VI Ice Shelf from 2013/2014 to 2020/2021.....	124-125
5.10 15-day surface meltwater products for the 2019/2020 melt season across the north George VI Ice Shelf.....	126
5.11 Base true-colour composite image of the full Wilkins Ice Shelf and close-up classifier results over Wilkins Ice Shelf.....	134
5.12 Base true-colour composite image of the full Bach Ice Shelf and close-up classifier results over Wilkins Ice Shelf.....	136
5.13 Base true-colour composite image of the full north George VI Ice Shelf and close-up classifier results over Wilkins Ice Shelf.....	138

List of tables

Table 2.1 Key properties of the Landsat 8 OLI and TIRS bands.....	24
Table 2.2 Key properties of the Sentinel-2 multispectral bands	25
Table 3.1 Total area, total volume, and mean depth of all meltwater bodies on the Nivlisen Ice Shelf	53
Table 3.2 Maximum Area and Volume for each water body category on the Nivlisen Ice Shelf.....	56
Table 4.1 Accuracy scores for the intercomparison dataset	81
Table 4.2 High confidence accuracy scores for the intercomparison dataset.....	81
Table 4.3 Accuracy scores for the main validation dataset	82
Table 4.4 High confidence accuracy scores for the main validation dataset.....	83
Table 4.5 Relative importance of each of the Landsat 8 bands used by the supervised classifier	83

List of nomenclature

Roman symbols

z Pixel water depth

A_d Lake-bottom albedo

R_{pix} Satellite-measured pixel reflectance

R_∞ Reflectance for optically-deep water (>40 m deep).

g Coefficient for upwards and downward losses from travel in a water column

Acronyms / abbreviations

BOA: Bottom-of-atmosphere

CDW: Circumpolar Deep Water

CMIP: Coupled Model Intercomparison Project CNN: Convolutional Neural Network

CORDEX: Coordinated Regional Climate Downscaling Experiment DEM: Digital Elevation Model

ES: Eastern System FAC: Firn Air Content

FAST: Fully Automated Supraglacial lake area and volume Tracking

FASTER: Fully Automated Supraglacial Lake Tracking at Enhanced Resolution

FASTISH: Fully Automated Supraglacial Lake and Stream Tracking Algorithm for Ice Shelves

GEE: Google Earth Engine

k-NN: K-nearest neighbours

LIMA: Landsat Image Mosaic of Antarctica MAR: Modèle Atmosphérique Régional

MEaSURES: Making Earth System Data Records for Use in Research Environments

MetUM: Met Office Unified Model

MODIS: Moderate Resolution Imaging Spectroradiometer NDSI: Normalised Difference Snow Index

NDW_{ice}: normalised difference water index adapted for ice NIR: Near-Infrared

OLI: Operational Land Imager

RA1M: Regional Atmosphere Mid-latitude

REMA: Reference Elevation Model of Antarctica

RMSE: Root Mean Square Error

SAM: Southern Annular Mode SAR: Synthetic Aperture Radar

SCAR: Scientific Committee on Antarctic Research SWIR: Short-wave Infrared

TIRS: Thermal Infrared Imager TOA: Top-of-atmosphere

WS: Western System

IPCC: Intergovernmental Panel on Climate Change USGS: United States Geological Survey

DN(s): Digital Numbers(s)

Chapter 1

Introduction

1.1 Thesis motivation

Between 2006 and 2015, the Intergovernmental Panel on Climate Change (IPCC) reported a mass balance for the Antarctic Ice Sheet of $-155 \pm 19 \text{ Gt yr}^{-1}$, contributing $0.43 \pm 0.05 \text{ mm yr}^{-1}$ to global mean sea level rise (IPCC, 2019). These mass loss trends are dominated by glacier acceleration across West Antarctica and the Antarctic Peninsula, and result from a reduction in ice-shelf buttressing. Ice shelves currently border 75% of the Antarctic Ice Sheet and inhibit discharge into the Southern Ocean (Fürst et al., 2016). Where ice shelves thin, or in some cases collapse, the buttressing they provide may be lost, facilitating increased mass loss from grounded ice (Dupont and Alley, 2005; Fürst et al., 2016; Gudmundsson et al., 2019). Ice-shelf thinning and disintegration are driven by rising atmospheric (van den Broeke, 2005; Gilbert and Kittel, 2021) and/or ocean temperatures (Pritchard et al., 2012; Smith et al., 2020), which are predicted to increase into the future.

Since the 1950s, ice-shelf disintegration and retreat have been predominantly concentrated on the Antarctic Peninsula, where the area of ice shelves has been reduced by more than 28,000 km² between the 1950s and the 2008/2009 austral summer (Cook and Vaughan, 2010). Full or partial ice shelf collapse may lead to the acceleration of tributary glaciers; for example the collapse of Larsen B Ice Shelf in 2002 resulted in a two to six times increase in glacier velocities of its four tributary glaciers (Scambos et al., 2004). The current stability of the remaining ice shelves around Antarctica, therefore, has become a key research focus.

Current understanding of the factors that contribute to ice-shelf disintegration has therefore been developed largely from observations and modelling of the conditions that preceded recent collapse events on the Antarctic Peninsula. In particular, the collapse of the Larsen B Ice Shelf in 2002 has been attributed largely to rising atmospheric temperatures, which led to an increase in the duration and intensity of its melt season (e.g. Scambos et al., 2003; van den Broeke, 2005). These changes facilitated the widespread development of surface lakes that subsequently drained via hydrofracture, splintering the ice shelf into numerous icebergs, and causing widespread disintegration (e.g. Banwell et al., 2013; Robel and Banwell, 2019; Leeson et al., 2020). This event highlighted the potential damage that could be initiated by increased surface meltwater production on ice shelves.

However, whilst it is widely acknowledged that surface meltwater is now prevalent across many Antarctic ice shelves in both East and West Antarctica (e.g. Kingslake et al., 2017; Stokes et al., 2019), the varying impact(s) that surface meltwater may have on ice-shelf stability are still under discussion, and depend on how surface meltwater is stored and transferred across the ice shelf. For example, on the Nansen Ice Shelf, a persistent drainage network effectively transports surface meltwater across the ice-shelf surface and channels it off the ice-shelf edge, mitigating against ice-shelf instability, as water is prevented from accumulating on the ice-shelf surface (Bell et al., 2017). Therefore, whilst the accumulation of surface meltwater is an important factor in determining ice-shelf stability, its sole presence is not necessarily sufficient to drive widespread ice-shelf disintegration, as much depends on the surrounding hydrological and topological contexts (Banwell, 2017).

Whilst studies such as those conducted on Larsen B and Nansen ice shelves (e.g. Glasser and Scambos 2008; Bell et al., 2017), have provided us with a better understanding of the various ways surface meltwater may be stored and transferred across an ice shelf, a spatially and temporally broader understanding of the role these surface meltwater systems play in ice-shelf stability is still required. More studies need to monitor and track the inter- and intra-seasonal development of surface meltwater extent (slush and ponded water) on ice shelves, in addition to tracking how this water is stored and/or transferred across ice shelves. Such studies will allow us to better

constrain the factor(s) that influence the effect surface meltwater has on ice-shelf stability.

Although our understanding of hydrological conditions on Antarctic ice shelves continues to develop, the focus of ongoing studies largely remains on ponded surface water (i.e. medium-depth to deep water bodies on the ice-shelf surface), and the majority of studies neglect to consider the importance of slush (saturated firn) for ice shelf stability. The work presented in this thesis considers ponded water to have depths greater than or equal to 0.2 m, and slush to have depths less than 0.2 m, following Bell et al. (2017). Slush formation can (i) enhance the formation of ponded water bodies, as it inhibits the percolation of any further surface melt into the firn layer, and (ii) through re-freezing of meltwater in the firn layer, can drive a reduction in firn air content (FAC) over time, which may subsequently increase an ice-shelf's susceptibility to meltwater ponding, and (potential) ultimate hydrofracture (Hubbard et al., 2016; Ashmore et al., 2017; Bevan et al., 2017).

Slush may be neglected from current and prior studies of surface meltwater for two main reasons: (i) it is often shallow, and therefore may not have the potential to initiate hydrofracture (unlike ponded water); and (ii) it is extremely difficult to classify through remotely sensed studies, as it is spectrally similar to other surface facies (e.g. blue ice, cloud shadows, and ponded water). However, as machine learning applications become increasingly popular in glaciology (e.g. Dirscherl et al., 2020; Halberstadt et al., 2020), and cloud-computing platforms such as Google Earth Engine (GEE) provide all researchers with the tools to run computationally expensive tasks without the need for access to high- performance computing clusters, there is potential for machine learning to offer solutions to such classification problems, ultimately allowing us to better map all surface meltwater across Antarctic ice shelves.

However, whilst the advent of remote sensing and freely available satellite imagery has provided us with the tools required to conduct such studies over larger spatial and temporal scales, the limiting factor is often the research time required to find, process, and analyse such vast quantities of data. It is therefore imperative that automatic and

semi-automatic workflows are developed that aid these processes, to allow us to interpret such large quantities of data quickly.

1.2 Aims and objectives

Based on the research gaps outlined above, the preliminary aim of this thesis is to develop semi-automated remote sensing and machine learning methods to identify and track surface meltwater across Antarctic ice shelves using satellite imagery. This aim is broken into three key objectives, which are as follows:

1. To develop a semi-automated remote sensing method capable of tracking the formation of surface meltwater systems over a melt season and to demonstrate the application of this method over the Nivlisen Ice Shelf. This work is presented in Chapter 3.
2. To train and validate a Random Forest Classifier capable of detecting slush and ponded water across all Antarctic ice shelves using the full Landsat 8 record (2013 to 2021), and to demonstrate the application of this method across the Roi Baudouin Ice Shelf. This work is presented in Chapter 4.
3. To apply the Random Forest Classifier developed in (2) to map the extent of slush and ponded water across the main ice shelves on the Antarctic Peninsula between 2013 and 2021 from Landsat 8 imagery. This work is presented in Chapter 5.

1.3 Thesis structure

This thesis consists of six chapters:

Chapter 1 introduces the rationale for studying surface meltwater on Antarctic ice shelves, and introduces the key aim and research objectives of the thesis.

Chapter 2 provides a review of the literature on Antarctic ice shelves and remote sensing and machine learning methodologies.

Chapter 3 describes the development of a Fully Automated Supraglacial-Water Tracking algorithm for Ice Shelves (FASTISh), which is subsequently applied to the Nivlisen Ice Shelf for the 2016/2017 melt season.

Chapter 4 describes the development and validation of a Random Forest Classifier, capable of detecting slush and ponded water across all Antarctic ice shelves. The classifier is also applied to the Roi Baudouin Ice Shelf between 2013 and 2020.

Chapter 5 presents a record of slush and ponded meltwater across the main eight Antarctic Peninsula ice shelves between 2013 and 2021. The methods used for this were introduced in Chapter 4.

Chapter 6 synthesises the key developments made through the work presented in this thesis, and highlights potential areas for future research.

1.4 Publications from this thesis

The material presented in Chapter 3 has been published (Dell et al., 2020a), and the material presented in Chapter 4 is currently under peer review (Dell et al., in review). For each of these publications, the co-authors (who are named in author contribution statements at the start of each relevant chapter and within the author contribution statements at the end of each publication) helped with research oversight, and/or provided raw data (e.g. climate data), provided data processing scripts (e.g. per pixel top-of-atmosphere (TOA) conversion scripts), and provided feedback during the

development of, and writing of, each publication. For both publications mentioned above, the analysis and manuscript writing was undertaken by the author of this thesis.

Chapter 2

Literature review

This chapter provides a brief introduction to the background literature and knowledge that underpins this thesis. It is divided into two sections: Section 2.1 focuses on the significance of Antarctic ice shelves and the factors that contribute to their mass loss, with a specific focus on surface melt and hydrology; and Section 2.2 introduces remote sensing and machine learning methodologies that have recently been, or are currently being, used in the study of ice-shelf surface hydrology.

2.1 Antarctic ice shelves

75% of Antarctica's perimeter is bordered by ice shelves (Fürst et al., 2016), which are floating extensions of the grounded ice sheet. Ice shelves are important as they buttress the flow of inland ice, and therefore inhibit ice discharge into the Southern Ocean (Scambos et al., 2004; De Rydt et al., 2015; Gudmundsson et al., 2019). If an ice shelf thins or disintegrates, its buttressing effect may be reduced or lost, which can facilitate increased mass loss from the ice sheet (Dupont and Alley 2005; Fürst et al., 2016; Gudmundsson et al., 2019). In addition, ice-shelf thinning can result in ocean freshening which can impact ocean circulation patterns (Hellmer, 2004), and also contribute to steric sea level rise (Shepherd et al., 2012; Hogg et al., 2020). Ice shelves are predominantly vulnerable to melting at their bases, due to rising oceanic temperatures (Pritchard et al., 2012; Smith et al., 2020), but also on their surfaces, due to rising atmospheric temperatures (van den Broeke, 2005; Gilbert and Kittel, 2021).

Around the Antarctic continent, high basal melt rates have been identified under ice shelves along the Amundsen and Bellingshausen Sea coastlines (Pritchard et al., 2012; Depoorter et al., 2013; Rignot et al., 2013) due to influxes of circumpolar deep water (CDW) (Pritchard et al., 2012; Adusumilli et al., 2020). For example, high basal melt rates have been identified at the Pine Island (6 m a^{-1}) and Getz (2 m a^{-1}) ice shelves (Pritchard et al., 2012), which have contributed towards the net thinning of both ice shelves (Fürst et al., 2016).

In addition to ocean-driven basal melting, ice shelves can undergo surface melt, which results in surface lowering and, when sustained, ice-shelf thinning (Paolo et al., 2015). Surface meltwater is initially stored in the firn layer on the ice shelf surface. The firn layer can be defined as an ice matrix that holds interstitial air within an irregular, interconnected pore space (Kuipers Munneke et al., 2014). If the FAC of the firn layer is high enough, then surface meltwater percolates into it, and often refreezes within the pore spaces (Figure 2.1) (Kuipers Munneke et al., 2014). However, the FAC can be depleted over time if the volume of pore space occupied by freezing meltwater exceeds the accumulation of fresh snowfall (Lenaerts et al., 2017; Bevan et al., 2017). In this scenario, surface meltwater either moves across the ice shelf and into crevasses, floods the firn (to form 'slush') (Scambos et al., 2000), or ponds in surface depressions forming surface lakes (Scambos et al., 2000; Kuipers Munneke et al., 2014). Surface lakes, streams, and rivers form surface drainage systems, and in some cases are highly connected, facilitating lateral meltwater transfer across the ice-shelf surface (Kingslake et al., 2017).

Ice shelf surface melt can have implications for ice-shelf stability by: (i) driving stress variations due to the ponding, drainage and transfer of meltwater across the ice shelf (discussed further in Section 2.1.2.2) (Scambos et al., 2000, 2003; MacAyeal et al., 2003; Banwell et al., 2013, 2019, 2021; Banwell and MacAyeal, 2015; Banwell, 2017), and (ii) causing firn densification and new ice formation, and therefore increasing an ice-shelf's vulnerability to surface meltwater ponding and subsequent hydrofracture (Hubbard et al., 2016; Ashmore et al., 2017; Bevan et al., 2017). Hydrofracture occurs when a hydrostatic pressure exceeds cryostatic pressure, resulting in the propagation

of a water-filled crevasse or rift (van der Veen, 2007; Das et al., 2008; Tsai and Rice, 2010; Chu, 2014).

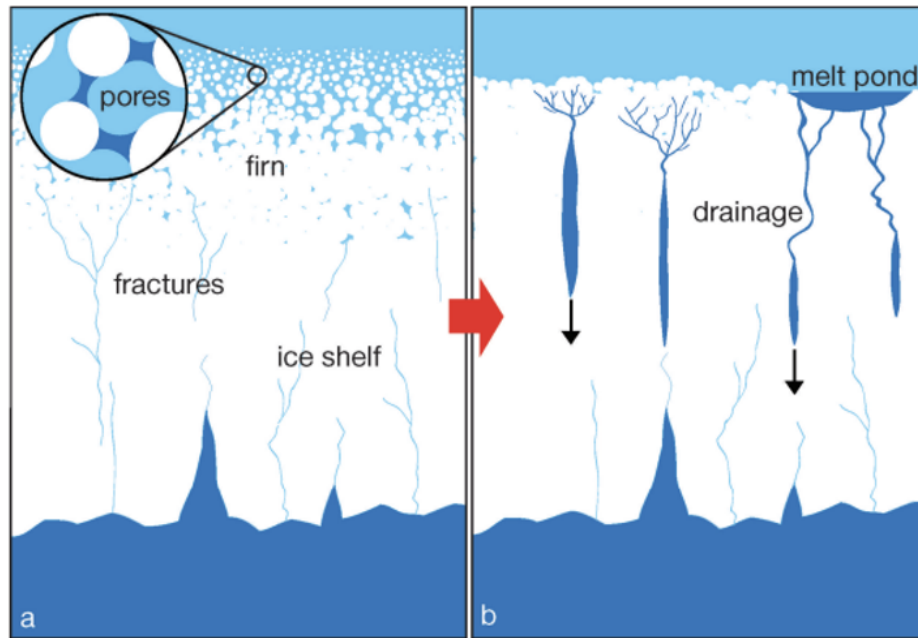


Figure 2.1: Conceptual diagram showing the process of firn air depletion and how it relates to ice-shelf hydrology (Kuipers Munneke et al., 2014). a) An ice shelf with sufficient FAC, meaning meltwater can be stored within the firn. b) An ice shelf with insufficient FAC, meaning meltwater can pond on the ice-shelf surface, and may drain through fractures.

Firn densification and the formation of ice lenses and ice slabs result from cycles of meltwater ponding and refreezing, which alters the physical properties of the ice. These features have been studied in most detail across the Greenland Ice Sheet, and these studies provide an understanding of the potential formation of ice layers on Antarctic ice shelves. Thin (0-10 cm) ice lenses can form in a single melt season within the percolation zone on the Greenland Ice Sheet, whilst thicker (10 cm - 1 m) ice layers are multiannual features (e.g. Benson, 1962; MacFerrin et al., 2019). These ice layers of varying thickness (0 - 1 m) generally reduce percolation rates but not enough to induce large-scale run off, partly as they have limited horizontal extents (e.g. Benson, 1962). Ice slabs are over 1 m thick and generally have a larger horizontal extent

(MacFerrin et al., 2019). These slabs reduce the near-surface permeability to near zero, and encourage large scale run-off (Sommers et al., 2017; Heilig et al., 2018). For example, the 2012 extreme melt event across the Greenland Ice Sheet led to the formation of extensive ice slabs, which have reduced the permeability of much of the percolation zone, resulting in increased surface meltwater run-off (MacFerrin et al., 2019; Culberg et al., 2021).

Whilst fewer studies have focussed on the formation of ice lenses and ice slabs in Antarctica, on the Larsen C Ice Shelf a 16 km-wide layer of subsurface ice was detected beneath a region prone to intermittent meltwater ponding (Hubbard et al., 2016). This layer was composed of two units: (i) an upper unit of solid ice, formed by the continual re-freezing of meltwater; and (ii) a lower unit of very dense firn, formed by the freezing of meltwater as it infiltrates the firn pack (Hubbard et al., 2016).

To date, ice-shelf retreat and disintegration have been most prominent on the Antarctic Peninsula, where between the 1950s and the summer of 2008/2009, the total area of ice shelves was reduced by more than 28,000 km² (Cook and Vaughan, 2010). Significant collapse has been documented at the Larsen B, Müller, and Wilkins ice shelves, and complete disintegration has been documented at Larsen A, Jones, Prince Gustav and Wordie ice shelves (Cook and Vaughan, 2010). Whilst many of the remaining ice shelves on the Antarctic Peninsula appear to be relatively stable, glaciological changes have been identified recently at Bach Ice Shelf and the northern George VI Ice Shelf, which could lead to the removal of passive shelf ice (Holt and Glasser, 2021). Whilst the ocean-driven changes observed along the Bellingshausen coastline (which borders part of the Antarctic Peninsula) cannot be ignored, the differing stability of ice shelves on the Antarctic Peninsula has been largely attributed to the atmospheric thermal limit of viability; the -9°C isotherm (Morris and Vaughn, 2003, Cook and Vaughn, 2010).

Of the ice shelves on the Antarctic Peninsula that have undergone collapse, the near-complete, and rapid (in less than a few weeks) disintegration of the Larsen B Ice Shelf in 2002 is the most documented, attributable in part to the availability of cloud-free satellite imagery before and after the collapse event (Scambos et al., 2003, 2009; Glasser and Scambos 2008; Leeson et al., 2020).

Since the collapse of Larsen B, an increasing number of studies have focussed on ice-shelf surface hydrology around Antarctica, and the significance of surface melt and hydrology on the long-term evolution of ice shelves (e.g. Arthur et al., 2020a ; Banwell et al., 2014; Langley et al., 2016; Bell et al., 2017; Kingslake et al., 2017; Macdonald et al., 2019; Stokes et al., 2019). These studies have been facilitated through the improved spatial, temporal, and spectral resolution of satellite imagery over time. For example, as a result of such advances, at least 696 drainage systems were identified across Antarctic ice shelves from the analysis of optical airborne and satellite imagery between 1947 and 2015 (Kingslake et al., 2017) (Figure 2.2). Surface drainage systems are now known to be widespread and pervasive across Antarctic ice shelves, although further studies are required to examine the impacts of these drainage systems on current and future ice-shelf stability. These surface drainage systems, and the factors that control their distribution through space and time, will be the focus of the remainder of Section 2.1.

2.1.1 Controls on ice-shelf surface melt

The distribution of Antarctic surface meltwater is influenced by regional climate and also influenced by local-scale processes (e.g. local foehn and katabatic winds, and the exposure of blue ice and bedrock) (Bell et al., 2018). Regional-scale climate shifts, such as the rapid atmospheric warming that was recorded between the 1950s and 2000s (King et al., 2003; Turner et al., 2006, 2014), have contributed to ice-shelf retreat and disintegration across the Antarctic Peninsula (Bevan et al., 2020; Banwell et al., 2021; Gilbert and Kittel 2021). This observed atmospheric warming that began in the 1950s was predominantly driven by a switch to a positive phase in the Southern Annular Mode (SAM), which is also often called the Southern Oscillation, and is the principal mode of variability in the Southern Hemisphere (Marshall, 2007; Lee et al., 2019). This trend was predominantly driven by anthropogenic depletion of stratospheric ozone (Fogt et al., 2009; Thompson et al., 2011). When the SAM is in a positive phase, the strength of westerly winds increases and they shift towards the pole

(Lee et al., 2019). These strengthened westerly winds deliver warm maritime air across the Antarctic Peninsula and to its eastern ice shelves in particular (Marshall et al., 2006; Turner et al., 2014), increasing surface melt rates there.

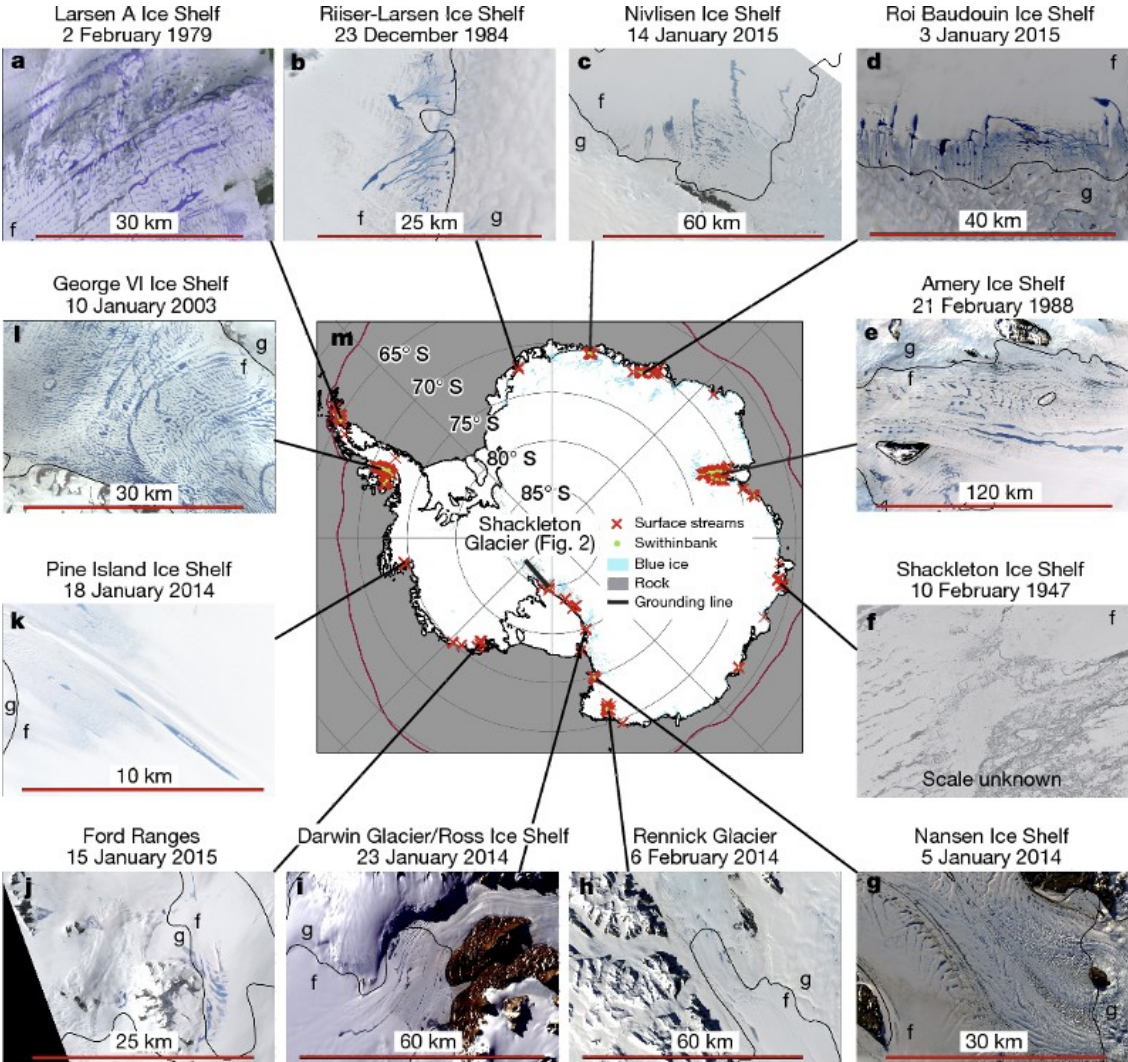


Figure 2.2: Examples of surface meltwater drainage systems across various Antarctic ice shelves (Kingslake et al., 2017). Images a-i show the drainage systems mapped by the study, which are represented by red crosses on the central image. Black lines on images a-l mark the grounding line, and letters 'f' and 'g' further mark grounded vs. floating ice.

However, the effects of a positive SAM vary across Antarctica and between seasons; (Marshall, 2007) investigated the relationship between the SAM and near-surface temperatures between 1957 and 2004. The tightening of the polar vortex caused by a

positive SAM results in warmer near-surface temperatures, over the Antarctic Peninsula (Picard et al., 2007; Bevan et al., 2020), but colder near-surface temperatures elsewhere on the continent. Furthermore, the study finds these correlations to be strongest during the austral summer and austral autumn; in the austral autumn the contribution of the SAM to changes in near-surface temperatures exceeds 1°C at seven of the 14 stations that were investigated (Marshall, 2007).

Whilst the Antarctic Peninsula was characterised by regional warming between the 1950s and 1990s, studies have identified downward trends in annual mean temperatures since then (Figure 2.3), as a consequence of cyclonic conditions in the northwestern Weddell Sea and Drake Passage which resulted from a strengthening of the mid-latitude jet (Turner et al., 2016). These changes in circulation patterns also resulted in sea ice advection towards the East Coast of the Antarctic Peninsula, further amplifying the cooling trends (Turner et al., 2016). However, in the 2019/2020 melt season, surface melting was a record high both in terms of the cumulative days of melting and areal extent across the George VI Ice Shelf (Banwell et al., 2021).

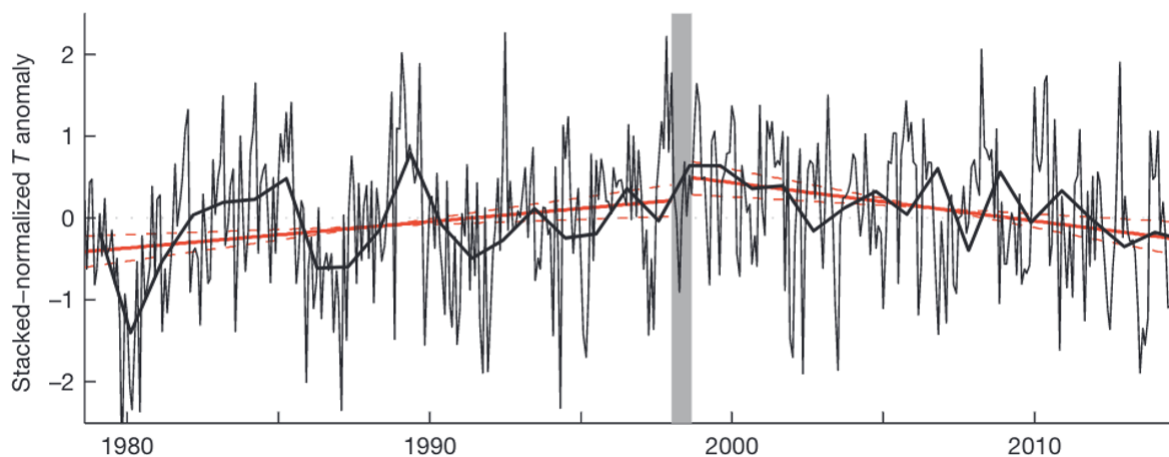


Figure 2.3: Air temperatures across the Antarctic Peninsula from 1979-2014 after Turner et al. (2016, their Figure 2a). The thin black line displays stacked-normalised surface air temperature anomalies, and the thick black line displays these data as mean annual values. The red line marks the two linear trends for the cooling and warming periods within 95% confidence limits (marked by the dashed red lines).

In addition to regional-scale climate dynamics, local foehn and katabatic winds also drive melt across Antarctic ice shelves. Warm foehn winds are formed as air is dried and warmed adiabatically as it flows down the leeward side of a mountain (Cape et al., 2015; Elvidge et al., 2020). More specifically, across the Antarctic Peninsula, foehn events are the result of interactions between circumpolar westerly winds and topography (Datta et al., 2019). The duration and frequency of foehn winds exerts a strong influence over regional temperature variability and is thought to have led to extensive surface melting across the eastern Antarctic Peninsula (Cape et al., 2015). Furthermore, a strong positive correlation between foehn wind frequency and a positive SAM was found across the Antarctic Peninsula between 1999 and 2010 (Cape et al., 2015).

Katabatic winds flow downslope, away from the interior of the ice sheet and towards the coastline. They mix and warm the air as they flow downwards, facilitating snow erosion and raising near-surface temperatures (Lenaerts et al., 2017). Evidence for enhanced melting as a result of katabatic winds has been found over Dronning Maud Land, the Ross Ice Shelf, and the Amery Ice Shelf (Liu et al., 2006; Trusel et al., 2012; Lenaerts et al., 2017).

Additionally, local-scale weather conditions, such as those observed by Banwell et al. (2021) on the George VI Ice Shelf may also drive melt events on ice shelves. The record melting observed across George VI Ice Shelf in 2019/2020 was attributed to sensible heat delivered at relatively low velocities by warm northeasterly and northwesterly winds. These northerly winds could have been driven by the Indian Ocean Dipole, which reached a record high early in the 2019/2020 melt season (Bevan et al., 2020).

As well as winds, local-scale processes such as the exposure of blue ice and bedrock can lead to increased melting of an ice-shelf surface due to the melt-albedo feedback (Kingslake et al., 2017; Lenaerts et al., 2017; Bell et al., 2018). Blue ice, which is often called 'bare ice', is defined as snow free-ice (e.g. Orheim and Luchitta, 1990) The exposure of blue ice and bedrock surfaces lowers the surface albedo relative to nearby

snow surfaces, increasing absorption of shortwave solar radiation, and thus increasing local melt rates. This effect is typically seen towards ice-shelf grounding lines, where katabatic winds often drive snow erosion (Lenaerts et al., 2017). Therefore, meltwater drainage systems on Antarctic ice shelves often originate from these low-albedo areas (Winther et al., 1996; Liston and Winther, 2005), making local scale processes (foehn winds, katabatic winds, blue ice and bedrock exposure) key controls on the spatial distribution of ice-shelf surface melt, the focus of the following section (2.1.2).

2.1.2 Surface meltwater storage

Local-scale processes such as the exposure of bedrock and blue ice due to wind erosion (see Section 2.1.1) can impact both the amount of surface meltwater generated, and also the organisation of surface meltwater system networks. Water generated by surface melting may: i) refreeze at the surface (Langley et al., 2016); ii) percolate vertically into snow/firn, and in some cases refreeze (Kuipers Munneke et al., 2014); iii) percolate vertically and flow laterally beneath the surface; iv) form surface lakes (Arthur et al., 2020b); or v) form interconnected stream networks that may link the surface and subsurface lakes/reservoirs, which may then flow towards or even reach the ice-shelf margin (Bell et al., 2017). Meltwater is therefore stored at the ice-shelf surface either as saturated firn ('slush'), in surface lakes, or it may flow in surface streams. Each of these three types of meltwater storage features, and their implications for mass balance, are discussed in more detail below.

2.1.2.1 Slush

Slush forms when the snow-pack or firn-pack is saturated, and often borders shallow areas of ponded water (Bell et al., 2017; Moussavi et al., 2020). It is prevalent and widespread across numerous Antarctic ice shelves, and has been identified specifically on the Nivlisen (Lefroy and Arnold, 2020), Nansen (Bell et al., 2017), and Shackleton (Arthur et al., 2020a) ice shelves. On a small section of the Nansen Ice Shelf, a study which mapped the areas of slush and medium and deep meltwater (water that is equal to or greater than 0.2 in depth) for the 2013/2014 melt season found the area of slush to be greatest in December 2013, and to decline in January 2014 (Bell et al., 2017). However, beyond this very little research has investigated the spatially and temporally varying extents of slush on ice shelves.

2.1.2.2 Surface lakes

Surface lakes collect in surface topographic depressions on ice shelves and form due to: (i) flexure at the grounding line (Walker et al., 2013); (ii) pressure rolls (LaBarbera and MacAyeal, 2011); (iii) basal crevasses (McGrath et al., 2012); (iv) basal channelling (Le Brocq et al., 2013); or (v) incomplete flexural rebound from previous lake-drainage events (Banwell and MacAyeal, 2015). Furthermore, for a lake to form, the base of the depression needs to be impermeable, in the form of bare ice or saturated firn (slush) (Scambos et al., 2000; Bevan et al., 2017; Lenaerts et al., 2017; Macdonald et al., 2018). Layers of slush may form above impermeable ice layers. Lakes may form in situ, or meltwater may be routed to lakes via streams, which capture meltwater from the surrounding catchment area (Banwell et al., 2012; Leeson et al., 2012). The basin of a lake may also deepen over time as meltwater collects, as a result of enhanced lake-bottom ablation, as has been modelled and measured on the Greenland Ice Sheet (Lüthje et al., 2006; Tedesco et al., 2012), as well as the flexural

response of the floating ice shelf to the ponding meltwater, which acts as a load (Banwell and MacAyeal, 2015; MacAyeal et al., 2015).

Surface lakes form predominantly in the melt season, which can stretch from November to April. They may evolve over time before: (i) rapidly draining (Banwell et al., 2013; Langley et al., 2016); (ii) slowly over-spilling into neighbouring lakes and/or streams (Langley et al., 2016; Macdonald et al., 2018); (iii) freezing through (Langley et al., 2016); (iii) freezing-over (Arthur et al., 2020a); or (iv) becoming buried by snowfall (Lenaerts et al., 2017; Dunmire et al., 2020). On the Greenland Ice Sheet's grounded ice, lake drainage events have also been categorised as 'slow' or 'fast' (Selmes et al., 2011; Fitzpatrick et al., 2014; Williamson et al., 2017; Williamson et al., 2018a, 2018b). Evidence suggests that rapid lake drainage occurs via hydrofracture, although still little is known about the conditions that initiate a hydrofracture event (Williamson et al., 2018b). In contrast, slow-draining lakes drain by over-spilling and the incision of an outlet channel (Hoffman et al., 2011; Tedesco et al., 2013; Koziol et al., 2017). Similar observations have been made across Antarctic ice shelves, with slow drainage events being observed on the McMurdo Ice Shelf, where a lake drained by channel incision and overflow (Banwell et al., 2019) and rapid drainage events have been both inferred (Scambos et al., 2009) and modelled on the former Larsen B Ice Shelf (Banwell et al., 2013; Robel and Banwell 2019).

The collapse of the Larsen B Ice Shelf in 2002 highlighted the significance of surface meltwater lakes and rapid drainage events for ice-shelf instability (Scambos et al., 2003; 2009; Glasser and Scambos, 2008; Banwell et al., 2013; Robel and Banwell, 2019). Prior to collapse, 5.3% of the Larsen B Ice Shelf was covered by surface lakes, which appeared to drain near-simultaneously in the weeks preceding the ice-shelf's disintegration (Banwell et al., 2014, 2021). A chain-reaction lake-drainage mechanism has been proposed as the process behind this, whereby a single lake drainage event generated sufficient flexural stresses to initiate the drainage of neighbouring lakes, which led to the widespread hydrofracture and drainage of surface lakes across the majority of the ice shelf (Figure 2.4) (Banwell et al., 2013). Fragments of the ice shelf (i.e. icebergs) then dispersed rapidly due to iceberg-capsize energy (Banwell et al.,

2013; Burton et al., 2013; Macayeal and Sergienko, 2013), a process which helped to accelerate the ice-shelf break-up process.

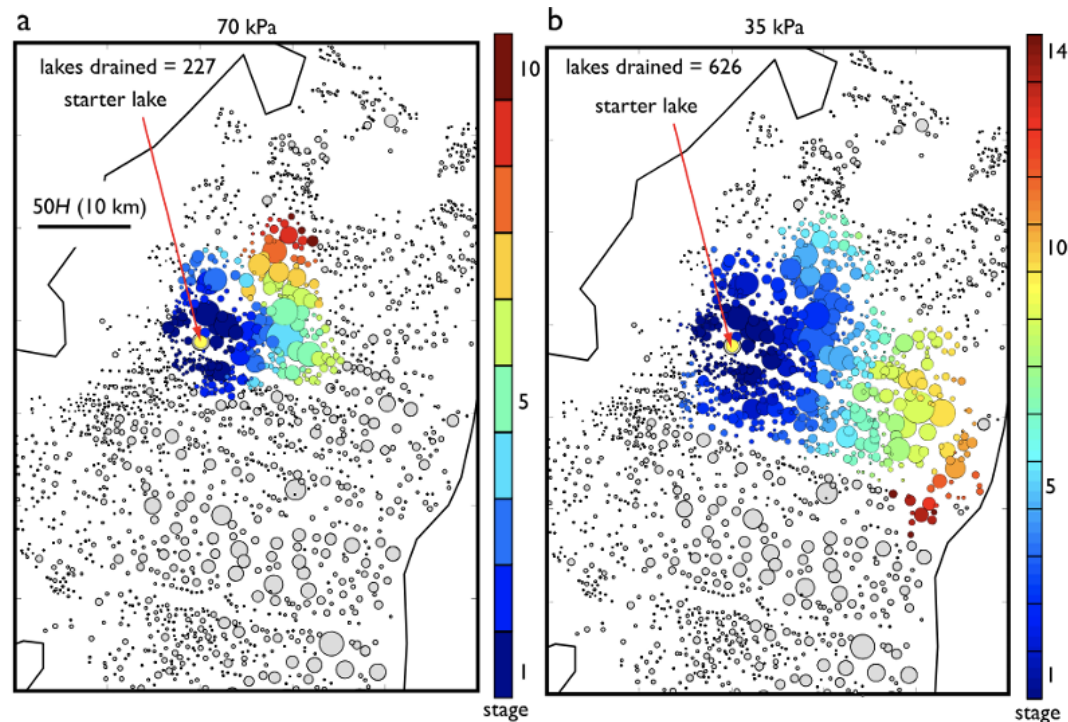


Figure 2.4: Results of a simulation to show a chain reaction of lake drainage events on the Larsen B Ice Shelf (Banwell et al., 2013). Circular disk loads represent lakes observed by Glasser and Scambos (2008). The colour of each lake indicates the stage when a lake drains within the simulation, with stage 1 representing drainage events that directly result from the drainage of the starter lake. a) uses a fracture criterion of 70 kPa and b) uses a fracture criterion of 35 kPa.

Given the potential for ponded surface meltwater to drive such rapid ice-shelf collapse, it is important that the quantity of surface meltwater across Antarctica's remaining ice shelves is monitored closely. Furthermore, it is important that the hydrological processes occurring on these ice shelves are better understood, and that such processes are incorporated into predictive models, which will improve estimates of Antarctica's future contributions to sea level rise.

In the years prior to its disintegration, Larsen B exhibited signs of structural weakening and damage (Vieli et al., 2007; Borstad et al., 2012), in the form of open rifts and crevasses at its shear zones. These weakened shear zones preconditioned the ice shelf for collapse, as surface meltwater became more widespread (Leeson et al., 2020) and penetrated these fractures, inducing further propagation (Glasser and Scambos,

2008). Similar structural weakening has also been observed in the Amundsen Sea Embayment, specifically at the Pine Island Thwaites shear margins (MacGregor et al., 2012; Joughin et al., 2014; Alley et al., 2019). Limited future surface melt has been projected in this region (Trusel et al., 2015; Gilbert and Kittel, 2021), making a complete disintegration event through similar mechanisms to those observed at Larsen B unlikely (Datta et al., 2019). However, as discussed in Section 2.1, basal melting in this region due to influxes of circumpolar deep water is likely to drive ice-shelf thinning (e.g. Pritchard et al., 2012; Adusumilli et al., 2020), leading to net mass loss (Smith et al., 2020).

In addition to surface lakes, meltwater can also be stored within buried (sometimes called ‘englacial’ or ‘subsurface’) lakes, which are situated within the firn pack, up to several metres below the ice-shelf surface (Lenaerts et al., 2017; Bell et al., 2018; MacAyeal et al., 2019; Dunmire et al., 2020), or within deeper firn aquifers (Schaap et al., 2019; Montgomery et al., 2020; Dunmire et al., 2021; MacDonell et al., 2021; Van Wessem et al., 2021). However, as both of these types of features exist beneath the surface of the ice shelf, they are not detectable in optical satellite imagery (Dunmire et al., 2020), and are therefore not investigated further within this thesis.

2.1.2.3 Surface streams and rivers

As described above, surface streams facilitate the transfer of water across ice shelves and are therefore a crucial part of their hydrological regime. They may: (i) transport meltwater to topographic depressions on the surface to form lakes; (ii) transport water to snow/firn regions where the water disappears beneath the surface (Kingslake et al., 2017); (iii) connect series of surface lakes (Kingslake et al., 2017); (iv) flow into rifts and fractures (Banwell et al., 2017); or v) flow off the edge of the ice shelf into the ocean as a waterfall (Bell et al., 2017).

Surface streams may also help to militate against ice-shelf instability (Banwell et al., 2017), depending on their characteristics. For example, the Nansen Ice Shelf has a

persistent drainage network which is dominated by a surface river that terminates in a 130 m waterfall at the ice-shelf edge (Bell et al., 2017) (Figure 2.5). This surface drainage network is large enough to export the ice shelf's total annual melt in only seven days and may act, therefore, to militate against ice-shelf instability as it prevents water build-up on the ice-shelf surface (Bell et al., 2017). This behaviour, however, appears to be atypical for an ice shelf; surface meltwater on other ice shelves generally appears to be retained within streams, lakes, or within the snow/firn layer, where it may freeze during the winter, or (if sufficiently insulated) remain as liquid water (Kuipers Munneke et al., 2018).



Figure 2.5: 130 m wide waterfall exporting surface melt off the Nansen Ice Shelf – 12 January 2013. Photo taken by Robert Fletcher (Bell et al., 2017).

2.1.3. Potential impact of increased future surface melting

The degree to which ice shelves will impact the Antarctic Ice Sheet's response to future atmospheric warming is dependent on: (i) the accumulation of surface meltwater on each ice shelf; (ii) the degree of vulnerability each ice shelf has to hydrofracture if it was to become inundated with meltwater; and (iii) the level of buttressing provided by each ice shelf (Figure 2.6) (Lai et al., 2020). At present, many of the ice-shelf areas inundated with meltwater are stable, and do not appear to be vulnerable to

hydrofracture; George VI Ice Shelf is a good example of such an ice shelf, due to its compressive flow regime. However, $60 \pm 10\%$ of the area of Antarctica's ice shelves both buttress grounded upstream ice, and are vulnerable to structural damage by hydrofracture if they become covered by meltwater (Lai et al., 2020).

For the reasons explained above, a number of studies have modelled surface melt, run off, surface mass balance and potential contributions to global sea levels across Antarctica, using the Coupled Model Intercomparison Project (CMIP) scenarios (DeConto et al., 2021; Edwards et al., 2021; Gilbert and Kittel, 2021; Kittel et al., 2021). CMIP5 and CMIP6 models were used to force the Modèle Atmosphérique Régional (MAR) model to investigate the future surface mass balance of ice shelves under 1.5°C, 2°C, and 4°C of warming above the pre-industrial temperature baseline (Gilbert and Kittel, 2021). If 4°C warming is reached, 34% of Antarctica's ice shelves (including Shackleton Ice Shelf, Larsen C Ice Shelf, Pine Island Glacier Ice Shelf, and Wilkins Ice Shelf) will experience increased surface meltwater runoff, as the snowpack is saturated, and it is therefore likely that these ice shelves are vulnerable to hydrofracture (Gilbert and Kittel, 2021). However, the modelled surface mass balance changes across Antarctica's ice shelves vary greatly depending on the CMIP scenario applied. For example, simulations by Kittel et al. (2021) project surface mass balance anomalies ranging from $+28 \text{ Gt yr}^{-1}$ to -335 Gt yr^{-1} . Ultimately, the future surface mass balance of Antarctic ice shelves is heavily dependent on the future climate pathway that is taken. This highlights the significance of anthropogenic forcing for the fate of the East and West Antarctic ice sheets, and global mean sea levels (Trusel et al., 2015).

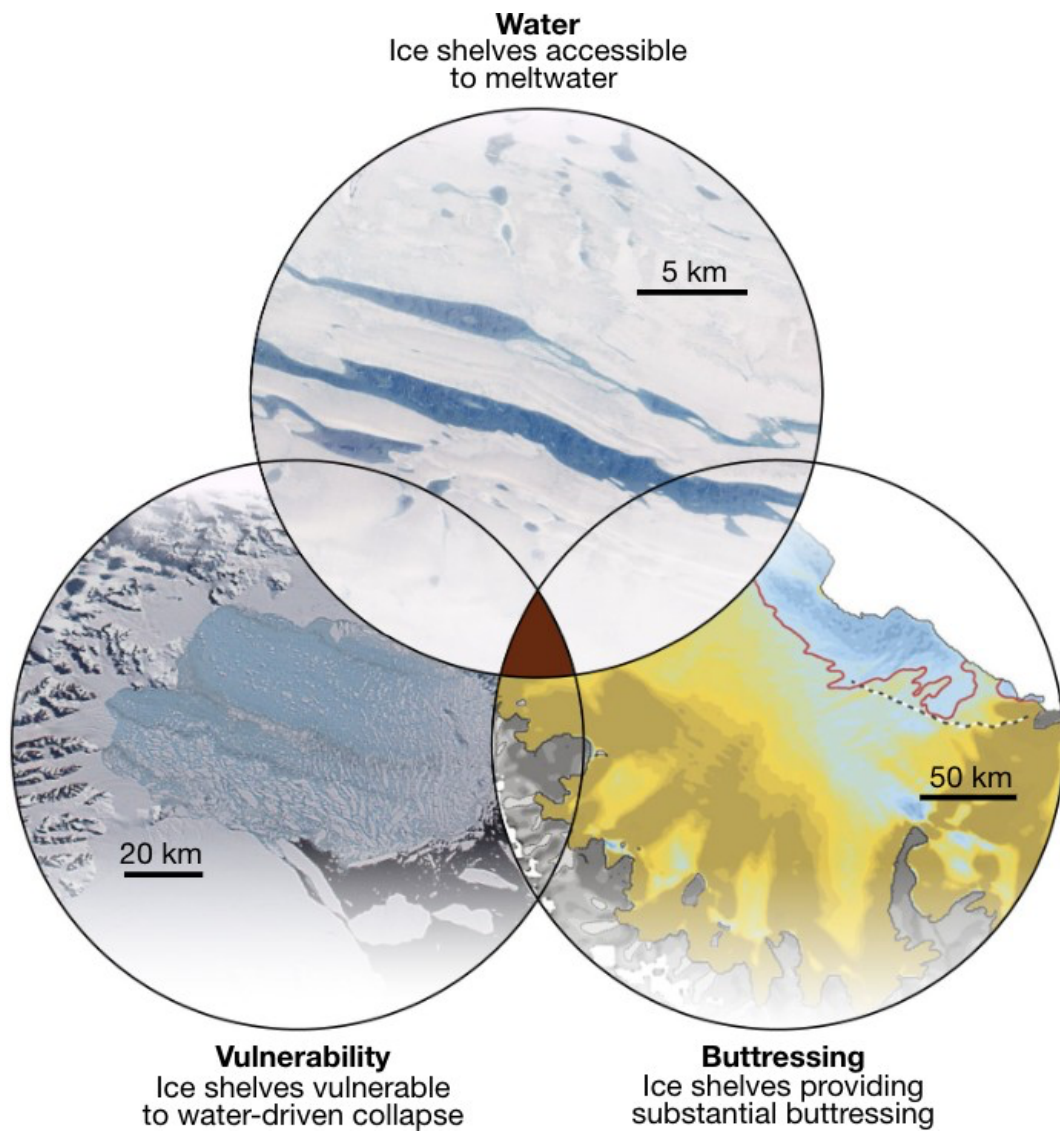


Figure 2.6: A venn diagram conceptualising the three factors that govern the degree to which ice shelves control the Antarctic Ice Sheet's response to atmospheric warming (Lai et al., 2020): The top circle represents regions of meltwater accumulation (image of Amery Ice Shelf from Landsat 4, NASA, 21-Feb-1989), the bottom left represents ice shelf regions vulnerable to hydrofracture (image of Larsen B Ice-Shelf collapse from Moderate Resolution Imaging Spectroradiometer (MODIS), NASA, 07-Mar-2002), and the bottom right represents ice-shelf regions that provide buttrressing to grounded ice, where blue regions are less significant for buttrressing than yellow regions (image reproduced from Fürst et al. (2016), Figure 2.3).

2.2 Remote sensing

Remote sensing uses a range of tools, sensors, data and techniques to study the Earth and Earth surface processes without making physical contact with the object being examined, through either in situ, airborne, or spaceborne sensors (Rees, 2005; Cracknell, 2007; Rees, 2012; Tedesco, 2015) It uses part(s) of the electromagnetic spectrum, recording the amount of energy emitted or reflected by a target object (Aggarwal, 2004). Human eyes are capable of registering solar light that is reflected by a target object within the 400 to 700 nm range of the electromagnetic spectrum, but tools within remote sensing enable us to visualise electromagnetic radiation outside of this range (Aggarwal, 2004).

Whilst early remote sensing of the Earth evolved from photographing from flight (Rees, 2005; Cracknell, 2007; Rees, 2012; Tedesco, 2015), the majority of present day remotely sensed observations are made from satellites, which image much of the Earth's surface. Landsat 1 was the first satellite to be launched with these capabilities, and this launch was followed by a series of other Landsat satellites (Landsat 1 - Landsat 8), with the launch of Landsat 9 originally planned for late 2020 (Markham et al., 2016) and now for 2021 (Markham et al., 2020). Many additional instruments with Earth imaging capabilities now exist, such as MODIS, Sentinel-1 and Sentinel-2.

Remote sensing instruments are categorised as either passive or active. Passive sensors measure naturally reflected radiation from the target body, whilst active sensors transmit signals from the sensor itself, and record the signal returned by the target body (Tedesco, 2015). Examples of passive sensors include those which operate within the visible range (400-700 nm) of the electromagnetic spectrum, by measuring the amount of light reflected from the target object (e.g. the Operational Land Imager (OLI) on board Landsat8) (Tedesco, 2015). Examples of active sensors include Synthetic Aperture Radar (SAR) sensors, such as those on board Sentinel-1, which are capable of measuring Earth surface properties regardless of the presence

of clouds or solar illumination, making them useful additions to the suite of available remote sensing tools.

Owing to the advantages discussed above, remote sensing methodologies are frequently used to investigate the surface hydrology of the Greenland and Antarctic ice sheets (e.g. Banwell et al., 2014; Kingslake et al., 2017; Williamson et al., 2017; Macdonald et al., 2018; Williamson et al., 2018a). In particular, the improved spatial and temporal resolution of freely available optical satellite imagery (e.g. Landsat 8 and Sentinel-2) has facilitated numerous studies of surface water bodies on ice (e.g. Bell et al., 2017; Kingslake et al., 2017; Williamson et al., 2017; Macdonald et al., 2018; Williamson et al., 2018a). These satellites (Landsat 8 and Sentinel-2) and the specific methods used to process such data for the study of ice sheet surface hydrology will be reviewed in the following sections.

2.2.1 Landsat 8

The Landsat satellite missions range from Landsat 1 (launched in 1972) to Landsat 8 (launched in 2013). The Landsat 8 satellite (from which data is used throughout this PhD) has a sun-synchronous, near-polar orbit. It operates on a 16-day repeat cycle and acquires scenes on the Worldwide Reference System-2 path/row system. The size of each scene is 185 km × 180 km. There are two instruments on board Landsat 8: the OLI and the Thermal Infrared Imager (TIRS) (Roy et al., 2014). The OLI collects data for 9 spectral bands; eight have a 30 m spatial resolution, and one (the panchromatic band) has a 15 m spatial resolution (Table 2.1). The TIRS collects thermal data within two bands, which have a native resolution of 100 m (Roy et al., 2014).

In 2017, a tiered collection management strategy was implemented for all Landsat data products, as it was recognised that there was a need for consistency and usability across Landsat sensors to be improved. Therefore, the full Landsat record (i.e. from Landsat 1 to Landsat 8) was reprocessed into Collection 1 (Dwyer et al., 2018). Within

Collection 1 there are three tiers: (i) Real Time (RT); (ii) Tier 1 (T1); and (iii) Tier 2 (T2). Landsat 7 and 8 data are available within the RT tier within 12 hours of acquisition, and once their radiometric and geometric parameters have been calculated, they are assigned to either T1 or T2 (U.S. Geological Survey, 2018). T1 scenes meet a set of radiometric and geometric criteria, which requires the radial root mean square error (RMSE) to be ≤ 12 m. The remaining scenes are put into T2 (U.S. Geological Survey, 2018; Wulder et al., 2019).

Table 2.1: Key properties of the Landsat 8 OLI and TIRS bands. Near-infrared (NIR) and short-wave infrared (SWIR) are represented by their respective acronyms. Modified from (Roy et al., 2014).

Band	Spatial Resolution (m)	Wavelength (μm)
1 - Ultra-blue (coastal/aerosol)	30	0.43-0.45
2 – Blue	30	0.45-0.51
3 – Green	30	0.53-0.59
4 – Red	30	0.64-0.67
5 – NIR	30	0.85-0.88
6 - SWIR 1	30	1.57-1.65
7 - SWIR 2	30	2.11-2.29
8 – Panchromatic	15	0.50-0.68
9 – Cirrus	30	1.36-1.38
10 - Thermal Infrared	100	10.60-11.19
11 - Thermal Infrared	100	11.50-12.51

2.2.2 Sentinel-2

The Sentinel-2 mission consists of two sun-synchronous, polar orbiting satellites: Sentinel-2A and Sentinel-2B. Both satellites have a swath width of 290 km, and individual revisit times of 10 days, or 5 days when combined (Drusch et al., 2012). Sentinel-2A data, which is used throughout this PhD thesis, consists of 13 multispectral bands, with a spatial resolution between 10 and 60 m (Table 2.2). Sentinel-2 data products are available as Level-1C, which provides TOA reflectances, or as Level-2A, which provides bottom- of-atmosphere (BOA) reflectances, both in cartographic geometries.

Table 2.2: Key properties of the Sentinel-2 multispectral bands.

Band	Spatial Resolution (m)	Wavelength (μm)
1 - Ultra-blue (coastal/ aerosol)	60	0.43-0.46
2 – Blue	10	0.45-0.55
3 – Green	10	0.54-0.58
4 – Red	10	0.65-0.68
5 - Vegetation red edge	20	0.69-0.71
6 - Vegetation red edge	20	0.73-0.75
7 - Vegetation red edge	20	0.77-0.80
8 – NIR	10	0.76-0.91
8A - Vegetation red edge	20	0.85-0.88
9 - Water Vapour	60	0.93-0.96
10 - SWIR (cirrus)	60	1.34-1.41
11 – SWIR	20	1.54-1.69
12 – SWIR	20	2.08-2.32

2.2.3 Methods for lake area quantification

Threshold-based methods classify pixels based on their spectral properties, therefore enabling the identification of surface meltwater (Haibo et al., 2011). These methods typically include: (i) single band thresholds (Haibo et al., 2011), (ii) dynamic thresholds (Williamson et al., 2017) and (iii) multi-band (ratio) thresholds (Box and Ski, 2007; Yang and Smith, 2013). Single band thresholds utilise a single band only to identify wet pixels within an image scene, whilst dynamic thresholds utilise a kernel to compare the spectral reflectance of a central pixel to the mean value of a set of surrounding pixels (Selmes et al., 2011).

Early multi-band thresholds used static blue / red band ratio thresholds to identify surface meltwater on ice sheets (Box and Ski, 2007). The use of this ratio is based upon the knowledge that red wavelengths are attenuated more than blue wavelengths within a water column, and these differences could therefore be used to classify water covered pixels within image scenes (Banwell et al., 2014; Pope et al., 2016).

However, the majority of recent studies have used $NDWI_{ice}$ (Yang and Smith, 2013) for the purpose of classifying a pixel as either 'dry' or 'wet' (Fitzpatrick et al., 2014; Moussavi et al., 2016; Miles et al., 2017; Arthur et al., 2020a; Benedek and Willis, 2021). This calculates the normalised ratio of the blue band and the red band as:

$$NDWI_{ice} = (\text{blue band} - \text{red band}) / (\text{blue band} + \text{red band})$$

[1]

Where the blue band is equivalent to digital numbers in band 2 and the red band is equivalent to digital numbers in band 4 in both Landsat 8 and Sentinel-2 TOA scenes. Typically, across both Greenland and Antarctica, a $NDWI_{ice}$ threshold of 0.25 has been used to map surface water bodies (e.g. Doyle et al., 2013; Williamson et al., 2017; Banwell et al., 2019). However, in at least two studies, the $NDWI_{ice}$ equation has also

been used to map water area and provide a qualitative estimate of water depth. On both the Greenland Ice Sheet (Yang and Smith, 2013) and the Nansen Ice Shelf (Bell et al., 2017), water bodies were classified as shallow ($0.12 < NDWI_{ice} < 0.14$), medium-deep ($0.14 < NDWI_{ice} < 0.25$), or deep ($NDWI_{ice} > 0.25$).

2.2.4 Methods for lake depth quantification

Two main approaches exist within the literature for deriving quantitative estimates of surface lake depths: (i) the empirically-based approach (e.g. Liang et al., 2012); and (ii) the physically-based approach (Williamson et al., 2017). The empirically-based approach either assumes a first order relationship between lake area and lake volume, assuming the lake basin is cone shaped (Liang et al., 2012), or uses field data to derive a depth-reflectance curve from which pixel depths can be approximated. These pixel depths can then be summed and multiplied by pixel area to approximate lake volumes (Box and Ski, 2007; Fitzpatrick et al., 2014). As the empirically-based approach requires field data to derive a depth-reflectance curve, it is a site-specific approach, and is therefore not suitable for use in other regions, limiting its applicability (Williamson et al., 2017).

Therefore, for application across multiple regions or across the scale of the full ice sheet, studies use the physically-based depth approach. This approach has been successfully applied across both Antarctica (Arthur et al., 2020a; Fricker et al., 2021) and Greenland (Sneed and Hamilton 2007; Arnold et al., 2014; Pope et al., 2016; Williamson et al., 2017), and centers on light attenuation in a water column following the Beer-Lambert-Bouguer law (Williamson et al., 2017). In this relationship, which originates from (Philpot, 1989) pixel water depth (z) is calculated as:

$$z = \frac{[\ln(A_d - R_\infty) - \ln(R_{pix} - R_\infty)]}{g}$$

[2]

In this equation, A_d is the lake bottom albedo, R_{pix} is satellite-measured pixel reflectance, R_∞ is the returned reflectance value for optically deep water ($> 40\text{m}$), and g is the coefficient representing losses due to upward and downward travel within the water column. When using the physically-based approach to calculate lake depths using Landsat 8 scenes, studies opted to calculate lake depths using TOA reflectance data in both the panchromatic and red bands, and then average the results (Pope et al., 2016; Williamson et al., 2018a), as this approach minimised the mean difference between digital elevation model (DEM)-derived lake depths and spectrally-derived lake depths ($0.0 \pm 1.6 \text{ m}$) (Pope et al., 2016). As no panchromatic band exists in Sentinel-2 scenes, the red band only was used (Williamson et al., 2017).

The physically-based lake depth approach is based on a number of assumptions, as described fully by Pope et al. (2016). Briefly, these are: (i) there are no waves on the surface of the lake; (ii) the lake contains little to no dissolved or suspended sediment; (iii) there is no inelastic scattering; and (iv) the water body substrate is homogenous and parallel to the lake surface (Sneed and Hamilton, 2011). Furthermore, as red light is rapidly attenuated by a water column, the physically-based lake depth equation only works up to a maximum depth of approximately 5 m (Pope et al., 2016).

2.2.5 Methods for lake tracking

In addition to static measurements of lake and stream areas and depths, it is also possible to track the evolution of surface lakes on the Greenland Ice Sheet through space and time. The 'FASTER' (Fully Automated Supraglacial lake Tracking at Enhanced Resolution) algorithm (Williamson et al., 2018a) combines optical imagery from Landsat 8 and Sentinel-2 to identify lake evolution and rapid (≤ 4 day) lake drainage events over a melt season (Williamson et al., 2018a). This work demonstrates the potential for combining high-resolution optical satellite imagery to identify lake drainage events with an error of 1.1 days (Williamson et al., 2018a).

2.3 Machine learning methods

Machine learning methods apply artificial intelligence to create systems capable of automatically evolving and learning in response to an environment (El Naqa and Murphy, 2015). The basic model of machine learning is as follows: (i) information from an external environment (training data) is sent to the system; (ii) the system then learns from this external information, converting the information to knowledge; (iii) this knowledge is then stored in a repository; and (iv) the model then executes the output. The model may loop between execution and learning multiple times before the final product is delivered (Figure 2.7) (Wang et al., 2009).

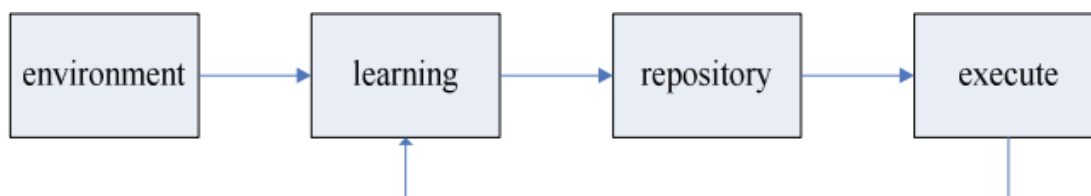


Figure 2.7: A basic machine learning model (Wang et al., 2009).

Machine learning is increasingly used within remote sensing studies (Pal and Mather 2003; Dirscherl et al., 2020, 2021; Halberstadt et al., 2020), as it offers an efficient and effective way to classify remotely sensed data (Maxwell et al., 2018). In comparison to traditional classifiers (such as threshold-based methods), machine learning classifiers are better at handling complex data with a high number of predictor variables or of high dimensionality (Hansen et al., 1996; Pal, 2005; Ghimire et al., 2012; Maxwell et al., 2018). Established machine learning methods include support vector machines (Rüping, 2001), single decision trees, boosted decision trees (Faddoul et al., 2012), Random Forests (Pal, 2005), artificial neural networks (Dongare et al., 2012), and k-nearest neighbors (k-NN) (Bezdek et al., 1986; Maxwell et al., 2018). This thesis uses a random forest classifier, and the remainder of this section will therefore provide further detail on this method.

2.3.1 Random Forest Classifiers

A random forest classifier is an ensemble classifier; it uses numerous uncorrelated decision trees based on sample subsets of the training data (Breiman, 2001; Pal, 2005; Belgiu and Drăgu, 2016; Maxwell et al., 2018; Dirscherl et al., 2020) which are amalgamated to produce an overall most-likely outcome. The randomly sampled data typically contain two thirds of the input training data, whilst the remaining training data are used as an Out-Of-Bag sample, for internal cross validation (Breiman, 2001; Dirscherl et al., 2020). The user inputs unclassified data to the random forest classifier, and each decision tree then individually votes for the most popular class for each input (Breiman, 2001; Pal, 2005). Unclassified input data are classified based upon the maximum votes from each individual decision tree, leading to a classification output (Breiman, 2001; Pal, 2005; Belgiu and Drăgu, 2016; Dirscherl et al., 2020). Random forest classifiers require only two user defined inputs; the number of decision trees and the number of variables to randomly sample at each node (Maxwell et al., 2018). Studies have shown that increasing the number of trees improves the classification accuracy up until a point, but that these returns diminish as additional trees are added (e.g. Pal, 2005; Shi and Yang, 2016; Behnamian et al., 2017; Maxwell et al., 2018). Therefore, once the number of trees is high enough, adding further trees does not improve the classification accuracy.

Random forest classifiers have recently been employed to map surface lakes on ice (e.g. Dirscherl et al., 2020, 2021; Halberstadt et al., 2020; Yuan et al., 2020). For example, Halberstadt et al. (2020) developed and tested numerous supervised classifiers using Landsat 8 imagery for the purpose of surface lake identification over the Amery and Roi Baudouin ice shelves. Overall, they found the random forest classifier to be the most successful method, as it returned a pixel-based accuracy score of 92.6% (Halberstadt et al., 2020). Furthermore, the training data used in their

study was generated using unsupervised k-means clustering; a clustering technique that assigns data points to clusters, aiming to minimise the variance within each cluster, whilst maximising the variance between different clusters (Ray and Turi, 1999; Arthur and Vassilvitskii, 2007). By using k-means clustering as opposed to manually selected training data, the study was able to utilise the full spectral diversity of the input data, which a human user could not fully interpret.

Similarly, Dirscherl et al. (2020) developed a random forest classifier capable of lake detection on Antarctic ice shelves, which they trained using auxiliary TanDEM-X data and Sentinel-2 scenes. The classifier was trained on 14 sites, and tested on eight additional sites, in order to produce a classifier capable of accurately mapping surface lakes across all Antarctic ice shelves. This work was then further developed (Dirscherl et al., 2021) using a convolutional neural network (CNN) to include input data from Sentinel-1 SAR, to facilitate the identification of surface lakes despite cloud cover and a lack of daylight. These methods were combined and applied to George VI Ice Shelf, providing a more complete picture of maximum surface lake extent, which returned a total meltwater coverage of 770 km² in January 2020.

Furthermore, the application of CNNs across the Greenland Ice Sheet has recently been used to automatically map buried lakes using a combination of Sentinel-1 SAR and Sentinel-2 optical imagery (Dunmire et al., 2021). Methods similar to this could feasibly be applied across Antarctica in the future, to detect buried water bodies.

Of the studies introduced above to map lake extents across Antarctic ice shelves, both Halberstadt et al. (2020) and Dirscherl et al. (2020) conduct all or part of the analysis within GEE, a free to use, cloud-based geoprocessing platform (<https://earthengine.google.com/>). Platforms such as GEE make machine learning methods, which would normally be computationally expensive and therefore hard to conduct without access to capital intensive high performance computing, accessible to anyone with access to the internet. This thesis also makes use of GEE to facilitate the development and application of these techniques across large areas of Antarctica for the period since 2013.

Chapter 3

Results I: Lateral meltwater transfer across an Antarctic ice shelf

Chapter published in **The Cryosphere**, July 2020. Small edits made for the purpose of this thesis.

Citation Dell, R., Arnold, N., Willis, I., Banwell, A., Williamson, A., Pritchard, H., & Orr, A. (2020). **Lateral meltwater transfer across an Antarctic ice shelf**. *The Cryosphere*, 14(7), 2313-2330. <https://doi.org/10.5194/tc-14-2313-2020>

Contributions Rebecca Dell developed the methodology and scripts, building on the prior work of Andrew Williamson. Neil Arnold developed the script to convert Landsat Digital Number (DN) values to per-pixel TOA values. Andrew Orr performed the Regional Climate Model run using the Met Office Unified Model to provide the meteorological data. Rebecca Dell conducted all other analysis and wrote the draft manuscript, under the supervision of all other authors. All authors discussed the results and were involved in editing of the manuscript.

Abstract

Surface meltwater on ice shelves can exist as slush, it can pond in lakes or crevasses, or it can flow in surface streams and rivers. The collapse of the Larsen B Ice Shelf in

2002 has been attributed to the sudden drainage of ~ 3000 surface lakes and has highlighted the potential for surface water to cause ice-shelf instability. Surface meltwater systems have been identified across numerous Antarctic ice shelves, although the extent to which these systems impact ice-shelf instability is poorly constrained. To better understand the role of surface meltwater systems on ice shelves, it is important to track their seasonal development, monitoring the fluctuations in surface water volume and the transfer of water across ice-shelf surfaces. Here, we use Landsat 8 and Sentinel-2 imagery to track surface meltwater across the Nivlisen Ice Shelf in the 2016–2017 melt season. We develop the Fully Automated Supraglacial-Water Tracking algorithm for Ice Shelves (FASTISh) and use it to identify and track the development of 1598 water bodies, which we classify as either circular or linear. The total volume of surface meltwater peaks on 26 January 2017 at 5.5×10^7 m³. At this time, 63% of the total volume is held within two linear surface meltwater systems, which are up to 27 km long, are orientated along the ice shelf's north–south axis, and follow the surface slope. Over the course of the melt season, they appear to migrate away from the grounding line, while growing in size and enveloping smaller water bodies. This suggests there is large-scale lateral water transfer through the surface meltwater system and the firn pack towards the ice-shelf front during the summer.

3.1 Introduction

The total mass loss from Antarctica has increased from 40 ± 9 Gt yr⁻¹ in 1979–1990 to 252 ± 26 Gt yr⁻¹ in 2009–2017, providing a cumulative contribution to sea-level rise of 14.0 ± 2.0 mm since 1979 (Rignot et al., 2019). Mass loss from Antarctica will likely increase in the near future due, at least in part, to the shrinkage and thinning of some of its ice shelves (Kuipers Munneke et al., 2014; DeConto and Pollard, 2016; Siegert et al., 2019) and the associated acceleration of inland ice across the grounding lines (Fürst et al., 2016; Gudmundsson et al., 2019). Seven out of 12 ice shelves that bordered the Antarctic Peninsula have collapsed in the last 50 years (Cook and Vaughan, 2010). One of the most notable events was the February–March 2002

collapse of Larsen B, leading to both an instantaneous and a longer-term speedup of the glaciers previously buttressed by the ice shelf (Scambos et al., 2004; Wuite et al., 2015; De Rydt et al., 2015) and resulting in their increased contribution to sea-level rise (Rignot et al., 2004).

The unforeseen catastrophic disintegration of Larsen B highlighted the unpredictable nature of ice-shelf collapse and prompted a search for the causes of ice-shelf instability. Current understanding of the factors causing ice-shelf instability stems from the very limited number of airborne and satellite observations prior to and following collapse events (e.g. Glasser and Scambos, 2008; Scambos et al., 2009; Banwell et al., 2014; Leeson et al., 2020), numerical modelling (e.g. Vieli et al., 2006; Banwell et al., 2013; Banwell and MacAyeal, 2015), and the few in situ measurements investigating recent and current ice-shelf processes (e.g. Hubbard et al., 2016; Bevan et al., 2017; Banwell et al., 2019). It has been suggested that the chain reaction drainage of ~ 3000 surface meltwater lakes, which covered 5.3% of the total ice shelf area and had a mean depth of 0.82 m (Banwell et al., 2014), may have triggered the near-instantaneous breakup of Larsen B (Banwell et al., 2013; Robel and Banwell, 2019), highlighting the potential importance of surface hydrology for ice-shelf instability. The formation of these ~ 3000 surface lakes has been attributed to the saturation of the ice shelf's firn layer, making it impermeable (Kupiers Munneke et al., 2014; Leeson et al., 2020). Given this possible role of surface water in ice-shelf instability, it is important to monitor changes in the area and volume of surface meltwater systems across ice shelves and compare any trends with those observed at Larsen B prior to its collapse.

Kingslake et al. (2017) identified numerous pervasive surface meltwater systems across many of Antarctica's ice shelves. Meltwater production is often highest around grounding lines, driven by high net shortwave radiation associated with low-albedo blue ice areas, high net longwave radiation around nunataks, and high sensible heat transfer from adiabatic warming of katabatic (Lenaerts et al., 2017) and foehn winds (Bell et al., 2018; Datta et al., 2019). Ice shelf hydrological systems may then take several forms as meltwater may (i) form surface streams and flow downslope (e.g. Liston and Winther, 2005; Bell et al., 2017), (ii) collect in surface lakes (e.g. Langley et al., 2016), (iii) percolate into the sub-surface and refreeze (Luckman et al., 2014;

Hubbard et al., 2016; Bevan et al., 2017), (iv) percolate into the subsurface and flow laterally (Winther et al., 1996; Liston et al., 1999), or (v) percolate into the subsurface and form sub-surface lakes and reservoirs (e.g. Lenaerts et al., 2017; Dunmire et al., 2020). Despite the identification of pervasive meltwater systems, very little is known about their spatial and temporal evolution, both between and within melt seasons (Arthur et al., 2020b). Furthermore, while surface water ponding and the formation of lakes have been implicated in past ice-shelf collapse (Scambos et al., 2003; Banwell et al., 2013), the formation of surface water streams that route water quickly to the ice-shelf front may not necessarily cause instability but rather militate against potential surface meltwater-driven collapse (Bell et al., 2017; Banwell, 2017). Thus, whether future projected increased surface melt on ice shelves forms lakes or flows rapidly to the ocean via streams has important implications for future ice-shelf stability and potential collapse. To better understand the behaviour of surface meltwater lakes and streams, it is important to investigate their spatial and temporal evolution across entire ice shelves through entire summer melt seasons and over multiple melt seasons.

In this paper, our objective is to develop a tool that can identify surface meltwater bodies on Antarctic ice shelves and track their evolution over time. We build on the work of Pope et al. (2016) and Selmes et al. (2011, 2013) and especially Williamson et al. (2017, 2018b), who developed and used the FAST algorithm for tracking lakes on the Greenland Ice Sheet using MODIS imagery. More specifically, we have adapted the FASTER algorithm of Williamson et al. (2018a) and Miles et al. (2017), who adapted the FAST method to track Greenland Ice Sheet lakes from the higher-resolution Landsat 8 and Sentinel-1 and Sentinel-2 imagery.

These previous methods need adapting for application on Antarctic ice shelves for three main reasons: first, to account for the observed differences in the geometry of surface meltwater bodies compared to those on the Greenland Ice Sheet; second, to recognise the marked geometry changes that occur over time on Antarctic ice shelves, including the joining of water bodies and the enveloping of some water bodies by others; and third, to identify the apparent transfer of surface meltwater over large distances across ice shelves. In Greenland, the majority of surface water bodies form in surface depressions that result from undulations in the bedrock topography and ice

flow (Echelmeyer et al., 1991; Sergienko, 2013), and therefore these water bodies evolve in the same location on an inter- and intra-annual basis (Banwell et al., 2014; Bell et al., 2018). By contrast, the location of surface water bodies on Antarctic ice shelves reflects variations in the surface topography, which are controlled by a combination of factors including (i) basal channels formed by ocean melting (Dow et al., 2018), (ii) basal crevassing (McGrath et al., 2012), (iii) the development of ice flow stripes in the grounding zone (Glasser and Gudmundsson, 2012), and (iv) suture zone depressions (Bell et al., 2017). In Antarctica, these factors result in a wide range of surface water body geometries, from circular forms to long linear features that can extend significant distances across an ice shelf, and might therefore have significant implications for the lateral transfer of surface meltwater.

Here, we advance the work of Williamson et al. (2018a) and Miles et al. (2017) to produce “FASTISh”, a Fully Automated Supraglacial Lake and Stream Tracking Algorithm for Ice Shelves. We adapt the FASTER algorithm for use with Landsat 8 and Sentinel-2 data to make it applicable to Antarctic ice shelves. Such adaptations include (i) assigning approximate depths to pixels with floating ice cover; (ii) acknowledging the geometric variability of surface water bodies across Antarctica and the impact this variability has on the lateral transfer of surface meltwater by categorising water bodies as either circular or linear; (iii) assigning each water body that is tracked over the melt season to one of four categories (always circular, always linear, simple transitions (from circular to linear or vice versa), and envelopment transitions (where water bodies spread and merge with neighbouring circular and linear water bodies to form a new water body, or where a water body splits into smaller circular and linear water bodies)) to quantify and illustrate the interaction between individual water bodies as the melt season progresses. We then apply the FASTISh algorithm to the Nivlisen Ice Shelf, Antarctica, for the 2016–2017 melt season, the first full melt season to have data coverage over the ice shelf from both Landsat 8 and Sentinel-2.

3.2. Study area

The Nivlisen Ice Shelf (70.3° S, 11.3° E) is situated in Dronning Maud Land, East Antarctica, between the Vigrid and Lazarev ice shelves (Figure 3.1). It has a surface area of 7600 km² and is ~ 123 km wide by 92 km long. Ice thickness ranges from 150 m at the calving front to ~ 700 m towards the ice shelf's grounding line in the southeast, and it exhibits flow velocities of around 20 to 130 m yr⁻¹ (Horwath et al., 2006). To the southeast of the Nivlisen Ice Shelf, there is a blue ice region maintained by katabatic winds, which extends in a southeasterly direction for ~ 100 km (Horwath et al., 2006). This blue ice region is characterised by ablation and adjoins the exposed bedrock nunatak (called Schirmacheroasen), which is positioned where the ice shelf meets the inland ice (Horwath et al., 2006) (Figure 3.1). Beyond this blue ice region, towards the north, the ice shelf transitions into an accumulation zone as the firn layer thickens (Horwath et al., 2006). In the 2016–2017 melt season, mean daily near-surface temperatures on the Nivlisen Ice Shelf ranged between ~ -25 and 2 °C, and 1.6% of the study area was occupied by a surface water body at least once during this time. The Nivlisen Ice Shelf was selected for this study as (i) pervasive surface meltwater features have previously been identified here in optical satellite imagery, showing evidence of widespread melt ponding in both circular and linear water bodies (Kingslake et al., 2017); (ii) these meltwater features have shown significant development over a melt season, as source lakes upstream of the grounding line appeared to drain laterally, rapidly flooding large areas of the ice shelf (Kingslake et al., 2015); and (iii) the ice shelf is relatively small, allowing quick and efficient development and application of FASTISh before its use more widely across larger Antarctic ice shelves.

3.3 Methods

There are four main components to the FASTISh algorithm: (i) delineating water body areas, (ii) calculating water body depths and volumes, (iii) categorising water bodies as either circular or linear based on their geometries, and (iv) tracking individual water bodies and measuring their changing dimensions and geometries over time (Figure

3.2). These will be discussed in Sect. 3.2 to 3.5 respectively, once the pre-processing steps applied to the imagery used have been outlined (Sect. 3.1).

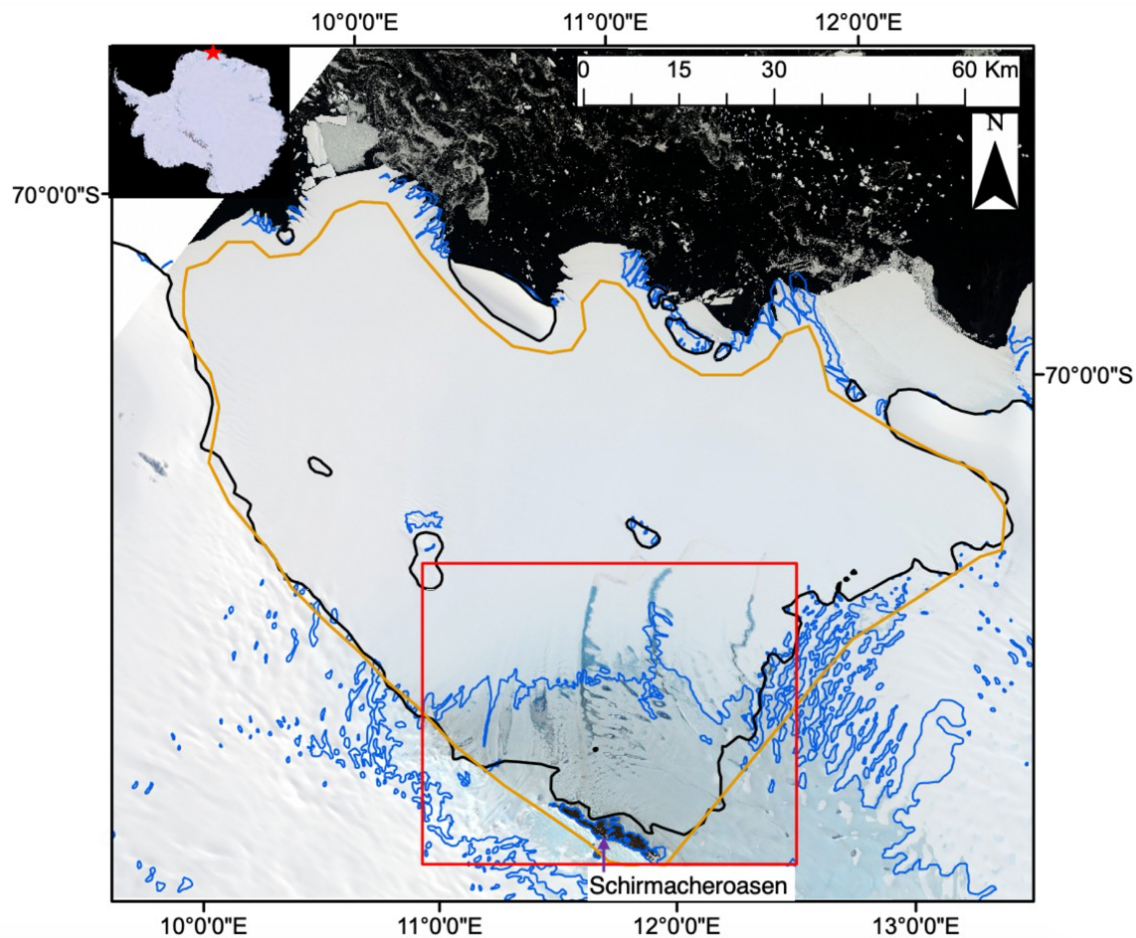


Figure 3.1. A map of the study area. The base image is a mosaicked true-colour composite Sentinel-2 image of the Nivlisen Ice Shelf acquired on 26 January 2017. The solid black line marks the grounding line, according to the NASA Making Earth System Data Records for Use in Research Environments (MEaSUREs) Antarctic boundaries dataset (Mouginot et al., 2017). The solid blue line represents the blue ice areas in the region according to Hui et al. (2014). The solid orange line roughly delineates the ice shelf and shows the study area extent used for this study, and the solid red line marks the area shown in all subsequent figures. The red star on the inset shows the location of the Nivlisen Ice Shelf in the context of an image of Antarctica, which is a mosaic product based on sources from United States Geological Survey (USGS), NASA, National Science Foundation, and the British Antarctic Survey (<https://visibleearth.nasa.gov/images/78592/landsat-image-mosaic-of-antarctica>, last access: 10 July 2020).

3.3.1 Images and pre-processing

3.3.1.1 Landsat 8

A total of 12 Landsat 8 scenes with minimal cloud cover, from between 2 November 2016 and 24 March 2017, and each partially covering the ice-shelf extent, were identified and downloaded from the USGS Earth Explorer website (<https://earthexplorer.usgs.gov>, last access: 10 July 2020) (Appendix A Table A.1 in the Supplement). Each scene was downloaded as a Tier 2 data product, in the form of raw digital numbers (DNs). Bands 2 (blue), 3 (green), 4 (red), and 8 (panchromatic) were used for this study (Figure 3.2). Bands 2, 3, and 4 have a 30 m spatial resolution, and band 8 has a 15 m spatial resolution. Image scene values were first converted from DN to TOA reflectance values. Typically, Landsat scenes are converted to TOA reflectance values using a single solar angle over the whole image scene. However, here we correct each pixel for the specific solar illumination angle, based on metadata stored in the .ANG file and using the “Solar and View Angle Generation Algorithm” provided by NASA (<https://www.usgs.gov/land-resources/nli/landsat/solar-illumination-and-sensor-viewing-angle-coefficient-files>, last access: 10 July 2020). Converting from DN to TOA values on a per-pixel basis is imperative when mosaicking and comparing images obtained at high latitudes, as the solar angle at the time of acquisition can vary significantly across each scene due to the large change in longitude.

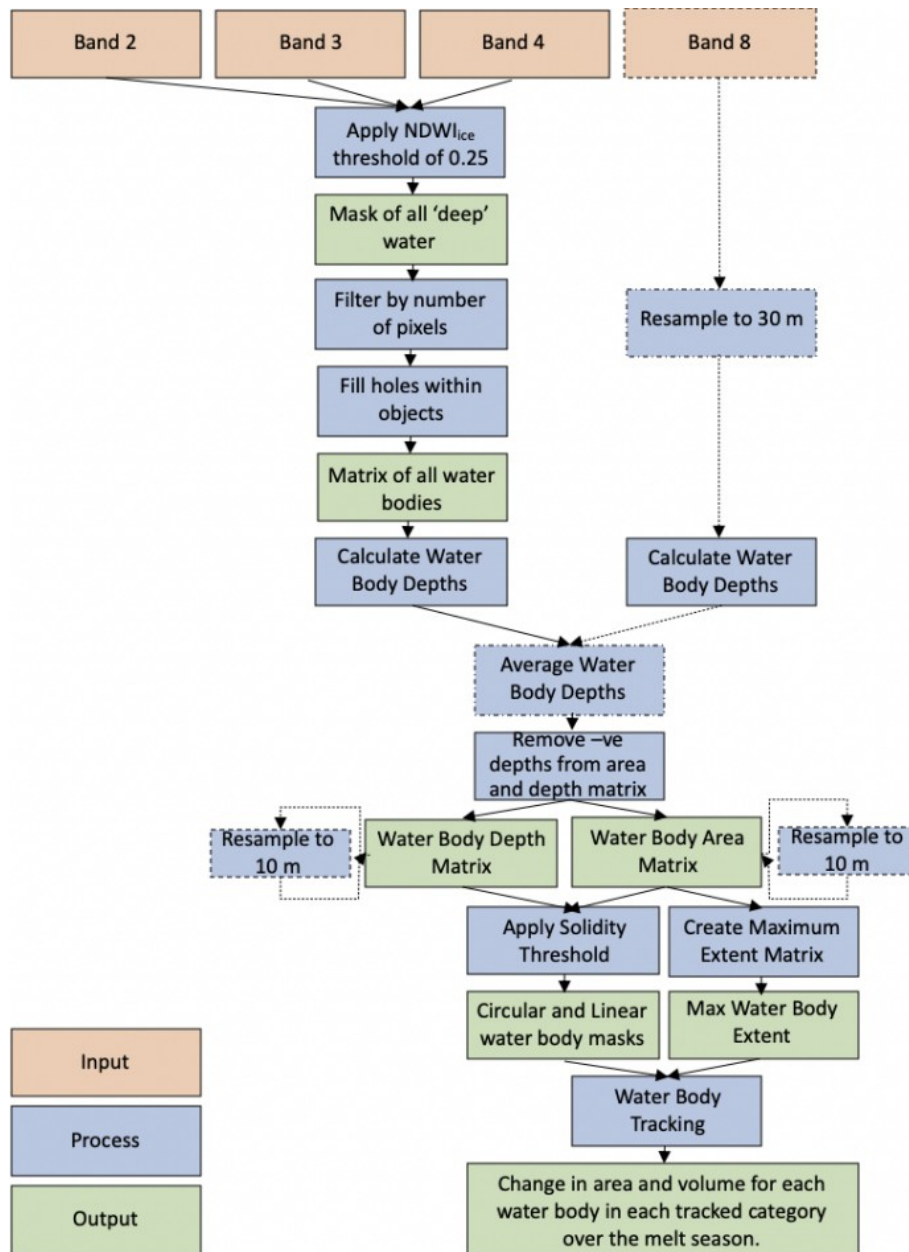


Figure 3.2. Workflow detailing the methods applied to both the Landsat 8 and Sentinel-2 images through the FASTISH algorithm in MATLAB. Dashed lines indicate steps that were applied to Landsat 8 images only, whereas solid lines indicate steps that were applied to both sets of image types. Modified from Williamson et al. (2018a).

For each Landsat scene, a cloud mask was generated and downloaded from GEE using the “Simple Cloud Score Algorithm” (ee.Algorithms.Landsat.simpleCloudScore). The simple cloud score algorithm assigns a “cloud score” to every pixel in the image

based on the following criteria: (i) brightness in bands 2 (blue), 3 (green), and 4 (red); brightness in just band 2 (blue); (iii) brightness in bands 5 (near infrared), 6 (shortwave Infrared 1), and 7 (shortwave infrared 2); and (iv) temperature in band 10 (thermal). The algorithm also uses the normalised difference snow index (NDSI) to distinguish between clouds and snow, which prevents snow from being incorrectly incorporated in the cloud mask. The NDSI was developed by Hall et al. (2001) to distinguish between snow/ice and cumulus clouds and is calculated from the following bands:

$$\text{NDSI} = (\text{blue band} - \text{near infrared band}) / (\text{blue band} + \text{near infrared band}) \quad [3]$$

Here, the blue band represents band 2 in both Landsat 8 and Sentinel-2 scenes and the near infrared band represents band 5 in Landsat 8 scenes and band 8 in Sentinel-2 scenes. We found the “simple cloud score algorithm” to be the most effective cloud masking method for Landsat 8 images, as it assesses each pixel using multiple criteria, making it more effective than any single band threshold. Prior to implementing the FASTISh algorithm, each Landsat scene and corresponding cloud mask was clipped to the study area extent in ArcGIS using the batch clip process. Clipping each scene to the same extent is required when comparing images through the FASTISh algorithm, as tracking individual features over time requires images with a consistent spatial reference frame to determine the location of each water body. The 12 scenes formed six pairs (Appendix A, Figure A.1), with two scenes per day, each covering part of the ice shelf. Each scene pair was mosaicked using ArcGIS’s “mosaic to new raster” tool to produce six images providing near-complete coverage of the ice shelf for 6 days of the 2016–2017 melt season (Appendix A, Table A.1). All images were projected into the 1984 Stereographic South Pole co-ordinate system (EPSG: 3031).

3.3.1.2 Sentinel-2

A total of 20 Sentinel-2A level-1C scenes obtained between 11 November 2016 and 25 February 2017 with minimal cloud cover were downloaded from the Copernicus Hub web site (<https://scihub.copernicus.eu>, last access: 10 July 2020) (Appendix A, Table A.1). Bands 2 (blue), 3 (green), 4 (red), and 11 (SWIR) were used. Bands 2, 3,

and 4 have a spatial resolution of 10 m, and band 11 has a spatial resolution of 20 m. The Sentinel-2 data for all bands were downloaded as TOA reflectance values and were divided by the “quantification value” of 10 000 (from metadata), to convert the numbers into values that lie within the 0 to 1 range (Traganos et al., 2018). We applied this conversion to bands 2, 3, and 4 as these are the bands used to identify water and calculate its depth, and their values need to be comparable to the values provided by Landsat 8. Each downloaded scene was clipped, mosaicked to produce images with full coverage of the ice shelf, and then reprojected to the WGS 1984 Stereographic South Pole co-ordinate system (EPSG: 3031), in line with the Landsat scenes. As the simple cloud score algorithm had not been adapted for application to Sentinel-2 imagery at the time of writing, we computed a cloud mask for each image using a thresholding approach, whereby pixels were categorised as cloudy if the SWIR band value was $> 10\,000$. This threshold was selected through visually assessing the effectiveness of various thresholds against the corresponding true-colour composite scenes. As the resolution of the original SWIR band was 20 m, the resultant cloud masks were resampled using nearest-neighbour interpolation to 10 m spatial resolution. On two image dates (14 November 2016 and 25 February 2017), this cloud masking approach was not entirely successful as not all clouds were fully masked. Additional individual masks were manually digitised in ArcGIS to ensure all clouds were masked for these images.

3.3.2 Delineating water body areas

Water body areas were determined using the normalised difference water index for ice ($NDWI_{ice}$), which has been widely used previously to calculate the distribution of surface meltwater features on the Greenland Ice Sheet and on Antarctic ice shelves (e.g. Yang and Smith, 2013; Moussavi et al., 2016; Koziol et al., 2017; Macdonald et al., 2018; Williamson et al., 2018a; Banwell et al., 2019). It is calculated using the $NDWI_{ice}$ equation (see Equation 1 in Section 2.2.3).

The $NDWI_{ice}$ equation uses digital numbers from the blue band (band 2) and red band (band 4) from TOA scenes. These bands are used because water has high reflectance values in the blue band, and there is a relatively large contrast between ice and water in the red band (Yang and Smith, 2013). Studies typically apply a single $NDWI_{ice}$ threshold to an image in order to classify pixels as either “wet” or “dry” (e.g. Fitzpatrick et al., 2014; Moussavi et al., 2016; Miles et al., 2017). Across both Greenland and Antarctica, most studies have used a relatively high $NDWI_{ice}$ threshold of 0.25 to map “deep” water bodies on ice (Yang and Smith, 2013; Bell et al., 2017; Williamson et al., 2018a). The same approach was applied to the Nivlisen Ice Shelf in this study in order to facilitate the detection of deep water bodies only. This is important because if too much shallow water and slush is detected, identifying and subsequently tracking individual water bodies over time becomes difficult. Having applied a 0.25 $NDWI_{ice}$ threshold to each image, the resulting water masks were filtered using a two-dimensional eight- connected threshold (i.e. grouping pixels if they were connected by their edges or corners) to identify each individual water body. Water bodies consisting of less than or equal to 2 pixels (Landsat 8) and less than or equal to 18 pixels (Sentinel-2) were removed to ensure only water bodies with an area greater than or equal to 1800 m² were assessed further. To ensure that pixels with floating ice cover were still included in the analysis, we then used the “imfill” function within MATLAB to classify any dry pixels situated within a water body as water.

3.3.3 Water body depth calculations

Having identified the extent of water bodies, we use a physically based approach (Sneed and Hamilton, 2007; Arnold et al., 2014; Banwell et al., 2014, 2019; Pope, 2016; Pope et al., 2016; Williamson et al., 2017, 2018a) based on the original work of Philpot (1989) to calculate pixel water depths. Water depth, z , is calculated from

$$z = \frac{[\ln(A_d - R_\infty) - \ln(R_{pix} - R_\infty)]}{g}$$

[4]

where R_{pix} is the satellite-measured pixel reflectance, A_d is the lake-bottom albedo, R_∞ is the reflectance value for optically deep (> 40 m) water, and g is the coefficient associated with the losses made during downward and upward travel in a water column.

For the Landsat 8 images, pixel water depths were calculated using TOA reflectance data for both the red and panchromatic bands separately and then averaging these values to give a single final value (Pope et al., 2016; Williamson et al., 2018a). Pope et al. (2016) show that this approach gives the smallest mean difference (0.0 ± 1.6 m) between spectrally derived and DEM-derived lake depths. However, it should be noted that owing to the rapid attenuation of red light by a water column, this algorithm is only able to retrieve depths up to a maximum of ~ 5 m (Pope et al., 2016). Furthermore, this method assumes (i) no wind and waves at the water body surface, (ii) little to no dissolved/suspended material within the water body, (iii) no inelastic scattering, and (iv) a water body substrate that is parallel to the surface and homogenous (Sneed and Hamilton, 2011).

For Landsat 8 images, the panchromatic band was first resampled using bilinear interpolation from 15 to 30 m spatial resolution to match the resolution of the red band. For the Sentinel-2 images, water body depths were calculated using the TOA reflectance values in the red band only, as there is no equivalent panchromatic band (Williamson et al., 2018a). To calculate A_d , the mean reflectance value of the second (Landsat) and sixth (Sentinel) rings of pixels outside of each water body was calculated, following a similar approach used by Arnold et al. (2014) and Banwell et al. (2014). The second or sixth ring of pixels surrounding each lake was used to avoid calculating A_d from slushy areas that border each water body; sixth-pixel rings were used for Sentinel-2 images as these represent the same distance away from the water body as second pixel rings in Landsat images. In very rare cases, wet pixels within a

water body could have a reflectance higher than the calculated A_d value, leading to negative water depths. All such pixels were removed from the area and depth matrix (Figure 3.2).

Values for R_∞ were assessed on an image-by-image basis by taking the minimum reflectance value found over optically deep water (the ocean). For images that did not contain optically deep water, the R_∞ value was set to 0 (Banwell et al., 2019). For Landsat 8 imagery we used a g value of 0.7507 m^{-1} for the red band and 0.3817 m^{-1} for the panchromatic band (Pope et al., 2016), and for Sentinel-2 imagery, we used a value of 0.8304 m^{-1} (Williamson et al., 2018a). Pixels in the lake masks that were filled (normally those with a floating ice cover; see Sect. 3.2) were assigned the mean water depth of their respective water bodies. Individual water body volumes were calculated by multiplying each pixel area by its calculated water depth and then summing across the water body. To facilitate comparisons between Landsat 8 and Sentinel-2 data, area and depth arrays generated from Landsat 8 images were then resampled to 10 m spatial resolution using nearest neighbour interpolation.

3.3.4 Classifying water body types

Having produced area and depth masks for each date, each identified water body was categorised as either circular or linear based on its solidity (defined as the proportion of pixels of the water body that fall within its convex hull), which was calculated using the “regionprops” function in MATLAB (Banwell et al., 2014). Linear water bodies have a solidity score closer to 0 reflecting the smaller proportion of wet pixels within the convex hull due to likely greater concavity of the edges, whereas more circular water bodies have a solidity score closer to 1 due to the larger proportion of wet pixels within the convex hull due to the more convex shape. Here, water bodies with a solidity score greater than or equal to 0.45 were classified as circular, and water bodies with a solidity score less than 0.45 were classified as linear. This threshold was selected by visually assessing the masks generated from thresholds ranging between 0.42 and 0.49, in

increments of 0.01, and selecting the threshold that appears to best distinguish between more circular and more linear water bodies (Figure 3.3).

3.3.5 Tracking water bodies

A 3D matrix of all water bodies was compiled, recording the area and volume of each water body over time, as well as whether the water body had a circular or linear geometry (as defined in Sect. 3.3.4). To track changes in the area and volume of surface meltwater bodies throughout the 2016–2017 melt season, a maximum extent mask (Figure 3.4b) was also generated by superimposing the areas of all water bodies identified in each image (Williamson et al., 2018a). The maximum extent mask was then used to guide the tracking process. Each individual water body within the maximum extent was assigned an ID, and changes to the area and volume of each individual water body over time were tracked within its maximum extent (Williamson et al., 2018a).

In addition to tracking changes in the area and volume of each water body, the FASTISh algorithm also tracks the water body type. From this tracking process, four categories were defined: (i) always circular, (ii) always linear, (iii) “simple transitions” where a water body is defined as *either* circular or linear and switches between the two categories (either once or more than once, and in either direction), and (iv) “envelopment transitions” where water bodies spread and merge with neighbouring circular and linear water bodies to form new, larger bodies, or where larger bodies split into smaller circular and linear water bodies. This final category allows us to track the development of large surface water bodies across the ice-shelf surface as it identifies smaller water bodies being subsumed into larger water bodies as the melt season progresses.

3.3.6 Digital elevation model

To aid interpretations of the tracking results produced by the FASTISh algorithm, we used surface elevation data from the Reference Elevation Model of Antarctica (REMA) database (Howat et al., 2019). Figure 3.4a shows the REMA DEM of the ice shelf at 8 m resolution, produced by mosaicking four 8 m resolution REMA tiles. In addition, a single 2 m REMA data strip from 31 January 2016 was used to extract the elevation profiles along two tracked water bodies, the eastern system and the western system, which are introduced in Sect. 4.2.2.

3.3.7 Regional climate simulation

In order to understand how climate variability influences the findings, we analysed results from an atmosphere-only regional climate CORDEX (Coordinated Regional Climate Downscaling Experiment) simulation of Antarctica using the limited-area configuration of version 11.1 of the UK Met Office Unified Model (MetUM) for the period 2016–2017. The MetUM is a weather prediction model, which uses a semi-Lagrangian semi-implicit scheme for solving the fully compressible, non-hydrostatic, deep-atmosphere equations of motion (Walters et al., 2017).

The setup of the MetUM is similar to that used by Mottram et al. (2020), with the exception that the horizontal resolution for the limited-area Antarctic domain has been increased from 50 to 12 km (and consists of 392×504 grid points). The Antarctic domain uses the regional atmosphere mid-latitude (RA1M) science configuration (Bush et al., 2020), a rotated latitude–longitude grid in order to ensure that the grid points are evenly spaced, and 70 vertical levels up to an altitude of 40 km.

The required start data and lateral boundary conditions for the Antarctic domain are supplied by a global version run of the MetUM at N320 resolution (640×480 grid points, equivalent to a horizontal resolution of 40 km at mid-latitudes), which is itself initialised by ERA-Interim atmospheric reanalysis (Dee et al., 2011). The model is used to provide a series of 6 to 18 hour forecasts, provided every 12 hours, for the period 20151231T0600Z to 20171231T1800Z; i.e. the initial 6 hours of each forecast is discarded as spin-up. We extracted a continuous forecast time-series for the period November 2016 to April 2017. We extracted daily mean and daily maximum near-surface diurnal air temperatures (at a height of 1.5 m above the ground) for the model grid point immediately to the north of Schirmacheroasen.

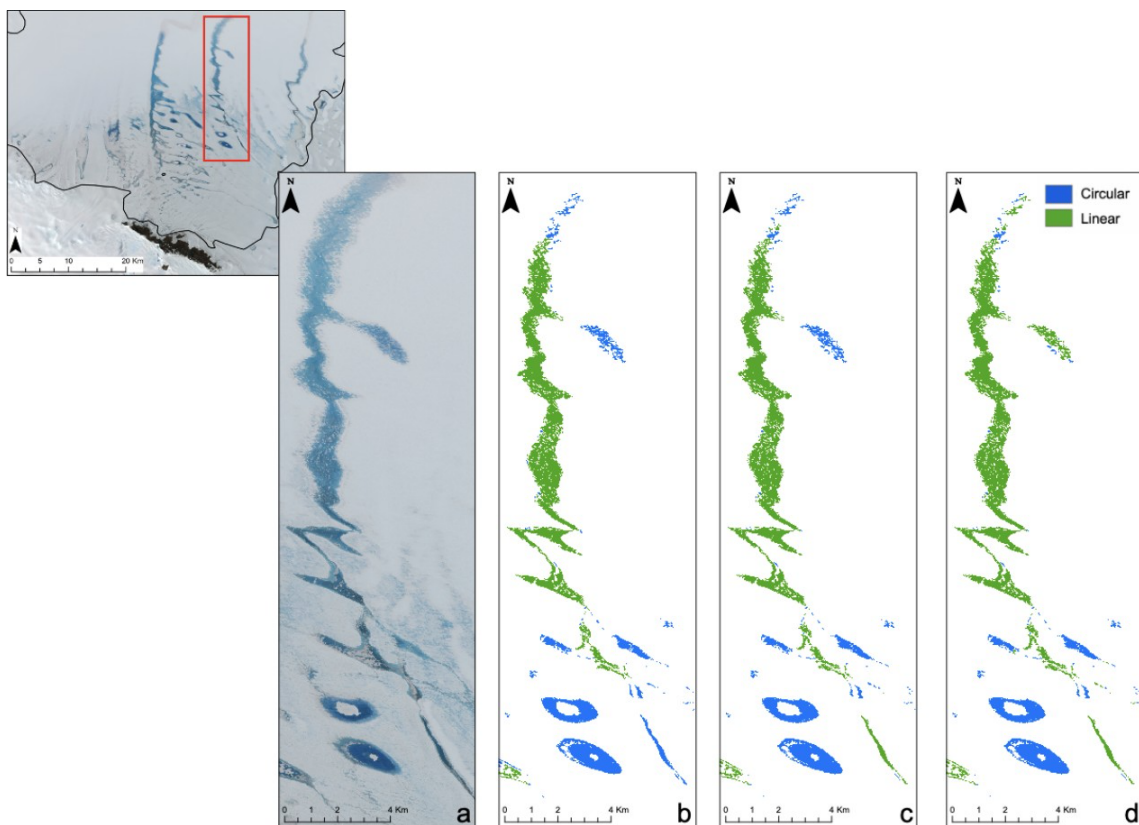


Figure 3.3. Solidity thresholds applied to water bodies identified on the Nivlisen Ice Shelf. The subset Sentinel-2 image is from 26 January 2017, and the red box indicates the area shown in panels (a)–(d). Panel (a) shows this area as a true-colour composite, and panel (b) shows the water bodies identified and separated into linear or circular water bodies using a threshold of 0.42, (c) a threshold of 0.45, and (d) a threshold of 0.49.

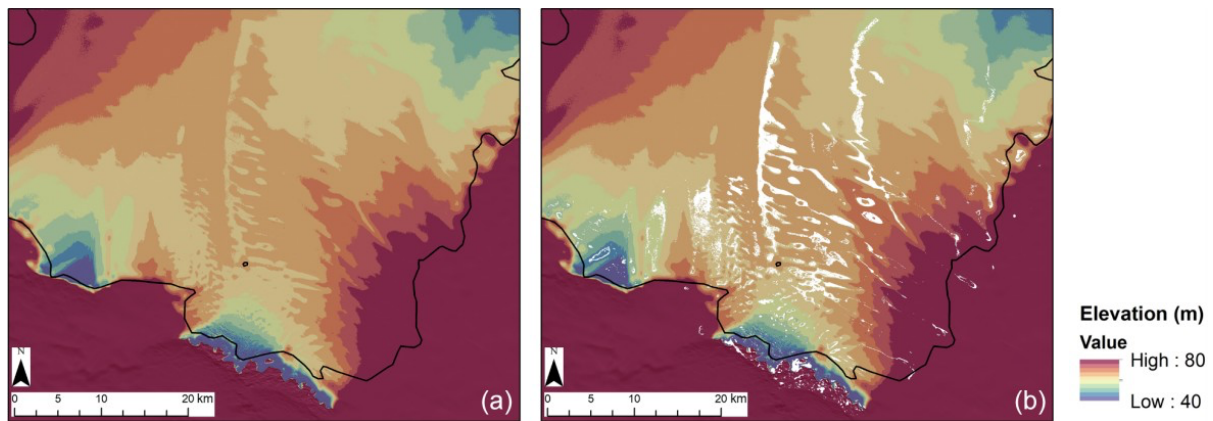


Figure 3.4. REMA DEM data for the Nivlisen Ice Shelf. (a) The DEM and (b) overlain with the maximum melt extent matrix for the 2016–2017 melt season in white. DEM data sourced from the REMA dataset (Howat et al., 2019).

3.4 Results

3.4.1 Spatial extent and distribution of surface water bodies

The seasonal evolution of meltwater bodies during the 2016 – 2017 summer is shown in Figure 3.5. The surface meltwater system transitions from a series of small isolated water bodies clustered towards the grounding line (Figure 3.5a) to a connected system dominated by two linear water bodies with a length of (a) ~ 20.5 km and (b) ~ 16.9 km that propagate towards the ice-shelf front (Figure 3.5d).

For example, on 11 December 2016, few meltwater bodies exist, and they are predominantly clustered within the blue ice region towards the grounding line in the southwest (Figure 3.5a). The majority of these water bodies exist as distinct entities and do not connect to one another. Some meltwater ponds are identified in close proximity to the nunatak. The total volume and area of all surface meltwater bodies on

11 December is $2.8 \times 10^6 \text{ m}^3$ and $2.8 \times 10^6 \text{ m}^2$ respectively (Table 3.1). The mean water depth is 1.0 m, and the maximum water depth is 3.4 m (Table 3.1). By 17 December (Figure 3.5b), there has been a marked increase in the total volume ($3.2 \times 10^7 \text{ m}^3$) and area ($4.7 \times 10^7 \text{ m}^2$) of surface meltwater, held in both circular and linear surface water bodies (Table 3.1). The mean water depth is 0.7 m and the maximum water depth is 3.1 m (Table 3.1). Several of the previously isolated ponds have coalesced in some of the main topographic lows. The spatial extent of the surface water bodies extends ~ 2 km further towards the ice-shelf front. In addition, some water bodies have begun to develop towards the eastern edge of the grounding line in a blue ice region.

A marked shift in the surface meltwater system is identified by 27 December (Figure 3.5c), as two large linear water bodies have formed along the north–south axis (labelled a and b in Figure 3.5c). The western linear water body (a) is ~ 6.5 km long and ~ 10 km from the eastern linear water body (b), which is ~ 8.5 km long and proximal to the surface lakes on the ice shelf’s eastern margin (Figure 3.5c). Overall, there are fewer isolated lakes towards the grounding line, and the majority of the surface meltwater is proximal to the two large linear systems, at elevations of ~ 60 to 65 m (Figure 3.4). The total volume and area of all surface meltwater bodies is $4.9 \times 10^7 \text{ m}^3$ and $5.4 \times 10^7 \text{ m}^2$ respectively (Table 3.1). The mean water depth of all identified water bodies is 0.9 m and the maximum water depth is 4.7 m (Table 3.1).

By 26 January 2017 (Figure 3.5d), the total volume and area of surface meltwater reaches a peak for the summer, at $5.5 \times 10^7 \text{ m}^3$ and $9.1 \times 10^7 \text{ m}^2$ respectively (Table 3.1). This is facilitated by the enlargement of the two large linear systems, which involves the flooding of topographic lows as water appears towards the firn further north on the ice shelf. These linear systems are now (a) ~ 20.5 km and (b) ~ 16.9 km in length and have a mean depth of (a) 0.8 m and (b) 0.7 m. The mean depth of all water on 26 January 2017 is 0.6 m and the maximum water depth is 3.3 m (Table 3.1).

By 13 February (Figure 3.5e), the two large linear systems remain prominent on the ice shelf, but they have lost area, depth, and volume at their southern ends. The mean water depth of all water is 0.6 m and the maximum water depth is 4.3 m (Table 3.1).

The total volume and area of surface meltwater bodies falls to $3.7 \times 10^7 \text{ m}^3$ and $6.3 \times 10^7 \text{ m}^2$ (Table 3.1), reflecting the shrinkage of the two linear systems.

3.4.2 Tracking results

Of the 1598 water bodies identified and tracked within the maximum extent matrix, 1458 (91%) are defined as always circular, 42 (3%) are identified as always linear, 51 (3%) are defined as simple transitions, and 47 (3%) are categorised as envelopment transitions. Water bodies that are always circular are predominantly clustered further south on the ice shelf towards the grounding line, while water bodies defined as envelopment transitions are found further north, towards the ice-shelf front (Figure 3.6).

3.4.2.1 Total area and volume of tracked surface water bodies

For each of the tracked water body categories, Table 3.2 shows the maximum area and volume and the corresponding dates on which these maxima were reached. The minimum area and volume for all tracked categories are zero on 14 November 2016, as no deep surface meltwater was detected on that date. Although 91% of water bodies identified are classified as circular, they do not dominate the total area or volume of surface meltwater (Figure 3.7). Conversely, the envelopment transitions, of which there are only 47 in total, peak at $8.0 \times 10^7 \text{ m}^2$ in area and $4.5 \times 10^7 \text{ m}^3$ in volume on 26 January 2017, over a month later than the peaks in area and volume recorded for the other three categories. These envelopment transitions dominate the total area and volume signals for all water bodies, which also reach their maxima on 26 January (Table 3.2, Figure 3.7). Between 17 and 27 December 2016 all water bodies are effectively deepening, as their mean depth increases whilst the total area increases, whereas between the 27 December and the 26 January all water bodies are effectively

spreading, as their mean depth decreases whilst total area increases (Table 3.1, Figure 3.7).

Table 3.1: Total area, total volume, and mean depth of all meltwater bodies on the Nivlisen Ice Shelf on various dates in the 2016-2017 melt season.

Date	Total Area (m²)	Total Volume (m³)	Mean Depth (m)	Max Depth (m)
2 November 2016	2.2×10^6	2.6×10^6	1.2	2.9
11 November 2016	1.7×10^6	1.2×10^6	0.7	2.6
14 November 2016	0.0	0.0	0.0	0.0
4 December 2016	4.4×10^4	4.0×10^4	0.9	3.1
11 December 2016	2.8×10^6	2.8×10^6	1.0	3.4
17 December 2016	4.7×10^7	3.2×10^7	0.7	3.1
27 December 2016	5.4×10^7	4.9×10^7	0.9	4.7
26 January 2017	9.1×10^7	5.5×10^7	0.6	3.3
13 February 2017	6.3×10^7	3.7×10^7	0.6	4.3
25 February 2017	2.9×10^6	2.4×10^6	0.8	3.0
24 March 2017	3.7×10^6	7.2×10^6	2.0	5.0

3.4.2.2 Tracking individual water bodies

In addition to quantifying total surface water area and volume for each of the four water body categories (Figure 3.7), the FASTISh algorithm also tracks changes in the area and volume of *individual* water bodies. Over the 2016–2017 melt season, the two largest envelopment transitions, referred to as the western system (WS) and the eastern system (ES) hereafter, propagate towards the ice-shelf front as the melt season progresses and contain 62.6% of the total surface water volume on 26 January 2017. The remainder of this sub-section focuses solely on presenting the tracking results for these two water bodies.

The WS is active between 11 December 2016 and 25 February 2017. The area and volume of meltwater within the WS reaches a maximum of $4.6 \times 10^7 \text{ m}^2$ and $2.5 \times 10^7 \text{ m}^3$ respectively on 26 January 2017 (Figure 3.8). The ES has a shorter lifespan and is active between 27 December 2016 and 25 February 2017 (Figure 3.8). The area and volume of the ES peak at $1.9 \times 10^7 \text{ m}^2$ and $9.6 \times 10^6 \text{ m}^3$ on 26 January 2017. Figure 3.9 shows the surface elevation profiles for the WS and the ES, which are extracted from the maximum extent mask (see Sect. 3.5). Both systems are characterised by a surface sloping downwards towards the ice-shelf front. The WS has a very shallow slope, with the elevation decreasing by $\sim 2 \text{ m}$ over the 25.7 km profile (Figure 3.9a); the ES is slightly steeper, showing a $\sim 7 \text{ m}$ decrease in elevation over its 27 km profile (Figure 3.9b).

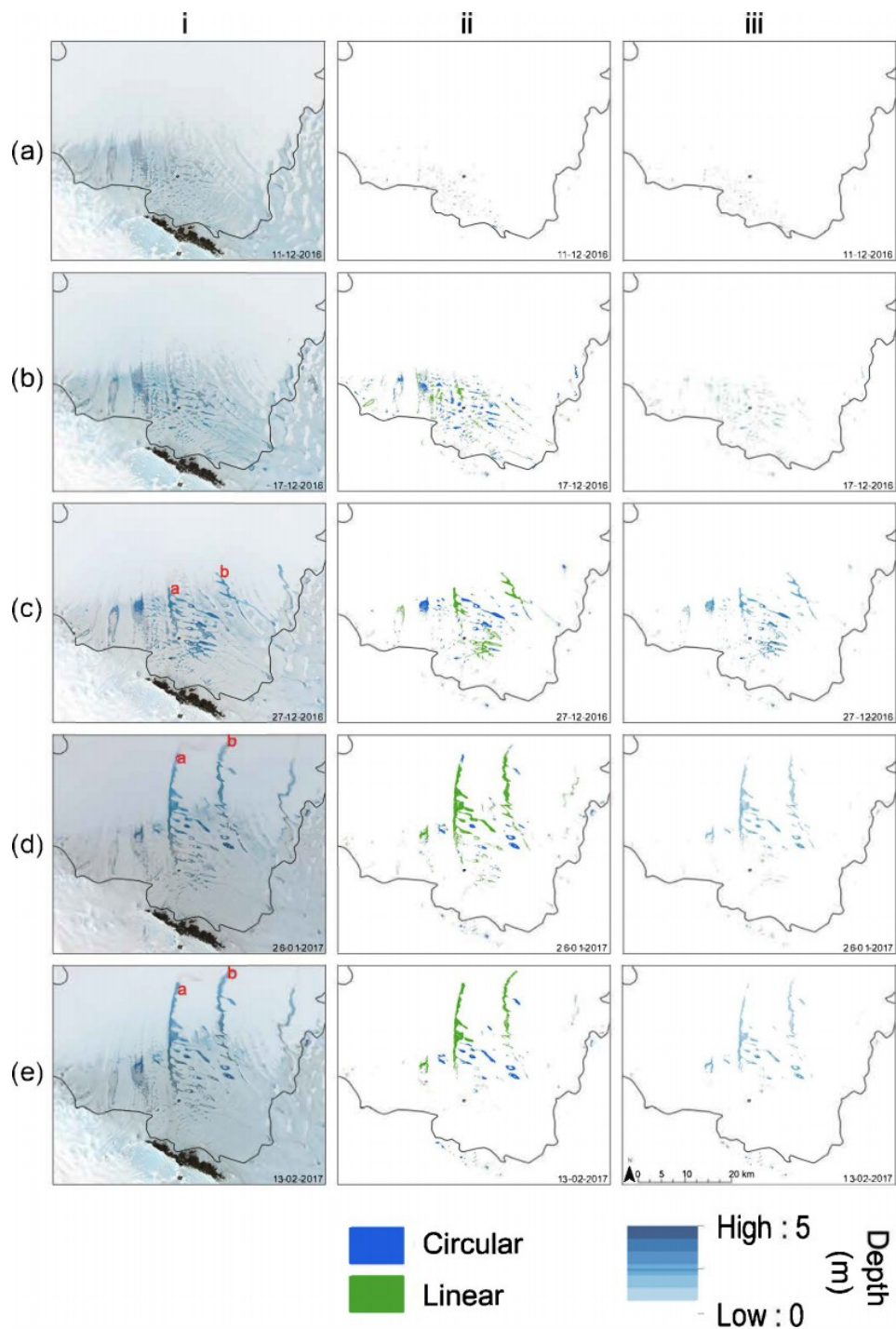


Figure 3.5. Five of the 11 dates studied in the 2016–2017 melt season (represented by labels a–e), and their corresponding (i) true-colour composite images, (ii) area masks for circular and linear features, and (iii) depth masks. Date stamps are in the bottom right-hand corner of each image. See Appendix A, Movie A.1 (<https://doi.org/10.5446/47526>, Dell et al., 2020b) for all true-colour composite images, Appendix A, Movie A.2 (<https://doi.org/10.5446/47524>, Dell et al., 2020c) for all lake and stream area masks, and Appendix A, Movie A.3 (<https://doi.org/10.5446/47525>, Dell et al., 2020d) for all depth masks produced in this study.

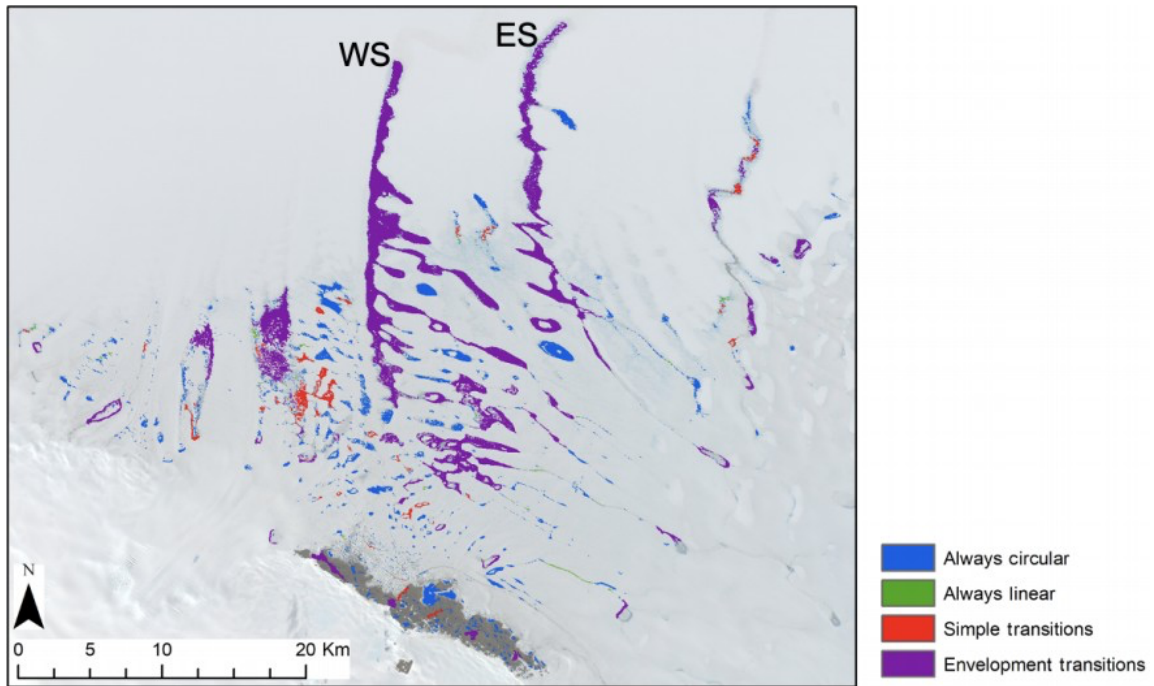


Figure 3.6. Maximum extent of all identified water bodies on the Nivlisen Ice Shelf for the 2016–2017 melt season, colour coded by water body type. “WS” denotes “western system”, and “ES” is eastern system. Base image acquired by Sentinel-2 on 26 January 2017.

Table 3.2: Maximum Area and Volume for each water body category on the Nivlisen Ice Shelf on various dates in the 2016-2017 melt season.

	Maximum Area (m ²)	Maximum Volume (m ³)	Date of Maximum Volume	Date of Maximum Area
All Water Bodies	9.1×10^7	5.5×10^7	26 January 2017	26 January 2017
Always Circular	1.5×10^7	1.4×10^7	17 December 2016	17 December 2016
Always Linear	1.3×10^6	3.9×10^5	17 December 2016	17 December 2016
Simple Transitions	3.2×10^6	3.2×10^6	17 December 2016	17 December 2016
Envelopment Transitions	8.0×10^7	4.5×10^7	26 January 2017	26 January 2017

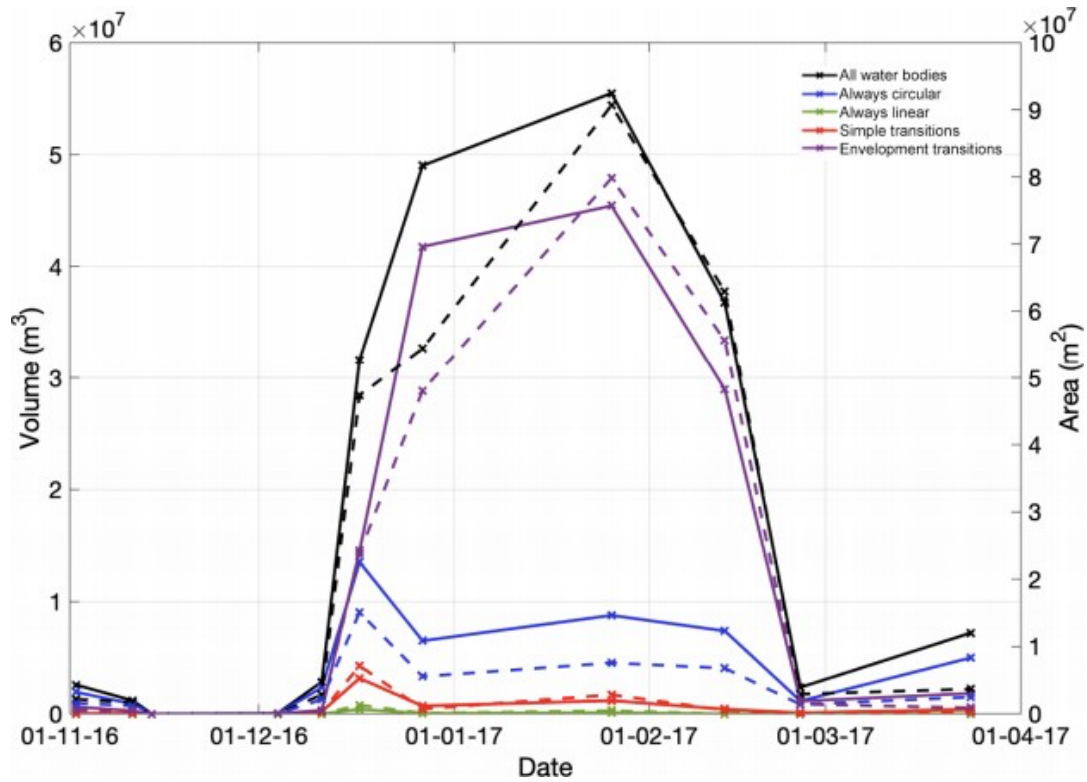


Figure 3.7. Time-series of the total area and volume held in each water body category over the 2016–2017 melt season on the Nivlisen Ice Shelf. Volumes are indicated by the solid lines and areas by the dashed lines.

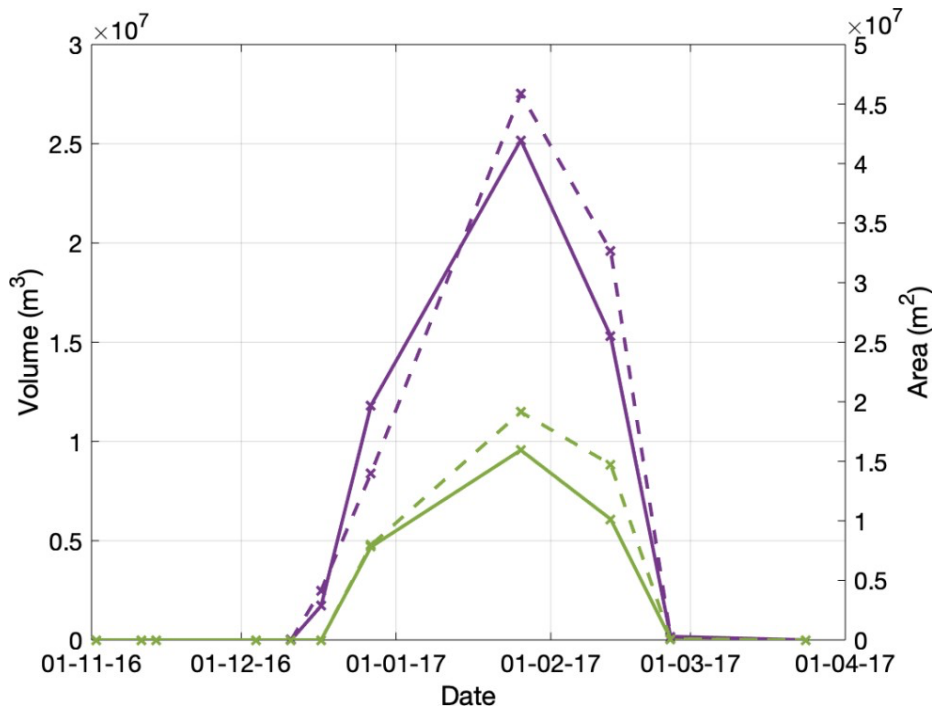


Figure 3.8. Time-series showing the area (dashed line) and volume (solid line) of the WS (purple) and ES (green).

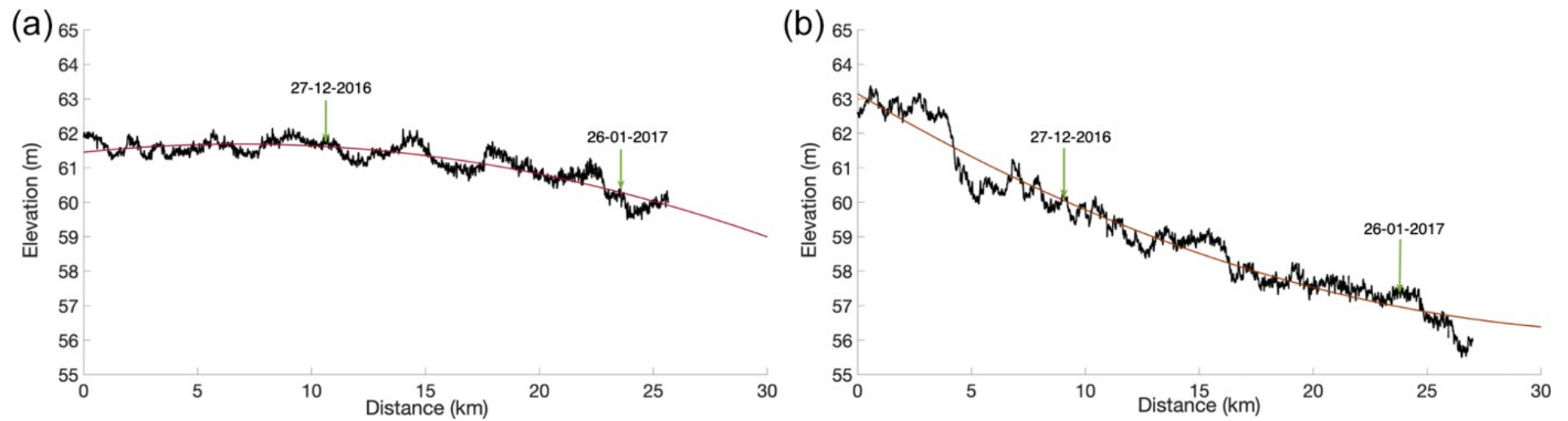


Figure 3.9. Elevation profiles for (a) the WS and (b) the ES. Quadratic trend lines are shown in red. Data are extracted from REMA (Howat et al., 2019), and the path of data extraction was guided using the maximum depth matrix of both the WS and ES over the full 2016–2017 melt season (see Appendix A, Figure A.1). The labelled green arrows mark the down-ice extent of each system on 27 December 2016 and 26 January 2017.

3.4.2.3 Identifying individual lake freeze-through and drainage events

Previous studies have attempted to identify rapid drainage events, defined as events where lakes lose $> 80\%$ of their maximum volume in ≤ 4 days (e.g. Fitzpatrick et al., 2014; Miles et al., 2017; Williamson et al., 2018a). Here, however, the temporal resolution of available imagery for the Nivlisen Ice Shelf is not high enough to allow this. Therefore, we used the calculated volume time-series to identify water bodies in the always circular category that lost $> 80\%$ of their maximum volume over the full melt season, through either drainage or freeze-through. We focus solely on the always circular category to better understand the local loss of surface meltwater in seemingly isolated and stationary water bodies. These events are referred to as “loss events” hereafter.

Figure 3.10 shows the loss in water volume through freeze through or drainage for the always circular category over the melt season, together with the 7 day moving average for the mean daily and daily maximum near-surface air temperatures over the ice shelf from the MetUM simulation. This shows that 805 lakes have a loss event by 18 December 2017, losing a total volume of $1.5 \times 10^7 \text{ m}^3$, which occurs following sustained relatively warmer atmospheric conditions since the beginning of December 2016, e.g. characterised by daily maximum near-surface air temperatures reaching 0°C .

3.5 Discussion

3.5.1 Spatial and temporal distribution of surface meltwater bodies

In the early melt season, surface meltwater on the Nivlisen Ice Shelf ponds in small surface lakes that form in relatively flat areas towards the grounding line, in close proximity to Schirmacheroasen and the blue ice regions (Figs. 3.4 and 3.5).

This initial generation of surface meltwater is likely driven by regional wind patterns and the effects of local ice albedo, as the relatively low albedo of the blue ice can lead to increased local melt rates (Lenaerts et al., 2017; Bell et al., 2018; Stokes et al., 2019). Furthermore, areas of lower elevation towards the grounding line are likely to be exposed to katabatic winds, which can result in near-surface temperatures that are 3 K greater than temperatures further up-ice and down-ice (Lenaerts et al., 2017). These persistent katabatic winds can also result in the production of blue ice regions, as snow is eroded from the ice-shelf surface (Lenaerts et al., 2017). Our results for the early melt season on the Nivlisen Ice Shelf therefore support the findings of Kingslake et al. (2017), who found, for a variety of ice shelves around Antarctica, that 50% of the ice-shelf drainage systems are either within 8 km of rock exposures or within 3.6 km of blue ice surfaces.

Seasonal variations in the amount of surface meltwater on the Nivlisen Ice Shelf are driven by temperature fluctuations, with increases in surface water area and volume corresponding with rising mean daily near-surface temperatures and daily maximum near-surface temperatures (Figure 3.10). However, as the melt season progresses, there is a transition to a connected surface drainage network, which facilitates a progressive transfer of surface meltwater away from the grounding line towards the ice-shelf front. As mean daily and daily maximum temperatures rise (Figure 3.10) and

surface water bodies increase in area and volume (Figure 3.7), they grow, merge with nearby water bodies, and form new extended networks of surface water on the ice-shelf surface (Figure 3.6). While rising near-surface temperatures are a strong control on the amount of surface meltwater, the direction and extent of the identified lateral water transfer are controlled by the ice shelf’s surface topography (Figure 3.4b). Over the course of the melt season, the area and volume of surface meltwater decrease in the regions close to the grounding line and increase in more distal parts of the ice shelf (Figure 3.5).

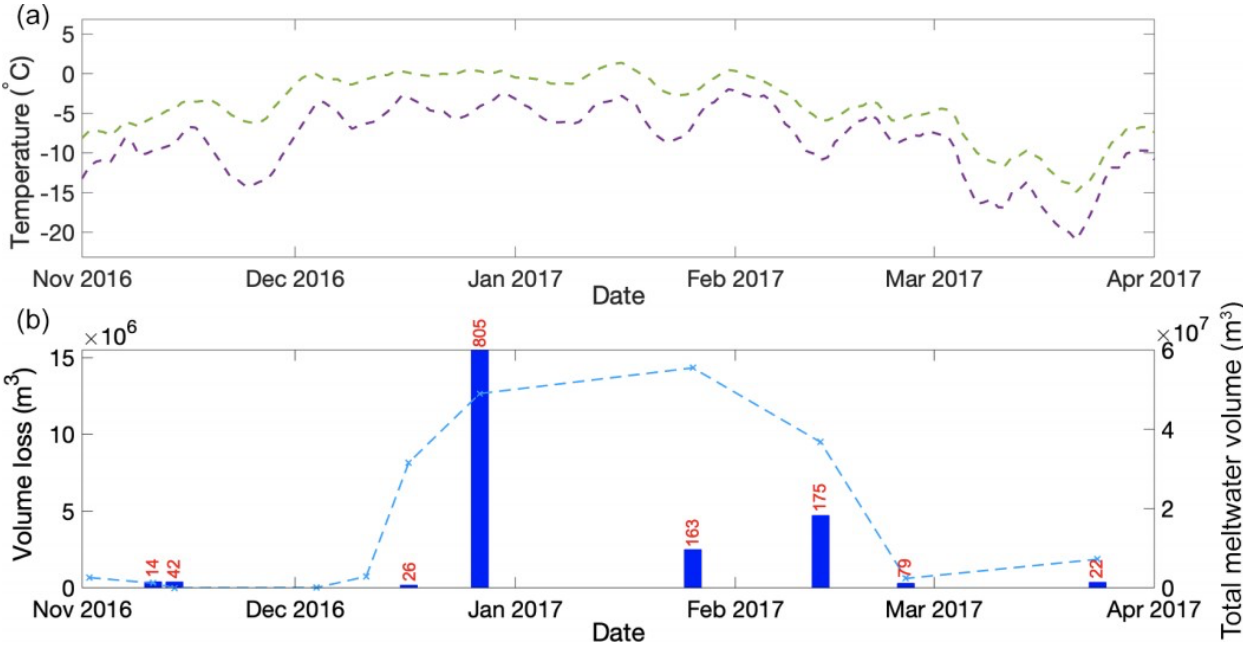


Figure 3.10. Meteorological context of circular lake loss events. (a) The 7 day moving average of mean daily (purple line) and daily maximum (green line) near-surface air temperature from the MetUM simulation for the period from November 2016 to April 2017 at the model point immediately to the north of Schirmacheroasen. (b) The total volume lost in “loss events” by each image date from water bodies in the “always circular” category (blue bars) and the total combined water volume (blue line). A loss event is defined as a > 80% loss in water body volume through either lake drainage or freeze-through. The total number of loss events for each date is indicated above each bar.

The development of the two largest enveloping water bodies (WS and ES) dominates the transition to a generally more connected drainage network. This is because these

systems facilitate large-scale transfer of water across the shelf, as water ponds within linear depressions. The ES and WS appear to be fed by smaller circular and linear surface meltwater bodies, and as the area and volume of the ES and WS increase, they spread and envelop nearby water bodies. Smaller water bodies likely contribute surface melt to the ES and WS by (i) overtopping their local basin sides and flowing over impermeable ice, which may be refrozen surface or shallow subsurface meltwater from previous years (Kingslake et al., 2015) or (ii) percolating into the firn pack and spreading laterally towards the ES and WS. However, the “pulse” forward of the ES and WS between 27 December 2016 and 26 January 2017 does not appear to be due to a breach of a topographic “lip” or “dam” (Figure 3.9). It is likely, therefore, to be primarily the result of increased meltwater production, resulting in saturation of the surrounding firn pack, which may bring it up to isothermal conditions, thereby facilitating further melt and lateral transfer.

By 26 January 2017, the ES and WS are the dominant features within the entire Nivlisen Ice Shelf meltwater system, together holding 62.6% of the surface meltwater volume. On this date, the ES and WS reach a length of ~ 16.9 and ~ 20.5 km respectively, although unlike observations on the Nansen Ice Shelf (Bell et al., 2017), they do not facilitate the export of surface meltwater off the ice-shelf front via a waterfall. Instead, both systems always terminate at least ~ 35 – 55 km from the ice-shelf front, suggesting that the water percolates into the surrounding firn in that area of the ice shelf. This interpretation is supported by Figure 3.11 which shows a Sentinel-1 SAR image (Figure 3.11b) from 26 January 2017 together with the Sentinel-2 image (Figure 3.11a). Areas of low backscatter (appearing as dark areas in Figure 3.11b) extend across the grounding line onto the upper part of the ice shelf. Whilst areas of low backscatter may result from relatively small dry-snow grain sizes, shallow dry-snow depths to underlying rougher surfaces, high surface roughnesses, or complex internal stratigraphies (Rott and Mätzler, 1987; Sun et al., 2015), it seems more likely that areas of low backscatter north of the blue ice areas represent saturated firn and/or surface melt (Bindschadler and Vornberger, 1992; Miles et al., 2017). Areas of low backscatter clearly extend beyond areas of visible surface melt in the optical imagery, indicating the presence of subsurface meltwater. For example, there are prominent areas of low backscatter (~ -5 to -15 dB) extending ~ 10 km north of both the ES and

WS as detected by FASTISh (Figure 3.11b). This shows that the linear water features visible in the optical imagery are part of much larger water bodies, with a lot of the water existing as slush at the surface or in the shallow subsurface.

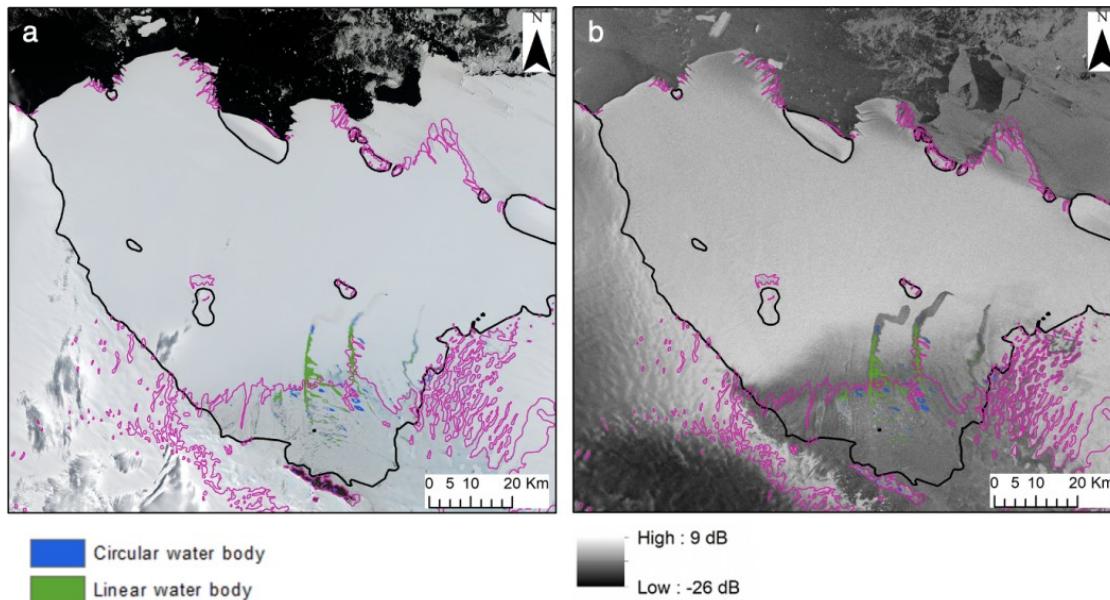


Figure 3.11. Comparison of optical imagery and radar imagery on 26 January 2017: panel (a) is a mosaicked Sentinel-2 image, and panel (b) is a Sentinel-1 SAR image. Both (a) and (b) are overlain with the blue ice extent (pink) and the mapped area of all linear and circular surface water bodies, based on the FASTISh analysis of (a).

Whilst the drainage system currently observed on the Nivlisen Ice Shelf does not transfer surface meltwater all the way to the ice-shelf front, it is plausible that such a system could develop in the future as the quantity of surface meltwater produced increases. Whilst the water may pond (possibly resulting in eventual hydrofracture and ice-shelf collapse), the ES and WS may also evolve quickly and efficiently, over increasingly saturated firn layers, to allow water to flow off the ice-shelf front, thereby exporting some excess meltwater and mitigating the potential threat to the ice shelf (Bell et al., 2017; Banwell, 2017).

Overall, 1.6% of the Nivlisen Ice Shelf is occupied by some form of surface meltwater body at some point during the 2016–2017 melt season, and over those areas, the

mean water depth is 0.85 m. Comparatively, prior to its collapse, 5.3% the Larsen B Ice Shelf was covered by a surface meltwater body, and the mean water depth was 0.82 m (Banwell et al., 2014). Whilst the mean water body depths between the Larsen B and Nivlisen Ice Shelves are comparable, the spatial distributions of these water bodies, and the proportion of the ice shelf that they cover, are different. Surface water bodies were distributed relatively evenly across the entire surface of Larsen B before it collapsed, whereas surface water bodies are predominantly clustered towards the grounding line on the Nivlisen Ice Shelf, and the transfer of surface melt towards the ice-shelf front and across snow- and firn-covered regions is predominantly facilitated by the larger WS and ES. The development of these large, linear water bodies is likely facilitated by ice-shelf surface topography and allows the transfer of summer meltwater towards the ice-shelf front. This large-scale lateral transfer of meltwater is likely further facilitated as the ES and WS develop over frozen meltwater paths from previous years (Kingslake et al., 2015).

3.5.2 Loss of water volume from circular surface water bodies

The loss of $1.5 \times 10^7 \text{ m}^3$ of surface water from the circular water bodies by 27 December 2017 follows sustained relatively warmer atmospheric conditions since the beginning of December 2017 (Figure 3.10) and coincides with an increase in the total surface water volume on the ice shelf (Figure 3.10b). In particular, we see an increase in the volume of water held within the enveloping water bodies, which continues to increase up to a maximum of $4.5 \times 10^7 \text{ m}^3$ on 26 January 2017 (Figure 3.7). It is likely, therefore, that the loss of water from circular water bodies at this early stage in the melt season signifies the lateral transfer of water away from the small “isolated” bodies near the grounding line into the large enveloping water bodies which hold and transport the surface meltwater across the ice shelf to more distal regions. This lateral transfer of water may be occurring through two mechanisms: (i) the over-topping of surface lakes, which results in the formation of shallow channels that connect water bodies and

facilitate the transfer of water towards the ice-shelf front (e.g. Banwell et al., 2019), or (ii) the gradual percolation of surface meltwater into the cold firn pack, which reduces the FAC of a region (Lenaerts et al., 2017), therefore creating an impermeable surface over which water can flow (e.g. Kingslake et al., 2015). The firn may also become saturated enough to be isothermal, therefore melting and facilitating the flow of upstream ponded meltwater. This is particularly likely to occur near surface depressions such as those that are later occupied by the WS and ES.

3.5.3 Potential implications for ice-shelf stability

It is expected that the area of coverage and volume of surface meltwater on Antarctic ice shelves will increase into the future, in line with rising atmospheric temperatures (Bell et al., 2018; IPCC, 2019; Kingslake et al., 2017; Siegert et al., 2019). This surface water may have significant implications for ice-shelf stability, as meltwater accumulation can lead to hydrofracture which could subsequently result in the collapse of an ice shelf, as seen on the Larsen B Ice Shelf in 2002 (Robel and Banwell, 2019; Banwell et al., 2013). An ice shelf may become increasingly vulnerable to hydrofracture if its FAC is reduced (Lenaerts et al., 2017). On ice shelves like the Nivlisen Ice Shelf, where large-scale lateral water transfer prevails, meltwater is delivered to locations that may otherwise not receive or experience much melt (Bell et al., 2017), and the FAC of these locations will, in turn, be reduced, increasing their susceptibility to surface meltwater ponding and hydrofracture.

Surface meltwater refreezing at the end of the melt season will also act as a significant source of heat, and the lateral transfer of surface melt could cause increased warming of the ice shelf and possible weakening in areas which currently do not experience significant summer melt. Were the maximum volume of surface meltwater we observe on the Nivlisen Ice Shelf in the 2016–2017 melt season ($5.5 \times 10^7 \text{ m}^3$) to refreeze over the maximum area of surface meltwater ($9.1 \times 10^7 \text{ m}^2$), it would release an amount of energy equivalent to 49 days of potential solar energy receipts (calculated using the methods of Arnold and Rees, 2009), assuming an ice surface albedo of 0.86, the mean

value calculated for a water-free distal area of the ice shelf. Furthermore, large-scale lateral water transfer and subsequent ponding may lead to ice-shelf flexure (and therefore potential fracture) at locations that may have otherwise not been affected by flexure in response to meltwater loading (Banwell et al., 2013, 2019; Macayeal and Sergienko, 2013). However, evidence of lateral water transfer and export off the Nansen Ice Shelf has highlighted the potential for surface drainage systems to mitigate some of these meltwater-driven instabilities (Bell et al., 2017).

3.6 Conclusions

We have adapted the pre-existing FASTER algorithm, developed for studying lakes on the Greenland Ice Sheet (Williamson et al., 2018a), so that we can identify and track the area, depth, and volume of water bodies across Antarctic ice shelves. We refer to this new algorithm as FASTISh and have used it to study the changing geometry and spatial patterns of water bodies across the Nivlisen Ice Shelf in the 2016–2017 melt season. In total, we identify and track 1598 water bodies on the ice shelf over the course of the melt season. Surface water is initially generated towards the nunatak and blue ice region, in proximity to the grounding line. This region is relatively flat and has a low albedo, and we therefore observe localised ponding of surface meltwater. As the melt season progresses and mean daily and daily maximum temperatures increase, we see a transition from isolated, localised ponding towards the grounding line to a more connected drainage system that is influenced by the ice-shelf topography. The middle of the melt season (e.g. 27 December 2016) is characterised by the progression of surface meltwater bodies towards the ice-shelf front, as two large extensive drainage systems (the east system, ES, and the west system, WS) develop in long linear surface depressions. Around the peak of the melt season (26 January 2017), the ES and WS have developed to their largest observed extent and facilitate the lateral transfer of surface melt up to 16.9 and 20.5 km north, into the firn pack and towards the ice-shelf front. The transfer of surface meltwater to regions on the ice shelf that otherwise experience little surface melt may have implications for the structure and stability of the ice shelf in the future. Our findings could be useful in comparing to

ICESat-2-derived lake depths (Fair et al., 2020), in addition to constraining ice-shelf surface hydrology models (Buzzard et al., 2018).

Chapter 4

Results II: Supervised classification of ponded water and slush on Antarctic ice shelves using Landsat 8 imagery

This chapter presents the steps taken to train and validate a Random Forest Classifier, capable of mapping the extent of ponded water and slush across Antarctic ice shelves. This classifier is then applied to the Roi Baudouin Ice Shelf between 2013 and 2020, and the outputs of this application are subsequently presented.

The work presented in this chapter has been submitted to the **Journal of Glaciology** for consideration, and is currently under review. Small edits made for the purpose of this thesis.

Contributions Rebecca Dell modified original scripts and methodologies from Ruthie Halberstadt and developed the training and validation datasets to create a Random Forest Classifier. Tom Chudley further modified the script used for expert elicitation. Neil Arnold, Alison Banwell, Ian Willis, and Tom Chudley were the four experts, and conducted the expert elicitation for the study. Rebecca Dell conducted the analysis, and wrote the manuscript, with advice from all authors.

Dell, R., Banwell, A., Willis, I., Arnold, N., Chudley, T., Halberstadt, R., Pritchard, H., Supervised classification of slush and ponded water on Antarctic ice shelves using Landsat 8 imagery. Journal of Glaciology, in review

Abstract

Surface meltwater is becoming increasingly widespread on Antarctic ice shelves. It is either stored within surface melt ponds and streams, or within firn pore spaces, which saturate to form slush. Slush can play an important role in reducing FAC, and may increase an ice- shelf's vulnerability to break-up. However, no study has yet developed a method capable of mapping the extent of slush across all Antarctic ice shelves. Here, we use GEE to train a supervised classifier capable of identifying both slush and ponded meltwater. We use Landsat 8 image scenes from six ice shelves (Nivlisen Ice Shelf, Roi Baudouin Ice Shelf, Amery Ice Shelf, Shackleton Ice Shelf, Nansen Ice Shelf, George VI Ice Shelf) to generate training classes using a k-means clustering algorithm, which are used to train a Random Forest Classifier. We use expert elicitation to validate our dataset, finding accuracies of 84% and 82% for the ponded water and slush classes respectively. Sources of error result from subjectivity when identifying the ponded water and slush boundary, and errors of commission due to cloud, cloud shadows, and topographic shadows. We apply our trained classifier to the Roi Baudouin Ice Shelf for the full Landsat 8 record (2013 to 2020). On average, 64% of the meltwater is classified as slush and 36% as ponded water. The total surface meltwater extent is greatest between late January and mid February. This highlights the importance of not excluding the mapping of slush from studies of surface meltwater on ice shelves. Future work will apply the classifier across all Antarctic ice shelves.

4.1 Introduction

Surface meltwater is present on the majority of Antarctica's ice shelves (Langley et al., 2016; Kingslake et al., 2017; Macdonald et al., 2019; Stokes et al., 2019; Arthur et al 2020a; Dell et al., 2020a). It acts as a key control on ice shelf stability (Lai et al., 2020) and thus the contribution of Antarctica's grounded ice to global sea level rise (Rignot et al., 2004; Berthier et al., 2012; Furst et al., 2016). Surface meltwater is stored either in ponds on top of impermeable ice surfaces (Bell et al., 2018; Banwell et al. 2019) or in firn pore spaces (Dunmire et al. 2020; Montgomery et al., 2020). Slush is formed

where meltwater is stored within snow and firn pore spaces which become saturated. Ponded water has been shown to drive ice-shelf collapse events through hydrofracture (Banwell et al., 2013; Robel and Banwell, 2019; Scambos et al., 2003, 2004). Melting and refreezing of slush promotes FAC depletion, which increases an ice-shelf's vulnerability to hydrofracture (Kuipers Munneke et al., 2014; Alley et al., 2018).

Across Antarctic ice shelves, areas of slush and ponded water are more commonly observed near to grounding lines, as katabatic and/or foehn winds facilitate snow erosion, exposing widespread areas of blue ice and lowering the surface albedo, which in turn amplifies surface melting (Lenaerts et al., 2017). The extent of surface melting is expected to increase as air temperatures rise throughout the 21st Century (Trusel et al., 2015; IPCC, 2019), as demonstrated across the northern George VI Ice Shelf during the 2019/2020 melt season, when sustained periods of warm air temperatures above 0°C led to 32-year record high melting (Banwell et al., 2021). It is therefore crucial to quantify the area and volume of surface meltwater on the surface of ice shelves, and to evaluate the potential impacts of this meltwater on ice-shelf stability.

Remotely sensed data can be used to track surface water bodies (i.e. ponds and streams) across space and over time. At present, two key methodologies are used to map water bodies on Antarctic ice shelves: threshold-based mapping (e.g. Banwell et al., 2014; Dell et al., 2020a; Moussavi et al., 2020) and machine learning (e.g. Dirscherl et al., 2020, 2021; Halberstadt et al., 2020). The former identifies water bodies where pixels exceed a reflectance threshold in specific bands or band combinations. Whilst most threshold-based approaches rely solely on an $NDWI_{ice}$ threshold (e.g. Dell et al., 2020a; Williamson et al., 2018a), Moussavi et al. (2020) employ a multiple threshold approach to map surface lakes more accurately on a pan-Antarctic scale. Machine learning offers an alternative to the threshold-based approach, and typically utilises more spectral information than single or multi-band methodologies. Whilst machine learning is more computationally expensive, cloud-based geoprocessing platforms such as GEE have made possible its application on a pan-Antarctic scale, without the need for local capital-intensive high-performance computing clusters. Overall, the two

methods have been shown to produce comparable results on Antarctic ice shelves (Halberstadt et al., 2020).

Despite the significance of slush for firn-air depletion and as a possible precursor to the formation of surface water bodies, little is known about its spatial-temporal trends across Antarctic ice shelves on intra- and inter-annual timescales. Research on the Nansen Ice Shelf utilised a threshold-based approach on cloud-free imagery to identify areas of slush as those with an $NDWI_{ice}$ between 0.12 and 0.14 (Bell et al., 2017). This approach built upon the work of Yang and Smith (2013), who used $NDWI_{ice}$ thresholds to map surface streams on the southwestern Greenland Ice Sheet. They commented on the difficulties of using remote sensing to distinguish between water and slush on the ice sheet surface, as the high liquid water content of slush results in similar spectral reflectance values to water. However, they found that a low $NDWI_{ice}$ threshold of 0.12 identified all water pixels, and a moderate $NDWI_{ice}$ threshold of 0.14 helped to eliminate slush. Whilst this approach may perform well in particular locations, it cannot necessarily be upscaled for application across all Antarctic ice shelves, as the identification of slush is confounded by its spectral similarity to surface water, as well as to other surface facies such as blue ice and shaded snow (Moussavi et al., 2020). As such, the suitability of specific thresholds may be highly variable across a large number of scenes.

This study, therefore, aims to use a machine learning methodology to develop a supervised classifier within GEE capable of detecting, and differentiating between, ponded water and slush across all Antarctic ice shelves. To do this, we will: (1) Train a supervised classifier capable of lake and slush identification on six different Antarctic ice shelves; (2) Validate the classifier by investigating the agreement with manual classification by a set of experts; and (3) apply the final classifier to the Roi Baudouin Ice Shelf (for the period 2013 to 2020) to identify spatial patterns and temporal variability in ponded surface water and slush.

4.2 Materials and Methods

Here we introduce the study areas used to train and validate the classifier. We also describe the steps taken to select and pre-process the Landsat 8 Level 1 images used by the classifier. We then describe the methods used to build the classifier, before explaining how we validate it. Finally, we discuss how we apply the validated classifier to the Roi Baudouin Ice Shelf.

4.2.1 Study areas

We trained and validated our methods on six individual ice shelves (Figure 4.1); (i) Nivlisen Ice Shelf, (ii) Roi Baudouin Ice Shelf, (iii) Amery Ice Shelf, (iv) Shackleton Ice Shelf, (v) Nansen Ice Shelf, and (vi) George VI Ice Shelf. These ice shelves are characterised by a range of surface melt conditions and features, resulting in a wide variety of surface spectral characteristics. The Nivlisen Ice Shelf (70.3° S, 11.3° E), located in Dronning Maud Land, has a surface area of 7380 km². The ice shelf is characterised by several elongate surface lakes, which expand and transfer meltwater towards the ice-shelf's calving front as the melt season progresses (Dell et al., 2020a). The Roi Baudouin Ice Shelf (71.03°S, 26.30°E), also in Dronning Maud Land, has an area of 33,200 km², and is characterised by extensive melt near to the grounding line, partly attributable to wind-albedo interactions, in addition to the presence of buried lakes (Dunmire et al., 2020; Lenaerts et al., 2017). The Amery Ice Shelf (70°S, 70°E) has an area of 61,800 km² and buttresses the Lambert-Amery drainage basin system, which drains 14% of the total volume of the East Antarctic Ice Sheet (Fricker et al., 2020). The Shackleton Ice Shelf (65°S, 100°E) buttresses the Denman Glacier and has a surface area of 28,600 km². It is characterised by hundreds of surface lakes every melt season, which typically cluster at the grounding line (Arthur et al., 2020a).

The Nansen Ice Shelf (74.6°S, 163.5°E) is fed by the Reeves and Priestly Glaciers (Frezzotti, 1993), and has an area of 2270 km². It is characterised by a large surface river, which exports surface meltwater into the ocean via a 130 m wide waterfall (Bell et al., 2017). The George VI Ice Shelf (72°S, 67.4°W), situated in the southwest Antarctic Peninsula, has an area of 30,300 km², and extensive areas of ponded surface water have been observed in its northern region since at least the early 1940s (Banwell et al., 2021; Reynolds, 1981; Wagner, 1972).

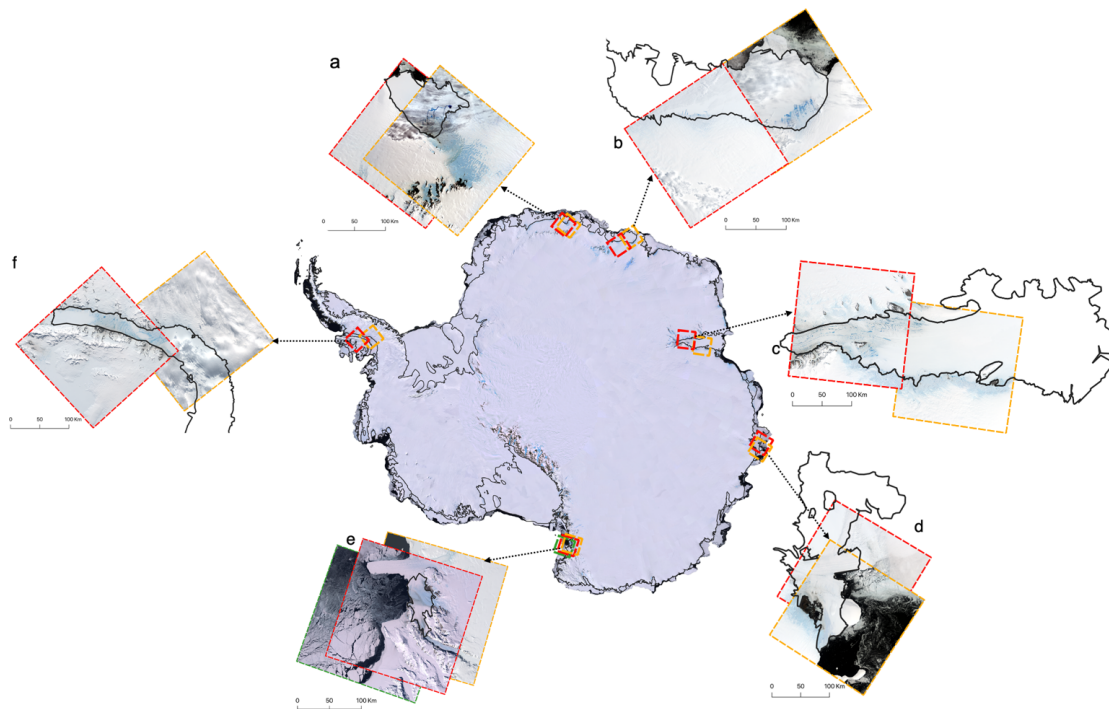


Figure 4.1: Study area figure showing the six ice shelves selected for use in the unsupervised k-means clustering algorithm. Dashed coloured boxes indicate the location of the surrounding Landsat-8 images for a) Nivlisen Ice Shelf, b) Roi Baudouin Ice Shelf, c) Amery Ice Shelf, d) Shackleton Ice Shelf, e) Nansen Ice Shelf, f) George VI Ice Shelf. Ice-shelf boundaries (from the Scientific Committee on Antarctic Research (SCAR) Antarctic Digital Database) are marked by a solid black line on both the main and subset images. The central map of Antarctica is the Center-filled Landsat Image Mosaic of Antarctica (LIMA) Mosaic (Bindschadler et al., 2008).

4.2.2 Methods

There are four main components to the FASTISh algorithm: (i) delineating water body areas, (ii) calculating water body depths and volumes, (iii) categorising water bodies as either circular or linear based on their geometries, and (iv) tracking individual water bodies and measuring their changing dimensions and geometries over time (Figure 3.2). These will be discussed in Sect. 3.2 to 3.5 respectively, once the pre-processing steps applied to the imagery used have been outlined (Sect. 3.1).

4.2.2.1 Scene selection and pre-processing

The criteria used to select suitable Landsat 8 scenes, and the methods used to pre-process them for classification, were identical across the training and validation steps of this methodology (Fig. 2). We first identified suitable image scenes for each study site by searching the full (2013 to 2020) Landsat 8 Level 1 image collection, filtering for images with less than 40% cloud cover and greater than 20° solar elevation (Halberstadt et al., 2020). 14 training images (two for each ice shelf, and an extra two for Nansen Ice Shelf; see section 4.2.2 for further explanation), and six separate validation images (one for each ice shelf) were then selected for the purpose of training and validating the classifier respectively (Appendix B, Table B.1). When choosing suitable training and validation images, we aimed to select a range of images that spanned the full austral melt season (1 November to 31 March) and were acquired at a range of solar elevations (20.9° to 36.6°) (Appendix B, Table B.1). This approach ensured that we were training and validating the classifier using images with a wide range of spectral characteristics.

Scenes were pre-processed by converting to per-pixel TOA values (Dell et al., 2020a), and by clipping to the ice-shelf boundaries (from the SCAR Antarctic Digital Database). A rock mask was then applied to each scene, following the method of Moussavi et al. (2020). This mask was then buffered by 1 km to ensure full removal of rock and rock

shadow from each scene (Halberstadt et al., 2020). Clouds (including cirrus) and cloud shadows were identified and masked using the Landsat 8 Quality Assessment Bands, with a 4 km buffer applied to ensure full removal.

Finally, all pixels with an $NDWI_{ice}$ value greater than 0.1 were selected for further analysis. We note that in previous studies, to identify slush in addition to shallow and deep water, a threshold of 0.12 has been used (Bell et al., 2017; Yang and Smith, 2013). However, in our study, we lowered the $NDWI_{ice}$ threshold to 0.1 to include more potentially wet pixels, which were then categorised as ‘slush’, ‘water’ or ‘other’ by the classifier at a later stage. $NDWI_{ice}$ was calculated using Equation 1 (see Section 2.2.3).

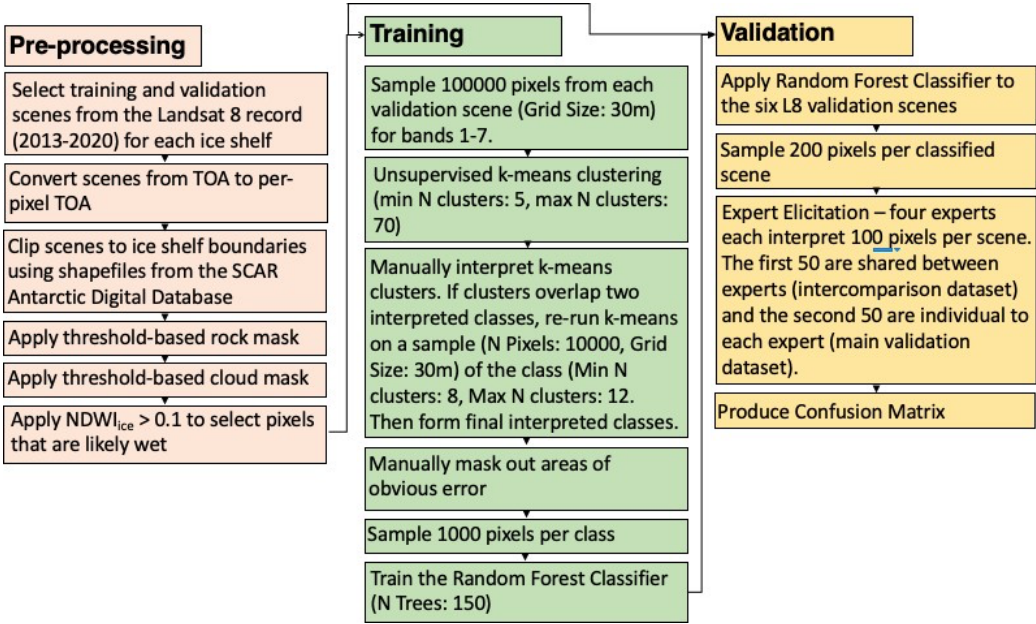


Figure 4.2: Workflow detailing the pre-processing, training, validation, and application steps for creating and using a supervised classifier to map slush and water across Antarctic ice shelves using GEE

4.2.2.2 Training data generation and supervised classification

To generate training data and to train a supervised classifier, we followed the general methodology of Halberstadt et al. (2020), which we briefly summarise here. Training data were generated by applying an unsupervised k-means clustering algorithm (Arthur and Vassilvitskii, 2007), which identifies clusters of spectrally-distinct pixels across a set of 14 scenes from bands 1-7 (Figure 4.3c). Initial training data were generated using two image scenes per ice shelf. Our initial trained classifier produced significant misclassification errors over 'dirty ice' regions; the inclusion of two additional Nansen Ice Shelf training scenes added 'dirty ice' training data and improved classifier performance.

The k-means clustering algorithm was executed by sampling 100,000 pixels from each image at the native grid size of 30 m. We specified a minimum of 5 clusters and a maximum of 70 clusters when running the k-means clustering algorithm, and around 20 clusters were returned. We then manually interpreted the resulting clusters and grouped them into interpreted classes: water, slush, and other (including, but not limited to, blue ice, snow, and dirty ice). However, in some cases, clusters identified using the k-means algorithm overlapped two interpreted classes. These clusters were therefore further subdivided using k-means (sampling 10,000 pixels) and the sub-clusters were assigned to an interpreted class. Once the final interpreted classes were formed, any areas of obvious error were manually masked from the training data. We then randomly sampled 1000 pixels from each interpreted class, to form the final training dataset for all ice shelves combined. These data were then used to train a Random Forest Classifier, implemented in GEE. The number of trees for this classifier was set to 150. The relative importance of each band within the Random Forest Classifier was also determined within GEE.

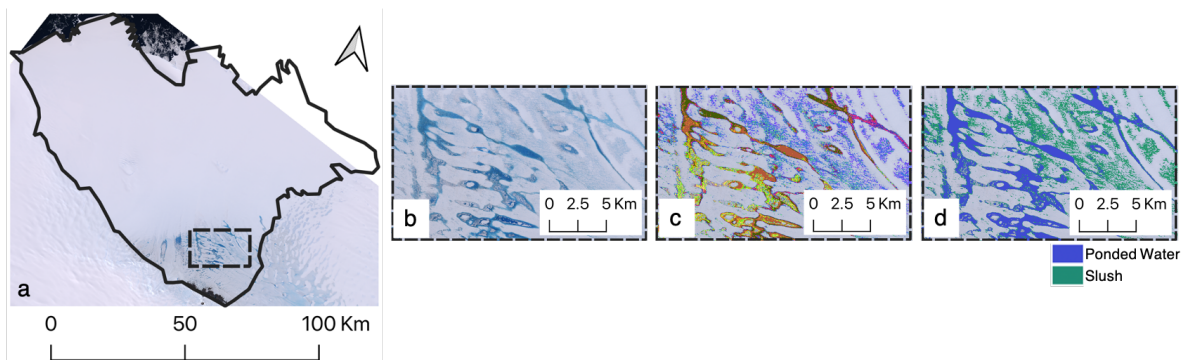


Figure 4.3: An example workflow for the k-means clustering algorithm over the Nivlisen Ice Shelf (Landsat 8, 2016-12-27. a) Base image of the Nivlisen Ice Shelf, the solid black line marks the ice- shelf area, the dashed box shows the zoomed area featured in b, c, and d. b) True Colour composite, c) k-means clusters (shown as different colours), d) interpreted ponded water and slush classes, identified from the k-means clusters in (c). In total, 10 k-means clusters were combined to form the ponded water class, and 10 k-means clusters were combined to form the slush class.

4.2.2.3 Validation

The performance of the supervised classifier was validated using the validation dataset, which included one image scene for each of the six study areas. For each of the six validation scenes, the Random Forest Classifier was applied (Figure 4.4), and 250 classified pixels were randomly sampled from each scene. We then used expert elicitation (Bamber and Aspinall, 2013), where four glaciologists, who we call ‘experts’, were each asked to manually interpret a total of 100 pixels for each image scene, classifying them as either ‘water’, ‘slush’, or ‘other’. The ‘experts’ were all familiar with looking at ice-sheet/-shelf surface hydrology using medium-resolution optical data and were not directly involved with training the classifier. Of the 100 pixels per image interpreted by each expert, the first 50 pixels for each of the six images were identical. These 300 pixels (the ‘intercomparison dataset’) were used to compare expert opinions to highlight the subjectivity of manually identifying ponded water and slush in satellite

imagery. The second 50 pixels per image were unique to each expert, and comprised the 'main validation dataset' (i.e. 1200 pixels in total).

For each pixel, in addition to providing an interpretation, each expert assigned a confidence score to reflect the certainty of their manual interpretation. The confidence score values were assigned as: (1) low confidence, (2) medium confidence, or (3) high confidence (Bamber and Aspinall, 2013). These confidence scores provided a way to identify pixels that were likely classified with less accuracy by the experts, due to their uncertainty. Finally, we produced confusion matrices to calculate the classifier accuracy for all pixels, as well as just for the high confidence pixels.

4.2.2.4 Application on the Roi Baudouin Ice Shelf

Once validated, the classifier was applied to the entire Roi Baudouin Ice Shelf for the full Landsat 8 record (2013 to 2020) to test how well the method upscaled through space and time. We deselected images with a solar elevation of less than 20° , but accepted any level of cloud cover in order to utilise as much of the available imagery as possible, thereby increasing data coverage through space and time. These selected images were then pre-processed using the same steps that were applied in the training and validation phases (see section 4.2.2). However, rather than processing individual scenes as we did previously, we created 15-day mosaiced products from the available scenes to maximise spatial coverage prior to applying an $NDWI_{ice}$ filter of greater than 0.1. Each 15-day mosaiced product was produced using the 'quality mosaic' function in GEE, which used the pixel with the greatest $NDWI_{ice}$ value for locations where pixels overlapped. For each melt-season, the products start on 1 November, and continue in blocks of exactly 15 days until 31 March (or until 1 April for leap years). The supervised classifier was applied to each 15-day product, and the total areas of both ponded water and slush were calculated. For 15-day periods coverage across the Roi Baudouin Ice Shelf, we scaled ponded water and slush areas

to full ice-shelf area by calculating the visible area of each 15-day product as a fraction of the full ice-shelf area, and then dividing by this fraction. In addition to 15-day products, for each melt season, we compiled maximum melt extent products (Williamson et al., 2018a) to show each pixel that was covered by either ponded meltwater, slush, or both ponded meltwater and slush.

4.3 Results

4.3.1 Classifier accuracy

Table 4.1 shows the results from the intercomparison dataset for each scene in the validation dataset, which were interpreted by all four experts, whilst Figure 4.4 shows the supervised classifier as applied to six validation images. The data shown in Table 4.1 include all interpreted pixels regardless of the associated confidence scores. Overall, the accuracy of the lake class is 78%, and the accuracy of the slush class is 71%. For the water class, the experts all produced similar accuracy scores for the Roi Baudouin Ice Shelf (8% spread), and more dissimilar scores for the Nansen Ice Shelf (30% spread), with an overall spread of just 6%. For the slush class, the experts are in closest agreement over the George VI Ice Shelf (11% spread), and in least close agreement over the Nansen Ice Shelf (79% spread). As with the water class, these discrepancies tend to cancel out between experts giving an overall spread of just 5%. Table 4.2 shows the same data as Table 4.1, but only for the pixels for which the experts had ‘high confidence’ in their interpretation.

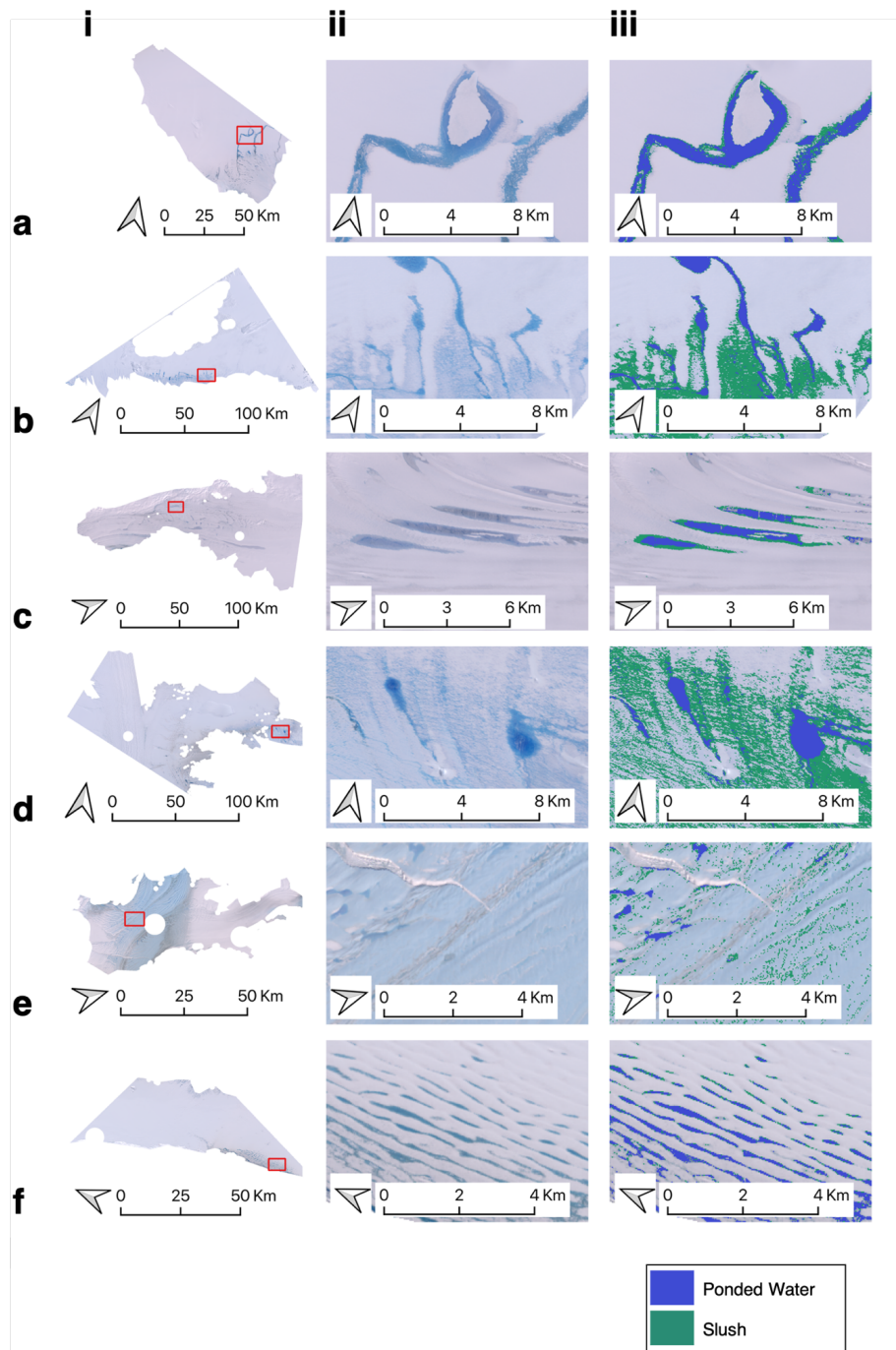


Figure 4.4: Preliminary outputs from the supervised classifier, as applied to six Landsat 8 validation images for a) Nivlisen Ice Shelf, b) Roi Baudouin Ice Shelf, c) Amery Ice Shelf, d) Shackleton Ice Shelf, e) Nansen Ice Shelf, f) George VI Ice Shelf. Panels in column i show the Landsat 8 true-colour composite images to be classified, with the black boxes delineating close-up areas shown in panels in columns ii and iii. Column ii panels show the close up areas in true-colour composite, and column iii panels show the results for these areas produced by the supervised classifier, with blue representing water and green representing slush.

Table 4.1: Accuracy scores for the intercomparison dataset (the 50 pixels shared by all experts for each ice-shelf validation image), listed by expert.

	Water							Slush						
	Roi B	Nansen	Nivlisen	Shackleton	GVI	Amery	Averaged	Roi B	Nansen	Nivlisen	Shackleton	GVI	Amery	Averaged
Expert 1	88%	91%	71%	84%	65%	64%	77%	70%	85%	71%	65%	67%	63%	70%
Expert 2	90%	80%	88%	88%	80%	69%	82%	76%	52%	92%	73%	76%	69%	73%
Expert 3	96%	94%	80%	78%	65%	50%	77%	88%	94%	83%	60%	65%	37%	71%
Expert 4	92%	64%	85%	88%	68%	58%	76%	68%	15%	82%	79%	70%	93%	68%
Averaged	91%	82%	81%	84%	70%	60%	78%	76%	61%	82%	69%	69%	65%	71%

Table 4.2: High confidence accuracy scores for the intercomparison dataset (the 50 pixels shared by all experts for each ice-shelf validation image), listed by expert.

	Water							Slush						
	Roi B	Nansen	Nivlisen	Shackleton	GVI	Amery	Averaged	Roi B	Nansen	Nivlisen	Shackleton	GVI	Amery	Averaged
Expert 1	83%	80%	83%	88%	89%	67%	82%	59%	86%	83%	64%	89%	67%	75%
Expert 2	94%	50%	94%	89%	88%	75%	82%	76%	33%	100%	89%	88%	67%	76%
Expert 3	100%	92%	83%	88%	91%	40%	82%	87%	92%	89%	70%	100%	40%	80%
Expert 4	100%	100%	100%	100%	77%	62%	90%	50%	25%	100%	100%	91%	57%	71%
Averaged	94%	81%	90%	91%	86%	61%	84%	68%	59%	93%	81%	92%	58%	75%

Table 4.3 shows the accuracy results for the classifier over the main validation dataset (where each expert interpreted 50 different pixels per ice shelf). The accuracy for the water class is 78% and for the slush class is 70%; virtually the same as they are for the intercomparison data set. The classifier is most accurate at identifying water for the Shackleton Ice Shelf (91%) and least accurate for the Amery Ice Shelf (61%). In contrast, the classifier is most accurate at identifying slush for the Nivlisen Ice Shelf (80%) and least accurate for the Nansen Ice Shelf (60%). The percentage of low confidence pixels ranges from 13% (Nivlisen and George VI ice shelves) to 28% (Shackleton Ice Shelf).

Table 4.4 shows the accuracy results for the main validation dataset using high-confidence pixels only. The mean accuracy for the lake class is 84% and for the slush class is 82%. Agreement between the experts and the classifier is greatest for water over the Shackleton Ice Shelf (96%) and for slush over the Nivlisen Ice Shelf (92%). This agreement is lowest for water over the Amery Ice Shelf (65%) and for slush over the Roi Baudouin Ice Shelf (72%).

Table 4.3: Accuracy scores for the main validation dataset (the 250 individual pixels (50 per expert) for each ice-shelf validation image) for the ponded water and slush classes separately. Percentage of pixel confidences for each ice shelf is also recorded.

	Ponded Water Accuracy	Slush Accuracy	Low Confidence Pixels	Medium Confidence Pixels	High Confidence Pixels
Nivlisen	80%	80%	13%	48%	40%
Roi Baudouin	87%	65%	19%	32%	50%
Amery	61%	64%	15%	59%	27%
Shackleton	91%	75%	28%	46%	26%
Nansen	81%	60%	22%	47%	31%
George VI	70%	74%	13%	52%	36%
Average	78%	70%	18%	47%	35%

Table 4.4: High confidence accuracy scores for the main validation dataset (the 250 individual pixels (50 per expert) for each ice-shelf validation image) for the ponded water and slush classes separately.

	Ponded Water	Slush
Nivlisen	92%	92%
Roi Baudouin	86%	72%
Amery	65%	73%
Shackleton	96%	88%
Nansen	80%	74%
George VI	86%	91%
Average	84%	82%

4.3.2 Relative importance of input bands

The relative importance of each band within our supervised classifier was determined within GEE, and the results show that all bands contribute towards the classification of ponded water and slush (Table 4.5). Band 5 (near-infrared) is of greatest importance for the supervised classifier, as it has an importance score of 20% (Table 4.5). Bands 1-4 (visible) and 6-7 (SWIR 1 and 2) all have similar weightings, with importance scores ranging between 12% and 15%.

Table 4.5: Relative importance of each of the Landsat 8 bands used by the supervised classifier.

B1	B2	B3	B4	B5	B6	B7
14%	13%	14%	15%	20%	12%	12%

4.3.3 Application to Roi Baudouin Ice Shelf

On the Roi Baudouin Ice Shelf for the austral summers from 2013/2014 to 2019/2020, the greatest area of slush ($1.3 \times 10^9 \text{ m}^2$) is observed between 15 January - 29 January 2014, whilst the greatest area of ponded water ($1.1 \times 10^9 \text{ m}^2$) is observed between 14 February - 28 February 2017 (Appendix B, Figure B.1). However, within the dataset scaled to the full area of the Roi Baudouin Ice Shelf (discussed from this point onwards) the maximum areas of ponded water and slush are reached between 30 January - 13 February 2017 ($1.9 \times 10^9 \text{ m}^2$) and 15 January - 29 January 2016 ($3.5 \times 10^9 \text{ m}^2$) respectively (Figure 4.5). In contrast, the lowest summer maximum areas of ponded water and slush occur between 14 February - 28 February 2019 (ponded water), and 15 January - 29 January 2019 (slush), reaching values of $2.9 \times 10^8 \text{ m}^2$ and $5.7 \times 10^8 \text{ m}^2$ respectively.

For all seven melt seasons, the total area of ponded water and slush is greatest in either January or February. Furthermore, for all melt seasons except 2018/2019, the greatest areas of ponded water and slush are observed in the same 15-day periods within each melt season. However, for the austral summer of 2018/2019, the greatest total area of slush is recorded approximately a month prior to the greatest total area of ponded water (Figure 4.5). Overall, the greatest areas of slush for each melt season are more variable than the greatest areas of ponded meltwater for each melt season. The former range from $5.7 \times 10^8 \text{ m}^2$ between 15 January - 29 January 2019 to $3.5 \times 10^9 \text{ m}^2$ between 15 January - 29 January 2016, whereas the latter vary from $2.9 \times 10^8 \text{ m}^2$ between 14 February 2019 - 28 February 2019 to $1.9 \times 10^9 \text{ m}^2$ between 30 January 2017 - 13 February 2017 (Appendix B, Table B.2). Slush dominates the total melt area across the Roi Baudouin Ice Shelf, making up over half of the total melt on 39 of the 48 15-day periods investigated, and on average accounts for 64% of the total meltwater area (Appendix B, Table B.2). From the 2014/2015 melt season onwards, the percentage slush on the Roi Baudouin Ice Shelf is greatest between 16 November and 30 December, when it accounts for between 84% and 96% of the total meltwater area.

Of the seven melt seasons investigated, the 2016/2017 melt season has the greatest recorded total meltwater area, reaching $5 \times 10^9 \text{ m}^2$ between 30 January - 13 February 2017. Of this total area, 38% is ponded water and 62% is slush (Appendix B, Table B.2). Conversely, the melt season that had the lowest total meltwater area is 2019/2020, with $7.5 \times 10^8 \text{ m}^2$ between 15 January - 29 January 2019. Of that total area, 24% is ponded water and 76% is slush (Appendix B, Table B.2).

Figure 4.6 shows each of the 15-day data products that were produced within GEE for the 2016/2017 melt season. In these 15-day products, we manually inspected each image and ignored errors of commission (across the central and distal regions of the ice shelf). Therefore, the following results focus on the true positive results for the 2016/2017 season, which show meltwater in proximity to the ice-shelf's grounding line. Little meltwater is detected between 1 November - 15 December 2016. However, from 16 December - 30 December 2016 onwards, areas of slush begin to develop in proximity to the grounding line in both the southeast and central southern parts. By early January (31 December 2016 - 14 January 2017) ponded water also begins to form amongst the areas of slush, and the areas of both classes increase until 30 January - 13 February 2017, after which the areas of both classes begin to decrease (Figures 4.5 and 4.6). A number of the 15-day products for this melt season have data gaps resulting from cloud masking, or a lack of image scenes covering the area of interest. The percentage ice-shelf area coverage for the 2016/2017 melt season ranges from 38% (30 January - 13 February 2017) to 99% (1 December - 15 December 2016) (Appendix B, Table B.2).

Data were combined to produce maximum melt extent across the Roi Baudouin Ice Shelf for each melt season (1 November - 31 March) from 2013/2014 to 2019/2020 (Figure 4.7). In every melt season, both ponded water and slush are present predominantly in the southeast of the ice shelf, towards the grounding line. This area of ponded water and slush is the most spatially extensive in 2016/2017 and 2017/2018 (Figure 4.7d, e), when it extends approximately 47 km from the grounding line towards the ice-shelf front. In this region, slush is more spatially extensive than ponded water. Compared to slush, ponded water is typically observed further towards the northern

edge of the melt zone (i.e., closer to the ice front) each year. The exception is in the 2015/2016 melt season, where slush dominates the northern edge of the melt zone and ponded water sits amongst the slush (Fig 7).

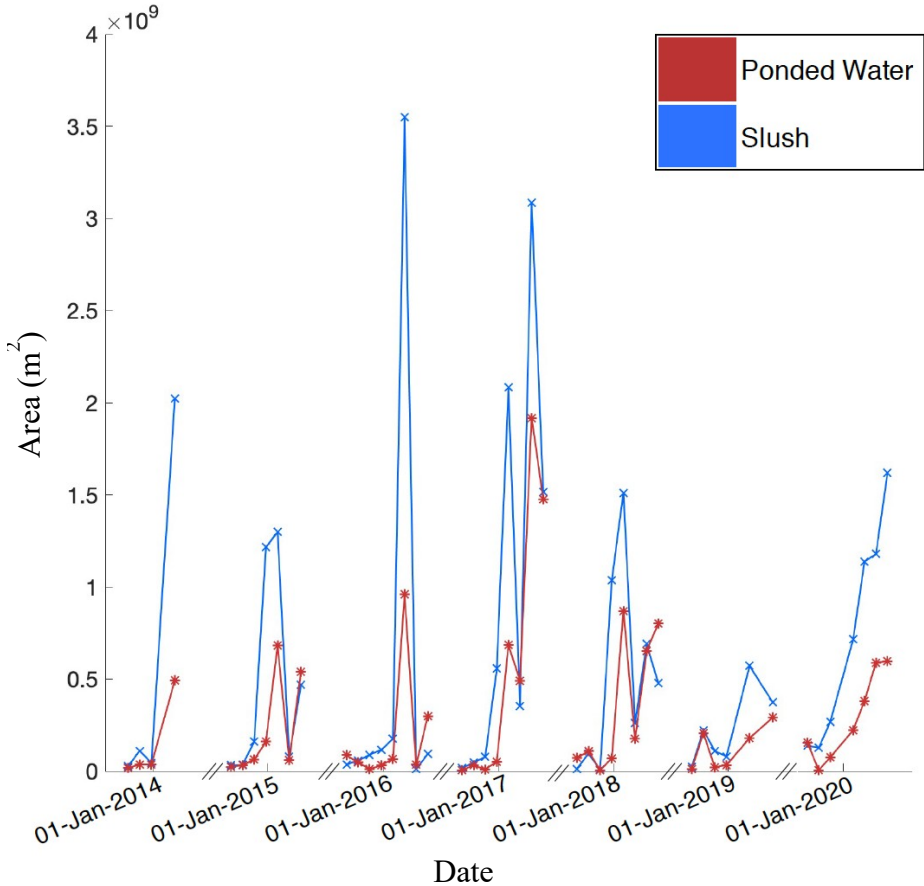


Figure 4.5: Scaled areas of ponded water (red line) and slush (blue line) on the Roi Baudouin Ice Shelf from 2013/14 to 2019/20, derived from supervised classification of 15-day Landsat 8 mosaic products created in GEE (see section 4.2.2.4). Data are only plotted where $\geq 20\%$ coverage of the Roi Baudouin Ice Shelf is met, and all plotted data are scaled to the full ice- shelf area.

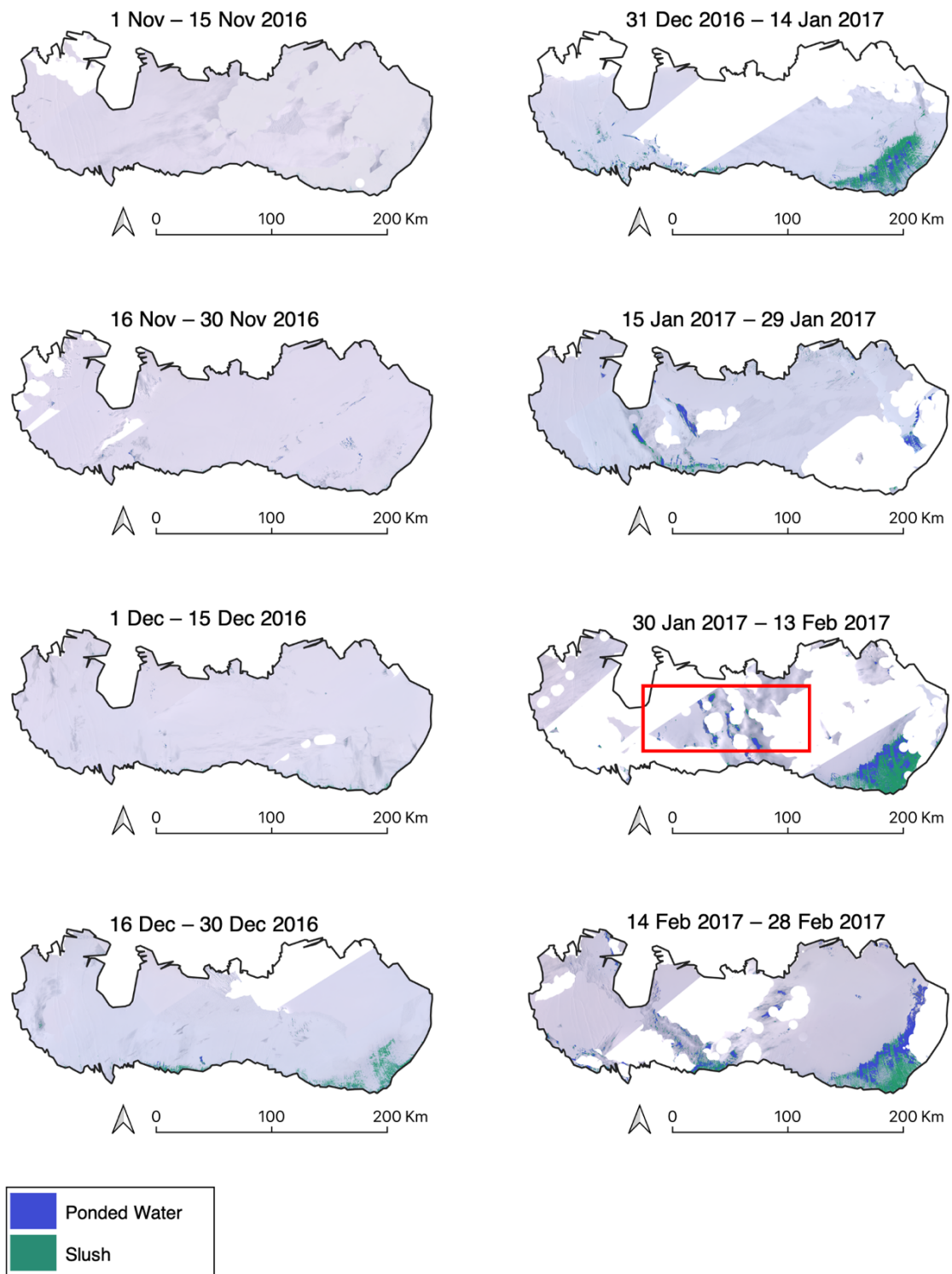


Figure 4.6: 15-day melt products for the 2016/2017 melt season across the Roi Baudouin Ice Shelf. The red box in the 30 Jan 2017 – 13 Feb 2017 panel roughly denotes the area where errors of commission due to cloud and cloud shadows are generally found.

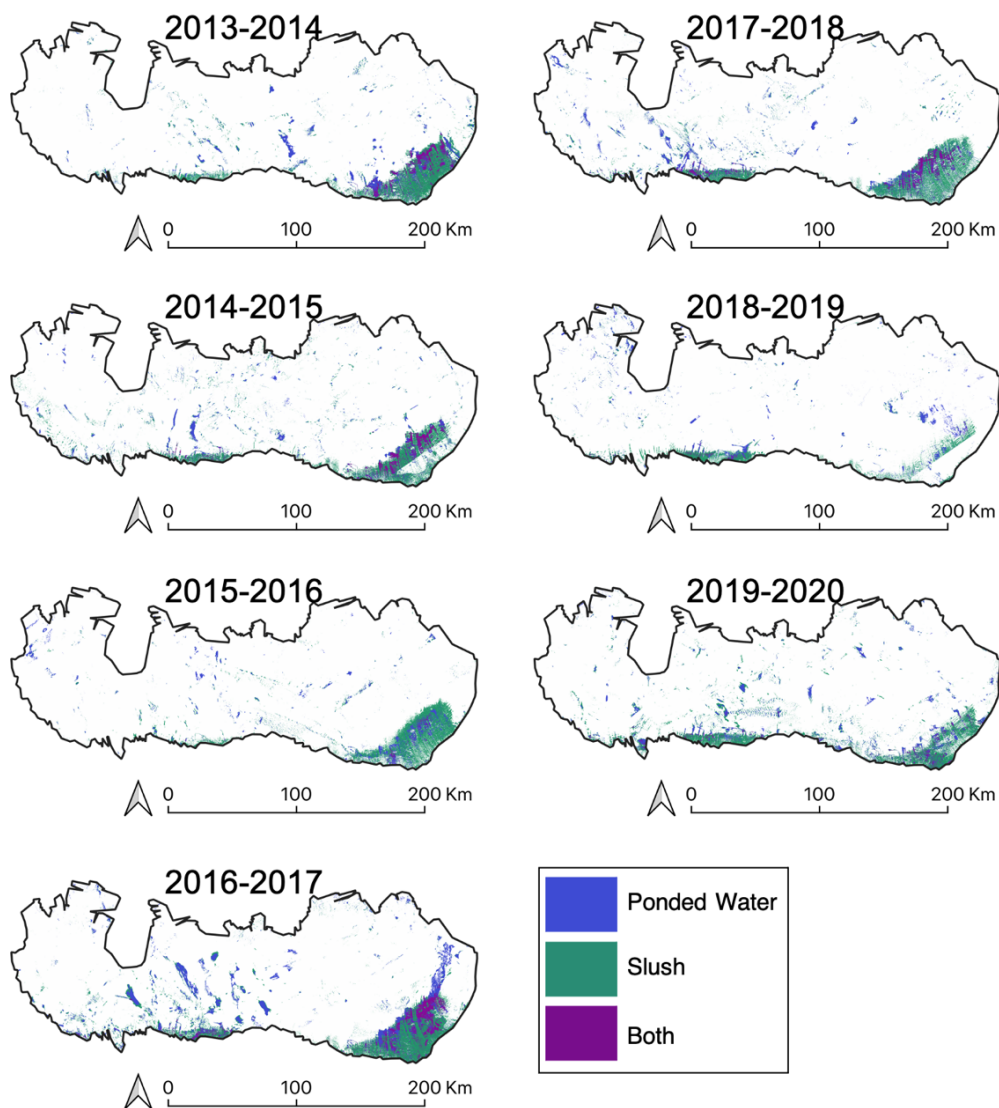


Figure 4.7: Maximum melt extent plots for each melt season, calculated by mosaicking all 15- day melt products for each melt season. Maximum areas of ponded water, slush, and both (where both ponded water and slush are identified within the melt season) are mapped.

4.4 Discussion

4.4.1 Classifier accuracy

The overall accuracies of the ponded water and slush classes are 84% and 82% respectively when comparing the classifier's outputs to high confidence expert interpretations (Table 4.4). Over all ice shelves, the percentage of pixels that are classified with high confidence do not exceed 50% (Table 4.2), highlighting that even 'experts' are unable to classify all pixels with total confidence. Thus, although we use expert opinion to assess the accuracy of our classifier, each expert may be no more accurate than the classifier output itself. A solution to this would be to use ground based multi- or hyper-spectral data from ice shelves as ground truth data. However, to the author's knowledge, no such data currently exist.

By collecting four expert interpretations, we aimed to minimize the effects of bias that each expert might have, and to get a more holistic set of expert interpretations for each ice shelf. The need for this approach is indicated by the spread between high-confidence pixels classified by experts for each ice shelf in the intercomparison dataset (Table 4.2). For example, the Nansen Ice shelf agreement between the experts and the classifier ranges from 50% to 100% for ponded water, and from 25% to 86% for slush. For the ponded water class, Expert 2 has the lowest agreement with the classifier. This is due to the classifier designating certain pixels as 'other' (e.g. non-wet surface facies), whilst the expert interprets the pixels to be ponded water. For the slush class, Expert 4 has the lowest agreement with the classifier, which classifies certain pixels as 'other' that are interpreted to be slush by the expert. Whilst the accuracy assessment attempts to best mimic ground-truthing through the use of multiple experts, it should be noted that the classifier is trained predominantly by a single person (separate to the experts used to validate the classifier), and so the classifier may reflect the biases of that individual. In addition, whilst experts are able to interpret a pixel within its surrounding spatial context, including both the immediate surrounding pixels as well as those elsewhere on the ice shelf, the classifier assesses the spectral characteristics of the pixel alone. Overall, the trained classifier scores best against

interpretations made by Expert 4, suggesting that the individual training the classifier and Expert 4 share similar glaciological interpretations of Landsat 8 imagery. Whilst these factors are unavoidable, they further highlight the need for ground based multi- or hyper-spectral data across ice shelves, which would facilitate a more robust assessment of this classifier's accuracy.

As previously mentioned, the main validation dataset for high confidence pixels returns accuracy scores of 84% for ponded water and 82% for slush. Similar work for supervised classification of surface lakes only (i.e. not including slush) on Antarctic ice shelves achieved a mean pixel- based accuracy score of 93% (Halberstadt et al., 2020). Our slightly lower scores likely reflect the incorporation of slush into the classifier, in addition to the fact that we used a wider range of training sites. Furthermore, our validation techniques are different, as they validate the classifier against multiple expert opinions, as opposed to just one expert in Halberstadt et al. (2020).

In our study, agreement between the classifier and the expert interpretations for high-confidence pixels only is greatest for ponded water over Shackleton Ice Shelf (96%) and for slush over Nivlisen Ice Shelf (92%). However, the classifier accuracy is lowest over Amery Ice Shelf, achieving 65% accuracy for ponded water and 73% for slush. The majority of the classification errors on the Amery Ice Shelf in particular appear to result from topographic shadows being incorrectly classified as either ponded water or slush (Figure 4.4). Additionally on the Amery Ice Shelf, some pixels are classified as slush, whilst experts interpret them to be ponded water. This confusion is likely because many of the lakes in the validation image for Amery Ice Shelf may be covered by a thin layer of frozen ice, which adjusts the pixel's spectral properties within the classifier (Figure 3.4). However, expert confusion also occurs over Amery Ice shelf, as experts struggle to classify ponded water and slush that has frozen over.

Another source of classifier-error is subjectivity when defining the slush/ponded- water boundary. Whilst the classifier utilises training data to determine the slush/ ponded- water boundary, comparing classifier results with expert interpretations reveals some disagreement. However, we note that this disagreement is likely no greater than

disagreement between the experts themselves, resulting from individual subjectivity. Again, considering future work, without ground based multi- or hyper-spectral data it would be difficult to further improve such estimations of the slush/ponded-water boundary.

A final source of classifier-error is errors of commission resulting from cloud and cloud shadows and this is discussed separately in section 4.4.4.

4.4.2 Comparison to $NDWI_{ice}$

Whilst threshold-based methods have been used for the identification of surface meltwater bodies (e.g. surface lakes and streams) on Antarctic ice shelves (e.g. Banwell et al., 2014; Dell et al., 2020a; Moussavi et al., 2020), no prior studies have also attempted to map slush across an entire ice shelf for multiple melt seasons. Upscaling slush identification through space and time using simple threshold-based mapping approaches would lead to significant errors of omission and commission, owing to the spectral similarities between slush and other surface facies (e.g. lakes, blue ice, dirty ice) (Figure 4.8). For example, we found that applying $NDWI_{ice}$ thresholds of greater than 0.12 and less than or equal to 0.14 for slush and greater than 0.14 for ponded water (following Yang and Smith, 2013 and Bell et al., 2017) over the Shackleton Ice Shelf leads to large errors of omission for slush when compared to the classifier output, due to confusion between water and slush (Figure 4.8a). In contrast, applying these $NDWI_{ice}$ thresholds over the Nansen Ice Shelf leads to errors of commission for slush, due to confusion between blue ice and slush (Figure 4.8b). On the George VI Ice Shelf, however, there are few differences between the threshold method and the classifier output, although even here the threshold method tends to underestimate slush area compared to the classifier (Figure 4.8c).

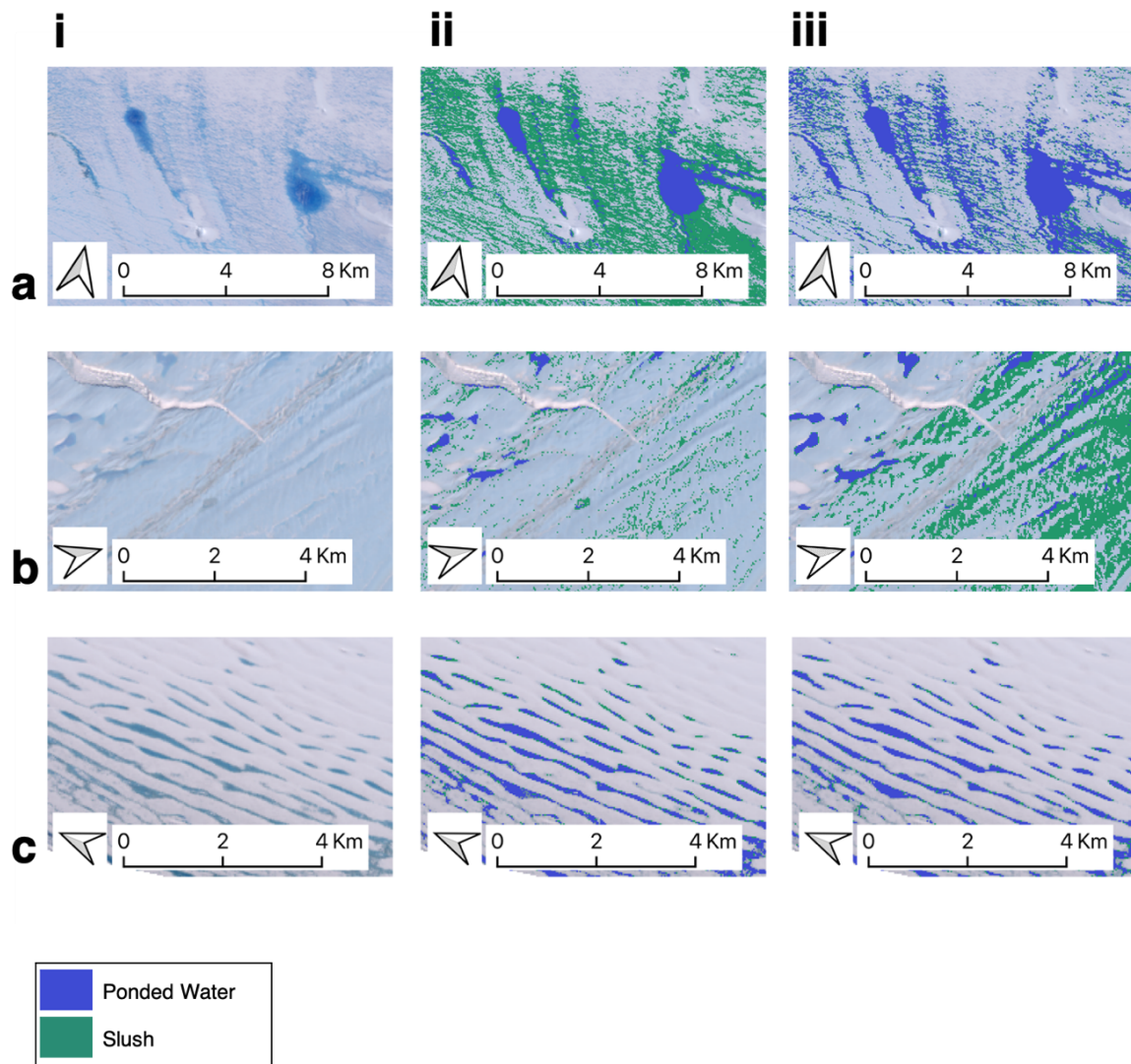


Figure 4.8: Outputs from the supervised classifier and from NDWI_{ice} thresholding applied to sections of a) Shackleton Ice Shelf, b) Nansen Ice Shelf and c) George VI Ice Shelf. Panels in column i show the base true-colour composite images, panels in column ii show the area classified using the supervised classifier developed in this study, and panels in column iii show the area classified using NDWI_{ice} thresholds, where slush has NDWI_{ice} values greater than 0.12 and less than or equal to 0.14, and ponded water has NDWI_{ice} values greater than 0.14.

The limitations of the NDWI_{ice} method that we have described above are overcome through our supervised classifier, as it is trained using seven Landsat 8 bands (Bands 1-7) as opposed to just two (Bands 2 and 4) for NDWI_{ice}, and it is therefore better able to distinguish between surface classes using a broader range of spectral information. For our classifier, the near infrared band (Band 5) is found to be the most important

when distinguishing between classes (Table 4.5). This is likely related to the low reflectivity of water in NIR wavelengths (Work and Gilmer, 1976; Haibo et al., 2011). Overall, whilst simple threshold-based methods seem capable of accurately classifying ponded meltwater on ice shelves, classifying surface facies such as slush, which have similar spectral properties to much of their surroundings, requires more spectral information. Whilst threshold-based approaches do not exclude the use of more spectral information, the manual selection of each threshold is arduous. Machine learning overcomes this as it is able to determine which spectral information is of value for each classification based upon the training data.

4.4.3 Evolution of ponded water and slush over the Roi Baudouin Ice Shelf

To demonstrate the capability of our supervised classifier for pan-Antarctic identification of ponded water and slush over time, we apply it across the Roi Baudouin Ice Shelf for the full Landsat 8 record. Of the seven melt seasons investigated (2013/2014 to 2019/2020), the greatest total meltwater extent ($5.0 \times 10^9 \text{ m}^2$) is recorded between 30 January and 13 February 2017. This observation is corroborated by Halberstadt et al. (2020) who classified surface lakes on the Roi Baudouin Ice Shelf over a number of image scenes between 2013 and 2018, and found peak melt area on the 25th February 2017. Furthermore, our findings align with studies on the Amery Ice Shelf, where threshold-based methods (Moussavi et al., 2020) and machine learning methods (Halberstadt et al., 2020) were used to calculate the area of surface lakes over a single path/row. Similarly to Moussavi et al. (2020), whilst we identify marked inter-annual variability in both ponded melt and slush areas, we find the intra-seasonal trends for inferred meltwater storage to be fairly consistent.

As slush (which may be saturated firn or saturated snow perched on blue ice or refrozen lakes) accounts for an average of 64% of the total meltwater area on the Roi Baudouin Ice Shelf over the full study period, our findings highlight the importance of

accurately mapping slush extent in addition to ponded water extent when investigating surface meltwater on Antarctic ice shelves. Most work until this point has focussed on meltwater stored in surface lakes, owing to their significance for potential hydrofracture-induced ice-shelf collapse. For example, work by Stokes et al. (2019) identified over 1300 km² of surface meltwater held in surface lakes across East Antarctica in January 2017. Based on our findings, in January 2017 the mean proportion of slush on the Roi Baudouin Ice Shelf is 59%. Assuming the proportion of slush is similar across other East Antarctic ice shelves, it is likely that the area of surface meltwater in January 2017 across East Antarctica was at least double the area covered by surface lakes reported by Stokes et al. (2019). Therefore, by studying meltwater held only in surface lakes, the total area of surface water across Antarctic ice shelves is likely to be significantly underestimated.

We found that the proportion of slush relative to ponded meltwater across the Roi Baudouin Ice Shelf is greatest between 16 November and 30 December each melt season (excluding 2013/2014, when it is greatest between 15 January and 29 January 2014). Whilst no previous literature has mapped the extent of slush on an interannual timescale, Bell et al. (2017) used a simple $NDWI_{ice}$ threshold to identify slush on a small area of the Nansen Ice Shelf in the 2013/2014 melt season. They found the area of slush was greatest on 26th December 2013 and then gradually declined throughout early January 2014 (Bell et al., 2017). Whilst this trend contradicts our findings for the 2013/2014 season on the Roi Baudouin Ice Shelf, it corroborates the trends we identify through the remaining six melt seasons (2014/2015 to 2019/2020). Bell et al. (2017) suggested that the expansive slush identified on the Nansen Ice Shelf in December coalesced to form ponded meltwater by early January. We propose that a similar transition occurs across the Roi Baudouin Ice Shelf, as the percentage of the total meltwater on the ice shelf held in slush generally falls from the end of December and into early January, and an increasing amount of melt is therefore held in water bodies.

For surface meltwater to pond, the underlying surface needs to be impermeable, and is likely, therefore, to be either blue ice or saturated firn (slush). Based on the results presented here (Figure 4.7) many pixels that are classified as ponded water, are also

classified as slush at least once in the melt season, and over the full study period (2013-2020), 26% of all water-covered pixels are occupied by ponded water and slush at least once. In these locations, therefore, it is likely that as melt increases throughout the melt season, the firn layer becomes increasingly saturated and water can no longer percolate into the firn pack, which results in ponding at the surface. However, we also note that some pixels are only ever classified as ponded meltwater during a melt season, and are therefore not preceded by slush (Figure 4.7). Evidence for this is seen in all melt seasons and is particularly prominent towards the central grounding line. We postulate that these areas of ponded melt are filling depressions within blue ice surfaces or are forming on top of melt ponds from previous melt seasons.

Exposed blue ice surfaces have been identified before in proximity to the Roi Baudouin Ice Shelf grounding line, and result from katabatic winds which cause snow erosion and an increase in near-surface temperatures (Lenaerts et al., 2017). Lenaerts et al. (2017) attributed a doubling in summer surface melt at the grounding line to the katabatic winds, and they also noted that the exposed blue ice surfaces will contribute to further melt, as they have a lower surface albedo than snow covered surfaces. These processes help to explain the main patterns of ponded meltwater that we observe across the Roi Baudouin Ice Shelf, as ponded meltwater is clustered near to the grounding line (Figures 4.6 and 4.7).

4.4.4 Errors arising from cloud and cloud shadows

In both the validation dataset and the larger Roi Baudouin Ice Shelf dataset, errors of commission due to cloud and cloud shadows are evident (Figures 4.4-6), which highlights a limitation of our classifier. For example, from 31 December 2016 to 14 January 2017, and through to the end of the melt season, errors of commission are identified over the central and distal regions of the Roi Baudouin Ice Shelf (Figure 4.6). Similar errors are identified within the maximum melt extent products (Figure 4.7). This

limitation has also been found in similar previous work (e.g. Halberstadt et al., 2020), with errors resulting from imperfect cloud masking methods.

The transient nature of cloud and cloud shadows mean that these errors of commission will have a low persistence over an entire melt season. This is demonstrated by Figure 4.9, which shows the number of times over the full study period that a pixel is classified as either ponded water or slush over the Roi Baudouin Ice Shelf. The errors of commission in the central and distal regions of the ice shelf have a persistence score of one (Figure 4.9, grey pixels), meaning that each pixel was classified as water at only a single point in time. In contrast, areas of extensive meltwater towards the southeast and central southern grounding line generally have higher persistence values (Figure 4.9). Therefore, a potential solution to errors of commission resulting from cloud and cloud shadows when looking at maximum melt products for each melt season would be to filter out pixels with a persistence of one. However, this would lead to the removal of some true positives, where water has been correctly classified at its maximum extent for the melt season, but for only a single point in time. Future work is needed to develop methods to reduce the errors of commission introduced by clouds, either at the pre-processing stage prior to classifier development, or post classifier application.

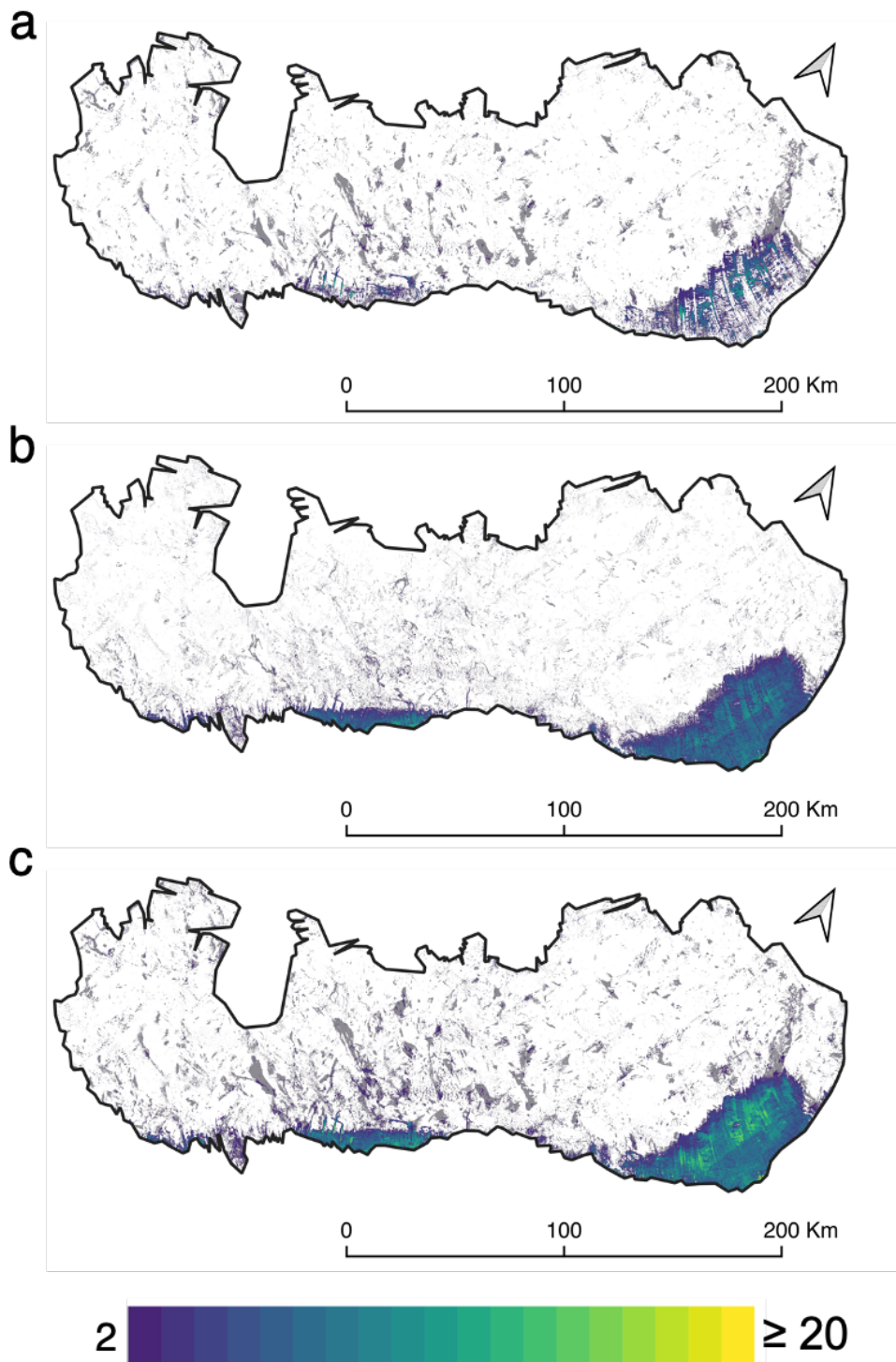


Figure 4.9: Heatmap showing the number of times each pixel is classified as a) ponded water, b) slush and c) either ponded water or slush between 1 November 2013 and 31 March 2020. Pixels with a value of 1 have been set to grey.

4.5 Conclusions

We have presented a new machine learning method that is capable of accurately classifying ponded water and slush across Antarctic ice shelves using the full Landsat 8 record. This is achieved by using a Random Forest Classifier, which is trained using spectral data from six different ice shelves around the continent. The classifier performs well across all ice shelves throughout multiple melt seasons, achieving accuracies of 84% for ponded water and 82% for slush. Whilst the classifier encounters errors when defining the slush/ponded-water boundary, we also find that experts disagree on where this boundary should lie, and it is therefore likely that the extent of slush can not be more accurately mapped without the collection of ground-truthed data. Errors of commission caused by cloud and cloud shadows are the main source of error associated with this method. Future work should look to improve cloud masking approaches before applying the classifier, or to develop a means of filtering out false positives caused by clouds after the classifier has been applied. In this way, it will be possible to produce accurate time-series of slush and ponded meltwater extent across all Antarctic ice shelves.

Finally, we applied the classifier to the Roi Baudouin Ice Shelf for the 2013/2014 to 2019/2020 melt seasons to produce a time-series of slush and ponded melt extent. For each melt season, many of the pixels classified as ponded water were also classified as slush; an observation that likely captures the saturation of firn and subsequent formation of surface ponds as the melt season progresses. On average, slush accounts for about two thirds of the total meltwater extent over the full study period. This highlights the need to map slush in addition to ponded water on ice shelves over a pan-Antarctic scale, to ensure we do not underestimate the area of surface meltwater.

Chapter 5

Results III: Mapping ponded water and slush extent across Antarctic

Peninsula ice shelves, 2013 to 2021

5.1 Introduction

In this chapter, the methods presented in Chapter 4 are further developed and applied to eight ice shelves on the Antarctic Peninsula (Figure 5.1). As discussed in Chapter 2 (Section 2.1), the Antarctic Peninsula has experienced several ice-shelf collapse events since the 1950s (e.g. Cook and Vaughan, 2010), such as the collapse of the Larsen B Ice Shelf in 2002, which was likely driven by the chain-reaction hydrofracture of ~ 3000 surface lakes (e.g. Banwell et al., 2013). Prior to collapse, the formation of the lakes was determined by the rate of firn-air depletion on the ice shelf, as the ability of the firn to retain surface meltwater (and consequently enable surface meltwater ponding) is dependent on its pore space (Leeson et al., 2020). Firn-air depletion is often driven by re-freezing of surface meltwater in the firn, and refreezing slush (i.e. saturated firn) will drive firn-air depletion very rapidly.

This chapter, therefore, aims to quantify the extent of both slush and ponded water across eight ice shelves on the Antarctic Peninsula for the full Landsat 8 record (2013 to 2021). Section 5.2 briefly introduces each of these ice shelves, and Section 5.3 details the data and methods used that go beyond or differ from those already outlined in Chapter 4. In Section 5.4, time-series of observations for both slush and ponded meltwater extent are presented, and inter- and intra-annual variability for each ice shelf

are identified. Sections 5.4.1 - 5.4.3 present the key temporal and spatial patterns observed in the full dataset, for all ice shelves studied on the Peninsula. Sections 5.4.4 - 5.4.6 then focus in greater detail on the spatial and temporal variability observed on three neighbouring ice shelves on the west Antarctic Peninsula: Wilkins (Section 5.4.4), Bach (Section 5.4.5), and north George VI (Section 5.4.6) ice shelves, in order to assess local variability in surface meltwater extents, and to highlight the various successes or shortcomings of the applied methodology. Section 5.5 presents a discussion on the variability observed with reference to potential climatic drivers, and Section 5.6 concludes the chapter.

5.2 Study Areas

This chapter focuses on eight remaining ice shelves across the Peninsula: (i) Müller Ice Shelf, (ii) Wilkins Ice Shelf, (iii) Bach Ice Shelf, (iv) George VI Ice Shelf, (v) Stange Ice Shelf, (vi) Scar Inlet Ice Shelf, (vii) Larsen C Ice Shelf, and (viii) Larsen D Ice Shelf (Figure 5.1).

The Müller Ice Shelf (38 km²) is the Antarctic Peninsula's northernmost remaining ice shelf, and is located on the west coast (MacDonell et al., 2021). It undergoes both surface melting and subsurface refreezing, with firn aquifer(s) also being found during field seasons in 2018/2019 and 2019/2020 (MacDonell et al., 2020, 2021). Bach Ice Shelf is one of four ice shelves located on the southwest Antarctic Peninsula, and neighbours both the Wilkins and George VI ice shelves. It has an area of 4380 km², and extensive surface and subsurface water bodies have been identified across the ice-shelf surface over recent years (Willis et al., 2017). George VI Ice Shelf (another southwestern ice shelf) is the second largest ice shelf on the Antarctic Peninsula (Banwell et al., 2021) (22300 km²), and has two ice fronts; a northern ice front and a southern ice front, which terminate in Marguerite Bay and the Ronne Entrance respectively (Holt et al., 2013). Despite the high number of surface lakes on George VI Ice Shelf, it is thought to be currently stable, owing to its compressive flow regime (e.g. Alley et al., 2018; Lai et al., 2020). The northern George VI Ice Shelf experiences lower accumulation rates and higher melt rates than the southern George VI Ice Shelf (e.g.

Reynolds, 1981; Datta et al., 2018), with record melting recorded in the 2019/2020 melt season (Banwell et al., 2021). Owing to these differences, this study splits the George VI Ice Shelf into northern and southern sections, following Banwell et al. (2021), to better reflect the contrasting melt and accumulation conditions between the two halves of this ice shelf (Figure 5.1). For the remainder of this chapter, north George VI and south George VI will be referred to as separate ice shelves, to aid the simplicity of analysis and discussion. Stange Ice Shelf neighbours the George VI Ice Shelf on the southwestern Antarctic Peninsula, and has an area of 7740 km². Despite observed shear fracturing across the southern section of the ice shelf, it is currently relatively stable (Holt et al., 2014; Holt and Glasser, 2021).

The Scar Inlet Ice Shelf, which is also known as the remnant Larsen B Ice Shelf, has an area of 1710 km². It is situated on the eastern Antarctic Peninsula and is considered a structurally weak ice shelf that is prone to major rifting (Wellner et al., 2019). It neighbours the Larsen C Ice Shelf, which is the largest remaining ice shelf on the Antarctic Peninsula, and has a total surface area of 43200 km². Surface melt trends across the Larsen C Ice Shelf are linked to foehn wind conditions across the Antarctic Peninsula's eastern ice shelves, which are associated with circumpolar westerlies (e.g. King et al., 2017; Wiesenekker et al., 2018; Turton et al., 2020). Finally, the Larsen D Ice Shelf, which is immediately adjacent to the Larsen C Ice Shelf, has a total surface area of 24700 km² (Jansen et al., 2010). This ice shelf remains largely unstudied within the literature. All of the areas given above are calculated using the shapefiles generated for this study, although the area given for George VI Ice Shelf reflects the areas of the north and southern George VI ice shelves combined (see section 5.3).

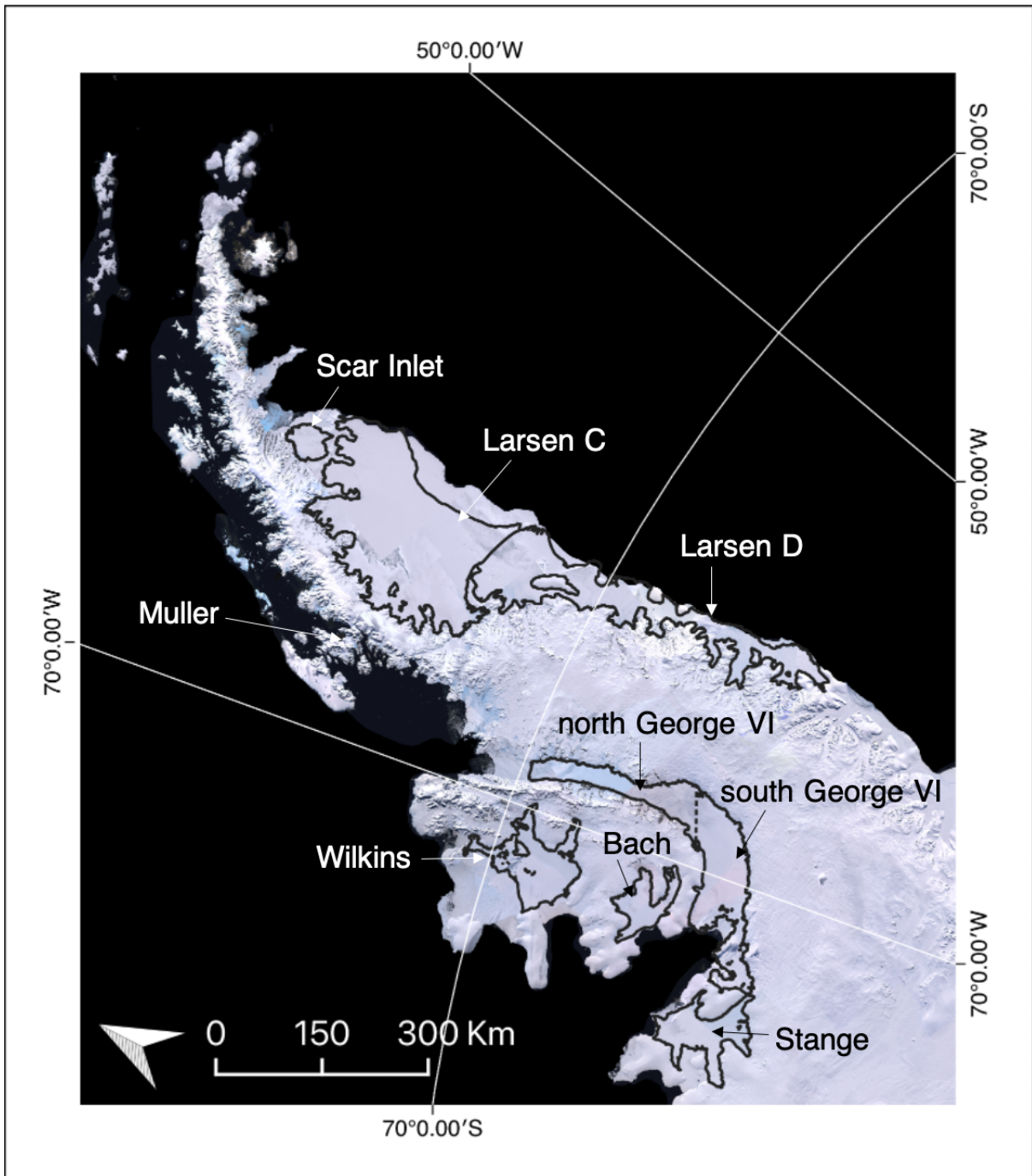


Figure 5.1: Centre-filled LIMA mosaic (Bindschlader et al., 2008) overlain with the nine ice-shelf shapefiles used in this study. Ice-shelf shapefiles are high resolution vector polygons of the Antarctic Coastline downloaded from the SCAR Antarctic Digital Database (Gerrish et al., 2021), with some boundary modifications made according to the MEASUREs database. The boundaries for the Scar Inlet Ice Shelf were further manually modified to reflect changes in the ice front position.

5.3 Data and Methods

Time-series data of slush and ponded meltwater extent across eight Antarctic Peninsula ice shelves (or nine if George VI Ice Shelf is split in two) were produced using the supervised classifier presented in Chapter 4. This supervised classifier produces 15-day ponded water and slush products between 1 November and 31 March (or 1 April in leap years) using the full Landsat 8 record (i.e. 2013 to 2021). For details on the methods used to pre-process Landsat 8 scenes, in addition to the methods used to train and validate the supervised classifier, see Chapter 4.

Shapefiles of the ice shelves from the 'High resolution vector polygons of the Antarctic Coastline', from the SCAR Antarctic Digital Database (Gerrish et al., 2021) were used. These shapefiles were considered to be the most accurate available, as the dataset is updated twice a year. However, the raw products from this dataset occasionally failed to separate neighbouring ice shelves (e.g. for Larsen C Ice Shelf and Larsen D Ice Shelf, and George VI Ice Shelf and Stange Ice Shelf). To rectify this, polygons from the MEaSURES Antarctic Boundaries dataset (Mouginot et al., 2017) were used to split the SCAR polygons along each ice-shelf boundary. In addition, the George VI Ice Shelf was further split into northern and southern sections, following Banwell et al. (2021). The margin of Scar Inlet Ice Shelf was also manually modified to reflect the new ice-shelf front geometry following a series of recent calving events.

15-day products were derived using the methods described in Chapter 4 and exported from GEE at native resolution. These products were post-processed in MATLAB, and for all 15-day products that had greater than or equal to 20% coverage over the ice-shelf area, time-series of ponded water and slush area for each ice shelf were subsequently calculated. In addition to the time-series data for each ice shelf, scaled areas of ponded water and slush were also calculated. For each ice shelf, this was done by calculating the ratio of total ice-shelf area to total area covered, and multiplying this by the raw water area for each 15-day product.

5.3.1 Cloud Post-Processing

The workflow presented in Chapter 4 used Landsat 8 Quality Assessment bands in the pre-processing steps to automatically mask clouds and cloud shadows from each Landsat 8 scene prior to running the supervised classifier, and buffered this mask by 4 km for optimum cloud removal. However, this method, like all current cloud masking methods, was imperfect, and not all clouds were fully masked from each scene. Therefore, errors of commission due to cloud and cloud shadow were found within the dataset, and extra steps were needed in post-processing to remove these errors.

The additional post-processing step applied here relied on the transient nature of clouds and cloud shadows to automatically remove pixels that were likely to be cloud or cloud shadow from each of the 15-day products. For the full study period (2013 to 2021) over each individual ice shelf, a heatmap was generated, which identified the number of times a pixel was classified as either ponded water or slush (Figure 4.9, Chapter 4). Where a pixel in the heatmap had a persistency of one (i.e. it was only classified as 'meltwater' in a single 15-day product throughout the entire eight year study period), it was assumed that the pixel was covered by cloud or cloud shadow, and it was therefore masked out of each 15-day product. The remaining areas of ponded water and slush were then calculated, and presented as time-series data for each ice shelf. The limitation of this approach was that it resulted in the removal of some true positives, where ponded water and slush had been correctly classified, potentially removing the maximum extent of correctly classified meltwater for each ice shelf (see Chapter 4). It should also be noted that whilst this approach was found to effectively remove the majority of cloud and cloud shadow, some erroneously classified pixels still remained within the data products, and were carried through the remainder of this study.

5.4 Results

5.4.1. Temporal variability in total surface meltwater extent

The extent of surface meltwater shows marked inter- and intra-annual variability across the eight ice shelves (or nine if George VI Ice Shelf is split into two) on the Antarctic Peninsula throughout the austral summers of 2013/2014 to 2020/2021 (Figure 5.2).

On four of the nine ice shelves investigated (Müller Ice Shelf, Wilkins Ice Shelf, north George VI Ice Shelf, and Larsen C Ice Shelf), the total surface meltwater extent (i.e. both ponded water and slush combined) is greatest (on any given date) in 2019/2020 (Figure 5.2). On the Bach and south George VI ice shelves, the total area of surface meltwater is greatest in 2017/2018, whilst the total area of surface meltwater is greatest over the Stange, Scar Inlet, and Larsen D ice shelves in 2016/2017 (Figure 5.2). Generally, for the ice shelves on the west side of the Antarctic Peninsula, total surface meltwater extents are relatively low from 2013/2014 through to 2015/2016, before increasing from 2016/2017 onwards. For the ice shelves on the eastern Antarctic Peninsula (Scar Inlet Ice Shelf, Larsen C Ice Shelf, and Larsen D Ice Shelf), no clear trends through time are observed.

The greatest total surface meltwater extent is observed on the north George VI Ice Shelf between 15 January 2020 and 29 January 2020 (Figure 5.2), when it covers 11.6% of the total ice-shelf surface area. Across the other ice shelves, the maximum observed total surface meltwater area covers between 0.4% (Larsen C Ice Shelf) and 4.5% (Scar Inlet Ice Shelf) of the total ice-shelf area.

5.4.2 Temporal variability in ponded water and slush extent

The ponded water extent is greatest in 2019/2020 on four of the nine ice shelves: Müller Ice Shelf, Bach Ice Shelf, north George VI Ice Shelf, and Larsen C Ice Shelf (Figure 5.3, Appendix C Tables C.1, C.3, C.4, and C.8). On Wilkins Ice Shelf and south George VI Ice Shelf, the area of ponded water is greatest in 2017/2018 (Figure 5.3, Appendix C Tables C.2 and C.5). Across all ice shelves investigated, 88.6% of the maximum seasonal ponded water extents are reached between January and March of each melt season. The slush extent is greatest in 2019/2020 across the Wilkins, north George VI, and Larsen C ice shelves, and greatest in 2017/2018 across the Müller, Bach, and south George VI ice shelves (Figure 5.3, Appendix C Tables C.1, C.3, and C.5). On five of the nine ice shelves studied, the maximum ponded water extent exceeds the maximum slush extent. However, on the Bach, Stange, Scar Inlet, and Larsen D ice shelves the reverse is observed (Figure 5.3, Appendix C Tables C.3, C.7, C.9). Across the majority of the ice shelves studied, the area of ponded water tends to rise and fall synchronously with the area of slush both within and between melt seasons. However, this phenomenon is less apparent on the Müller, Larsen D and Scar Inlet ice shelves (Figure 5.3). On the Larsen D Ice Shelf, the area of slush appears to reach its seasonal maximum earlier in the melt season, and then falls as the area of ponded water increases (Figure 5.3). Infrequent examples of this can also be seen elsewhere on the Antarctic Peninsula; for example on Müller Ice Shelf (2019/2020), Stange Ice Shelf (2020/2021), and the Scar Inlet Ice Shelf (2018/2019) (Figure 5.3). However, it should be noted that spatial and temporal data coverage across the Scar Inlet Ice Shelf is sparse, and that patterns and variations are therefore interpreted with less confidence. Across all ice shelves, for 45.7% of the time, the area of slush reaches its maximum seasonal extent before the area of ponded water reaches its maximum seasonal extent. For 40% of the time, the areas of slush and ponded water reach their maximum seasonal extents at the same time.

5.4.3 Spatial patterns in the total surface meltwater extent, total ponded meltwater extent, and total slush extent

Figure 5.4 shows the maximum meltwater extent for all melt seasons (2013 to 2021) on each ice shelf. Across the Müller, Wilkins, Bach, Scar Inlet, Larsen C and Larsen D ice shelves, meltwater is concentrated predominantly towards the grounding line. Contrastingly on the north George VI Ice Shelf, total surface meltwater (i.e. both ponded water and slush) extends across the majority of the ice shelf, particularly in the central region. On the south George VI and Stange ice shelves, meltwater is apparent across the central and distal portions of the ice shelves, although these results are predominantly errors of commission caused by cloud and cloud shadows. Across all ice shelves, between 43.5% (Larsen C Ice Shelf) and 65.7% (Müller Ice Shelf) of the 'wet' pixels are classified as both water and slush at least once in the full study period (Figure 5.4). Expansive areas of pixels which are 'slush only' are prominent on both the Bach and Scar Inlet ice shelves. Areas of 'ponded water only' are less expansive, but can be seen, for example, on north George VI Ice Shelf.

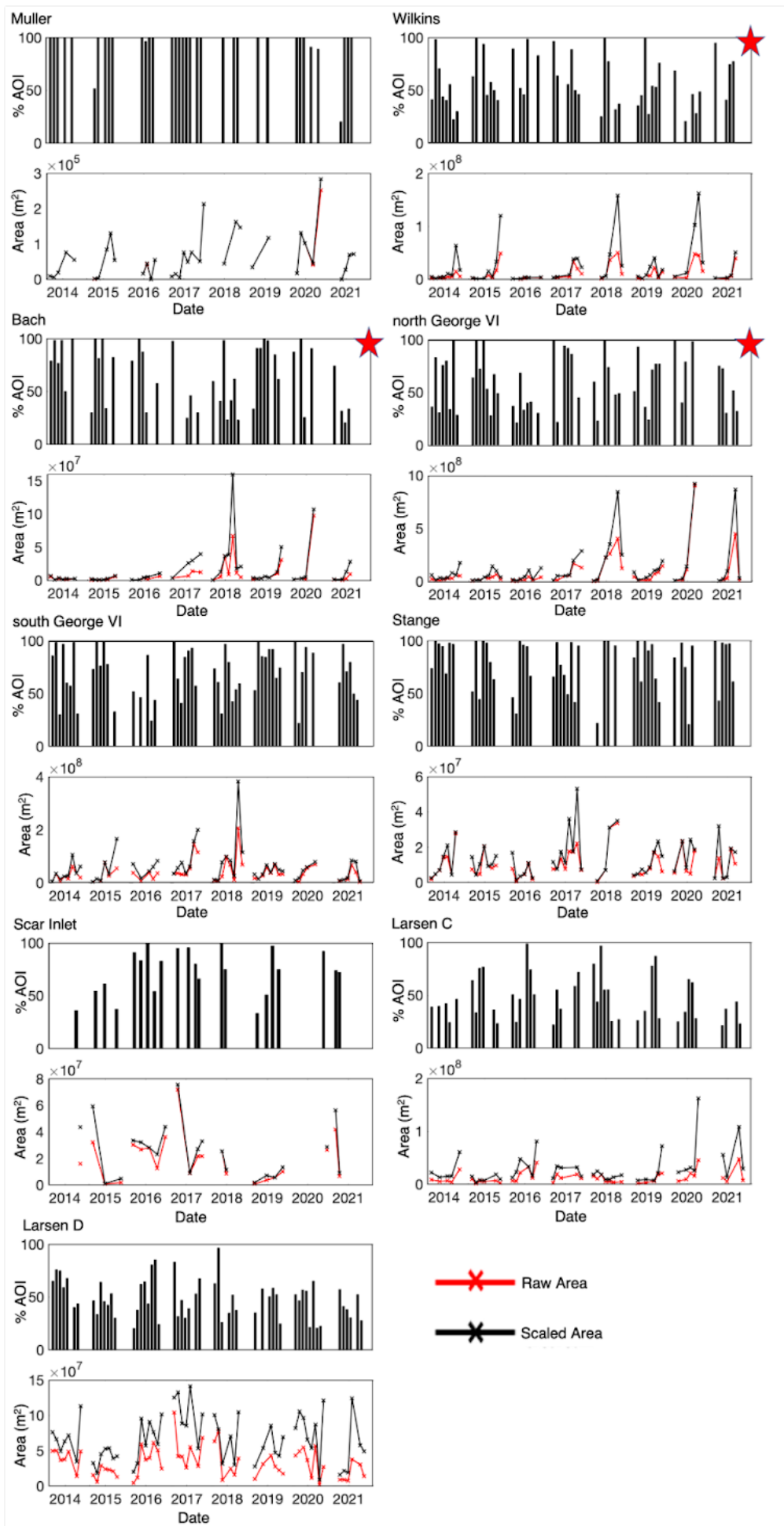


Figure 5.2: Plots showing total time-series data for the nine Antarctic Peninsula ice shelves investigated. The upper plots for each ice shelf show the percentage area-of-interest (% AOI) coverage for each pre-processed 15-day image product over the ice-shelf area, and the lower plots show the raw total surface meltwater area (red line), and the total surface meltwater area scaled to the full ice-shelf area (black line). Only 15-day products with greater than or equal to 20% coverage over the full ice-shelf area are plotted. Data for each 15-day product are plotted on the end date of each 15-day period. Years on the X-axis represent 1 January of each respective year. Red stars mark the three ice shelves investigated in greater detail within this chapter.

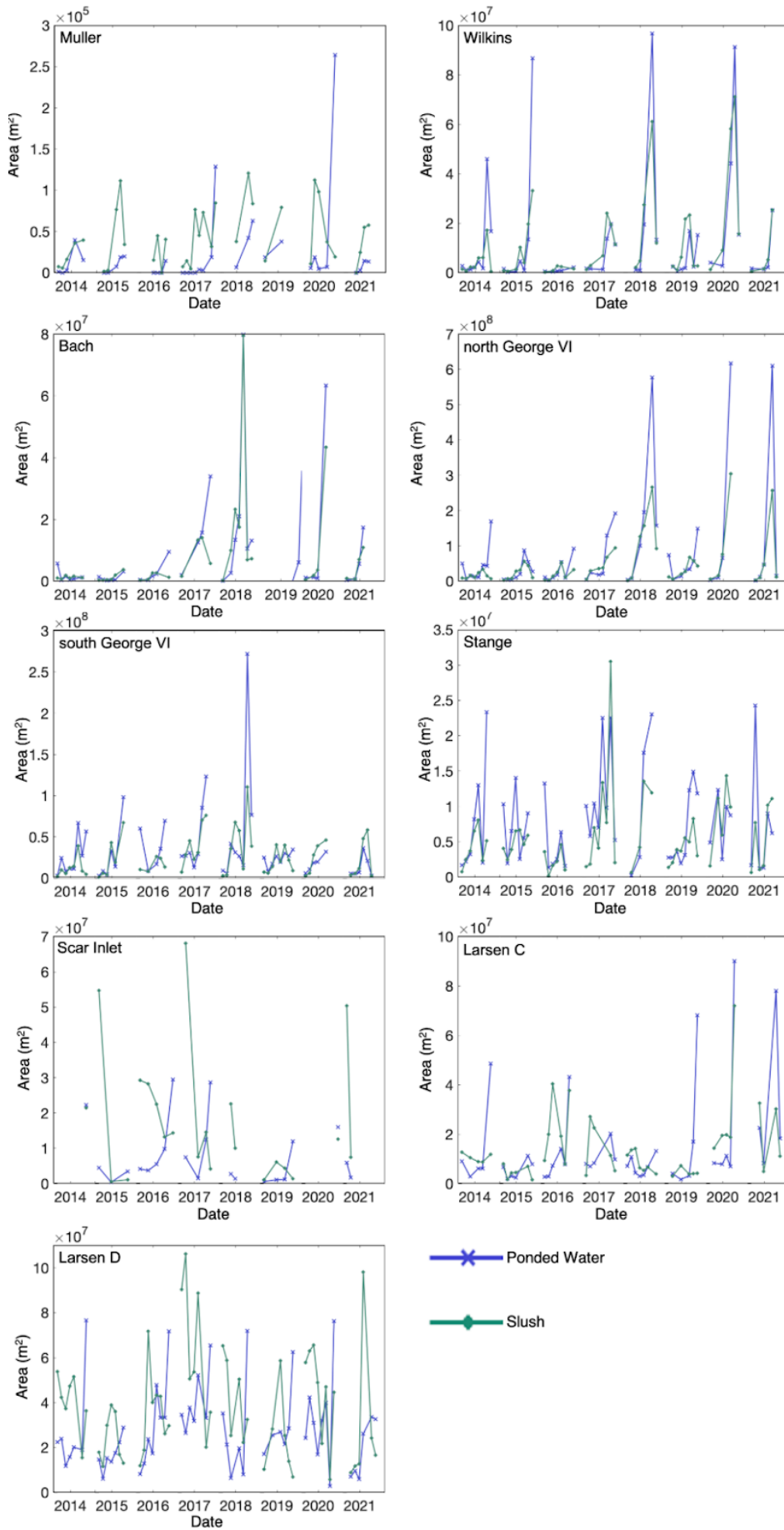
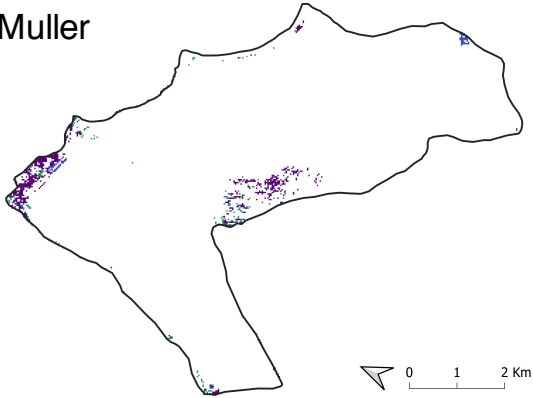
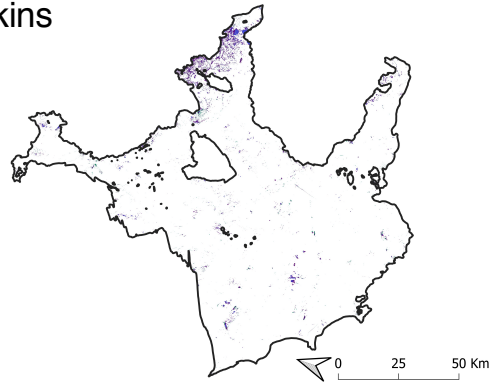


Figure 5.3: Plots showing scaled ponded water (blue) and slush (green) time-series data for each of the nine Antarctic Peninsula ice shelves studied. Only 15-day products with greater than or equal to 20% coverage over the full ice-shelf area are plotted. Data for each 15-day product are plotted on the end date of each 15-day period. Years on the x-axis represent 1 January of each respective year.

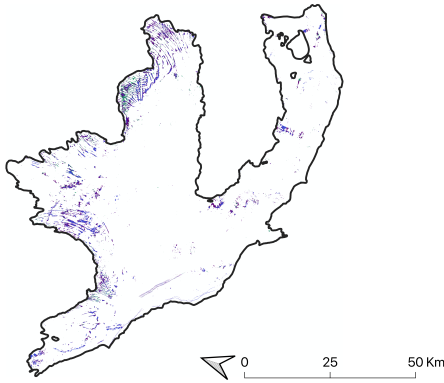
Muller



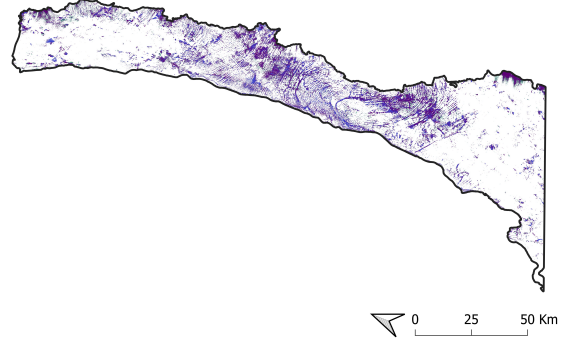
Wilkins



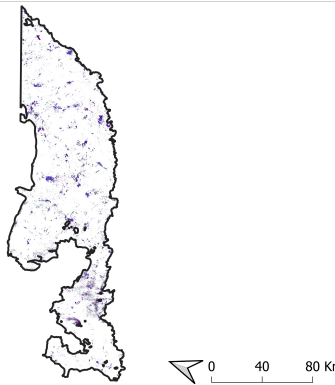
Bach



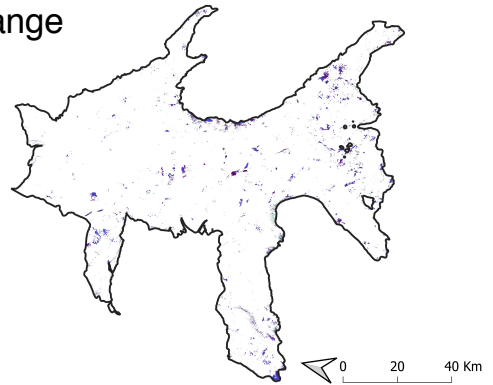
north GVI



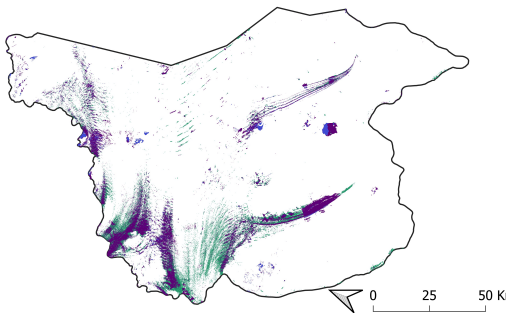
South GVI



Stange



Scar Inlet



Larsen C



Larsen D

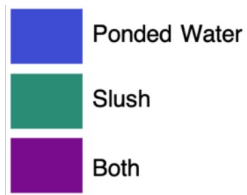
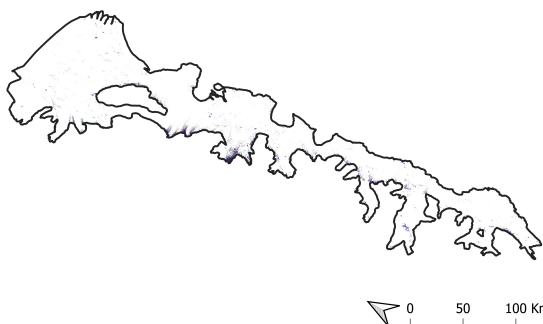


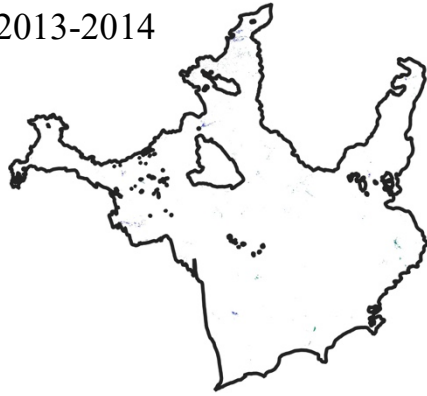
Figure 5.4: Maps showing maximum surface meltwater extents for each ice shelf produced by mosaicking all 15-day products between 2013 and 2021. Areas classified as both ponded water and slush (purple) are mapped preferentially over areas classified as just ponded water (blue), and just slush (green). White areas are areas where no surface meltwater was identified or where there was no image coverage.

5.4.4 Wilkins Ice Shelf

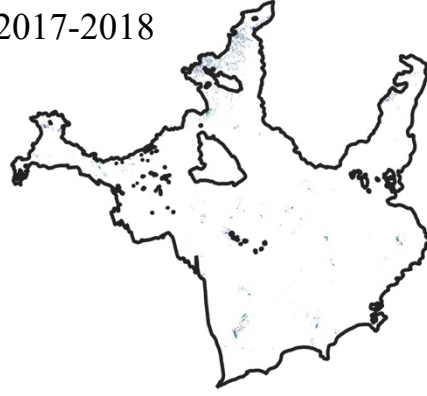
On the Wilkins Ice Shelf, high surface melt years (i.e. years with the highest maximum meltwater extents) are observed in both 2017/2018 and 2019/2020 (Fig 5.2). Ponded water reaches a maximum extent of $9.7 \times 10^7 \text{ m}^2$ between 30 Jan 2018 and 13 Feb 2018, and slush reaches a maximum extent of $7.1 \times 10^7 \text{ m}^2$ between 30 Jan 2020 and 13 Feb 2020 (Figure 5.3, Appendix C Table C.2). Contrastingly, the lowest summer maximum area of ponded water ($2.2 \times 10^6 \text{ m}^2$) and slush ($2.7 \times 10^6 \text{ m}^2$) is recorded from 14 Feb 2016 to 28 Feb 2016 and 16 Dec 2015 to 30 Dec 2015 respectively (Figure 5.3, Appendix C Table C.2). Through all eight melt seasons, the areas of ponded water and slush reach their maximum extent in January or February, with the exception of the 2015/2016 melt season, when the extent of slush is greatest in December. On average, slush accounts for 54.9% of the total surface meltwater extent on the Wilkins Ice Shelf across all 15-day periods, and ponded water accounts for 45.1% of the total surface meltwater extent across all 15-day periods.

Figure 5.5 shows the maximum total surface meltwater extent across the Wilkins Ice Shelf for each austral summer from 2013/2014 to 2020/2021. Every year, surface meltwater is clustered predominantly towards the eastern grounding line. This area is most spatially extensive in 2019/2020, and extends $\sim 27 \text{ km}$ from the grounding line. Figure 5.6 shows the 15-day products for the 2019/2020 melt season, when the maximum total surface meltwater extent is observed over the

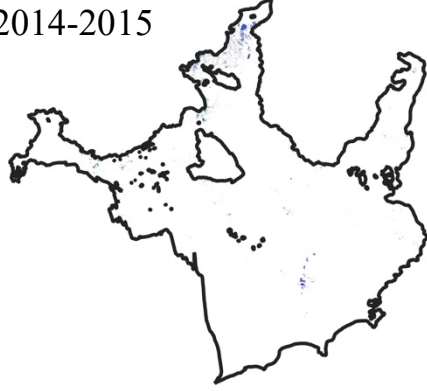
2013-2014



2017-2018



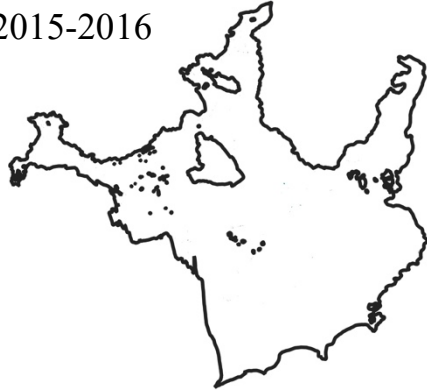
2014-2015



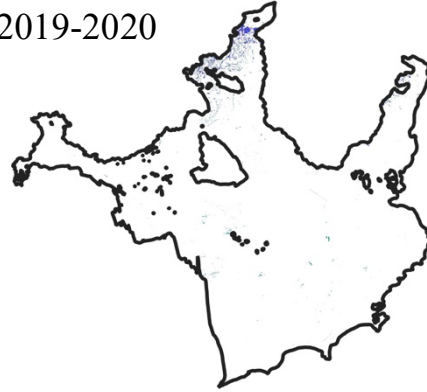
2018-2019



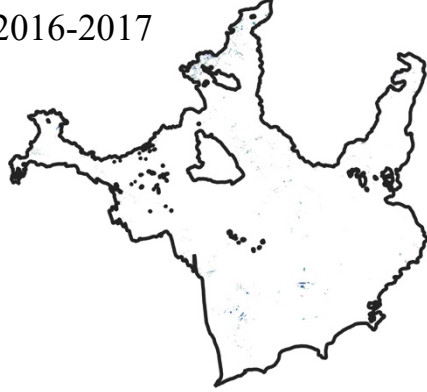
2015-2016



2019-2020



2016-2017



2020-2021

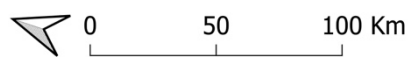
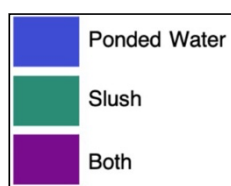
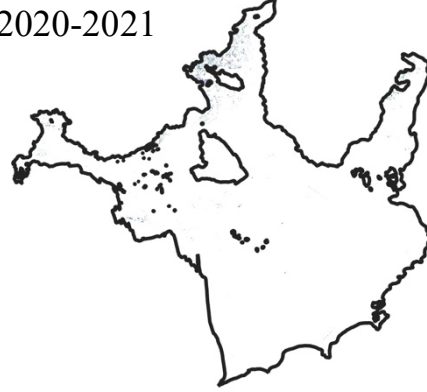
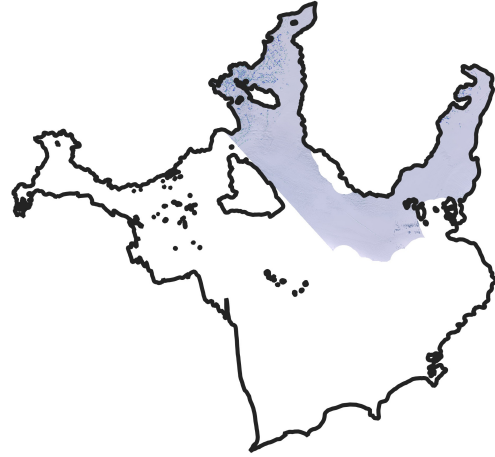
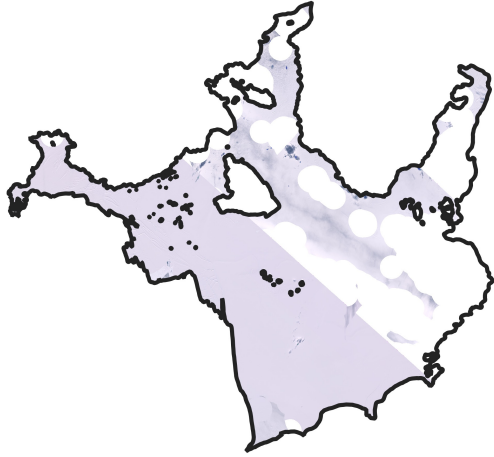
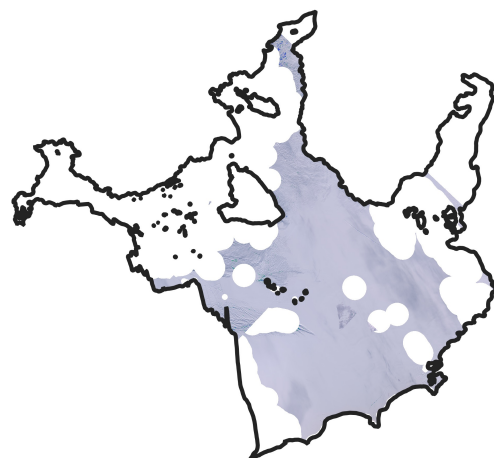
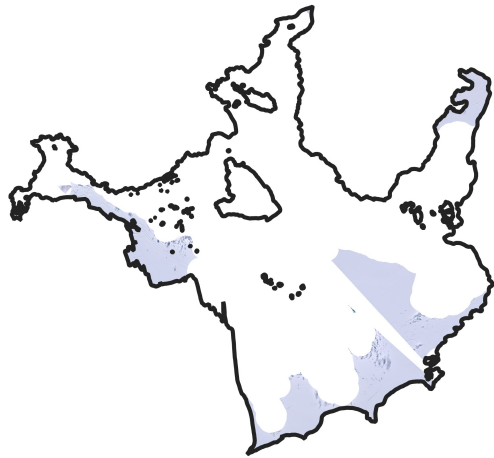


Figure 5.5: Maximum surface meltwater extent across the Wilkins Ice Shelf from 2013/2014 to 2020/2021, calculated by mosaicking all 15-day surface meltwater products for each melt season. Areas classified as both ponded water and slush (purple) are mapped preferentially over areas classified as just ponded water (blue), and just slush (green). White areas are areas where no surface meltwater was identified or where there was no image coverage.

01 Nov 2019 - 15 Nov 2019 30 Jan 2020 - 13 Feb 2020



16 Dec 2019 - 30 Dec 2019 14 Feb 2020 - 28 Feb 2020



15 Jan 2020 - 29 Jan 2020

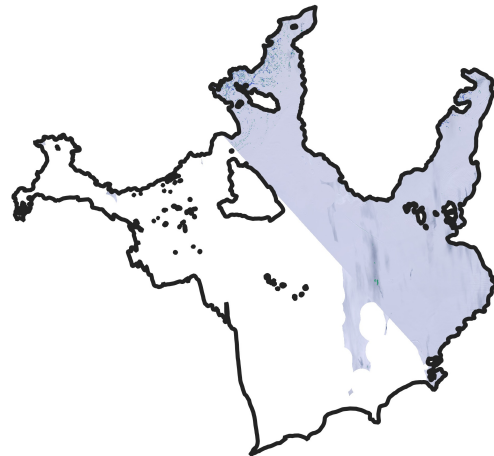


Figure 5.6: 15-day surface meltwater products for the 2019/2020 melt season across the Wilkins Ice Shelf. White areas not covered by a true-colour composite image are areas that were not covered by a Landsat scene during the period investigated.

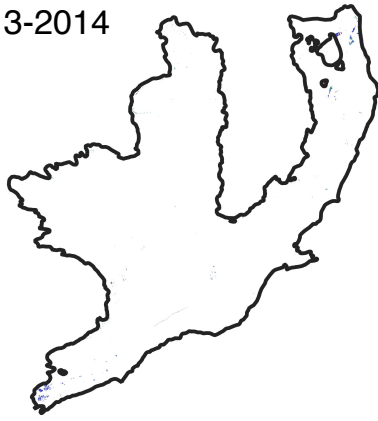
Wilkins Ice Shelf. Overall, these products have poor image coverage over the full ice shelf, although the products for 15 Jan 2020 to 29 Jan 2020 and 30 Jan 2020 to 13 Feb 2020 show that surface meltwater is clustered in the east, towards the grounding line (Figure 5.6). Earlier in the season (15 Jan 2020 - 29 Jan 2020) the surface meltwater extent is dominated by slush, rather than ponded water; slush accounts for 56.9% of the total surface meltwater extent. However, from 30 Jan 2020 to 13 Feb 2020, the surface meltwater extent is ponded water dominated rather than slush dominated, as ponded water accounts for 56.2% of the total surface meltwater extent.

5.4.5 Bach Ice Shelf

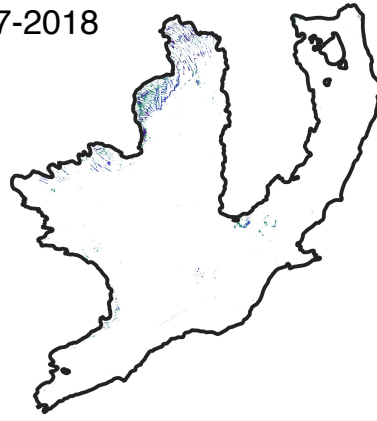
The greatest total surface meltwater extent on the Bach Ice Shelf is recorded between 15 Jan 2018 and 29 Jan 2018 (Figure 5.2), when the maximum extent of both ponded water ($8.0 \times 10^7 \text{ m}^2$) and slush ($8.0 \times 10^7 \text{ m}^2$) were greatest (Figure 5.3; Appendix C Table C.3). The 2019/2020 melt season is the second largest melt season after 2017/2018, and has a high maximum total surface meltwater extent of $1.1 \times 10^8 \text{ m}^2$, between 15 Jan 2020 and 29 Jan 2020. Between these dates, the area of ponded water dominates, accounting for 59.4% of the total surface meltwater extent (Appendix C Table C.3). Figure 5.7 shows the spatial distribution of ponded water and slush as maximum-extent products for each melt season (2013/2014 to 2020/2021). These figures corroborate the time-series data, showing particularly extensive surface meltwater in both the 2017/2018 and 2019/2020 melt seasons. However, surface meltwater is more extensive in 2020/2021 than both 2017/2018 and 2019/2020 because the data presented in Figure 5.3 are scaled to account for partial area-of-interest coverage and the coverage in 2020/2021 is greater than for the other two seasons.

Figure 5.8 shows the 15-day products for the 2017/2018 melt season, when the maximum total surface meltwater extent was observed. Whilst there is variable coverage over the ice shelf in different image periods, evidence for extensive ponding towards the eastern grounding line is first observed from 16 Dec 2017 to 30 Dec 2017, and is most extensive from 15 Jan 2018 to 29 Jan 2018 (Figure 5.8). Both ponded water and slush are observed in this area, with slush appearing to be particularly extensive in the northeast.

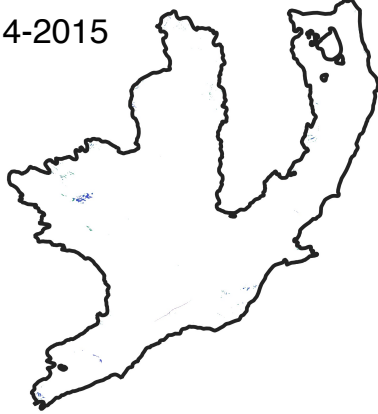
2013-2014



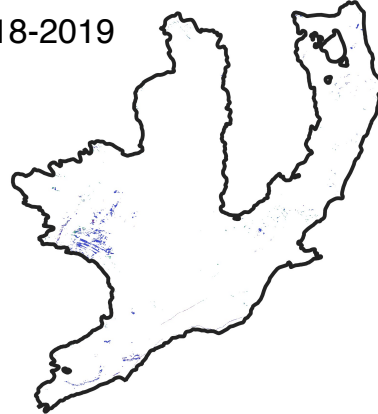
2017-2018



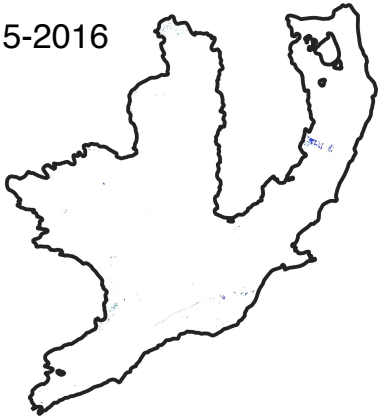
2014-2015



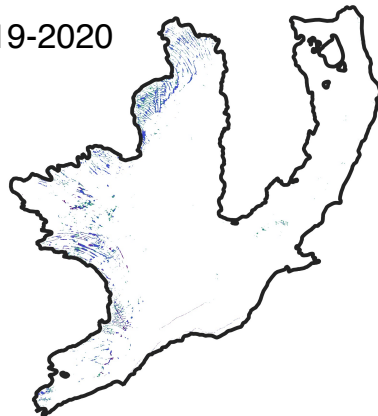
2018-2019



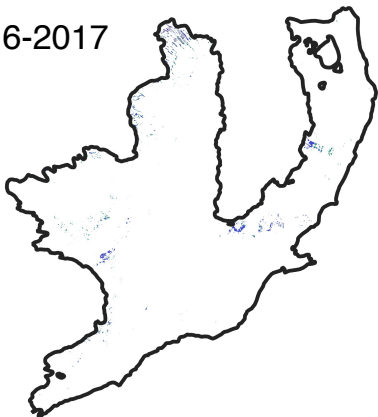
2015-2016



2019-2020



2016-2017



2020-2021

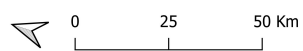
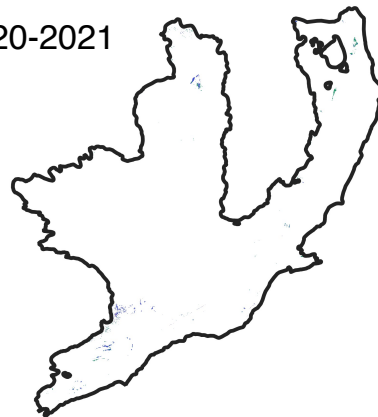
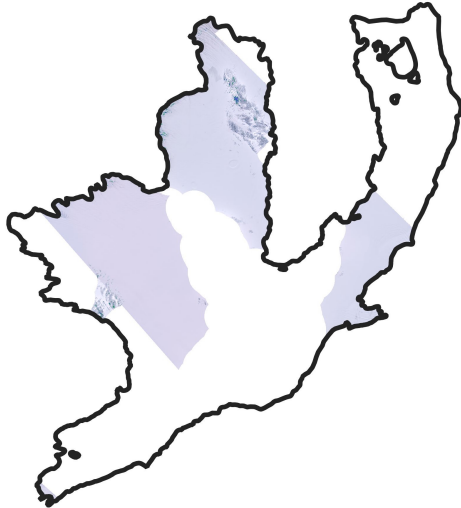
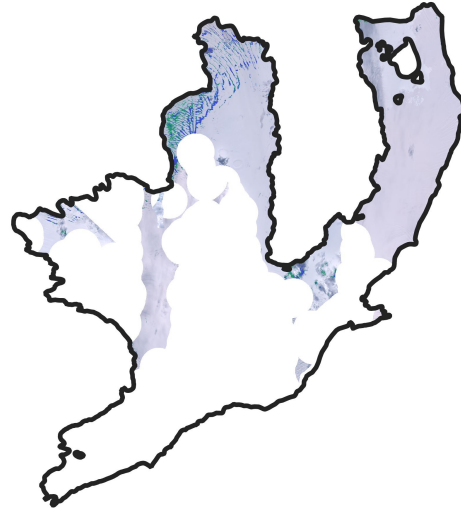


Figure 5.7: Maximum surface meltwater extent across the Bach Ice Shelf from 2013/2014 to 2020/2021, calculated by mosaicking all 15-day surface meltwater products for each melt season. Areas classified as both ponded water and slush (purple) are mapped preferentially over areas classified as just ponded water (blue), and just slush (green). White areas are areas where no surface meltwater was identified or where there was no image coverage.

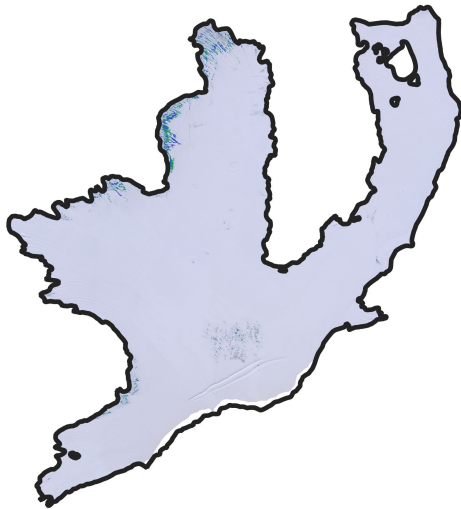
01 Dec 2017 - 15 Dec 2017



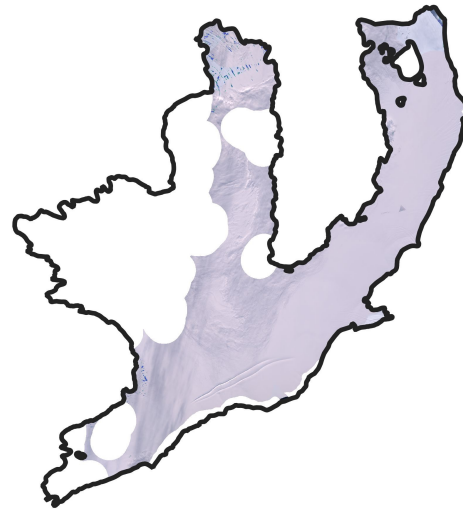
15 Jan 2018 - 29 Jan 2018



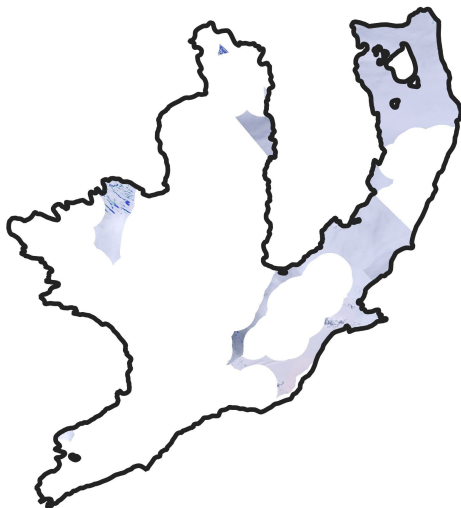
16 Dec 2017 - 30 Dec 2017



30 Jan 2018 - 13 Feb 2018



31 Dec 2017 - 14 Jan 2018



14 Feb 2018 - 28 Feb 2018

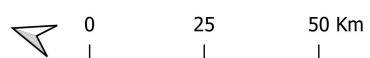
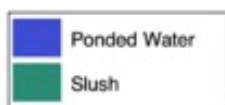
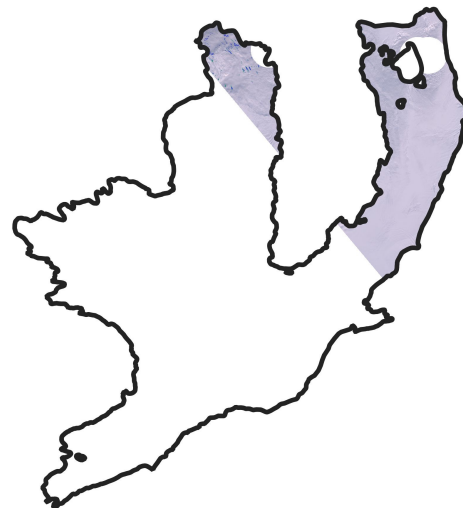


Figure 5.8: 15-day surface meltwater products for the 2017/2018 melt season across the Bach Ice Shelf. White areas not covered by a true-colour composite image are areas that were not covered by a Landsat scene during the time period investigated.

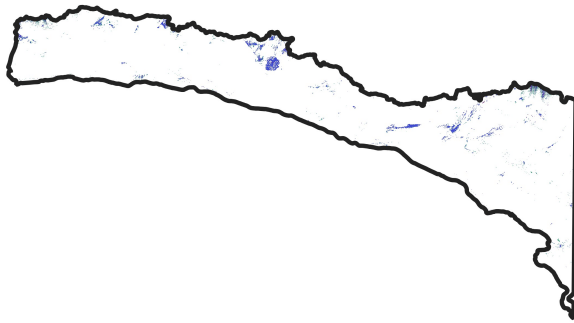
5.4.6 North George VI Ice Shelf

Of the eight melt seasons investigated, the maximum total surface meltwater is observed on the north George VI Ice Shelf in the 2019/2020 melt season, reaching ($9.2 \times 10^8 \text{ m}^2$) between 15 Jan 2020 and 29 Jan 2020 (Figure 5.2; Appendix C Table C.4). Between these dates, ponded water and slush account for 67.0% and 33.0% of the total surface meltwater signal respectively. The extent of ponded water is greatest between these dates ($6.2 \times 10^8 \text{ m}^2$), but it is also high between 30 Jan 2018 and 13 Feb 2018 ($5.8 \times 10^8 \text{ m}^2$) and from 15 Jan 2021 to 29 Jan 2021 ($6.1 \times 10^8 \text{ m}^2$). Similarly, the area of slush is greatest between 15 Jan 2020 and 29 Jan 2020 ($3.0 \times 10^8 \text{ m}^2$), but is also high on 30 Jan 2018 to 13 Feb 2018 ($2.7 \times 10^8 \text{ m}^2$) and 15 Jan 2021 to 29 Jan 2021 ($2.6 \times 10^8 \text{ m}^2$) (Figure 5.3, Appendix C Table C.4). Averaged across these three date periods, ponded water accounts for 68.6% of the total meltwater area, and slush accounts for 31.4% of the total meltwater area. Typically the extent of ponded water and slush rises and falls synchronously, except at the end of the 2013/2014 melt season (13 Feb 2014 - 28 Feb 2014) and the end of the 2018/2019 melt season (13 Feb 2019 - 28 Feb 2019), when the area of slush falls and the area of ponded water increases (Figure 5.3).

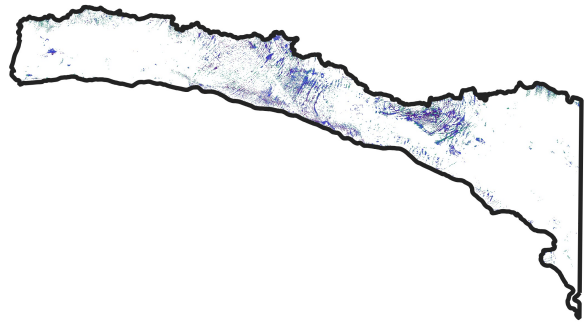
Figure 5.9 shows maximum surface meltwater extent products for each melt season investigated. Overall, relatively little surface meltwater is observed between 2013/2014 and 2016/2017. After this, particularly high surface meltwater extents are observed in the 2017/2018, 2019/2020, and 2020/2021 melt seasons. This surface meltwater is concentrated predominantly in the central areas of the ice shelf, in a series of heavily connected ponded surface meltwater features, which are often surrounded by regions of slush (Figure 5.9).

Figure 5.10 shows these connected meltwater features throughout 2019/2020; the melt season with the greatest total surface meltwater extent. The 15-day products show minimal surface meltwater extent until 15 Jan 2020 to 29 Jan 2020, when a total surface meltwater area of $(9.2 \times 10^8 \text{ m}^2)$ is observed, with regions of extensive surface meltwater ponding and slush forming across the ice shelf.

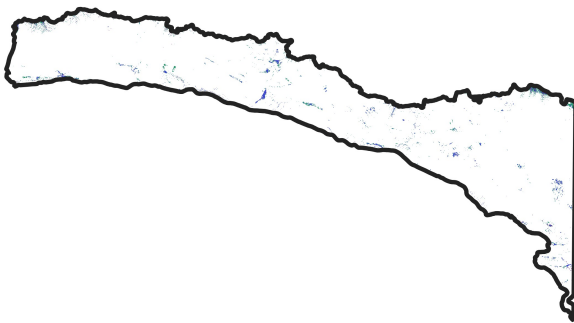
2013-2014



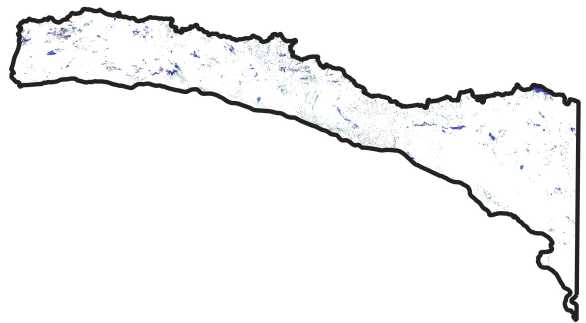
2017-2018



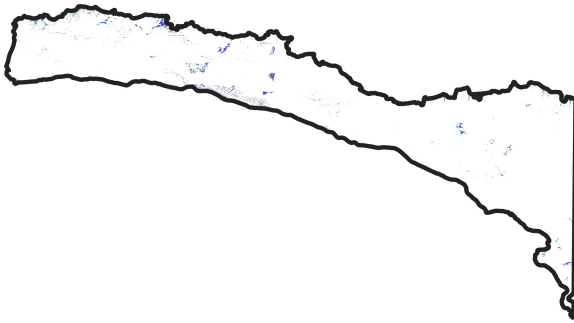
2014-2015



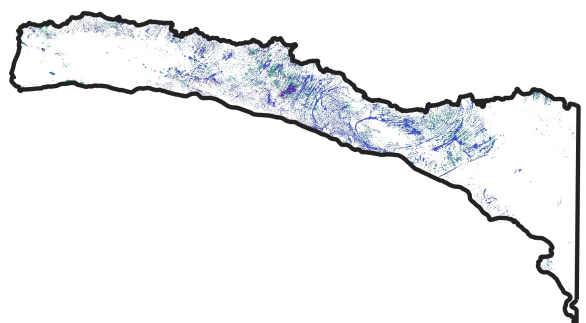
2018-2019



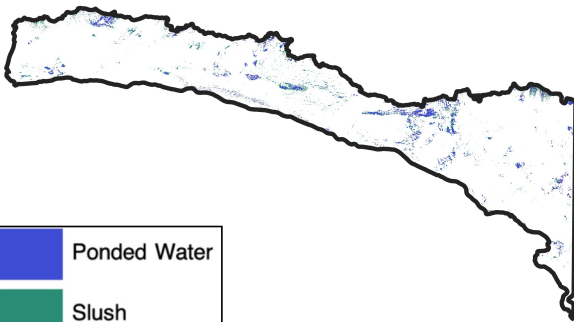
2015-2016



2019-2020



2016-2017



2020-2021

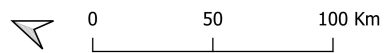
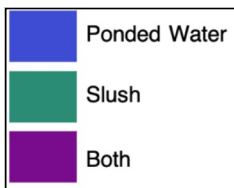
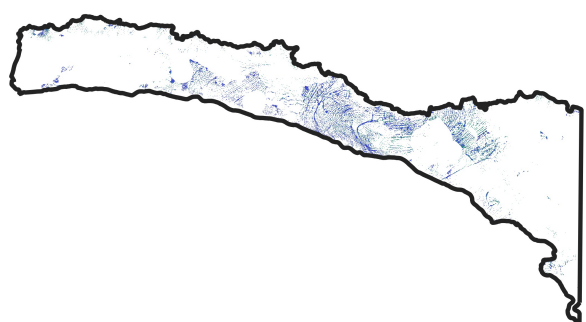
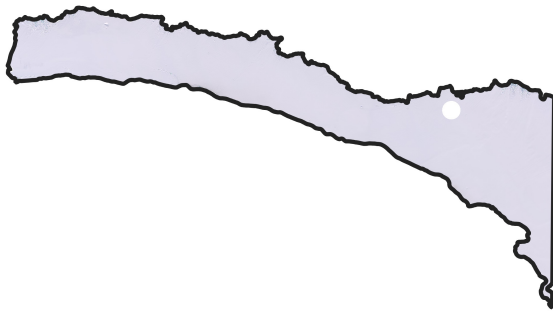
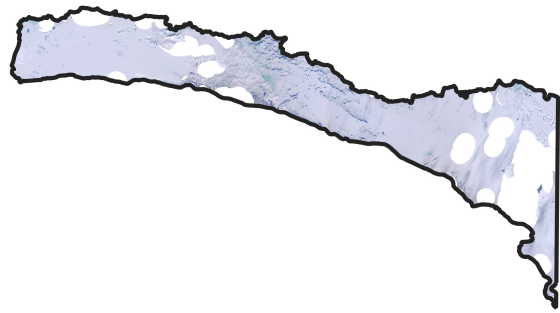


Figure 5.9: Maximum surface meltwater extent across the north George VI Ice Shelf from 2013/2014 to 2020/2021, calculated by mosaicking all 15-day surface meltwater products for each melt season. Areas classified as both ponded water and slush (purple) are mapped preferentially over areas classified as just ponded water (blue), and just slush (green). White areas are areas where no surface meltwater was identified or where there was no image coverage.

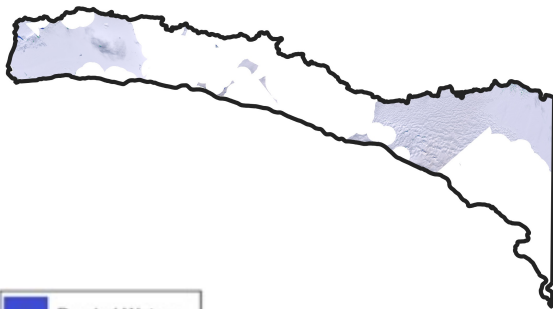
01 Nov 2019 - 15 Nov 2019



16 Dec 2019 - 30 Dec 2019



01 Dec 2019 - 15 Dec 2019



15 Jan 2020 - 29 Jan 2020

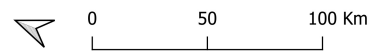
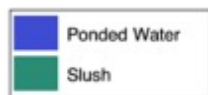
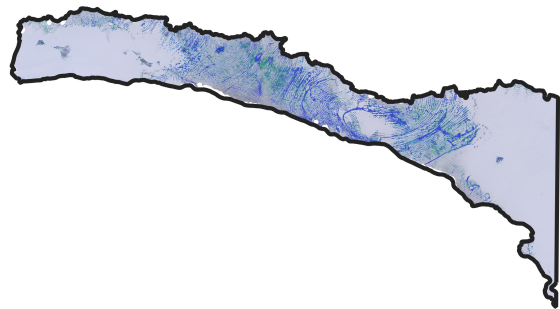


Figure 5.10: 15-day surface meltwater products for the 2019/2020 melt season across the north George VI Ice Shelf. White areas not covered by a true-colour composite image are areas that were not covered by a Landsat scene during the period investigated.

5.5 Discussion

5.5.1 Inter-annual variability in total surface meltwater extent across the Antarctic Peninsula

Overall, the results presented above show that across eight Antarctic Peninsula ice shelves, the total surface meltwater extent was generally greatest in 2016/2017 on the Stange, Scar Inlet, and Larsen D ice shelves, whereas it is greatest in 2017/2018 on the Bach and south George VI ice shelves, and greatest in 2019/2020 on the Müller, Wilkins, north George VI, and Larsen C ice shelves. Therefore, from the data presented, there are no marked inter-annual trends in total surface meltwater extent across the Antarctic Peninsula as a whole. However, the peaks in total surface meltwater extent in 2017/2018 and 2019/2020 are predominantly across ice shelves on the west Antarctic Peninsula rather than across those on the east, whilst the high melt years in 2016/2017 are predominantly across ice shelves in the east Antarctic Peninsula, rather than across those in the west. It seems likely, therefore, that these high melt years are driven by regional climate patterns (discussed further in Section 5.5.4). Beyond this, there is high inter-annual spatial heterogeneity in total surface meltwater extent between ice shelves, and in some cases even neighbouring ice shelves show contrasting patterns in meltwater extent (e.g. Larsen C and Larsen D ice shelves in 2016/2017). This lack of synchronicity between neighbouring ice shelves and across larger regions has also been observed in studies of ponded water across East Antarctica (Stokes et al., 2019; Arthur et al., 2021). In these situations, it is likely that variability in the total surface meltwater extent is influenced by more local-scale climate factors and ice- surface properties rather than larger-scale synoptic drivers (Stokes et al., 2019). The complex interplay between regional-scale winds, and albedo, firn properties, and topography may result in highly variable melt conditions through

space and time (Leeson et al., 2017; Lenaerts et al., 2017; Melchior Van Wessem et al., 2018; Stokes et al., 2019).

5.5.2 Variability in ponded water and slush extent across the Antarctic Peninsula

For 88.6% of the full study period (2013 to 2021) and across all ice shelves, the area of ponded water reaches its maximum seasonal extent between 1 January and 31 March. The seasonal extent of slush also tends to reach its maximum at this time (40% of the time) or prior to this (45.7% of the time). This is most notable on the Larsen D Ice Shelf, as the slush extent reaches its maximum prior to ponded water in all of the nine melt seasons investigated (Figure 5.3). This variability, with the area of slush often reaching its maximum extent earlier in the melt season than that of ponded water, likely occurs as surface meltwater initially infiltrates the snow and firn pack where possible, filling pore spaces and therefore forming slush. Once the firn layer is saturated, and therefore impermeable to further surface meltwater infiltration, meltwater begins to pond on the ice-shelf surface (e.g. Scambos et al., 2000; Kuipers Munneke et al., 2014; Bevan et al., 2017), allowing the area of ponded water to rise. This is further corroborated as across all ice shelves, between 43.5% (Larsen C Ice Shelf) and 65.7% (Müller Ice Shelf) of the pixels within the maps showing maximum meltwater extent are classified as both ponded water and slush at least once in the full study period. Whereas the remaining pixels are only ever classified as either slush or ponded water over the full study period (Figure 5.4).

Across five of the nine ice shelves on the Antarctic Peninsula (Müller Ice Shelf, Wilkins Ice Shelf, south George VI Ice Shelf, north George VI Ice Shelf, and Larsen C Ice Shelf), the maximum ponded water extent is greater than the maximum slush extent that occurred during the full study period, whereas across the remaining four ice shelves, the reverse is true (Figure 5.3, Tables C.1-C.9). This variability is explained by the mechanisms described above; if firn layers are sufficiently extensive and have

enough firn pore space, meltwater will predominantly saturate these regions, forming slush (e.g. Scambos et al., 2000; Kuipers Munneke et al., 2014; Bevan et al., 2017). However, if the rate of meltwater production exceeds the capacity of the firn layer, or the firn layer is not extensive to begin with, surface meltwater ponds more readily, and the ponded meltwater extent will likely be greater. This is most likely towards ice-shelf grounding lines, as snow and firn is eroded by prevailing katabatic and/or foehn winds (Lenaerts et al., 2017).

5.5.3 Spatial patterns in ponded water and slush extent across the Antarctic Peninsula

Across all ice shelves that are investigated within this study, surface meltwater is found in proximity to the grounding lines (Figure 5.4). Prior research has shown that meltwater is typically greatest at the grounding line as this is where foehn and katabatic winds are often prevalent, and acts to strip away snow and firn cover, either reducing the capacity of the firn layer to store water within subsurface layers, or stripping the ice-shelf surface down to expose blue ice surfaces (e.g. Cape et al., 2015; Lenaerts et al., 2017). Blue ice surfaces have a lower surface albedo than snow-covered surfaces, and therefore these areas often experience higher surface melt rates (Lenaerts et al., 2017). Additionally, the presence of nunataks and exposed bedrock towards grounding lines can drive increased surface meltwater production, as these surfaces also have a relatively low albedo (Kingslake et al., 2017). Furthermore, at the grounding line ice transitions from being grounded to floating, and surface topographic depressions often form in these regions, where surface meltwater can collect.

The accumulation of both ponded meltwater and slush exists predominantly towards the grounding lines of all ice shelves investigated, rather than towards the ice-shelf fronts. In addition to the points made in the paragraph above, this may also reflect a reduction in the melt-to-accumulation ratio with increasing distance from the grounding line (Lenaerts et al., 2017). However, across north George VI Ice Shelf, the surface

meltwater extent is much more extensive, and is found across the central and distal regions of the northern part of this ice shelf (Figure 5.4). Across south George VI Ice Shelf, meltwater also appears to be extensive, although these findings predominantly reflect errors of commission caused by clouds. The findings for north George VI Ice Shelf, however, accurately reflect extensive areas of ponded meltwater and slush.

5.5.4 Potential climate drivers of inter-annual surface meltwater variability across the Antarctic Peninsula

Whilst it is beyond the scope of this current study to investigate fully the regional- and local-scale climate variations that may have caused the observed variability in total surface meltwater extent across the Antarctic Peninsula between 2013 and 2021, this section starts to address this topic with reference to recent studies of regional- and local-scale climate factors that are relevant to the results presented above.

West Antarctic Peninsula

High total surface meltwater extents are identified in the 2017/2018 melt season over the west Antarctic Peninsula, and in particular over Wilkins, Bach, north George VI, and south George VI ice shelves (Figure 5.2). Similarly, the 2019/2020 melt season exhibits relatively high total surface meltwater extents, particularly over the Müller, Wilkins, Bach, and north George VI ice shelves. Such observations are corroborated by Banwell et al. (2021), who find the 2019/2020 melt season to be a 32-year record high in terms of melt duration and areal extent across the north George VI Ice Shelf. They attribute this record melt to sustained warm periods (air temperatures greater than 0°C for up to a week at a time), which would have limited meltwater refreezing

during these periods. These warm periods likely resulted from the advection of warm, low speed northwesterly and northeasterly winds during the 2019/2020 season (Banwell et al., 2021). These warm winds may have been driven by interactions between a record-high Indian Ocean Dipole and a sudden stratospheric warming event (Bevan et al., 2020).

Given that the surface meltwater extents found in this study were also high in 2019/2020 across the Müller, Wilkins and Bach ice shelves, it seems likely that the meteorological conditions that drove high melt rates across George VI Ice Shelf in 2019/2020 are also applicable more broadly across the west Antarctic Peninsula in that year. Similarly, these meteorological conditions may also have driven the high tidal surface meltwater extents observed over Wilkins, Bach, north George VI, and south George VI ice shelves in 2017/2018.

However, it should be noted that across the south George VI and Stange ice shelves, total surface meltwater extents are relatively low in 2019/2020, despite good spatial and temporal image coverage across both ice shelves for that melt season. This could be attributed to high winter accumulation rates, which have been observed over south George VI Ice Shelf (e.g. Reynolds, 1981), and therefore likely also occur over Stange Ice Shelf. Across these ice shelves, if accumulation rates are high and melt rates are low, it is unlikely that impermeable surfaces will form, further explaining the lack of surface water ponding. Furthermore, the southerly position of both ice shelves on the West Antarctic Peninsula may further explain the patterns observed, as air temperatures may be lower in these regions (Cook and Vaughan, 2010).

Northeast Antarctic Peninsula

Across the northeast Antarctic Peninsula (Scar Inlet Ice Shelf, Larsen C Ice Shelf, and Larsen D Ice Shelf), slightly different patterns in meltwater extent are observed to those observed on the west Antarctic Peninsula. On the Larsen C and Larsen D ice shelves,

high total surface meltwater extents are observed in 2019/2020 and 2020/2021, and the greatest maximum total surface meltwater extent on the Larsen C ice shelf is recorded in 2019/2020. However, the greatest maximum total surface meltwater extent on the Larsen D Ice Shelf is observed in 2016/2017, which was not a particularly high melt year for Larsen C Ice Shelf. High meltwater extent and melt-season duration across the Larsen C Ice Shelf in 2019/2020 has previously been investigated by Bevan et al. (2020). As briefly mentioned above, they attribute this to typical interactions between the Indian Ocean Dipole and a sudden stratospheric warming event, which drove northwesterly and northeasterly winds on each side of the Antarctic Peninsula. These forcing factors may also explain the relatively high meltwater extents recorded for the Larsen D Ice Shelf in 2019/2020, and could potentially explain the high surface meltwater extents observed across both Larsen C and D ice shelves in 2020/2021. The data for Scar Inlet Ice Shelf has poor spatial and temporal coverage, which prohibits any key patterns from being identified (Figure 5.2).

Furthermore, previous studies have found that foehn winds are responsible for driving melt across the northeast Antarctic Peninsula, particularly on the Larsen C Ice Shelf (e.g. Datta et al., 2019; Elvidge et al., 2020; Kirchgaessner et al., 2021). In a study conducted between 1982 and 2017, Datta et al. (2019) record an increase in late season surface melt in response to increased foehn wind occurrence since 2015.

5.5.5 Site-specific variability in surface meltwater extent across Wilkins, Bach, and north George VI ice shelves

The data collected by this study can be used to conduct detailed assessments of inter- and intra-annual variability in surface meltwater extents across individual ice shelves. This is demonstrated through the results presented for Wilkins (Section 5.4.4), Bach (Section 5.4.5), and north George VI (Section 5.4.6) ice shelves. The rest of this

section discusses the patterns observed, with reference to current literature, whilst also highlighting apparent methodological successes or shortcomings.

Wilkins Ice Shelf

The total surface meltwater extent is greatest across the Wilkins Ice Shelf in 2019/2020 and reaches $1.6 \times 10^8 \text{ m}^2$ between 30 Jan 2020 and 13 Feb 2020. However, even at its maximum extent, water predominantly accumulates within $\sim 27 \text{ km}$ of the grounding line and does not extend towards the ice-shelf front (Figure 5.5). As discussed in section 5.5.3, these patterns are likely driven by the presence of foehn and/or katabatic winds across the grounding line, which remove firn from the surface, reducing the capacity for meltwater storage in subsurface layers, and also deliver heat, facilitating surface melt (e.g. Cape et al., 2015; Lenaerts et al., 2017). Furthermore, our results show that surface melt accumulates close to exposed bedrock on the Wilkins Ice Shelf, due to the lower surface albedo of these surfaces (Kingslake et al., 2017) (Figure 5.11). Surface meltwater ponding is also more likely to close the grounding line, where depressions often form as the glacier transitions from grounded ice to floating ice.

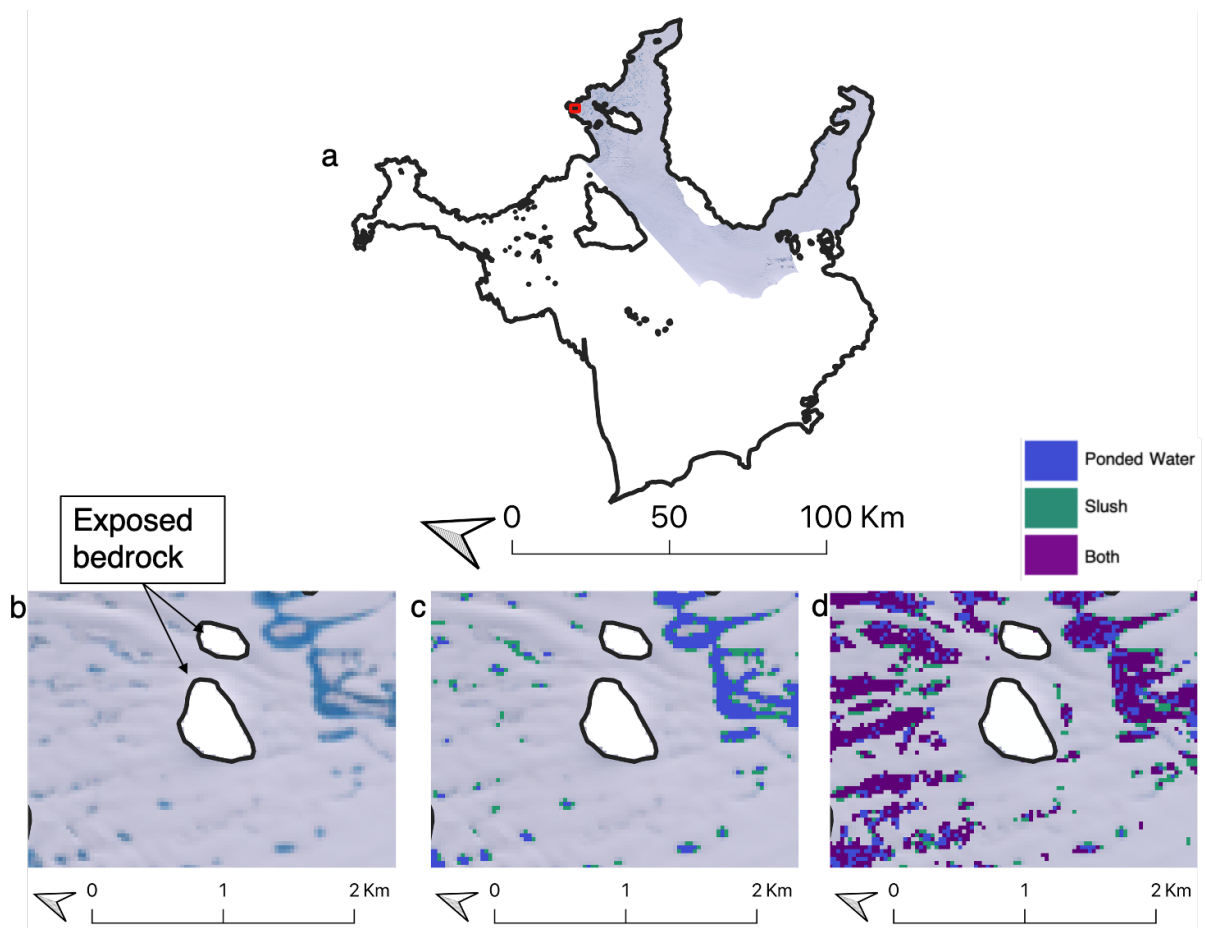


Figure 5.11: The Wilkins Ice Shelf on a) mosaicked true-colour composite Landsat images from 30 Jan 2020 to 13 Feb 2020. The subset images (outlined by the red box in a)) shows b) the true-colour composite base image for this period, c) the output of the Random Forest Classifier for this 15-day period, marking ponded water in blue and slush in green, and c) the maximum meltwater extent (i.e. all 15-day products mosaicked) for the full study period (2013 to 2021), showing pixels classified as both ponded water and slush as purple, pixels only ever classified as ponded water in blue, and pixels only ever classified as slush in green.

Figure 5.6 shows the 15-day melt products for the 2019/2020 melt season (i.e. the melt season with the maximum total surface meltwater extent) across the Wilkins Ice Shelf. These products highlight the impact that a lack of available imagery has on the study, as seen most markedly from 16 Dec 2019 to 30 Dec 2019 and 30 Jan 2020 to 13 Feb 2020 (Figure 5.6). Whilst this study scales the raw observed meltwater areas to the full area of interest (see Section 5.3), if the available imagery for a 15-day product does

not cover the region of melt (i.e. as from 14 Feb 2020 - 28 Feb 2020), the scaled values may not reflect the total surface meltwater extent over the ice shelf for that period. In such cases, therefore, it may be more prudent to analyse yearly maximum surface meltwater extent products (Figure 5.5), and to avoid relying too heavily on the 15-day surface meltwater extents.

Bach Ice Shelf

Across the Bach Ice Shelf, the greatest total surface meltwater extent is recorded in the 2017/2018 melt season, reaching $1.6 \times 10^8 \text{ m}^2$ between 15 Jan 2018 and 29 Jan 2018. As discussed for the Wilkins Ice Shelf, meltwater on the Bach Ice Shelf also predominantly accumulates towards the grounding line, and this can likely be attributed to foehn and/or katabatic winds (e.g. Cape et al., 2015; Lenaerts et al., 2017) and the presence of exposed bedrock (Kingslake et al., 2017). However, Figure 5.12, which shows in detail a smaller area of Bach Ice Shelf towards the eastern grounding line, and the associated classifier outputs, reveals a region of slush near the grounding line. Most notably, Figure 5.12c shows the maximum meltwater extent products for the full study period (2013 to 2021), which also shows a region of pixels that are only ever classified as slush. Therefore, it is likely that if foehn and/or katabatic winds are helping to enhance melting in the grounding zone area, they are not fully scouring the snow and/or firn from Bach Ice-Shelf's surface, and areas of slush therefore persist.

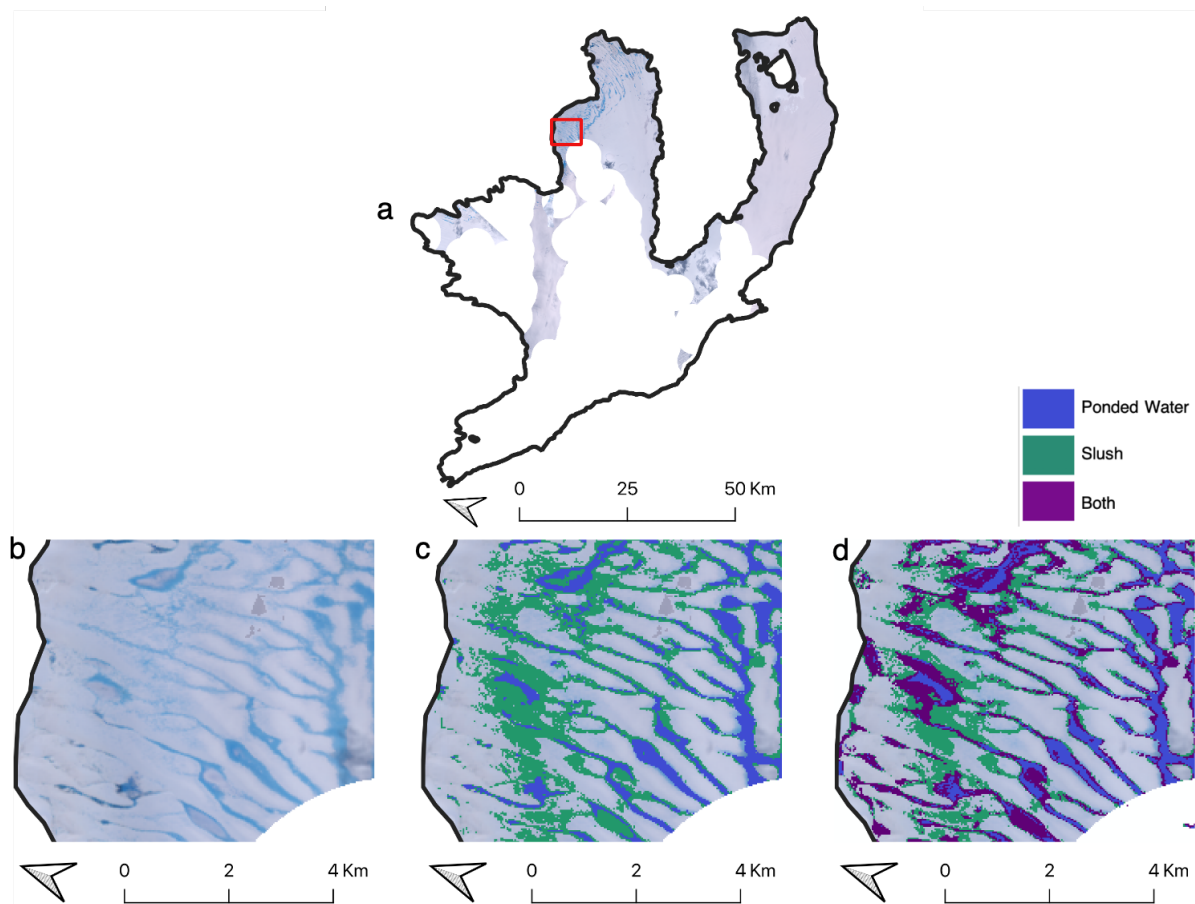


Figure 5.12: Figure of Bach Ice Shelf on a) mosaicked true-colour composite Landsat images between 15 Jan 2018 to 29 Jan 2018. The subset images (outlined by the red box in a)) shows b) the true-colour composite base image for this time period, c) the output of the Random Forest Classifier for this 15-day period, marking ponded water in blue and slush in green, and c) the maximum meltwater extent (i.e. all 15-day products mosaicked) for the full study period (2013 to 2021), showing pixels classified as both ponded water and slush as purple, pixels only ever classified as ponded water in blue, and pixels only ever classified as slush in green.

As also discussed for Wilkins Ice Shelf, the problems stemming from sparse image availability are most apparent when looking at the individual 15-day melt products. This is best illustrated on Bach Ice Shelf by the period of 31 Dec 2017 to 14 Jan 2018 (Figure 5.8), where a region that typically melts towards the eastern grounding line, is not covered by any available Landsat 8 imagery. This means that the true surface meltwater extent over this time period is likely to be underestimated.

North George VI Ice Shelf

The total surface meltwater extent was greatest across north George VI Ice Shelf in the 2019/2020 melt season, reaching $9.2 \times 10^8 \text{ m}^2$ between 15 Jan 2020 and 29 Jan 2020. Relatively high total surface meltwater extents in the 2017/2018 ($8.4 \times 10^8 \text{ m}^2$ between 30 Jan 2018 and 13 Feb 2018) and 2020/2021 ($8.7 \times 10^8 \text{ m}^2$ between 15 Jan 2021 and 29 Jan 2021) melt seasons are also observed. These observations are corroborated by Banwell et al. (2021), who find the 2019/2020 melt season on north George VI Ice Shelf to be a 32-year record in duration and total extent. Whilst Banwell et al. (2021) do not extend their study through to 2021, they also note that after 2019/2020, the second-highest melt season was 2017/2018, with the highest meltwater extent in that season recorded on 29 January 2018 ($4.6 \times 10^8 \text{ m}^2$). However, they find that the maximum extent of surface meltwater in 2018 ($1.2 \times 10^8 \text{ m}^2$) is less than half of what they observed on 19 January 2020.

Whilst this study and the work of Banwell et al. (2021) broadly agree, the total calculated meltwater extents do differ. For example, Banwell et al. (2021) find a greater maximum meltwater extent in 2019/2020. This likely reflects the fact that they use a combination of Landsat 8 and Sentinel-2 data to map ponded surface meltwater, whereas this study relies solely on data from Landsat 8. Another key difference between the two studies is the maximum total meltwater extent observed in the 2017/2018 melt season, as this study reports an area almost twice as great as that reported by Banwell et al. (2021). To some extent, this may be explained by the inclusion of slush within the total surface meltwater extent in this study, meaning more surface meltwater is classified than in Banwell et al. (2021). Furthermore, this difference could be due to the fact that this study presents 15-day meltwater products, whereas the data presented by Banwell et al. (2021) are single day meltwater products.

Figures 5.9 and 5.10 show the yearly maximum surface meltwater extent products and the 15-day meltwater products for the 2019/2020 melt season across north George VI Ice Shelf. The most notable finding from these products is arguably the extent of all

surface meltwater (both ponded water and slush) in regions that are distal from the grounding line. Furthermore, across north George VI Ice Shelf, there are areas of surface meltwater that are only ever classified as ponded surface meltwater (and never slush) over the full study period (2013 to 2021) (Figure 5.13).

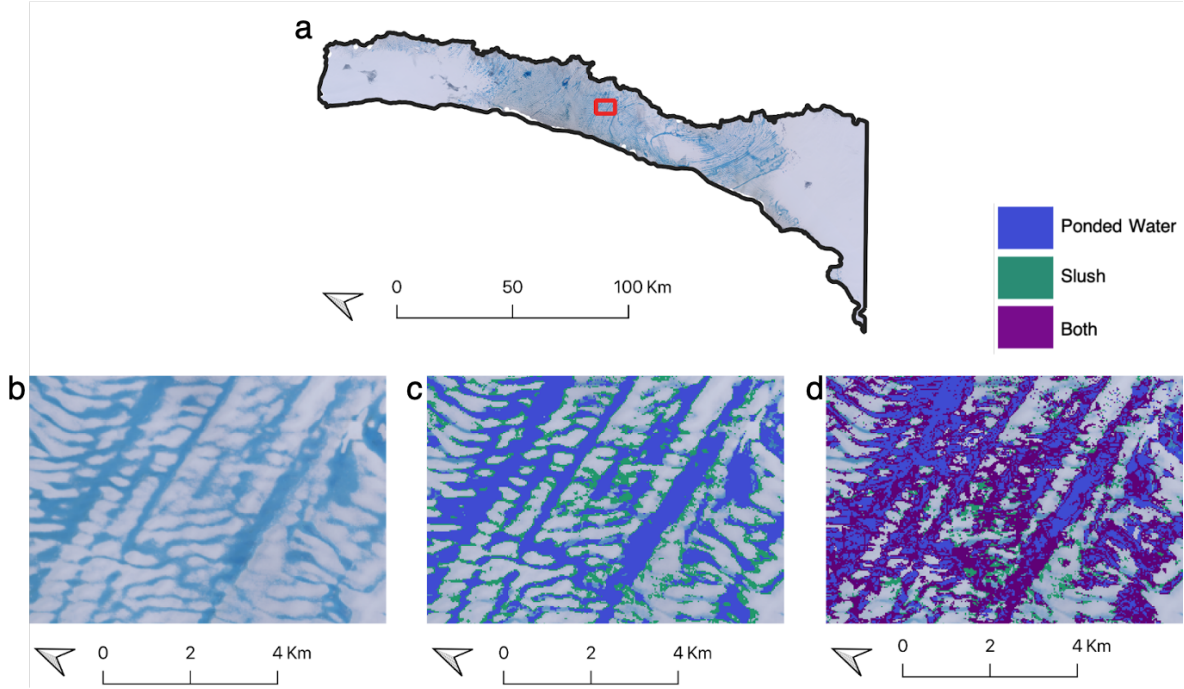


Figure 5.13: North George VI Ice Shelf shown as an a) mosaicked true-colour composite Landsat image from 15 Jan 2020 to 29 Jan 2020. The subset images (outlined by the red box in a)) shows b) the true-colour composite base image for this period, c) the output of the Random Forest Classifier for this 15-day period, marking ponded water in blue and slush in green, and c) the maximum meltwater extent (i.e. all 15-day products mosaicked) for the full study period (2013 to 2021), showing pixels classified as both ponded water and slush as purple, pixels only ever classified as ponded water in blue, and pixels only ever classified as slush in green.

These observations could be explained by the low accumulation rates across north George VI Ice Shelf (e.g. Reynolds, 1981), which are caused by a precipitation shadow from Alexander Island (situated on the northwest side of the north George VI Ice Shelf). This decreased snow accumulation will reduce the capacity for meltwater to be stored within snow and firn layers, meaning surface meltwater is more likely to pond on the ice-shelf surface.

5.6 Conclusions

This chapter has presented a novel dataset of ponded water and slush extents across eight remaining ice shelves on the Antarctic Peninsula from 2013 to 2021. This has been achieved using the Random Forest Classifier (as introduced in Chapter 4), which was applied to the full Landsat 8 record. Overall, no marked inter-annual trends in total surface meltwater extent have been identified across the Antarctic Peninsula, although peaks in total surface meltwater extent across the west Antarctic Peninsula ice shelves were predominantly observed in 2017/2018 and 2019/2020, whilst across the east Antarctica Peninsula ice shelves, these peaks are predominantly observed in 2016/2017. High surface meltwater extents across both the west and east Antarctic Peninsula in 2019/2020 could be attributed to the advection of warm air by northwesterly and northeasterly winds, driven by interactions between the IOD and a sudden stratospheric warming event (Bevan et al., 2020; Banwell et al., 2021). Foehn winds may also have driven increased melt since 2015, particularly across the northeast Antarctic Peninsula (Datta et al., 2019). Beyond the broad regional patterns in total surface meltwater extent identified, this study also finds high inter-annual spatial heterogeneity in surface meltwater extents between ice shelves. Such variability is likely driven by local-scale ice-surface properties and local climate patterns as opposed to larger-scale synoptic climate drivers (Stokes et al., 2019).

On an intra-annual timescale, ponded water typically reaches its maximum seasonal extent between 1 January and 31 March for each ice shelf, whilst slush reaches its maximum seasonal extent either prior to ponded water (45.7% of the time) or simultaneously with ponded water (40.0% of the time). This variability likely reflects the process of surface meltwater initially saturating the firn pack, before meltwater begins to pond (e.g. Scambos et al. 2000; Kuipers Munneke et al. 2014; Bevan et al., 2017).

Ponded water and slush across the Antarctic Peninsula from 2013 to 2021 predominantly accumulates in proximity to the grounding lines of all ice shelves, apart

from on north George VI Ice Shelf, where surface meltwater extends across the central and distal portions of the ice shelf. The widespread surface meltwater across north George VI Ice Shelf is likely explained by low accumulation rates across the northern part of this ice shelf, reducing the capacity for meltwater to be stored in snow or firn. On other ice shelves, surface meltwater may predominantly pond near to grounding lines as (i) prevailing foehn and/or katabatic winds cause local snow and firn erosion, reducing the capacity for meltwater storage within the ice-shelf sub- surface and exposing lower albedo blue ice surfaces (Cape et al., 2015; Lenaerts et al., 2017), (ii) foehn and/or katabatic winds deliver warm air to the grounding line, enhancing melt rates (Lenaerts et al., 2017) (iii) exposed bedrock lowers the surface albedo, increasing solar absorption (Kingslake et al., 2017), and (iv) surface depressions form where grounded ice transitions to floating ice; encouraging meltwater ponding. Future work will investigate the climate drivers of the regional- and local- scale variability in total surface meltwater extents observed across the Antarctic Peninsula, in addition to extending this dataset across all ice shelves around the Antarctic Ice Sheet.

Chapter 6

Synthesis and Conclusions

Over the last decade, surface meltwater on Antarctic ice shelves has been increasingly studied using remote sensing methodologies. This thesis has advanced this research, through the development of semi-automated remote sensing and machine learning methods to identify and track surface meltwater across Antarctic ice shelves using satellite imagery. This aim was broken down into three key objectives in Chapter 1 as follows:

1. To develop a semi-automated method that utilises established thresholds and equations to track the formation of surface meltwater systems over a melt season and to demonstrate the application of this method over the Nivlisen Ice Shelf. This work was presented in Chapter 3.
2. To train and validate a Random Forest Classifier (a machine learning tool) capable of detecting ponded water and slush across all Antarctic ice shelves using the full Landsat 8 record (2013-2020), and to demonstrate the application of this method across the Roi Baudouin Ice Shelf. This work was presented in Chapter 4.
3. To apply the Random Forest Classifier developed in (2) to map the extent of ponded water and slush across eight ice shelves on the Antarctic Peninsula between 2013 and 2021. This work was presented in Chapter 5.

This final chapter summarises the key findings, limitations, and potential avenues for future research for each of the three preceding chapters (Chapters 3-5), before finally concluding this thesis.

6.1 Objective 1 - Develop a semi-automated method capable of tracking the formation of surface meltwater systems

6.1.1 Key findings from this study

This first study (Chapter 3) was designed to better automate the methodologies that are used to monitor changes in the area, volume, and geometry of meltwater bodies on ice shelves. It presents a new algorithm: 'FASTISh', which is a semi-automated method capable of identifying and tracking changes in water bodies on an ice shelf, throughout a full melt season. The algorithm is capable of collecting data from both Landsat 8 and Sentinel-2 scenes, which improves the temporal resolution of the observations made in comparison to the temporal resolution that would have been achieved by using just a single satellite. The FASTISh algorithm builds on and adapts the FASTER algorithm (Williamson et al., 2018a) for application on Antarctic ice shelves. Key changes to the FASTER algorithm meant that the new method could (i) account for differences in surface meltwater bodies in Antarctica compared to Greenland, (ii) identify marked changes in water-body geometries over time, and (iii) identify the transfer of surface meltwater over large distances across an ice shelf.

The capabilities of this method were demonstrated on the Nivlisen Ice Shelf for the 2016/2017 melt season, and it successfully tracked a total of 1598 water bodies between 2nd November 2016 and 24 March 2017. Early in the melt season, the algorithm found that the majority of surface water bodies were formed in proximity to the grounding line, close to an exposed nunatak and in a blue ice region. However, as the melt season progressed, and a more complex, interconnected surface drainage system developed, the algorithm tracked the development of two major meltwater bodies (the Eastern System (ES) and Western System (WS)) that facilitated the lateral

transfer of surface meltwater over distances up to 20.5 km. Overall, the algorithm provided a robust dataset of water-body areas, volumes, and geometries, which, when applied, provided new insights into lateral water transfer across the Nivlisen Ice Shelf.

6.1.2 Directions for future research

Whilst the FASTISh algorithm presented in Chapter 3 has provided a semi-automated methodology for tracking surface meltwater across ice shelves, it does not currently have the capacity to detect or track water within the ice-shelf subsurface. By incorporating Sentinel-1 SAR data into the workflow, the algorithm could be extended to account for the presence of subsurface water, which would improve our current understanding of meltwater percolation into the firn layer. This application would be particularly useful on the Nivlisen Ice Shelf, as the fate of the water transferred within the ES and WS could be better understood. Figure 3.11 introduces a Sentinel-1 SAR image for qualitative analysis; however, if Sentinel-1 SAR imagery was fully integrated within FASTISh, a quantitative dataset could be obtained.

Furthermore, meltwater body geometries could be better categorised into lakes and streams as opposed to 'linear' and 'circular' water bodies with the potential application of object-based image analysis techniques, or with the addition of flow-routing analysis. These advances would allow more confident interpretation of how and where water flows across ice-shelf surfaces, as opposed to classifying water bodies based purely on their geometries.

It would also be beneficial for future research to collect 'in situ' data of lake depths, to validate the water body depths calculated using the physically-based lake depth equation.

6.2 Objective 2 - Train and validate a Random Forest Classifier capable of detecting slush and ponded water across all Antarctic ice shelves

6.2.1 Key findings from this study

The second study (Chapter 4) focussed on training and validating a Random Forest Classifier capable of detecting ponded water and slush using data from six Antarctic ice shelves using the full Landsat 8 record available at the time (2013-2020). This study was motivated by the lack of research into slush extent across Antarctic ice shelves, despite its significance for meltwater ponding and firn densification. Prior to this study, slush extent had only been mapped on a few individual ice shelves, using simple $NDWI_{ice}$ thresholds. However, owing to the spectral similarities between slush and other ice-shelf surface facies (e.g. blue ice, ponded water, snow), $NDWI_{ice}$ thresholds cannot be successfully and widely applied across Antarctic ice shelves for accurate slush identification.

Providing the first supervised classifier capable of detecting ponded water and slush on ice shelves, with accuracies of 82% and 84% respectively, this study has the potential to provide records of the total surface meltwater extent across Antarctic ice shelves, whilst previous studies have only considered ponded water extents. Halberstadt et al. (2020) used a similar supervised Random Forest Classifier for a study on the Roi Baudouin and Amery Ice Shelves, which had a higher classification accuracy score of 93%. However, Halberstadt et al. (2020) classified ponded water only, and validated the classifier using just a single expert's opinion, whilst the study presented in this thesis validated the classifier against four experts' opinions.

Within this chapter, the Random Forest Classifier was applied to the Roi Baudouin Ice Shelf between 2013 and 2020, to demonstrate its applicability. Over the study period, the greatest total melt extent on the Roi Baudouin Ice Shelf was $5.0 \times 10^9 \text{ m}^2$ between 30 January and 13 February 2017. These findings are broadly corroborated by Halberstadt et al. (2020), who conducted a similar investigation over the Roi Baudouin Ice Shelf between 2013 and 2018 to calculate the extent of ponded water bodies, and found the meltwater area to be greatest on 25 February 2017.

Furthermore, results from the Roi Baudouin Ice Shelf revealed that slush accounts for 64% of the total meltwater area over the study period. Such findings highlight the need to map slush extent as well as ponded water extent when conducting surface meltwater studies across Antarctic ice shelves. Until now, the majority of studies have investigated the area of ponded water only (e.g. Langley et al., 2016; Stokes et al., 2019; Moussavi et al. 2020; Banwell et al. 2021), owing to its significance for hydrofracture-driven ice-shelf collapse. The presence of slush can lead to a reduction in FAC, encouraging surface meltwater ponding (e.g. Scambos et al., 2000; Kuipers Munneke et al., 2014; Bevan et al., 2017).

6.2.2 Directions for future research

Whilst the Random Forest Classifier presented in Chapter 4 was able to effectively and accurately classify ponded water and slush across six ice shelves, future work should look to improve the classification accuracy further. This study utilised only Landsat 8 bands 1-7 to classify ponded water and slush. A similar approach was taken by Dirscherl et al. (2020), who also included Sentinel-2 bands 2-8A in their classifier for the purposes of mapping ponded surface meltwater. Whilst the Landsat 8 panchromatic band (Band 8), and the cirrus band (Band 9) are excluded from the study presented for the reasons discussed above in Chapter 4, it could be expected that the thermal infrared bands (Bands 10-11) might be useful for distinguishing between ice-shelf surface facies. However, the lower spatial resolution of these thermal bands (100

m) limited their effectiveness within the classifier in this study, even when resampled to finer spatial resolutions (30 m). However, future work could look further into incorporating thermal data of a higher spatial resolution into a classifier, to improve classification accuracies.

In addition to the inclusion of thermal data, future work could also investigate incorporating auxiliary Tandem-X topographic data into a classifier, following the approach of Dirscherl et al. (2021); this would allow training data such as relief, roughness, and slope to be put into the classifier.

At present, the Random Forest Classifier developed in this study can only be applied during the austral summer, as polar darkness in the austral winter prevents optical data collection. Furthermore, cloud cover often obscures large regions of each ice shelf, preventing surface meltwater from being mapped in such conditions. A solution to this, as presented by Dirscherl et al. (2021) is to use Sentinel-1 SAR data, to facilitate surface meltwater classification through the polar night and through cloudy conditions. Whilst Dirscherl et al. (2021) used a CNN to automatically map surface lake extents, and combined the outputs with those from a supervised classifier (which uses Sentinel-2 and auxiliary Tandem-X topographic data), future work could look to combine these data sets into a single Random Forest Classifier, streamlining this methodology. Furthermore, future work could investigate the potential for Sentinel-1 SAR data to be used to classify subsurface meltwater in addition to surface meltwater.

Finally, future work could look to develop similar supervised classifiers using a range of other satellites (e.g. Sentinel-2, Landsat 7 ETM+, Landsat 4-5 TM, WorldView). These supervised classifiers will increase the current temporal resolution of mapped ponded water and slush products, as well as extending the record of slush and ponded water back to the 1980s (i.e. with Landsat). Such classifiers could then be applied across all ice shelves in Antarctica, providing us with a continent-wide dataset from which total surface meltwater extent can be analysed. Ideally, the classifiers developed for each of these satellites could also be validated through the collection of ground

based multi- or hyper-spectral data, facilitating a robust assessment of each classifier's accuracy.

6.3 Objective 3 - Map the extent of ponded water and slush across all ice shelves on the Antarctic Peninsula between 2013 and 2021

6.3.1 Key findings from this study

The third study (Chapter 5) applied the Random Forest Classifier developed in Chapter 4 to the main remaining eight ice shelves on the Antarctic Peninsula (Müller, Wilkins, Bach, George VI, Stange, Scar Inlet, Larsen C and Larsen D ice shelves), using the full Landsat 8 record (2013-2021). This study was particularly motivated by the lack of data on total meltwater extent (comprising both ponded water and slush) across Antarctic ice shelves, as the majority of studies focus solely on ponded water extent.

This study therefore provided a data set that maps the extent of both ponded water and slush across the Antarctic Peninsula ice shelves listed above. The data products include 15-day meltwater extent maps, maximum meltwater extent composites for each melt season, and maximum meltwater composites for the full study period (2013-2021).

Key results from this chapter included the identification of high total surface meltwater extents across most ice shelves on the west Antarctic Peninsula in 2017/2018 and 2019/2020, whilst total surface meltwater extents were greatest across most ice shelves on the east Antarctic Peninsula in 2016/2017 and 2019/2020. The increased surface melt that was identified across most of the Antarctic Peninsula in 2019/2020 is

likely driven by interactions between a positive IOD and a sudden stratospheric warming event (Bevan et al., 2020). The study presented in Chapter 5 also identified high inter-annual spatial heterogeneity in the extent of total meltwater, ponded meltwater and slush. This variability is postulated to reflect a combination of local-scale ice-surface properties and climate factors, rather than larger-scale synoptic drivers (Stokes et al., 2019).

The study also reveals that 45.7% of the time (when looking at the full study period from 2013 to 2021), slush reached its seasonal maximum extent prior to ponded water, and 40% of the time, the seasonal maximum extent of ponded water and slush peaked simultaneously. These findings suggest that earlier in the melt season surface meltwater is occupying available firn pore spaces, prior to ponding at the surface. Where firn exists, only when the firn layer is saturated does water begin to pond (e.g. Scambos et al. 2000; Kuipers Munneke et al. 2014; Bevan et al. 2017).

6.3.2 Directions for future research

Future work should look to further apply the Random Forest Classifier developed in Chapter 4, and as applied to ice shelves on the Antarctic Peninsula in Chapter 5, across all remaining ice shelves around Antarctica. This would produce a dataset of ponded meltwater and slush extent between 2013 and 2021, and any key trends in both ponded water and slush extents could then be identified.

Furthermore, whilst it was not within the scope of this PhD thesis to conduct climate analysis, future research should investigate the climate variables that may have driven and may be driving variability in surface meltwater trends across Antarctic ice shelves. Such research could utilise gridded climate variables from regional climate models (e.g. land-surface temperatures, sea-surface temperatures, sea-ice concentration,

sea-ice thickness, and wind speed and direction) to find local- and regional-scale relationships between climate and ice-shelf melt.

6.4 Conclusions

In summary, this thesis presents (i) a semi-automatic algorithm (FASTISh), which is capable of identifying and tracking changes in the area, volume, and geometry of water bodies on ice shelves over time, (ii) a Random Forest Classifier, which is capable of mapping the extent of ponded water and slush across Antarctic ice shelves; and (iii) a dataset of ponded water and slush extent across eight ice shelves on the Antarctic Peninsula, from 2013 to present day.

Overall, the work undertaken in this thesis has advanced the methods available for the study of surface meltwater across Antarctic Ice Shelves, as it provides semi- automatic solutions to handling large amounts of optical satellite imagery. Without such methodological advances, it would be difficult to continue to monitor the changes in surface meltwater distribution across Antarctic ice shelves through time, as there is not enough 'manpower' to manually process all the available data.

The FASTISh algorithm provides a method capable of automatically detecting key volumetric changes in water bodies on ice shelves, and to categorise the geometry of these water bodies, to allow us to begin to better understand how supraglacial hydrological systems on ice shelves are organised and developed as a melt season progresses. If applied across all Antarctic ice shelves, this method could significantly advance our understanding of lateral meltwater transfer across ice-shelf surfaces.

The Random Forest Classifier developed in Chapter 4 and applied in Chapter 5, which is capable of mapping the extent of ponded water and slush from Landsat 8 image scenes, provides the first semi-automatic approach for accurately mapping slush across numerous ice shelves in Antarctica. It is the first method of its kind to accurately quantify the extent of slush, which until now, has been largely ignored within

glaciological research. Given the significance of slush for firn air depletion, and subsequent surface meltwater ponding, it is crucial that studies continue to investigate its changing extent over time, and as surface melting across Antarctic ice shelves continues.

References

Adusumilli, S., Fricker, H.A., Medley, B., Padman, L., and Siegfried, M.R., 2020. Interannual variations in meltwater input to the Southern Ocean from Antarctic ice shelves. *Nature Geoscience*, 13 (9), 616–620.

Aggarwal, S., 2004. Principles of remote sensing. *Satellite Remote Sensing and GIS Applications in Agricultural Meteorology*, 23, 23–28.

Alley, K.E., Scambos, T.A., Alley, R.B. and Holschuh, N., 2019. Troughs developed in ice-stream shear margins precondition ice shelves for ocean-driven breakup. *Science Advances*, 5(10), p.eaax2215.

Alley, K.E., Scambos, T.A., Miller, J.Z., Long, D.G., and MacFerrin, M., 2018. Quantifying vulnerability of Antarctic ice shelves to hydrofracture using microwave scattering properties. *Remote Sensing of Environment*, 210, 297–306.

Arnold, N. and Rees, G., 2009. Effects of digital elevation model spatial resolution on distributed calculations of solar radiation loading on a high arctic glacier. *Journal of Glaciology*, 55 (194), 973–984.

Arnold, N.S., Banwell, A.F., and Willis, I.C., 2014. High-resolution modelling of the seasonal evolution of surface water storage on the Greenland Ice Sheet. *The Cryosphere*, 8 (4), 1149–1160.

Arthur, D. and Vassilvitskii, S., 2007. K-means++: The advantages of careful seeding. In: *Proceedings of the Annual ACM-SIAM Symposium on Discrete Algorithms*. Stanford, 1027–1035.

Arthur, J., Stokes, C., Jamieson, S., Carr, J.R., and Leeson, A., 2020a. Distribution and seasonal evolution of supraglacial lakes on Shackleton Ice Shelf, East Antarctica. *The Cryosphere Discussions*, 1–36.

Arthur, J.F., Stokes, C., Jamieson, S.S., Carr, J.R. and Leeson, A.A., 2020. Recent understanding of Antarctic supraglacial lakes using satellite remote sensing. *Progress in Physical Geography: Earth and Environment*, 44(6), 837-869.

Arthur, J.F., Stokes, C.R., Jamieson, S.S., Miles, B.W., Carr, J.R. and Leeson, A.A., 2021. The triggers of the disaggregation of Voyeykov Ice Shelf (2007), Wilkes Land, East Antarctica, and its subsequent evolution. *Journal of Glaciology*, 1-19.

Ashmore, D.W., Hubbard, B., Luckman, A., Kulesa, B., Bevan, S., Booth, A., Munneke, P.K., O’Leary, M., Sevestre, H., and Holland, P.R., 2017. Ice and firn heterogeneity within Larsen C Ice Shelf from borehole optical televiewing. *Journal of Geophysical Research: Earth Surface*, 122 (5), 1139–1153.

Bamber, J. L., & Aspinall, W. P. 2013. An expert judgement assessment of future sea level rise from the ice sheets. *Nature Climate Change*, 3(4), 424–427.

- Banwell, A., 2017. Ice-shelf stability questioned. *Nature*, 544(7650), 306-307.
- Banwell, A.F. and MacAyeal, D.R., 2015. Ice-shelf fracture due to viscoelastic flexure stress induced by fill/drain cycles of supraglacial lakes. *Antarctic Science*, 27 (6), 587–597.
- Banwell, A.F., Arnold, N.S., Willis, I.C., Tedesco, M., and Ahlström, A.P., 2012. Modeling supraglacial water routing and lake filling on the Greenland Ice Sheet. *Journal of Geophysical Research: Earth Surface*, 117 (4).
- Banwell, A.F., Caballero, M., Arnold, N.S., Glasser, N.F., Cathles, L.M., and MacAyeal, D.R., 2014. Supraglacial lakes on the Larsen B ice shelf, Antarctica, and at Paakitsoq, West Greenland: A comparative study. *Annals of Glaciology*, 55 (66), 1–8.
- Banwell, A.F., Datta, R.T., Dell, R.L., Moussavi, M., Brucker, L., Picard, G., Shuman, C.A., and Stevens, L.A., 2021. The 32-year record-high surface melt in 2019/2020 on the northern George VI Ice Shelf, Antarctic Peninsula. *The Cryosphere*, 15 (2), 909–925.
- Banwell, A.F., MacAyeal, D.R., and Sergienko, O. V., 2013. Breakup of the Larsen B Ice Shelf triggered by chain reaction drainage of supraglacial lakes. *Geophysical Research Letters*, 40 (22), 5872–5876.
- Banwell, A.F., Willis, I.C., Macdonald, G.J., Goodsell, B., and MacAyeal, D.R., 2019. Direct measurements of ice-shelf flexure caused by surface meltwater ponding and drainage. *Nature Communications*, 10 (1), 1–10.
- Banwell, A.F., Willis, I.C., MacDonald, G.J., Goodsell, B., Mayer, D.P., Powell, A., and MacAyeal, D.R., 2017. Calving and rifting on the McMurdo Ice Shelf, Antarctica. *Annals of Glaciology*, 58 (75), 78–87.
- Behnamian, A., Millard, K., Banks, S.N., White, L., Richardson, M., and Pasher, J., 2017. A Systematic Approach for Variable Selection With Random Forests: Achieving Stable Variable Importance Values. *IEEE Geoscience and Remote Sensing Letters*, 14 (11), 1988–1992.
- Belgiu, M. and Drăguț, L., 2016. Random forest in remote sensing: A review of applications and future directions. *ISPRS Journal of Photogrammetry and Remote Sensing*, 114, 24-31.
- Bell, R.E., Banwell, A.F., Trusel, L.D., and Kingslake, J., 2018. Antarctic surface hydrology and impacts on ice-sheet mass balance. *Nature Climate Change*, 8 (12), 1044–1052.
- Bell, R.E., Chu, W., Kingslake, J., Das, I., Tedesco, M., Tinto, K.J., Zappa, C.J., Frezzotti, M., Boghosian, A., and Lee, W.S., 2017. Antarctic ice shelf potentially stabilized by export of meltwater in surface river. *Nature*, 544 (7650), 344–348.

Benedek, C.L. and Willis, I.C., 2021. Winter drainage of surface lakes on the Greenland Ice Sheet from Sentinel-1 SAR imagery. *The Cryosphere*, 15 (3), 1587–1606.

Benson, C.S., 1962. *Stratigraphic studies in the snow and firn of the Greenland ice sheet*. Cold Regions Research And Engineering Lab HANOVER NH.

Berthier, E., Scambos, T. A., & Shuman, C. A. 2012. Mass loss of Larsen B tributary glaciers (Antarctic Peninsula) unabated since 2002. *Geophysical Research Letters*, 39(13)

Bevan, S., Luckman, A., Hendon, H., and Wang, G., 2020. The 2020 Larsen C Ice Shelf surface melt is a 40-year record high. *The Cryosphere*, 14 (10), 3551–3564.

Bevan, S.L., Luckman, A., Hubbard, B., Kulesa, B., Ashmore, D., Kuipers Munneke, P., O’Leary, M., Booth, A., Sevestre, H., and McGrath, D., 2017. Centuries of intense surface melt on Larsen C Ice Shelf. *The Cryosphere*, 11 (6), 2743–2753.

Bezdek, J.C., Chuah, S.K., and Leep, D., 1986. Generalized k-nearest neighbor rules. *Fuzzy Sets and Systems. An International Journal in Information Science and Engineering*, 18 (3), 237–256.

Bindschadler, R. and Vornberger, P., 1992. Interpretation of sar imagery of the greenland ice sheet using coregistered TM imagery. *Remote Sensing of Environment*, 42 (3), 167–175.

Bindschadler, R., Vornberger, P., Fleming, A., Fox, A., Mullins, J., Binnie, D., Paulsen, S.J., Granneman, B. and Gorodetzky, D., 2008. The Landsat image mosaic of Antarctica. *Remote Sensing of Environment*, 112(12), 4214-4226.

Borstad, C.P., Khazendar, A., Larour, E., Morlighem, M., Rignot, E., Schodlok, M.P., and Seroussi, H., 2012. A damage mechanics assessment of the Larsen B ice shelf prior to collapse: Toward a physically-based calving law. *Geophysical Research Letters*, 39 (17).

Box, J.E. and Ski, K., 2007. Remote sounding of Greenland supraglacial melt lakes: implications for subglacial hydraulics. *Journal of Glaciology*, 53 (181), 257–265.

Breiman, L., 2001. Random forests. *Machine learning*, 45(1), 5-32.

Burton, J.C., Mac Cathles, L., and Grant Wilder, W., 2013. The role of cooperative iceberg capsize in ice-shelf disintegration. *Annals of Glaciology*, 54 (63), 84–90.

Bush, M., Allen, T., Bain, C., Boutle, I., Edwards, J., Finnenkoetter, A., Franklin, C., Hanley, K., Lean, H., Lock, A., Manners, J., Mittermaier, M., Morcrette, C., North, R., Petch, J., Short, C., Vosper, S., Walters, D., Webster, S., Weeks, M., Wilkinson, J., Wood, N., and Zerroukat, M., 2020. The first Met Office Unified

Model/JULES Regional Atmosphere and Land configuration, RAL1. *Geoscientific Model Development Discussions*, 1–47.

Buzzard, S., Feltham, D., and Flocco, D., 2018. Modelling the fate of surface melt on the Larsen C Ice Shelf. *The Cryosphere*, 12 (11), 3565–3575.

Cape, M.R., Vernet, M., Skvarca, P., Marinsek, S., Scambos, T., and Domack, E., 2015. Foehn winds link climate-driven warming to ice shelf evolution in Antarctica. *Journal of Geophysical Research*, 120 (21), 11,037–11,057.

Chu, V.W., 2014. Greenland ice sheet hydrology: A review. *Progress in Physical Geography: Earth and Environment*, 38 (1), 19–54.

Cook, A.J. and Vaughan, D.G., 2010. Overviewing of areal changes of the ice shelves on the Antarctic Peninsula over the past 50 years. *The Cryosphere*, 4, 77–98.

Cracknell, A.P., 2007. *Introduction to Remote Sensing*. CRC Press.

Culberg, R., Schroeder, D.M., and Chu, W., 2021. Extreme melt season ice layers reduce firn permeability across Greenland. *Nature Communications*, 12 (1), 2336.

Das, S.B., Joughin, I., Behn, M.D., Howat, I.M., King, M.A., Lizarralde, D., and Bhatia, M.P., 2008. Fracture propagation to the base of the Greenland Ice Sheet during supraglacial lake drainage. *Science*, 320 (5877), 778–781.

Datta, R.T., Tedesco, M., Agosta, C., Fettweis, X., Kuipers Munneke, P., and van den Broeke, M.R., 2018. Melting over the northeast Antarctic Peninsula (1999–2009): evaluation of a high-resolution regional climate model. *The Cryosphere*, 12, 2901.

Datta, R.T., Tedesco, M., Fettweis, X., Agosta, C., Lhermitte, S., Lenaerts, J.T.M., and Wever, N., 2019. The Effect of Foehn-Induced Surface Melt on Firn Evolution Over the Northeast Antarctic Peninsula. *Geophysical Research Letters*, 46 (7), 3822–3831.

De Rydt, J., Gudmundsson, G.H., Rott, H., and Bamber, J.L., 2015. Modeling the instantaneous response of glaciers after the collapse of the Larsen B Ice Shelf. *Geophysical Research Letters*, 42 (13), 5355–5363.

DeConto, R.M. and Pollard, D., 2016. Contribution of Antarctica to past and future sea-level rise. *Nature*, 531 (7596), 591–597.

DeConto, R.M., Pollard, D., Alley, R.B., Velicogna, I., Gasson, E., Gomez, N., Sadai, S., Condrón, A., Gilford, D.M., Ashe, E.L., Kopp, R.E., Li, D., and Dutton, A., 2021. The Paris Climate Agreement and future sea-level rise from Antarctica. *Nature*, 593 (7857), 83–89.

Dee, D.P., Uppala, S.M., Simmons, A.J., Berrisford, P., Poli, P., Kobayashi, S., Andrae, U., Balmaseda, M.A., Balsamo, G., Bauer, P., Bechtold, P., Beljaars, A.C.M., van de Berg, L., Bidlot, J., Bormann, N., Delsol, C., Dragani, R., Fuentes, M., Geer, A.J., Haimberger, L., Healy, S.B., Hersbach, H., Hólm, E. V., Isaksen, I., Kållberg, P., Köhler, M., Matricardi, M., McNally, A.P., Monge-Sanz, B.M., Morcrette, J.J., Park, B.K., Peubey, C., de Rosnay, P., Tavolato, C., Thépaut, J.N., and Vitart, F., 2011. The ERA-Interim reanalysis: Configuration and performance of the data assimilation system. *Quarterly Journal of the Royal Meteorological Society*, 137 (656), 553–597.

Dell, R., Arnold, N., Willis, I., Banwell, A., Williamson, A., Pritchard, H. and Orr, A., 2020. Lateral meltwater transfer across an Antarctic ice shelf. *The Cryosphere*, 14(7), 2313-2330.

Dell, R., Arnold, N., Willis, I., Banwell, A., Williamson, A., Pritchard, H., and Orr, A., 2020a. Fully Automated Supraglacial-Water Tracking algorithm for Ice Shelves (FASTISh).

Dell, R., Arnold, N., Willis, I., Banwell, A., Williamson, A., Pritchard, H., and Orr, A., 2020b. S.2 (GIF of all 11 RGB base images), Supplementary GIF's (S2-S4) for the paper 'Lateral meltwater transfer across an Antarctic ice shelf'.

Dell, R., Arnold, N., Willis, I., Banwell, A., Williamson, A., Pritchard, H., and Orr, A., 2020c. S.3 (GIF of all 11 area matrices), Supplementary GIF's (S2-S4) for the paper 'Lateral meltwater transfer across an Antarctic ice shelf'.

Dell, R., Arnold, N., Willis, I., Banwell, A., Williamson, A., Pritchard, H., and Orr, A., 2020d. S.4 (GIF of all 11 depth matrices), Supplementary GIF's (S2-S4) for the paper 'Lateral meltwater transfer across an Antarctic ice shelf'.

Dell, R., Banwell, A., Willis, I., Arnold, N., Chudley, T., Halberstadt, R., Pritchard, H., Supervised classification of slush and ponded water on Antarctic ice shelves using Landsat 8 imagery. *Journal of Glaciology*, in review

Depoorter, M.A., Bamber, J.L., Griggs, J.A., Lenaerts, J.T.M., Ligtenberg, S.R.M., Van Den Broeke, M.R., and Moholdt, G., 2013. Calving fluxes and basal melt rates of Antarctic ice shelves. *Nature*, 502 (7469), 89–92.

Dirscherl, M., Dietz, A.J., Kneisel, C., and Kuenzer, C., 2020. Automated Mapping of Antarctic Supraglacial Lakes Using a Machine Learning Approach. *Remote Sensing*, 12 (7), 1203.

Dirscherl, M., Dietz, A.J., Kneisel, C., and Kuenzer, C., 2021. A novel method for automated supraglacial lake mapping in antarctica using sentinel-1 sar imagery and deep learning. *Remote Sensing*, 13 (2), 1–27.

Dongare, A.D., Kharde, R.R., and Kachare, A.D., 2012. Introduction to artificial neural network. *International Journal of Engineering and Innovative Technology (IJEIT)*, 2 (1), 189–194.

Dow, C.F., Lee, W.S., Greenbaum, J.S., Greene, C.A., Blankenship, D.D., Poinar, K., Forrest, A.L., Young, D.A., and Zappa, C.J., 2018. Basal channels drive active surface hydrology and transverse ice shelf fracture. *Science Advances*, 4 (6), eaao7212.

Doyle, S.H., Hubbard, A.L., Dow, C.F., Jones, G.A., Fitzpatrick, A., Gusmeroli, A., Kulesa, B., Lindback, K., Pettersson, R., and Box, J.E., 2013. Ice tectonic deformation during the rapid in situ drainage of a supraglacial lake on the Greenland Ice Sheet. *The Cryosphere*, 7 (1), 129–140.

Drusch, M., Del Bello, U., Carlier, S., Colin, O., Fernandez, V., Gascon, F., Hoersch, B., Isola, C., Laberinti, P., Martimort, P., Meygret, A., Spoto, F., Sy, O., Marchese, F., and Bargellini, P., 2012. Sentinel-2: ESA's Optical High-Resolution Mission for GMES Operational Services. *Remote Sensing of Environment*, 120, 25–36.

Dunmire, D., Banwell, A.F., Wever, N., Lenaerts, J. and Datta, R.T., 2021. Contrasting regional variability of buried meltwater extent over 2 years across the Greenland Ice Sheet. *The Cryosphere*, 15(6), 2983-3005.

Dunmire, D., Lenaerts, J.T.M., Banwell, A.F., Wever, N., Shragge, J., Lhermitte, S., Drews, R., Pattyn, F., Hansen, J.S.S., Willis, I.C., Miller, J., and Keenan, E., 2020. Observations of Buried Lake Drainage on the Antarctic Ice Sheet. *Geophysical Research Letters*, 47 (15), e2020GL087970.

Dupont, T.K. and Alley, R.B., 2005. Assessment of the importance of ice-shelf buttressing to ice-sheet flow. *Geophysical Research Letters*, 32 (4).

Dwyer, J.L., Roy, D.P., Sauer, B., Jenkerson, C.B., Zhang, H.K., and Lymburner, L., 2018. Analysis Ready Data: Enabling Analysis of the Landsat Archive. *Remote Sensing*, 10 (9), 1363.

Echelmeyer, K., Clarke, T.S., and Harrison, W.D., 1991. Surficial glaciology of Jakobshavns Isbrae, West Greenland: part I. Surface morphology. *Journal of Glaciology*, 37 (127), 368–382.

Edwards, T.L., Nowicki, S., Marzeion, B., Hock, R., Goelzer, H., Seroussi, H., Jourdain, N.C., Slater, D.A., Turner, F.E., Smith, C.J., McKenna, C.M., Simon, E., Abe-Ouchi, A., Gregory, J.M., Larour, E., Lipscomb, W.H., Payne, A.J., Shepherd, A., Agosta, C., Alexander, P., Albrecht, T., Anderson, B., Asay-Davis, X., Aschwanden, A., Barthel, A., Bliss, A., Calov, R., Chambers, C., Champollion, N., Choi, Y., Cullather, R., Cuzzone, J., Dumas, C., Felikson, D., Fettweis, X., Fujita, K., Galton-Fenzi, B.K., Gladstone, R., Golledge, N.R., Greve, R., Hattermann, T., Hoffman, M.J., Humbert, A., Huss, M., Huybrechts, P., Immerzeel, W., Kleiner, T., Kraaijenbrink, P., Le clec'h, S., Lee, V., Leguy, G.R., Little, C.M., Lowry, D.P., Malles, J.-H., Martin, D.F., Maussion, F., Morlighem, M., O'Neill, J.F., Nias, I., Pattyn, F., Pelle, T., Price, S.F., Quiquet, A., Radić, V., Reese, R., Rounce, D.R., Rückamp, M., Sakai, A., Shafer, C., Schlegel, N.-J., Shannon, S., Smith, R.S., Straneo, F., Sun, S., Tarasov, L., Trusel, L.D., Van Breedam, J., van de Wal, R., van den Broeke, M., Winkelmann, R., Zekollari, H., Zhao, C., Zhang, T., and Zwinger, T., 2021. Projected

land ice contributions to twenty-first-century sea level rise. *Nature*, 593 (7857), 74–82.

El Naqa, I. and Murphy, M.J., 2015. What Is Machine Learning? In: *Machine Learning in Radiation Oncology*. Springer International Publishing, 3–11.

Elvidge, A.D., Kuipers Munneke, P., King, J.C., Renfrew, I.A., and Gilbert, E., 2020. Atmospheric Drivers of Melt on Larsen C Ice Shelf: Surface Energy Budget Regimes and the Impact of Foehn. *Journal of Geophysical Research: Atmospheres*, 125 (17).

Faddoul, J.B., Chidlovskii, B., Gilleron, R. and Torre, F., 2012, September. Learning multiple tasks with boosted decision trees. In *Joint European Conference on Machine Learning and Knowledge Discovery in Databases* (pp. 681-696). Springer, Berlin, Heidelberg.

Fair, Z., Flanner, M., Brunt, K.M., Fricker, H.A. and Gardner, A., 2020. Using ICESat-2 and Operation IceBridge altimetry for supraglacial lake depth retrievals. *The Cryosphere*, 14(11), 4253-4263.

Fitzpatrick, A.A.W., Hubbard, A.L., Box, J.E., Quincey, D.J., Van As, D.,

Mikkelsen, A.P.B., Doyle, S.H., Dow, C.F., Hasholt, B., and Jones, G.A., 2014. A decade (2002-2012) of supraglacial lake volume estimates across Russell Glacier, West Greenland. *The Cryosphere*, 8 (1), 107–121.

Fogt, R.L., Perlwitz, J., Monaghan, A.J., Bromwich, D.H., Jones, J.M., and Marshall, G.J., 2009. Historical SAM Variability. Part II: Twentieth-Century Variability and Trends from Reconstructions, Observations, and the IPCC AR4 Models. *Journal of Climate*, 22 (20), 5346–5365.

Frezzotti, M. 1993. Glaciological study in Terra Nova Bay, Antarctica, inferred from remote sensing analysis. *Annals of Glaciology*, 17, 63–71.

Fricker, H.A., Arndt, P., Brunt, K.M., Datta, R.T., Fair, Z., Jasinski, M.F., Kingslake, J., Magruder, L.A., Moussavi, M., Pope, A., Spergel, J.J., Stoll, J.D., and Wouters, B., 2021. ICESat-2 Meltwater Depth Estimates: Application to Surface Melt on Amery Ice Shelf, East Antarctica. *Geophysical research letters*, 48 (8), e2020GL090550.

Fürst, J.J., Durand, G., Gillet-Chaulet, F., Tavard, L., Rankl, M., Braun, M., and Gagliardini, O., 2016. The safety band of Antarctic ice shelves. *Nature Climate Change*, 6 (5), 479–482.

Gerrish, L., Fretwell, P., & Cooper, P., 2021. High resolution vector polylines of the Antarctic coastline (7.4) [Data set]. UK Polar Data Centre, Natural Environment Research Council, UK Research & Innovation. <https://doi.org/10.5285/e46be5bc-ef8e-4fd5-967b-92863fbe2835>

Ghimire, B., Rogan, J., Galiano, V.R., Panday, P. and Neeti, N., 2012. An evaluation of bagging, boosting, and random forests for land-cover classification in Cape Cod, Massachusetts, USA. *GIScience & Remote Sensing*, 49(5), 623-643.

Gilbert, E. and Kittel, C., 2021. Surface melt and runoff on Antarctic ice shelves at 1.5°C, 2°C and 4°C of future warming. *Geophysical Research Letters*, e2020GL091733.

Glasser, N.F. and Gudmundsson, G.H., 2012. Longitudinal surface structures (flowstripes) on Antarctic glaciers. *The Cryosphere*, 6 (2), 383–391.

Glasser, N.F. and Scambos, T.A., 2008. A structural glaciological analysis of the 2002 Larsen B ice-shelf collapse. *Journal of Glaciology*, 54 (184), 3–16.

Gudmundsson, G.H., Paolo, F.S., Adusumilli, S., and Fricker, H.A., 2019. Instantaneous Antarctic ice sheet mass loss driven by thinning ice shelves. *Geophysical Research Letters*, 46 (23), 13903–13909.

Haibo, Y., Zongmin, W., Hongling, Z. and Yu, G., 2011. Water body extraction methods study based on RS and GIS. *Procedia Environmental Sciences*, 10, pp.2619-2624.

Halberstadt, A.R.W., Gleason, C.J., Moussavi, M.S., Pope, A., Trusel, L.D., and DeConto, R.M., 2020. Antarctic supraglacial lake identification using landsat-8 image classification. *Remote Sensing*, 12 (8), 1–29.

Hall, D.K., Riggs, G.A., Salomonson, V.V., Barton, J.S., Casey, K., Chien, J.Y.L., DiGirolamo, N.E., Klein, A.G., Powell, H.W. and Tait, A.B., 2001. Algorithm theoretical basis document (ATBD) for the MODIS snow and sea ice-mapping algorithms. *Nasa Gsfc*, 45.

Hansen, M., Dubayah, R., and Defries, R., 1996. Classification trees: An alternative to traditional land cover classifiers. *International Journal of Remote Sensing*, 17 (5), 1075–1081.

Heilig, A., Eisen, O., MacFerrin, M., Tedesco, M. and Fettweis, X., 2018. Seasonal monitoring of melt and accumulation within the deep percolation zone of the Greenland Ice Sheet and comparison with simulations of regional climate modeling. *The Cryosphere*, 12(6), 1851-1866.

Hellmer, H.H., 2004. Impact of Antarctic ice shelf basal melting on sea ice and deep ocean properties. *Geophysical Research Letters*, 31 (10).

Hoffman, M.J., Catania, G.A., Neumann, T.A., Andrews, L.C., and Rumrill, J.A., 2011. Links between acceleration, melting, and supraglacial lake drainage of the western Greenland Ice Sheet. *Journal of Geophysical Research: Earth Surface*, 116 (4), F04035.

Hogg, A.E., Gilbert, L., Shepherd, A., Muir, A.S. and McMillan, M., 2020. Extending the record of Antarctic ice shelf thickness change, from 1992 to 2017. *Advances in Space Research*.

Holt, T. and Glasser, N., 2021, April. Decadal changes in south west Antarctic Peninsula Ice Shelves. In *EGU General Assembly Conference Abstracts* (pp. EGU21-2617).

Holt, T.O., Glasser, N.F., Fricker, H.A., Padman, L., Luckman, A., King, O., Quincey, D.J. and Siegfried, M.R., 2014. The structural and dynamic responses of Stange Ice Shelf to recent environmental change. *Antarctic Science*, 26(6), 646-660.

Holt, T.O., Glasser, N.F., Quincey, D.J., and Siegfried, M.R., 2013. Speedup and fracturing of George VI Ice Shelf, Antarctic Peninsula. *The Cryosphere*, 7 (3), 797–816.

Horwath, M., Dietrich, R., Baessler, M., Nixdorf, U., Steinhage, D., Fritzsche, D., Damm, V., and Reitmayr, G., 2006. Nivlisen, an Antarctic ice shelf in Dronning Maud Land: Geodetic-glaciological results from a combined analysis of ice thickness, ice surface height and ice-flow observations. *Journal of Glaciology*, 52 (176), 17–30.

Howat, I.M., Porter, C., Smith, B.E., Noh, M.J., and Morin, P., 2019. The reference elevation model of Antarctica. *The Cryosphere*, 13 (2), 665–674.

Hubbard, B., Luckman, A., Ashmore, D.W., Bevan, S., Kulesa, B., Kuipers Munneke, P., Philippe, M., Jansen, D., Booth, A., Sevestre, H., Tison, J.L., O’Leary, M., and Rutt, I., 2016. Massive subsurface ice formed by refreezing of ice-shelf melt ponds. *Nature Communications*, 7 (1), 1–6.

Hui, F., Ci, T., Cheng, X., Scambos, T.A., Liu, Y., Zhang, Y., Chi, Z., Huang, H., Wang, X., Wang, F., Zhao, C., Jin, Z., and Wang, K., 2014. Mapping blue-ice areas in Antarctica using ETM+ and MODIS data. *Annals of Glaciology*, 55 (66), 129–137.

IPCC, 2019: IPCC Special Report on the Ocean and Cryosphere in a Changing Climate [H.-O. Pörtner, D.C. Roberts, V. Masson-Delmotte, P. Zhai, M. Tignor, E. Poloczanska, K. Mintenbeck, A. Alegría, M. Nicolai, A. Okem, J. Petzold, B. Rama, N.M. Weyer (eds.)].

Jansen, D., Kulesa, B., Sammonds, P.R., Luckman, A., King, E.C., and Glasser, N.F., 2010. Present stability of the Larsen C ice shelf, Antarctic Peninsula. *Journal of Glaciology*, 56 (198), 593–600.

Joughin, I., Smith, B.E., and Medley, B., 2014. Marine ice sheet collapse potentially under way for the Thwaites glacier basin, West Antarctica. *Science*, 344 (6185), 735–738.

King, J.C., Kirchgaessner, A., Bevan, S., Elvidge, A.D., Kuipers Munneke, P., Luckman, A., Orr, A., Renfrew, I.A., and van den Broeke, M.R., 2017. The impact of föhn winds on surface energy balance during the 2010-2011 melt season over

Larsen C ice shelf, Antarctica. *Journal of Geophysical Research*, 122 (22), 12,062–12,076.

King, J.C., Turner, J., Marshall, G.J., Connolley, W.M., and Lachlan-Cope, T.A., 2003. Antarctic Peninsula Climate Variability and Its Causes as Revealed by Analysis of Instrumental Records. *American Geophysical Union (AGU)*, 17–30.

Kingslake, J., Ely, J.C., Das, I., and Bell, R.E., 2017. Widespread movement of meltwater onto and across Antarctic ice shelves. *Nature*, 544 (7650), 349–352.

Kingslake, J., Ng, F., and Sole, A., 2015. Modelling channelized surface drainage of supraglacial lakes. *Journal of Glaciology*.

Kirchgaessner, A., King, J.C., and Anderson, P.S., 2021. The impact of föhn conditions across the antarctic peninsula on local meteorology based on AWS measurements. *Journal of Geophysical Research*, 126 (4).

Kittel, C., Amory, C., Agosta, C., Jourdain, N.C., Hofer, S., Delhasse, A., Doutreloup, S., Huot, P.-V., Lang, C., Fichet, T., and Fettweis, X., 2021. Diverging future surface mass balance between the Antarctic ice shelves and grounded ice sheet. *The Cryosphere*, 15, 1215–1236.

Koziol, C., Arnold, N., Pope, A., and Colgan, W., 2017. Quantifying supraglacial meltwater pathways in the Paakitsoq region, West Greenland. *Journal of Glaciology*, 63 (239), 464–476.

Kuipers Munneke, P., Ligtenberg, S.R.M., Van Den Broeke, M.R., and Vaughan, D.G., 2014. Firn air depletion as a precursor of Antarctic ice-shelf collapse. *Journal of Glaciology*, 60 (220), 205–214.

Munneke, P.K., Luckman, A.J., Bevan, S.L., Smeets, C.J.P.P., Gilbert, E., Van den Broeke, M.R., Wang, W., Zender, C., Hubbard, B., Ashmore, D. and Orr, A., 2018. Intense winter surface melt on an Antarctic ice shelf. *Geophysical Research Letters*, 45(15), 7615-7623.

LaBarbera, C.H. and MacAyeal, D.R., 2011. Traveling supraglacial lakes on George VI Ice Shelf, Antarctica. *Geophysical Research Letters*, 38 (24).

Lai, C.Y., Kingslake, J., Wearing, M.G., Chen, P.H.C., Gentine, P., Li, H., Spergel, J.J., and van Wessem, J.M., 2020. Vulnerability of Antarctica's ice shelves to meltwater-driven fracture. *Nature*, 584 (7822), 574–578.

Langley, E.S., Leeson, A.A., Stokes, C.R., and Jamieson, S.S.R., 2016. Seasonal evolution of supraglacial lakes on an East Antarctic outlet glacier. *Geophysical Research Letters*, 43 (16), 8563–8571.

Le Brocq, A.M., Ross, N., Griggs, J.A., Bingham, R.G., Corr, H.F.J., Ferraccioli, F., Jenkins, A., Jordan, T.A., Payne, A.J., Rippin, D.M., and Siegert, M.J., 2013. Evidence from ice shelves for channelized meltwater flow beneath the Antarctic Ice Sheet. *Nature Geoscience*, 6 (11), 945–948.

Lee, D.Y., Petersen, M.R. and Lin, W., 2019. The southern annular mode and southern ocean surface westerly winds in E3SM. *Earth and Space Science*, 6(12), 2624-2643.

Leeson, A.A., Forster, E., Rice, A., Gourmelen, N., and van Wessem, J.M., 2020. Evolution of Supraglacial Lakes on the Larsen B Ice Shelf in the Decades Before it Collapsed. *Geophysical Research Letters*, 47 (4).

Leeson, A.A., Shepherd, A., Palmer, S., Sundal, A., and Fettweis, X., 2012. Simulating the growth of supraglacial lakes at the western margin of the Greenland ice sheet. *The Cryosphere*, 6 (5), 1077–1086.

Leeson, A.A., Van Wessem, J.M., Ligtenberg, S.R.M., Shepherd, A., Van den Broeke, M.R., Killick, R., Skvarca, P., Marinsek, S., and Colwell, S., 2017. Regional climate of the Larsen B embayment 1980–2014. *Journal of Glaciology*, 63 (240), 683–690.

Lefroy, N. and Arnold, N., 2020, May. Quantification of the Impact of Supraglacial Lakes and Slush on Surface Energy Balance of Ice Shelves. In *EGU General Assembly Conference Abstracts* (p. 20847).

Lenaerts, J., Lhermitte, S., Drews, R., Ligtenberg, S.R.M., Berger, S., Helm, V., Smeets, P.C.J.P., van den Broeke, M.R., van De Berg, W.J., van Meijgaard, E., Eijkelboom, M., Eisen, O., and Pattyn, F., 2017. Meltwater produced by wind – albedo interaction stored in an East Antarctic ice shelf. *Nature Climate Change*, 7, 58–63.

Liang, Y.-L., Colgan, W., Lv, Q., Steffen, K., Abdalati, W., Stroeve, J., Gallaher, D., and Bayou, N., 2012. A decadal investigation of supraglacial lakes in West Greenland using a fully automatic detection and tracking algorithm. *Remote Sensing of Environment*, 123, 127–138.

Liston, G.E. and Winther, J.G., 2005. Antarctic surface and subsurface snow and ice melt fluxes. *Journal of Climate*, 18 (10), 1469–1481.

Liston, G.E., Winther, J.G., Bruland, O., Elvehøy, H., and Sand, K., 1999. Below-surface ice melt on the coastal Antarctic ice sheet. *Journal of Glaciology*, 45 (150), 273–285.

Liu, H., Wang, L., and Jezek, K.C., 2006. Spatiotemporal variations of snowmelt in Antarctica derived from satellite scanning multichannel microwave radiometer and Special Sensor Microwave Imager data (1978-2004). *Journal of Geophysical Research: Earth Surface*, 111 (1), F01003.

Luckman, A., Elvidge, A., Jansen, D., Kulesa, B., Kuipers Munneke, P., King, J., and Barrand, N.E., 2014. Surface melt and ponding on Larsen C Ice Shelf and the impact of föhn winds. *Antarctic Science*, 26 (6), 625–635.

Lüthje, M., Pedersen, L.T., Reeh, N., and Greuell, W., 2006. Modelling the evolution of supraglacial lakes on the west Greenland ice-sheet margin. *Journal of Glaciology*, 52 (179), 608–618.

MacAyeal, D.R. and Sergienko, O. V., 2013. The flexural dynamics of melting ice shelves. *Annals of Glaciology*, 54 (63), 1–10.

MacAyeal, D.R., Banwell, A.F., Okal, E.A., Lin, J., Willis, I.C., Goodsell, B. and MacDonald, G.J., 2019. Diurnal seismicity cycle linked to subsurface melting on an ice shelf. *Annals of Glaciology*, 60(79), 137-157.

MacAyeal, D.R., Scambos, T.A., Hulbe, C.L. and Fahnestock, M.A., 2003. Catastrophic ice-shelf break-up by an ice-shelf-fragment-capsize mechanism. *Journal of Glaciology*, 49(164), 22-36.

MacAyeal, D.R., Sergienko, O.V., and Banwell, A.F., 2015. A model of viscoelastic ice-shelf flexure. *Journal of Glaciology*, 61 (228), 635–645.

Macdonald, G.J., Banwell, A.F. and MacAYEAL, D.R., 2018. Seasonal evolution of supraglacial lakes on a floating ice tongue, Petermann Glacier, Greenland. *Annals of Glaciology*, 59(76pt1), 56-65.

Macdonald, G.J., Banwell, A.F., Willis, I.A.N.C., Mayer, D.P., Goodsell, B., and MacAyeal, D.R., 2019. Formation of pedestalled, relict lakes on the McMurdo Ice Shelf, Antarctica. *Journal of Glaciology*, 65 (250), 337–343.

MacDonell, S., Fernandoy, F., Villar, P., and Hammann, A., 2021. Stratigraphic Analysis of Firn Cores from an Antarctic Ice Shelf Firn Aquifer. *WATER*, 13 (5), 731.

MacDonell, S., Valois, R., Fernandoy, F., Villar, P., Casassa, G., Hammann, A. and Marambio, M., 2020, May. Exploring firn aquifers on the Muller Ice Shelf, Antarctica. In *EGU General Assembly Conference Abstracts* (p. 11695).

MacFerrin, M., Machguth, H., van As, D., Charalampidis, C., Stevens, C.M., Heilig, A., Vandecrux, B., Langen, P.L., Mottram, R., Fettweis, X., van den Broeke, M.R., Pfeffer, W.T., Moussavi, M.S., and Abdalati, W., 2019. Rapid expansion of Greenland's low-permeability ice slabs. *Nature*, 573 (7774), 403–407.

MacGregor, J.A., Catania, G.A., Markowski, M.S., and Andrews, A.G., 2012. Widespread rifting and retreat of ice-shelf margins in the eastern Amundsen Sea Embayment between 1972 and 2011. *Journal of Glaciology*, 58 (209), 458–466.

Markham, B., Jenstrom, D., Sauer, B., Pszcolka, S., Dulski, V., Hair, J., McCorkel, J., Kvaran, G., Thome, K., Montanaro, M. and Pedelty, J., 2020, August. Landsat 9 Mission update and status. In *Earth Observing Systems XXV* (Vol. 11501, p. 1150100). International Society for Optics and Photonics.

Markham, B.L., Jenstrom, D., Masek, J.G., Dabney, P., Pedelty, J.A., Barsi, J.A. and Montanaro, M., 2016, September. Landsat 9: status and plans. In *Earth*

Observing Systems XXI (Vol. 9972, p. 99720G). International Society for Optics and Photonics.

Marshall, G.J., 2007. Half-century seasonal relationships between the Southern Annular mode and Antarctic temperatures. *International Journal of Climatology*, 27 (3), 373–383.

Marshall, G.J., Orr, A., van Lipzig, N.P.M., and King, J.C., 2006. The impact of a changing Southern Hemisphere Annular Mode on Antarctic Peninsula summer temperatures. *Journal of climate*, 19 (20), 5388–5404.

Maxwell, A.E., Warner, T.A., and Fang, F., 2018. Implementation of machine-learning classification in remote sensing: an applied review. *International Journal of Remote Sensing*, 39 (9), 2784–2817.

McGrath, D., Steffen, K., Rajaram, H., Scambos, T., Abdalati, W., and Rignot, E., 2012. Basal crevasses on the Larsen C Ice Shelf, Antarctica: Implications for meltwater ponding and hydrofracture. *Geophysical Research Letters*, 39 (16).

Melchior Van Wessem, J., Jan Van De Berg, W., Noël, B.P.Y., Van Meijgaard, E., Amory, C., Birnbaum, G., Jakobs, C.L., Krüger, K., Lenaerts, J.T.M., Lhermitte, S., Ligtenberg, S.R.M., Medley, B., Reijmer, C.H., Van Tricht, K., Trusel, L.D., Van Uft, L.H., Wouters, B., Wuite, J., and Van Den Broeke, M.R., 2018. Modelling the climate and surface mass balance of polar ice sheets using RACMO2 - Part 2: Antarctica (1979-2016). *The Cryosphere*, 12 (4), 1479–1498.

Miles, K.E., Willis, I.C., Benedek, C.L., Williamson, A.G., and Tedesco, M., 2017. Toward Monitoring Surface and Subsurface Lakes on the Greenland Ice Sheet Using Sentinel-1 SAR and Landsat-8 OLI Imagery. *Frontiers of Earth Science in China*, 5.

Montgomery, L., Miège, C., Miller, J., Scambos, T.A., Wallin, B., Miller, O., Solomon, D.K., Forster, R., and Koenig, L., 2020. Hydrologic Properties of a Highly Permeable Firn Aquifer in the Wilkins Ice Shelf, Antarctica. *Geophysical Research Letters*, 47 (22), e2020GL089552.

Morris, E.M. and Vaughan, D.G., 2003. Spatial and temporal variation of surface temperature on the Antarctic Peninsula and the limit of viability of ice shelves. *Antarctic Research Series*, 79(10.1029).

Mottram, R., Hansen, N., Kittel, C., van Wessem, J. M., Agosta, C., Amory, C., Boberg, F., van de Berg, W. J., Fettweis, X., Gossart, A., van Lipzig, N. P. M., van Meijgaard, E., Orr, A., Phillips, T., Webster, S., Simonsen, S. B., and Souverijns, N., 2021. What is the surface mass balance of Antarctica? An intercomparison of regional climate model estimates. *The Cryosphere*, 15, 3751–3784

Mouginot, J., Scheuchl, B., and Rignot., E., 2017. MEaSURES Antarctic Boundaries for IPY 2007-2009 from Satellite Radar, Version 2. NASA National Snow and Ice Data Center Distributed Active Archive Center.

Moussavi, M., Pope, A., Halberstadt, A.R.W., Trusel, L.D., Cioffi, L., and Abdalati, W., 2020. Antarctic Supraglacial Lake Detection Using Landsat 8 and Sentinel-2 Imagery: Towards Continental Generation of Lake Volumes. *Remote Sensing*, 12 (1), 134.

Moussavi, M.S., Abdalati, W., Pope, A., Scambos, T., Tedesco, M., MacFerrin, M., and Grigsby, S., 2016. Derivation and validation of supraglacial lake volumes on the Greenland Ice Sheet from high-resolution satellite imagery. *Remote Sensing of Environment*, 183, 294–303.

Orheim, O. and Lucchitta, B., 1990. Investigating climate change by digital analysis of blue ice extent on satellite images of Antarctica. *Annals of Glaciology*, 14, 211-215.

Pal, M. and Mather, P.M., 2003. An assessment of the effectiveness of decision tree methods for land cover classification. *Remote Sensing of Environment*, 86 (4), 554–565.

Pal, M., 2005. Random forest classifier for remote sensing classification. *International Journal of Remote Sensing*, 26(1), 217-222.

Paolo, F.S., Fricker, H.A., and Padman, L., 2015. Ice sheets. Volume loss from Antarctic ice shelves is accelerating. *Science*, 348 (6232), 327–331.

Philpot, W.D., 1989. Bathymetric mapping with passive multispectral imagery. *Applied Optics*, 28(8), 1569-1578.

Picard, G., Fily, M., and Gallee, H., 2007. Surface melting derived from microwave radiometers: a climatic indicator in Antarctica. *Annals of Glaciology*, 46, 29–34.

Pope, A., 2016. Reproducibly estimating and evaluating supraglacial lake depth with Landsat 8 and other multispectral sensors. *Earth and Space Science*, 3 (4), 176–188.

Pope, A., Scambos, T.A., Moussavi, M., Tedesco, M., Willis, M., Shean, D., and Grigsby, S., 2016. Estimating supraglacial lake depth in West Greenland using Landsat 8 and comparison with other multispectral methods. *The Cryosphere*, 10 (1), 15–27.

Pritchard, H.D., Ligtenberg, S.R.M., Fricker, H.A., Vaughan, D.G., Van Den Broeke, M.R., and Padman, L., 2012. Antarctic ice-sheet loss driven by basal melting of ice shelves. *Nature*, 484 (7395), 502–505.

Ray, S. and Turi, R.H., 1999, December. Determination of number of clusters in k-means clustering and application in colour image segmentation. In *Proceedings of the 4th international conference on advances in pattern recognition and digital techniques* (137-143). Rees, W.G., 2005. *Remote sensing of snow and ice*. CRC press.

Rees, W.G., 2012. *Physical Principles of Remote Sensing*. Cambridge University Press.

Reynolds, J. M. 1981. Lakes on George VI ice shelf, Antarctica. *Polar Record*, 20(128), 425–432.

Rignot, E., Casassa, G., Gogineni, P., Krabill, W., Rivera, A., & Thomas, R. 2004. Accelerated ice discharge from the Antarctic Peninsula following the collapse of Larsen B ice shelf. *Geophysical Research Letters*, 31(18), L18401.

Rignot, E., Jacobs, S., Mouginot, J., and Scheuchl, B., 2013. Ice-shelf melting around Antarctica. *Science*, 341 (6143), 266–270.

Rignot, E., Mouginot, J., Scheuchl, B., Van Den Broeke, M., Van Wessem, M.J., and Morlighem, M., 2019. Four decades of Antarctic ice sheet mass balance from 1979–2017. *Proceedings of the National Academy of Sciences of the United States of America*.

Robel, A.A. and Banwell, A.F., 2019. A Speed Limit on Ice Shelf Collapse Through Hydrofracture. *Geophysical research letters*, 46 (21), 12092–12100.

Rott, H. and Mätzler, C., 1987. Possibilities and Limits of Synthetic Aperture Radar for Snow and Glacier Surveying. *Annals of Glaciology*, 9, 195–199.

Roy, D.P., Wulder, M.A., Loveland, T.R., C.e., W., Allen, R.G., Anderson, M.C., Helder, D., Irons, J.R., Johnson, D.M., Kennedy, R., Scambos, T.A., Schaaf,

C.B., Schott, J.R., Sheng, Y., Vermote, E.F., Belward, A.S., Bindshadler, R., Cohen, W.B., Gao, F., Hipple, J.D., Hostert, P., Huntington, J., Justice, C.O., Kilic, A., Kovalskyy, V., Lee, Z.P., Lyburner, L., Masek, J.G., McCorkel, J., Shuai, Y., Trezza, R., Vogelmann, J., Wynne, R.H., and Zhu, Z., 2014. Landsat-8: Science and product vision for terrestrial global change research. *Remote Sensing of Environment*, 145, 154–172.

Rüping, S., 2001. Incremental learning with support vector machines. In: *Proceedings - IEEE International Conference on Data Mining, ICDM*. 641–642.

Scambos, T. A., Bohlander, J. A., Shuman, C. A., & Skvarca, P. 2004. Glacier acceleration and thinning after ice shelf collapse in the Larsen B embayment, Antarctica. *Geophysical Research Letters*, 31(18), L18402.

Scambos, T., Fricker, H.A., Liu, C.C., Bohlander, J., Fastook, J., Sargent, A., Massom, R. and Wu, A.M., 2009. Ice shelf disintegration by plate bending and hydrofracture: Satellite observations and model results of the 2008 Wilkins ice shelf break-ups. *Earth and Planetary Science Letters*, 280(1-4), 51-60.

Scambos, T., Hulbe, C., and Fahnestock, M., 2003. Climate-induced ice shelf disintegration in the Antarctic Peninsula. In: *Antarctica Peninsula climate variability: a historical and paleo-environmental perspective*. 79–92.

Scambos, T., Hulbe, C., Fahnestock, M., and Bohlander, J., 2000. The link between climate warming and break-up of ice shelves in the Antarctic Peninsula. *Journal of Glaciology*, 46 (154), 516–530.

Schaap, T., Roach, M.J., Peters, L.E., Cook, S., Kulesa, B., and Schoof, C., 2019. Englacial drainage structures in an East Antarctic outlet glacier. *Journal of Glaciology*, 66 (255), 166–174.

Selmes, N., Murray, T., and James, T.D., 2011. Fast draining lakes on the Greenland Ice Sheet. *Geophysical Research Letters*, 38 (15).

Selmes, N., Murray, T. and James, T.D., 2013. Characterizing supraglacial lake drainage and freezing on the Greenland Ice Sheet. *The Cryosphere Discussions*, 7(1), 475-505.

Sergienko, O. V., 2013. Glaciological twins: Basally controlled subglacial and supraglacial lakes. *Journal of Glaciology*, 59 (213), 3–8.

Shepherd, A., Ivins, E.R., Geruo, A., Barletta, V.R., Bentley, M.J., Bettadpur, S., Briggs, K.H., Bromwich, D.H., Forsberg, R., Galin, N., Horwath, M., Jacobs, S., Joughin, I., King, M.A., Lenaerts, J.T.M., Li, J., Ligtenberg, S.R.M., Luckman, A., Luthcke, S.B., McMillan, M., Meister, R., Milne, G., Mouginot, J., Muir, A., Nicolas, J.P., Paden, J., Payne, A.J., Pritchard, H., Rignot, E., Rott, H., Sørensen, L.S., Scambos, T.A., Scheuchl, B., Schrama, E.J.O., Smith, B., Sundal, A.V., Van Angelen, J.H., Van De Berg, W.J., Van Den Broeke, M.R., Vaughan, D.G., Velicogna, I., Wahr, J., Whitehouse, P.L., Wingham, D.J., Yi, D., Young, D., and Zwally, H.J., 2012. A reconciled estimate of ice-sheet mass balance. *Science*, 338 (6111), 1183–1189.

Shi, D. and Yang, X., 2016. An Assessment of Algorithmic Parameters Affecting Image Classification Accuracy by Random Forests. *Photogrammetric Engineering & Remote Sensing*, 82 (6), 407–417.

Siegert, M., Atkinson, A., Banwell, A., Brandon, M., Convey, P., Davies, B., Downie, R., Edwards, T., Hubbard, B., Marshall, G. and Rogelji, J., 2019. The Antarctic Peninsula under a 1.5 C global warming scenario. *Frontiers in Environmental Science*, 7, 102.

Smith, B., Fricker, H.A., Gardner, A.S., Medley, B., Nilsson, J., Paolo Nicholas Holschuh, F.S., Adusumilli, S., Brunt, K., Csatho, B., Harbeck, K., Markus, T., Neumann, T., Siegfried, M.R., and Jay Zwally, H., 2020. Pervasive ice sheet mass loss reflects competing ocean and atmosphere processes. *Science*, 368 (6496), 1239–1242.

Sneed, W.A. and Hamilton, G.S., 2007. Evolution of melt pond volume on the surface of the Greenland Ice Sheet. *Geophysical Research Letters*, 34 (3), L03501.

Sneed, W.A. and Hamilton, G.S., 2011. Validation of a method for determining the depth of glacial melt ponds using satellite imagery. *Annals of Glaciology*, 52 (59), 15–22.

Sommers, A.N., Rajaram, H., Weber, E.P., MacFerrin, M.J., Colgan, W.T., and Stevens, C.M., 2017. Inferring Firn Permeability from Pneumatic Testing: A Case Study on the Greenland Ice Sheet. *Frontiers of Earth Science in China*, 5, 20.

Stokes, C.R., Sanderson, J.E., Miles, B.W.J., Jamieson, S.S.R., and Leeson, A.A., 2019. Widespread distribution of supraglacial lakes around the margin of the East Antarctic Ice Sheet. *Scientific reports*, 9 (1).

Sun, S., Che, T., Wang, J., Li, H., Hao, X., Wang, Z., and Wang, J., 2015. Estimation and analysis of snow water equivalents based on C-band SAR data and field measurements. *Arctic, Antarctic, and Alpine Research*, 47 (2), 313–326.

Tedesco, M., 2015. *Remote Sensing of the Cryosphere*. John Wiley & Sons.

Tedesco, M., Lthje, M., Steffen, K., Steiner, N., Fettweis, X., Willis, I., Bayou, N., and Banwell, A., 2012. Measurement and modeling of ablation of the bottom of supraglacial lakes in western Greenland. *Geophysical Research Letters*, 39 (2).

Tedesco, M., Willis, I.C., Hoffman, M.J., Banwell, A.F., Alexander, P. and Arnold, N.S., 2013. Ice dynamic response to two modes of surface lake drainage on the Greenland ice sheet. *Environmental Research Letters*, 8(3), p.034007.

Thompson, D.W., Solomon, S., Kushner, P.J., England, M.H., Grise, K.M. and Karoly, D.J., 2011. Signatures of the Antarctic ozone hole in Southern Hemisphere surface climate change. *Nature Geoscience*, 4(11), 741-749.

Traganos, D., Poursanidis, D., Aggarwal, B., Chrysoulakis, N., and Reinartz, P., 2018. Estimating satellite-derived bathymetry (SDB) with the Google Earth Engine and sentinel-2. *Remote Sensing*, 10 (6), 859.

Trusel, L.D., Frey, K.E., and Das, S.B., 2012. Antarctic surface melting dynamics: Enhanced perspectives from radar scatterometer data. *Journal of Geophysical Research: Earth Surface*, 117 (2).

Trusel, L.D., Frey, K.E., Das, S.B., Karnauskas, K.B., Munneke, P.K., Van Meijgaard, E. and Van Den Broeke, M.R., 2015. Divergent trajectories of Antarctic surface melt under two twenty-first-century climate scenarios. *Nature Geoscience*, 8(12), 927-932.

Tsai, V.C. and Rice, J.R., 2010. A model for turbulent hydraulic fracture and application to crack propagation at glacier beds. *Journal of Geophysical Research*, 115 (F3).

Turner, J., Barrand, N.E., Bracegirdle, T.J., Convey, P., Hodgson, D.A., Jarvis, M., Jenkins, A., Marshall, G., Meredith, M.P., Roscoe, H., Shanklin, J., French, J., Goosse, H., Guglielmin, M., Gutt, J., Jacobs, S., Kennicutt, M.C., Masson-Delmotte, V., Mayewski, P., Navarro, F., Robinson, S., Scambos, T., Sparrow, M.,

Summerhayes, C., Speer, K., and Klepikov, A., 2014. Antarctic climate change and the environment: An update. *Polar Record*, 50 (3), 237–259.

Turner, J., Lachlan-Cope, T.A., Colwell, S., Marshall, G.J., and Connolley, W.M., 2006. Significant warming of the antarctic winter troposphere. *Science*, 311 (5769), 1914–1917.

Turner, J., Lu, H., White, I., King, J.C., Phillips, T., Hosking, J.S., Bracegirdle, T.J., Marshall, G.J., Mulvaney, R., and Deb, P., 2016. Absence of 21st century warming on Antarctic Peninsula consistent with natural variability. *Nature*, 535 (7612), 411–415.

Turton, J.V., Kirchgaessner, A., Ross, A.N., King, J.C., and Kuipers Munneke, P., 2020. The influence of föhn winds on annual and seasonal surface melt on the Larsen C Ice Shelf, Antarctica. *The Cryosphere*, 14 (11), 4165–4180.

U.S. Geological Survey, 2018, Landsat collections: U.S. Geological Survey Fact Sheet 2018–3049, 2 p., <https://doi.org/10.3133/fs20183049>.

van den Broeke, M., 2005. Strong surface melting preceded collapse of Antarctic Peninsula ice shelf. *Geophysical Research Letters*, 32 (12).

van der Veen, C.J., 2007. Fracture propagation as means of rapidly transferring surface meltwater to the base of glaciers. *Geophysical Research Letters*, 34(1).

van Wessem, J.M., Steger, C.R., Wever, N. and van den Broeke, M.R., 2021. An exploratory modelling study of perennial firn aquifers in the Antarctic Peninsula for the period 1979–2016. *The Cryosphere*, 15(2), 695-714.

Vieli, A., Payne, A.J., Du, Z., and Shepherd, A., 2006. Numerical modelling and data assimilation of the Larsen B ice shelf, Antarctic Peninsula. *Philosophical Transactions of the Royal Society A: Mathematical, Physical and Engineering Sciences*, 364 (1844), 1815–1839.

Vieli, A., Payne, A.J., Shepherd, A., and Du, Z., 2007. Causes of pre-collapse changes of the Larsen B ice shelf: Numerical modelling and assimilation of satellite observations. *Earth and Planetary Science Letters*, 259 (3-4), 297–306.

Wagner, A. C. 1972. Flooding of the Ice Shelf in George VI Sound. *British Antarctic Survey Bulletin*, 28, 71–74.

Walker, R.T., Parizek, B.R., Alley, R.B., Anandakrishnan, S., Riverman, K.L., and Christianson, K., 2013. Ice-shelf tidal flexure and subglacial pressure variations. *Earth and Planetary Science Letters*, 361, 422–428.

Walters, D., Boutle, I., Brooks, M., Melvin, T., Stratton, R., Vosper, S., Wells, H., Williams, K., Wood, N., Allen, T., Bushell, A., Copsey, D., Earnshaw, P., Edwards, J., Gross, M., Hardiman, S., Harris, C., Heming, J., Klingaman, N., Levine, R., Manners, J., Martin, G., Milton, S., Mittermaier, M., Morcrette, C., Riddick, T., Roberts, M., Sanchez, C., Selwood, P., Stirling, A., Smith, C., Suri, D., Tennant, W.,

Luigi Vidale, P., Wilkinson, J., Willett, M., Woolnough, S., and Xavier, P., 2017. The Met Office Unified Model Global Atmosphere 6.0/6.1 and JULES Global Land 6.0/6.1 configurations. *Geoscientific Model Development*, 10 (4), 1487–1520.

Wang, H., Ma, C. and Zhou, L., 2009, December. A brief review of machine learning and its application. In *2009 international conference on information engineering and computer science* (pp.1-4). IEEE.

Wellner, J., Scambos, T., Domack, E., Vernet, M., Leventer, A., Balco, G., Brachfeld, S., Cape, M., Huber, B., Ishman, S., McCormick, M., Mosley-Thompson, E., Pettit, E., Smith, C., Truffer, M., Van Dover, C., and Yoo, K.-C., 2019. The Larsen ice shelf system, Antarctica (LARISSA): Polar systems bound together, changing fast. *GSA today: a publication of the Geological Society of America*, 29 (8), 4–10.

Wiesenekker, J.M., Kuipers Munneke, P., Van den Broeke, M.R., and Smeets, C.J.P.P., 2018. A Multidecadal Analysis of Föhn Winds over Larsen C Ice Shelf from a Combination of Observations and Modeling. *Atmosphere*, 9 (5), 172.

Williamson, A.G., Arnold, N.S., Banwell, A.F., and Willis, I.C., 2017. A Fully Automated Supraglacial lake area and volume Tracking ('FAST') algorithm: Development and application using MODIS imagery of West Greenland. *Remote Sensing of Environment*, 196, 113–133.

Williamson, A.G., Banwell, A.F., Willis, I.C., and Arnold, N.S., 2018a. Dual-satellite (Sentinel-2 and Landsat 8) remote sensing of supraglacial lakes in Greenland. *The Cryosphere*, 12 (9), 3045–3065.

Williamson, A.G., Willis, I.C., Arnold, N.S., and Banwell, A.F., 2018b. Controls on rapid supraglacial lake drainage in West Greenland: an Exploratory Data Analysis approach. *Journal of Glaciology*, 1–19.

Willis, I., Haggard, E., Benedek, C.L., MacAyeal, D.R. and Banwell, A.F., 2017, December. Surface and Subsurface Meltwater Ponding and Refreezing on the Bach Ice Shelf, Antarctic Peninsula. In *AGU Fall Meeting Abstracts* (Vol. 2017, pp.C51B-0971).

Winther, J.-G.G., Elvehøy, H., Bøggild, C.E., Sand, K., and Liston, G., 1996. Melting, runoff and the formation of frozen lakes in a mixed snow and blue-ice field in Dronning Maud Land, Antarctica. *Journal of Glaciology*, 42 (141), 271–278.

Work, E.A. and Gilmer, D.S., 1976. Utilization of satellite data for inventorying prairie ponds and lakes. *Photogrammetric Engineering and Remote Sensing*, 42(5), 685-694

Wuite, J., Rott, H., Hetzenecker, M., Floricioiu, D., De Rydt, J., Gudmundsson, G.H., Nagler, T., and Kern, M., 2015. Evolution of surface velocities and ice discharge of Larsen B outlet glaciers from 1995 to 2013. *The Cryosphere*, 9 (3), 957–969.

Wulder, M.A., Loveland, T.R., Roy, D.P., Crawford, C.J., Masek, J.G.,

Woodcock, C.E., Allen, R.G., Anderson, M.C., Belward, A.S., Cohen, W.B., Dwyer,

J., Erb, A., Gao, F., Griffiths, P., Helder, D., Hermosilla, T., Hipple, J.D., Hostert, P.,

Hughes, M.J., Huntington, J., Johnson, D.M., Kennedy, R., Kilic, A., Li, Z., Lymburner, L., McCorkel, J., Pahlevan, N., Scambos, T.A., Schaaf, C., Schott, J.R., Sheng, Y., Storey, J., Vermote, E., Vogelmann, J., White, J.C., Wynne, R.H., and Zhu, Z., 2019. Current status of Landsat program, science, and applications. *Remote Sensing of Environment*, 225, 127–147.

Yang, K. and Smith, L.C., 2013. Supraglacial streams on the Greenland Ice Sheet delineated from combined spectral – shape information in high-resolution satellite imagery. *IEEE Geoscience and Remote Sensing Letters*, 10 (4), 801–805.

Yuan, J., Chi, Z., Cheng, X., Zhang, T., Li, T., and Chen, Z., 2020. Automatic Extraction of Supraglacial Lakes in Southwest Greenland during the 2014–2018 Melt Seasons Based on Convolutional Neural Network. *WATER*, 12 (3), 891.

Appendix A

Results I Supplementary Material

Supplementary Tables

Table A.1: A record of all images used in this study, showing the image ID, associated satellite, acquisition date, and image group number. The image group number indicates which group of images the image was mosaicked with.

Image ID	Satellite	Image Acquisition Date	Image Group
LC08_L1GT_165109_20161102_20170318_01_T2	Landsat 8	02/11/2016	1
LC08_L1GT_165110_20161102_20170318_01_T2	Landsat 8	02/11/2016	1
S2A_MSIL1C_20161111T074922_N0204_R106_T32DNG_20161111T074922	Sentinel-2	11/11/2016	2
S2A_MSIL1C_20161111T074922_N0204_R106_T32DNH_20161111T074922	Sentinel-2	11/11/2016	2
S2A_MSIL1C_20161111T074922_N0204_R106_T32DPG_20161111T074922	Sentinel-2	11/11/2016	2

S2A_MSIL1C_20161111T074922_N0204_R106_T32DPH_20161111T074922	Sentinel-2	11/11/2016	2
S2A_MSIL1C_20161114T075922_N0204_R006_T32DNG_20161114T075925	Sentinel-2	14/11/2016	3
S2A_MSIL1C_20161114T075922_N0204_R006_T32DNH_20161114T075925	Sentinel-2	14/11/2016	3
S2A_MSIL1C_20161114T075922_N0204_R006_T32DPG_20161114T075925	Sentinel-2	14/11/2016	3
S2A_MSIL1C_20161114T075922_N0204_R006_T32DPH_20161114T075925	Sentinel-2	14/11/2016	3
LC08_L1GT_165109_20161204_20170317_01_T2	Landsat 8	04/12/2016	4
LC08_L1GT_165110_20161204_20170317_01_T2	Landsat 8	04/12/2016	4
LC08_L1GT_166109_20161211_20170316_01_T2	Landsat 8	11/12/2016	5
LC08_L1GT_166110_20161211_20170316_01_T2	Landsat 8	11/12/2016	5
S2A_MSIL1C_20161217T080922_N0204_R049_T32DNG_20161217T080925	Sentinel-2	17/12/2016	6
S2A_MSIL1C_20161217T080922_N0204_R049_T32DNH_20161217T080925	Sentinel-2	17/12/2016	6
S2A_MSIL1C_20161217T080922_N0204_R049_T32DPG_20161217T080925	Sentinel-2	17/12/2016	6
S2A_MSIL1C_20161217T080922_N0204_R049_T32DPH_20161217T080925	Sentinel-2	17/12/2016	6
LC08_L1GT_166109_20161227_20170314_01_T2	Landsat 8	27/12/2016	7
LC08_L1GT_166110_20161227_20170314_01_T2	Landsat 8	27/12/2016	7
S2A_MSIL1C_20170126T080921_N0204_R049_T32DNG_20170126T080920	Sentinel-2	26/01/2017	8
S2A_MSIL1C_20170126T080921_N0204_R049_T32DNH_20170126T080920	Sentinel-2	26/01/2017	8
S2A_MSIL1C_20170126T080921_N0204_R049_T32DPG_20170126T080920	Sentinel-2	26/01/2017	8
S2A_MSIL1C_20170126T080921_N0204_R049_T32DPH_20170126T080920	Sentinel-2	26/01/2017	8
LC08_L1GT_166109_20170213_20170228_01_T2	Landsat 8	13/02/2017	9
LC08_L1GT_166110_20170213_20170228_01_T2	Landsat 8	13/02/2017	9

S2A_MSIL1C_20170225T080921_N0204_R049_T32DNG_20170225T080922	Sentinel-2	25/02/2017	10
S2A_MSIL1C_20170225T080921_N0204_R049_T32DNH_20170225T080922	Sentinel-2	25/02/2017	10
S2A_MSIL1C_20170225T080921_N0204_R049_T32DPG_20170225T080922	Sentinel-2	25/02/2017	10
S2A_MSIL1C_20170225T080921_N0204_R049_T32DPH_20170225T080922	Sentinel-2	25/02/2017	10
LC08_L1GT_167109_20170324_20170329_01_T2	Landsat 8	24/03/2017	11
LC08_L1GT_167110_20170324_20170329_01_T2	Landsat 8	24/03/2017	11
S1B_EW_GRDM_1SSH_20170126T193341_20170126T193445_004023_006F36_234 F	Sentinel-1	26/01/2017	N/A
SETSM_WV02_20160131_10300100502E9A00_103001005041DF00_seg1_2m_v1.0_ dem.tif	REMA	31/01/2016	N/A
51_34_8m (accessed at http://data.pgc.umn.edu/elev/dem/setsm/REMA/mosaic/v1.1/8m/)	REMA	N/A	REMA 8m mosaic
51_35_8m (accessed at http://data.pgc.umn.edu/elev/dem/setsm/REMA/mosaic/v1.1/8m/)	REMA	N/A	REMA 8m mosaic
52_34_8m (accessed at http://data.pgc.umn.edu/elev/dem/setsm/REMA/mosaic/v1.1/8m/)	REMA	N/A	REMA 8m mosaic

52_35_8m (accessed at

<http://data.pgc.umn.edu/elev/dem/setsm/REMA/mosaic/v1.1/8m/>)

REMA

N/A

REMA 8m
mosaic

Supplementary Movies

Movie A.1: GIF of all 11 RGB base images (<https://doi.org/10.5446/47526>, (Dell et al., 2020b))

Movie A.2: GIF of all 11 area matrices (<https://doi.org/10.5446/47524>, (Dell et al., 2020c))

Movie A.3: GIF of all 11 depth matrices (<https://doi.org/10.5446/47525>, (Dell et al., 2020d))

Supplementary Figures

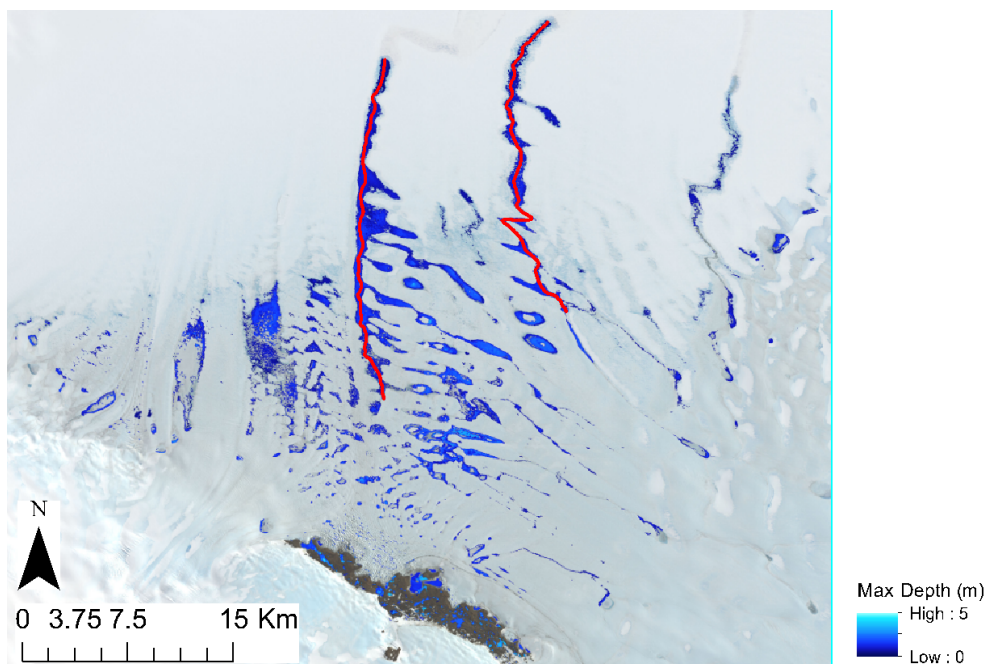


Figure A.1: The paths used for extracting the elevation profiles of the WS and ES (marked by the red lines), overlain on the maximum depth matrix. We used the maximum depth matrix to guide the digitisation of each path, following the deepest water where possible. The base satellite image for the figure was acquired by Landsat 8 on 13th February 2017.

Appendix B

Results II Supplementary Material

Supplementary Tables

Table B.1. Record of training and validation images .

Landsat Product ID	Acquisition Date	Sun Elevation	Cloud Cover	Study Site	Use
LC08_L1GT_218110_20200117_20200128_01_T2	17/01/2020	31.1	0.0	GVI	Training
LC08_L1GT_218111_20171226_20180103_01_T2	26/12/2017	33.0	15.7	GVI	Training
LC08_L1GT_128111_20181223_20181227_01_T2	23/12/2018	33.1	0.1	Amery	Training
LC08_L1GT_127110_20140204_20170426_01_T2	04/02/2014	26.5	0.0	Amery	Training
LC08_L1GT_112106_20200228_20200313_01_T2	28/02/2020	23.7	0.1	Shack	Training
LC08_L1GT_113106_20180112_20180119_01_T2	12/01/2018	36.6	0.5	Shack	Training
LC08_L1GT_063113_20140102_20170427_01_T2	02/01/2014	30.0	1.6	Nansen	Training
LC08_L1GT_063113_20170110_20170311_01_T2	10/01/2017	28.7	10.2	Nansen	Training

LC08_L1GT_062113_20141111_20170417_01_T2	11/11/2014	25.9	1.7	Nansen	Training
LC08_L1GT_061113_20161109_20170318_01_T2	09/11/2016	25.5	0.3	Nansen	Training
LC08_L1GT_166110_20161227_20170314_01_T2	27/12/2016	34.1	0.3	Nivlisen	Training
LC08_L1GT_165110_20180108_20180119_01_T2	08/01/2018	32.7	9.9	Nivlisen	Training
LC08_L1GT_154110_20180111_20180119_01_T2	11/01/2018	32.2	0.6	RoiB	Training
LC08_L1GT_154109_20140116_20170426_01_T2	16/01/2014	32.5	15.7	RoiB	Training
LC08_L1GT_219110_20160113_20170405_01_T2	13/01/2016	31.8	7.7	GVI	Validation
LC08_L1GT_127111_20190218_20190222_01_T2	18/02/2019	20.9	0.9	Amery	Validation
LC08_L1GT_112106_20170203_20170215_01_T2	03/02/2017	31.3	3.2	Shack	Validation
LC08_L1GT_061113_20141206_20170416_01_T2	06/12/2014	30.4	8.3	Nansen	Validation
LC08_L1GT_167110_20180207_20180221_01_T2	07/02/2018	25.5	1.4	Nivlisen	Validation
LC08_L1GT_154110_20150103_20170415_01_T2	03/01/2015	33.4	3.5	RoiB	Validation

Table B.2: A record of the data presented in Figure 5, detailing the scaled area of slush and ponded water for each 15-day period, the percentage of slush and ponded water relative to the total melt area for each 15-day period, and the AOI covered by each 15-day period.

	Scaled Slush Area (m²)	Scaled Ponded Water Area (m²)	Total Water Area (m²)	Slush (%)	Ponded Water (%)	AOI Coverage (%)
30-Nov-13	2.7E+07	1.7E+07	4.4E+07	60.6	39.4	99.5
15-Dec-13	1.1E+08	3.5E+07	1.4E+08	75.8	24.2	74.2
30-Dec-13	4.5E+07	3.6E+07	8.1E+07	55.8	44.2	35.9
29-Jan-14	2.0E+09	4.9E+08	2.5E+09	80.4	19.6	64.9
15-Nov-14	3.1E+07	2.3E+07	5.4E+07	57.4	42.6	53.6
30-Nov-14	3.4E+07	3.1E+07	6.5E+07	51.8	48.2	65.4
15-Dec-14	1.6E+08	6.2E+07	2.2E+08	72.0	28.0	64.5
30-Dec-14	1.2E+09	1.6E+08	1.4E+09	88.4	11.6	97.7
14-Jan-15	1.3E+09	6.8E+08	2.0E+09	65.6	34.4	56.4
29-Jan-15	7.8E+07	5.9E+07	1.4E+08	56.9	43.1	69.4
13-Feb-15	4.7E+08	5.4E+08	1.0E+09	46.5	53.5	83.0
15-Nov-15	3.5E+07	8.6E+07	1.2E+08	29.2	70.8	36.2
30-Nov-15	5.7E+07	4.7E+07	1.0E+08	54.7	45.3	94.4
15-Dec-15	8.9E+07	9.6E+06	9.8E+07	90.2	9.8	99.9
30-Dec-15	1.2E+08	3.2E+07	1.5E+08	78.1	21.9	85.7
14-Jan-16	1.7E+08	6.6E+07	2.4E+08	72.6	27.4	71.4

29-Jan-16	3.5E+09	9.6E+08	4.5E+09	78.7	21.3	36.8
13-Feb-16	1.1E+07	3.4E+07	4.5E+07	24.5	75.5	36.7
28-Feb-16	9.3E+07	3.0E+08	3.9E+08	23.7	76.3	37.4
15-Nov-16	1.6E+07	3.8E+06	2.0E+07	81.3	18.7	94.0
30-Nov-16	4.6E+07	3.2E+07	7.8E+07	59.2	40.8	94.8
15-Dec-16	7.7E+07	8.8E+06	8.6E+07	89.7	10.3	98.6
30-Dec-16	5.6E+08	5.1E+07	6.1E+08	91.6	8.4	88.8
14-Jan-17	2.1E+09	6.9E+08	2.8E+09	75.2	24.8	57.7
29-Jan-17	3.5E+08	4.9E+08	8.4E+08	41.8	58.2	76.2
13-Feb-17	3.1E+09	1.9E+09	5.0E+09	61.7	38.3	38.2
28-Feb-17	1.5E+09	1.5E+09	3.0E+09	50.6	49.4	71.8
15-Nov-17	1.2E+07	7.1E+07	8.3E+07	14.2	85.8	21.4
30-Nov-17	9.4E+07	1.1E+08	2.0E+08	46.8	53.2	32.4
15-Dec-17	7.2E+06	5.2E+06	1.2E+07	57.8	42.2	90.0
30-Dec-17	1.0E+09	6.8E+07	1.1E+09	93.8	6.2	94.3
14-Jan-18	1.5E+09	8.7E+08	2.4E+09	63.5	36.5	74.4
29-Jan-18	2.6E+08	1.7E+08	4.4E+08	60.1	39.9	33.5
13-Feb-18	6.9E+08	6.5E+08	1.3E+09	51.4	48.6	29.8
28-Feb-18	4.8E+08	8.0E+08	1.3E+09	37.3	62.7	32.1
15-Nov-18	2.1E+07	1.2E+07	3.3E+07	64.5	35.5	96.7
30-Nov-18	2.2E+08	2.0E+08	4.3E+08	52.1	47.9	42.0
15-Dec-18	1.1E+08	2.1E+07	1.3E+08	83.8	16.2	98.5
30-Dec-18	7.9E+07	3.3E+07	1.1E+08	70.8	29.2	72.1

29-Jan-19	5.7E+08	1.8E+08	7.5E+08	76.2	23.8	83.3
28-Feb-19	3.7E+08	2.9E+08	6.6E+08	56.2	43.8	66.2
15-Nov-19	1.4E+08	1.5E+08	2.9E+08	47.3	52.7	33.2
30-Nov-19	1.3E+08	4.9E+06	1.3E+08	96.3	3.7	89.1
15-Dec-19	2.7E+08	7.5E+07	3.4E+08	78.1	21.9	57.1
14-Jan-20	7.2E+08	2.2E+08	9.4E+08	76.4	23.6	71.1
29-Jan-20	1.1E+09	3.8E+08	1.5E+09	74.9	25.1	69.1
13-Feb-20	1.2E+09	5.9E+08	1.8E+09	66.7	33.3	60.1
28-Feb-20	1.6E+09	6.0E+08	2.2E+09	73.1	26.9	25.6

Appendix C

Results III Supplementary Material

Supplementary Tables

Table C.1: Data for all 15-day products that cover ≥ 20 % of the full area of Muller Ice Shelf. Columns record the end date for each 15-day product, scaled slush area, scaled ponded water area, scaled total melt area, percentage of the total area that is classified as slush, percentage of the total area that is classified as ponded water, and percentage coverage over the ice shelf area.

End Date	Scaled Slush Area (m²)	Scaled Ponded Water Area (m²)	Scaled Total Area (m²)	Slush (%)	Ponded Water (%)	AOI Coverage (%)
15/11/2013	7.2E+03	9.0E+02	8.1E+03	88.9	11.1	100
30/11/2013	5.4E+03	0.0E+00	5.4E+03	100.0	0.0	100
15/12/2013	1.6E+04	2.7E+03	1.9E+04	85.7	14.3	100
14/01/2014	3.6E+04	4.0E+04	7.6E+04	47.6	52.4	100
13/02/2014	4.0E+04	1.5E+04	5.5E+04	72.1	27.9	100
30/11/2014	1.7E+03	0.0E+00	1.7E+03	100.0	0.0	51.7
15/12/2014	2.7E+03	0.0E+00	2.7E+03	100.0	0.0	100
14/01/2015	7.7E+04	7.2E+03	8.4E+04	91.4	8.6	100
29/01/2015	1.1E+05	1.9E+04	1.3E+05	85.5	14.5	100
13/02/2015	3.4E+04	2.0E+04	5.4E+04	63.3	36.7	100
30/12/2015	1.5E+04	0.0E+00	1.5E+04	100.0	0.0	100
14/01/2016	4.5E+04	0.0E+00	4.5E+04	100.0	0.0	96.3
29/01/2016	0.0E+00	0.0E+00	0.0E+00	0.0	0.0	100

13/02/2016	4.1E+04	1.4E+04	5.5E+04	73.8	26.2	100
15/11/2016	7.2E+03	0.0E+00	7.2E+03	100.0	0.0	100
30/11/2016	1.4E+04	0.0E+00	1.4E+04	100.0	0.0	100
15/12/2016	4.5E+03	0.0E+00	4.5E+03	100.0	0.0	100
30/12/2016	7.7E+04	0.0E+00	7.7E+04	100.0	0.0	100
14/01/2017	4.5E+04	3.6E+03	4.9E+04	92.6	7.4	100
29/01/2017	7.3E+04	2.7E+03	7.6E+04	96.4	3.6	100
28/02/2017	3.2E+04	1.9E+04	5.0E+04	62.5	37.5	100
15/03/2017	8.5E+04	1.3E+05	2.1E+05	39.7	60.3	100
30/12/2017	3.8E+04	6.3E+03	4.4E+04	85.7	14.3	100
13/02/2018	1.2E+05	4.2E+04	1.6E+05	74.0	26.0	100
28/02/2018	8.4E+04	6.3E+04	1.5E+05	57.1	42.9	100
15/11/2018	1.4E+04	1.9E+04	3.3E+04	43.2	56.8	100
14/01/2019	7.9E+04	3.8E+04	1.2E+05	67.7	32.3	100
30/11/2019	1.1E+04	5.4E+03	1.6E+04	66.7	33.3	100
15/12/2019	1.1E+05	1.9E+04	1.3E+05	85.6	14.4	100
30/12/2019	9.8E+04	4.5E+03	1.0E+05	95.6	4.4	100
29/01/2020	3.7E+04	6.9E+03	4.4E+04	84.4	15.6	91.2
28/02/2020	1.9E+04	2.6E+05	2.8E+05	6.8	93.2	88.9
15/12/2020	0.0E+00	0.0E+00	0.0E+00	0.0	0.0	20.4
30/12/2020	2.4E+04	2.7E+03	2.7E+04	90.0	10.0	100
14/01/2021	5.5E+04	1.4E+04	6.9E+04	79.2	20.8	100
29/01/2021	5.8E+04	1.4E+04	7.1E+04	81.0	19.0	100

Table C.2: Data for all 15-day products that cover $\geq 20\%$ of the full area of Wilkins Ice Shelf. Columns record the end date for each 15-day product, scaled slush area, scaled ponded water area, scaled total melt area, percentage of the total area that is classified as slush, percentage of the total area that is classified as ponded water, and percentage coverage over the ice shelf area.

End Date	Scaled Slush Area (m²)	Scaled Ponded	Scaled Total Area (m²)	Slush (%)	Ponded Water (%)	AOI Coverage (%)
-----------------	--	----------------------	--	------------------	-------------------------	-------------------------

Water Area (m²)						
15/11/2013	1.5E+06	2.7E+06	4.2E+06	34.6	65.4	41.3
30/11/2013	7.3E+05	1.0E+06	1.8E+06	41.4	58.6	98.3
15/12/2013	2.3E+06	1.2E+06	3.5E+06	66.2	33.8	70.5
30/12/2013	2.1E+06	2.2E+06	4.3E+06	49.3	50.7	44.0
14/01/2014	6.0E+06	4.3E+06	1.0E+07	58.2	41.8	40.5
29/01/2014	6.2E+06	1.7E+06	7.8E+06	78.5	21.5	55.7
13/02/2014	1.7E+07	4.6E+07	6.3E+07	27.2	72.8	22.4
28/02/2014	5.0E+05	1.7E+07	1.7E+07	2.9	97.1	30.2
15/11/2014	8.2E+05	1.6E+06	2.4E+06	34.5	65.5	63.0
30/11/2014	5.8E+05	2.9E+05	8.7E+05	66.7	33.3	99.3
30/12/2014	1.4E+06	4.7E+05	1.9E+06	75.3	24.7	93.8
14/01/2015	1.0E+07	4.7E+06	1.5E+07	68.6	31.4	45.7
29/01/2015	4.1E+06	9.6E+05	5.1E+06	81.0	19.0	57.9
13/02/2015	2.0E+07	1.3E+07	3.3E+07	59.5	40.5	50.1
28/02/2015	3.3E+07	8.7E+07	1.2E+08	27.7	72.3	40.7
15/11/2015	2.4E+05	5.5E+05	7.9E+05	30.0	70.0	89.5
15/12/2015	7.8E+05	3.5E+05	1.1E+06	68.9	31.1	51.9
30/12/2015	2.7E+06	7.2E+05	3.4E+06	78.9	21.1	46.0
14/01/2016	2.5E+06	8.1E+05	3.3E+06	75.5	24.5	98.6
28/02/2016	1.5E+06	2.2E+06	3.7E+06	41.0	59.0	82.9
15/11/2016	1.3E+06	1.7E+06	3.0E+06	42.2	57.8	96.6
30/11/2016	2.9E+06	1.5E+06	4.4E+06	65.7	34.3	63.9
14/01/2017	6.9E+06	1.3E+06	8.2E+06	84.1	15.9	55.7
29/01/2017	2.4E+07	1.4E+07	3.8E+07	63.6	36.4	88.7
13/02/2017	2.0E+07	2.0E+07	3.9E+07	49.9	50.1	50.2
28/02/2017	1.1E+07	1.1E+07	2.3E+07	49.8	50.2	46.2
15/12/2017	2.1E+06	1.2E+06	3.3E+06	64.5	35.5	25.2
30/12/2017	4.8E+06	9.7E+05	5.8E+06	83.2	16.8	99.0
14/01/2018	2.7E+07	2.0E+07	4.7E+07	58.4	41.6	77.3
13/02/2018	6.1E+07	9.7E+07	1.6E+08	38.7	61.3	31.7

28/02/2018	1.2E+07	1.3E+07	2.5E+07	47.6	52.4	37.1
30/11/2018	2.6E+06	2.5E+06	5.0E+06	51.1	48.9	35.6
15/12/2018	1.1E+06	5.6E+05	1.6E+06	65.7	34.3	45.1
30/12/2018	6.2E+06	1.4E+06	7.6E+06	81.4	18.6	99.0
14/01/2019	2.2E+07	1.9E+06	2.4E+07	92.1	7.9	27.4
29/01/2019	2.3E+07	1.7E+07	4.0E+07	58.2	41.8	54.1
13/02/2019	2.7E+06	2.5E+06	5.2E+06	52.4	47.6	52.9
28/02/2019	2.7E+06	1.5E+07	1.8E+07	15.2	84.8	75.9
15/11/2019	1.2E+06	4.1E+06	5.3E+06	22.6	77.4	68.5
30/12/2019	9.0E+06	2.7E+06	1.2E+07	76.8	23.2	20.8
29/01/2020	5.8E+07	4.4E+07	1.0E+08	56.9	43.1	46.4
13/02/2020	7.1E+07	9.1E+07	1.6E+08	43.8	56.2	28.0
28/02/2020	1.6E+07	1.5E+07	3.1E+07	50.5	49.5	48.7
15/11/2020	5.8E+05	1.6E+06	2.2E+06	26.1	73.9	94.7
30/12/2020	1.6E+06	1.4E+06	3.0E+06	52.5	47.5	40.9
14/01/2021	5.2E+06	2.1E+06	7.3E+06	70.6	29.4	74.4
29/01/2021	2.5E+07	2.5E+07	5.1E+07	50.2	49.8	77.3

Table C.3: Data for all 15-day products that cover $\geq 20\%$ of the full area of Bach Ice Shelf. Columns record the end date for each 15-day product, scaled slush area, scaled ponded water area, scaled total melt area, percentage of the total area that is classified as slush, percentage of the total area that is classified as ponded water, and percentage coverage over the ice shelf area.

End Date	Scaled			Ponded Slush (%)	Ponded Water (%)	AOI Coverage (%)
	Scaled Slush Area (m ²)	Scaled Ponded Water Area (m ²)	Total Area (m ²)			
15/11/2013	1.0E+06	5.7E+06	6.7E+06	15.0	85.0	79.1
30/11/2013	6.9E+05	2.4E+05	9.3E+05	74.6	25.4	98.3
15/12/2013	1.8E+06	1.5E+06	3.3E+06	55.4	44.6	76.5
30/12/2013	9.7E+05	4.5E+05	1.4E+06	68.5	31.5	98.6

14/01/2014	1.6E+06	6.7E+05	2.3E+06	70.8	29.2	50.0
13/02/2014	1.1E+06	1.2E+06	2.4E+06	47.8	52.2	99.4
15/11/2014	3.1E+05	1.3E+06	1.6E+06	19.2	80.8	29.8
30/11/2014	2.9E+05	4.8E+05	7.7E+05	37.2	62.8	99.6
15/12/2014	4.0E+05	1.8E+05	5.8E+05	68.2	31.8	81.5
30/12/2014	4.8E+05	3.5E+05	8.3E+05	57.9	42.1	99.9
14/01/2015	1.9E+06	4.4E+05	2.4E+06	81.5	18.5	33.7
13/02/2015	3.8E+06	3.1E+06	6.8E+06	55.2	44.8	82.2
15/11/2015	3.0E+05	4.7E+05	7.6E+05	38.7	61.3	78.8
15/12/2015	5.6E+05	3.4E+05	9.0E+05	62.1	37.9	99.0
30/12/2015	2.6E+06	1.6E+06	4.2E+06	62.3	37.7	87.4
14/01/2016	2.6E+06	2.3E+06	4.9E+06	53.7	46.3	29.9
28/02/2016	1.2E+06	9.4E+06	1.1E+07	11.2	88.8	57.6
15/11/2016	1.6E+06	2.0E+06	3.6E+06	44.7	55.3	97.8
14/01/2017	1.3E+07	1.3E+07	2.6E+07	51.7	48.3	24.8
29/01/2017	1.4E+07	1.6E+07	3.0E+07	47.1	52.9	46.1
28/02/2017	5.7E+06	3.4E+07	4.0E+07	14.3	85.7	29.9
15/11/2017	1.3E+05	8.2E+04	2.1E+05	61.2	38.8	59.3
15/12/2017	9.9E+06	2.6E+06	1.3E+07	79.1	20.9	40.5
30/12/2017	2.3E+07	1.3E+07	3.7E+07	63.5	36.5	98.6
14/01/2018	1.7E+07	2.1E+07	3.8E+07	45.5	54.5	23.1
29/01/2018	8.0E+07	8.0E+07	1.6E+08	49.9	50.1	41.7
13/02/2018	6.9E+06	1.1E+07	1.7E+07	39.5	60.5	61.8
28/02/2018	7.2E+06	1.3E+07	2.0E+07	35.6	64.4	22.8
15/11/2018	8.3E+05	2.6E+06	3.4E+06	24.3	75.7	33.4
30/11/2018	7.6E+05	1.9E+06	2.6E+06	29.2	70.8	91.2
15/12/2018	8.4E+05	2.1E+06	3.0E+06	28.5	71.5	91.2
30/12/2018	3.0E+06	2.7E+06	5.8E+06	52.8	47.2	99.5
14/01/2019	2.4E+06	1.5E+06	3.9E+06	61.9	38.1	98.0
13/02/2019	2.8E+06	9.7E+06	1.3E+07	22.5	77.5	85.0
28/02/2019	1.2E+06	4.9E+07	5.0E+07	2.3	97.7	61.5
15/11/2019	3.8E+05	1.2E+06	1.6E+06	24.7	75.3	87.5

15/12/2019	1.8E+06	1.2E+06	3.0E+06	60.0	40.0	99.2
30/12/2019	3.6E+06	8.6E+05	4.4E+06	80.6	19.4	25.4
29/01/2020	4.3E+07	6.3E+07	1.1E+08	40.6	59.4	90.9
15/11/2020	8.4E+05	3.0E+05	1.1E+06	73.4	26.6	74.3
15/12/2020	6.0E+05	6.1E+05	1.2E+06	49.4	50.6	31.6
30/12/2020	7.0E+06	5.5E+06	1.3E+07	55.8	44.2	20.4
14/01/2021	1.1E+07	1.7E+07	2.8E+07	38.6	61.4	33.5

Table C.4: Data for all 15-day products that cover $\geq 20\%$ of the full area of north George VI Ice Shelf. Columns record the end date for each 15-day product, scaled slush area, scaled ponded water area, scaled total melt area, percentage of the total area that is classified as slush, percentage of the total area that is classified as ponded water, and percentage coverage over the ice shelf area.

End Date	Scaled Slush Area (m²)	Scaled Ponded Water Area (m²)	Scaled Total Area (m²)	Slush (%)	Ponded Water (%)	AOI Coverage (%)
15/11/2013	8.5E+06	5.0E+07	5.8E+07	14.5	85.5	36.4
30/11/2013	7.3E+06	4.6E+06	1.2E+07	61.2	38.8	83.1
15/12/2013	1.6E+07	1.5E+07	3.1E+07	51.4	48.6	30.9
30/12/2013	1.1E+07	1.3E+07	2.4E+07	46.0	54.0	75.9
14/01/2014	2.4E+07	1.1E+07	3.5E+07	67.9	32.1	80.1
29/01/2014	3.4E+07	4.6E+07	8.0E+07	42.4	57.6	34.2
13/02/2014	1.5E+07	4.3E+07	5.8E+07	25.8	74.2	99.1
28/02/2014	6.6E+06	1.7E+08	1.8E+08	3.8	96.2	28.7
15/11/2014	2.3E+06	4.6E+06	7.0E+06	33.5	66.5	64.3
30/11/2014	6.6E+06	3.8E+06	1.0E+07	63.5	36.5	99.7
15/12/2014	7.9E+06	4.1E+06	1.2E+07	65.8	34.2	72.3
30/12/2014	2.8E+07	1.1E+07	3.9E+07	72.7	27.3	99.6
14/01/2015	3.1E+07	2.0E+07	5.1E+07	61.4	38.6	53.4
29/01/2015	5.6E+07	8.7E+07	1.4E+08	39.1	60.9	28.2

13/02/2015	4.3E+07	5.4E+07	9.7E+07	44.5	55.5	67.0
28/02/2015	1.0E+07	2.8E+07	3.8E+07	26.7	73.3	48.8
15/11/2015	3.0E+06	1.1E+07	1.4E+07	21.3	78.7	37.4
30/11/2015	2.5E+06	2.7E+06	5.1E+06	47.9	52.1	21.2
15/12/2015	1.4E+07	9.3E+06	2.3E+07	60.1	39.9	68.4
30/12/2015	2.5E+07	1.8E+07	4.3E+07	58.8	41.2	33.5
14/01/2016	5.3E+07	5.4E+07	1.1E+08	49.8	50.2	40.1
29/01/2016	1.0E+07	1.0E+07	2.1E+07	50.6	49.4	41.2
28/02/2016	3.2E+07	9.2E+07	1.2E+08	25.9	74.1	30.6
15/11/2016	4.7E+06	4.0E+06	8.8E+06	53.9	46.1	99.7
30/11/2016	2.9E+07	2.4E+07	5.3E+07	54.4	45.6	22.2
30/12/2016	3.6E+07	1.8E+07	5.4E+07	66.9	33.1	94.1
14/01/2017	3.7E+07	2.1E+07	5.9E+07	64.0	36.0	92.0
29/01/2017	6.8E+07	1.3E+08	2.0E+08	34.5	65.5	86.3
28/02/2017	9.4E+07	1.9E+08	2.9E+08	32.9	67.1	44.9
15/11/2017	1.7E+06	3.1E+06	4.8E+06	34.9	65.1	60.0
30/11/2017	8.8E+06	7.9E+06	1.7E+07	52.8	47.2	23.1
30/12/2017	1.3E+08	1.0E+08	2.3E+08	55.7	44.3	98.9
14/01/2018	1.6E+08	2.0E+08	3.5E+08	44.6	55.4	74.0
13/02/2018	2.7E+08	5.8E+08	8.4E+08	31.6	68.4	47.9
28/02/2018	9.2E+07	1.6E+08	2.5E+08	37.0	63.0	49.1
15/11/2018	1.1E+07	7.3E+07	8.5E+07	13.5	86.5	51.2
30/11/2018	6.0E+06	4.2E+06	1.0E+07	59.1	40.9	93.3
30/12/2018	2.0E+07	1.4E+07	3.4E+07	59.3	40.7	36.2
14/01/2019	2.7E+07	3.1E+07	5.8E+07	47.3	52.7	24.2
29/01/2019	6.7E+07	3.4E+07	1.0E+08	66.6	33.4	71.7
13/02/2019	5.8E+07	5.6E+07	1.1E+08	50.7	49.3	76.8
28/02/2019	4.3E+07	1.5E+08	1.9E+08	22.2	77.8	76.9
15/11/2019	5.3E+06	2.8E+06	8.1E+06	65.4	34.6	98.8
15/12/2019	1.6E+07	1.0E+07	2.6E+07	60.8	39.2	40.5
30/12/2019	7.6E+07	6.5E+07	1.4E+08	53.8	46.2	78.8
29/01/2020	3.0E+08	6.2E+08	9.2E+08	33.0	67.0	98.1

30/11/2020	2.9E+06	1.6E+06	4.6E+06	64.4	35.6	75.2
15/12/2020	9.6E+06	1.2E+07	2.2E+07	44.2	55.8	72.7
30/12/2020	4.7E+07	4.7E+07	9.4E+07	49.8	50.2	30.4
29/01/2021	2.6E+08	6.1E+08	8.7E+08	29.6	70.4	51.7
13/02/2021	1.2E+07	1.5E+07	2.7E+07	44.6	55.4	32.0

Table C.5: Data for all 15-day products that cover $\geq 20\%$ of the full area of south George VI Ice Shelf. Columns record the end date for each 15-day product, scaled slush area, scaled ponded water area, scaled total melt area, percentage of the total area that is classified as slush, percentage of the total area that is classified as ponded water, and percentage coverage over the ice shelf area.

End Date	Scaled Slush Area (m²)	Scaled Ponded Water Area (m²)	Scaled Total Area (m²)	Slush (%)	Ponded Water (%)	AOI Coverage (%)
15/11/2013	1.8E+06	2.9E+06	4.8E+06	38.1	61.9	86.1
30/11/2013	1.0E+07	2.4E+07	3.4E+07	29.1	70.9	98.4
15/12/2013	5.4E+06	8.7E+06	1.4E+07	38.5	61.5	30.1
30/12/2013	1.2E+07	1.1E+07	2.4E+07	51.9	48.1	96.8
14/01/2014	1.5E+07	1.1E+07	2.6E+07	56.4	43.6	60.2
29/01/2014	3.9E+07	6.7E+07	1.1E+08	36.9	63.1	57.4
13/02/2014	8.8E+06	2.7E+07	3.6E+07	24.6	75.4	98.3
28/02/2014	4.8E+06	5.7E+07	6.1E+07	7.9	92.1	30.8
15/11/2014	1.1E+06	2.8E+06	3.9E+06	28.2	71.8	73.1
30/11/2014	6.0E+06	8.7E+06	1.5E+07	40.9	59.1	99.9
15/12/2014	4.3E+06	4.6E+06	8.9E+06	47.9	52.1	76.2
30/12/2014	4.3E+07	3.3E+07	7.7E+07	56.3	43.7	99.3
14/01/2015	1.9E+07	1.4E+07	3.3E+07	58.4	41.6	78.0
13/02/2015	6.7E+07	9.8E+07	1.7E+08	40.7	59.3	32.9
15/11/2015	1.0E+07	6.0E+07	7.1E+07	14.8	85.2	52.0
15/12/2015	8.1E+06	8.6E+06	1.7E+07	48.4	51.6	46.7
14/01/2016	2.6E+07	1.7E+07	4.3E+07	60.9	39.1	86.4

29/01/2016	2.4E+07	3.6E+07	6.0E+07	40.5	59.5	24.3
13/02/2016	1.3E+07	6.9E+07	8.3E+07	16.1	83.9	43.7
15/11/2016	7.4E+06	2.7E+07	3.4E+07	21.6	78.4	99.5
30/11/2016	2.9E+07	2.7E+07	5.6E+07	51.2	48.8	64.2
15/12/2016	4.5E+07	3.1E+07	7.6E+07	59.5	40.5	41.1
30/12/2016	2.3E+07	1.3E+07	3.6E+07	63.9	36.1	84.4
14/01/2017	3.1E+07	2.9E+07	6.0E+07	51.6	48.4	90.3
29/01/2017	7.1E+07	8.6E+07	1.6E+08	45.2	54.8	93.1
13/02/2017	7.6E+07	1.2E+08	2.0E+08	38.2	61.8	57.3
15/11/2017	2.8E+06	9.2E+06	1.2E+07	23.0	77.0	73.5
30/11/2017	3.7E+06	5.7E+06	9.3E+06	39.3	60.7	60.8
15/12/2017	3.6E+07	4.2E+07	7.7E+07	46.1	53.9	31.2
30/12/2017	6.8E+07	3.1E+07	9.9E+07	68.6	31.4	96.9
14/01/2018	5.7E+07	2.7E+07	8.4E+07	68.2	31.8	79.8
29/01/2018	1.1E+07	1.6E+07	2.7E+07	41.6	58.4	42.8
13/02/2018	1.1E+08	2.7E+08	3.8E+08	28.9	71.1	53.7
28/02/2018	3.9E+07	7.6E+07	1.2E+08	33.6	66.4	59.4
15/11/2018	7.4E+06	2.5E+07	3.2E+07	23.0	77.0	52.9
30/11/2018	6.1E+06	8.0E+06	1.4E+07	43.4	56.6	98.8
15/12/2018	1.4E+07	1.8E+07	3.1E+07	43.9	56.1	85.2
30/12/2018	4.0E+07	2.7E+07	6.7E+07	60.3	39.7	84.4
14/01/2019	2.0E+07	2.0E+07	4.0E+07	50.1	49.9	92.2
29/01/2019	4.0E+07	3.0E+07	7.0E+07	57.0	43.0	92.1
13/02/2019	2.2E+07	2.7E+07	4.9E+07	44.7	55.3	64.7
28/02/2019	9.1E+06	3.5E+07	4.4E+07	20.8	79.2	74.5
15/11/2019	2.9E+06	5.8E+06	8.7E+06	33.7	66.3	98.7
30/11/2019	5.8E+06	1.1E+07	1.7E+07	35.2	64.8	22.2
15/12/2019	2.8E+07	1.9E+07	4.7E+07	59.9	40.1	70.3
30/12/2019	3.9E+07	2.0E+07	5.9E+07	66.3	33.7	93.7
29/01/2020	4.6E+07	3.2E+07	7.8E+07	59.2	40.8	88.3
30/11/2020	3.7E+06	5.4E+06	9.1E+06	41.0	59.0	60.6
15/12/2020	5.6E+06	5.7E+06	1.1E+07	49.8	50.2	97.0

30/12/2020	1.2E+07	6.8E+06	1.9E+07	63.7	36.3	70.9
14/01/2021	4.8E+07	3.6E+07	8.4E+07	57.0	43.0	79.5
29/01/2021	5.8E+07	2.1E+07	7.9E+07	73.7	26.3	49.7
13/02/2021	2.9E+06	3.1E+06	6.0E+06	48.4	51.6	44.0

Table C.6: Data for all 15-day products that cover ≥ 20 % of the full area of Stange Ice Shelf. Columns record the end date for each 15-day product, scaled slush area, scaled ponded water area, scaled total melt area, percentage of the total area that is classified as slush, percentage of the total area that is classified as ponded water, and percentage coverage over the ice shelf area.

End Date	Scaled Slush Area (m²)	Scaled Ponded Water Area (m²)	Scaled Total Area (m²)	Slush (%)	Ponded Water (%)	AOI Coverage (%)
15/11/2013	7.6E+05	1.7E+06	2.4E+06	31.3	68.7	73.9
30/11/2013	2.5E+06	2.2E+06	4.7E+06	53.1	46.9	100.0
15/12/2013	3.7E+06	3.2E+06	6.9E+06	53.4	46.6	97.3
30/12/2013	6.5E+06	8.2E+06	1.5E+07	44.3	55.7	94.9
14/01/2014	8.1E+06	1.3E+07	2.1E+07	38.3	61.7	69.0
29/01/2014	2.3E+06	2.0E+06	4.4E+06	53.4	46.6	97.9
13/02/2014	5.1E+06	2.3E+07	2.8E+07	17.9	82.1	97.0
15/11/2014	4.1E+06	1.0E+07	1.4E+07	28.3	71.7	51.6
30/11/2014	2.4E+06	1.9E+06	4.4E+06	55.4	44.6	99.4
15/12/2014	3.9E+06	6.5E+06	1.0E+07	37.2	62.8	44.6
30/12/2014	6.5E+06	1.4E+07	2.1E+07	31.7	68.3	99.4
14/01/2015	6.7E+06	2.6E+06	9.2E+06	72.3	27.7	98.1
29/01/2015	4.6E+06	5.5E+06	1.0E+07	45.4	54.6	79.6
13/02/2015	5.9E+06	9.0E+06	1.5E+07	39.6	60.4	63.5
15/11/2015	3.6E+06	1.3E+07	1.7E+07	21.3	78.7	46.3
30/11/2015	1.6E+05	1.3E+06	1.5E+06	10.8	89.2	30.7
15/12/2015	1.6E+06	1.9E+06	3.5E+06	46.1	53.9	99.1

30/12/2015	2.2E+06	2.6E+06	4.7E+06	45.9	54.1	96.2
14/01/2016	4.5E+06	6.3E+06	1.1E+07	41.6	58.4	94.4
29/01/2016	1.0E+06	1.6E+06	2.6E+06	39.3	60.7	66.7
15/11/2016	1.4E+06	1.0E+07	1.2E+07	12.5	87.5	65.8
30/11/2016	1.9E+06	5.8E+06	7.6E+06	24.2	75.8	98.5
15/12/2016	7.0E+06	1.0E+07	1.7E+07	40.0	60.0	76.8
30/12/2016	4.1E+06	7.0E+06	1.1E+07	37.1	62.9	67.4
14/01/2017	1.3E+07	2.3E+07	3.6E+07	37.3	62.7	49.0
29/01/2017	7.7E+06	9.8E+06	1.8E+07	44.0	56.0	98.4
13/02/2017	3.1E+07	2.3E+07	5.3E+07	57.5	42.5	41.5
28/02/2017	2.0E+06	5.2E+06	7.2E+06	27.9	72.1	95.0
30/11/2017	6.2E+05	2.2E+05	8.4E+05	73.9	26.1	22.2
30/12/2017	4.2E+06	2.8E+06	7.0E+06	60.0	40.0	99.8
14/01/2018	1.4E+07	1.8E+07	3.1E+07	43.5	56.5	99.8
13/02/2018	1.2E+07	2.3E+07	3.5E+07	34.1	65.9	95.6
15/11/2018	1.4E+06	2.8E+06	4.1E+06	32.9	67.1	84.0
30/11/2018	2.0E+06	2.8E+06	4.8E+06	42.0	58.0	99.4
15/12/2018	3.9E+06	3.6E+06	7.4E+06	52.0	48.0	61.2
30/12/2018	3.7E+06	1.9E+06	5.6E+06	65.7	34.3	99.1
14/01/2019	5.5E+06	3.1E+06	8.6E+06	64.2	35.8	90.4
29/01/2019	5.0E+06	1.2E+07	1.7E+07	28.9	71.1	96.4
13/02/2019	8.3E+06	1.5E+07	2.3E+07	35.7	64.3	64.0
28/02/2019	3.0E+06	1.2E+07	1.5E+07	20.2	79.8	41.6
15/11/2019	1.6E+06	4.9E+06	6.4E+06	24.3	75.7	84.0
15/12/2019	1.1E+07	1.2E+07	2.4E+07	47.5	52.5	98.3
30/12/2019	5.9E+06	2.5E+06	8.4E+06	70.3	29.7	74.9
14/01/2020	1.4E+07	1.0E+07	2.4E+07	59.1	40.9	20.6
29/01/2020	9.9E+06	8.7E+06	1.9E+07	53.2	46.8	95.0
15/11/2020	6.6E+05	1.7E+06	2.4E+06	28.0	72.0	99.4
30/11/2020	7.7E+06	2.4E+07	3.2E+07	24.1	75.9	43.3
15/12/2020	1.0E+06	1.2E+06	2.2E+06	46.0	54.0	98.1
30/12/2020	1.6E+06	1.3E+06	2.9E+06	55.4	44.6	96.5

14/01/2021	1.0E+07	9.0E+06	1.9E+07	53.1	46.9	97.1
29/01/2021	1.1E+07	6.2E+06	1.7E+07	64.1	35.9	61.0

Table C.7: Data for all 15-day products that cover ≥ 20 % of the full area of Scar Inlet Ice Shelf. Columns record the end date for each 15-day product, scaled slush area, scaled ponded water area, scaled total melt area, percentage of the total area that is classified as slush, percentage of the total area that is classified as ponded water, and percentage coverage over the ice shelf area.

End Date	Scaled					AOI Coverage (%)
	Scaled Slush Area (m²)	Ponded Water Area (m²)	Scaled Total Area (m²)	Slush (%)	Ponded Water (%)	
28/02/2014	2.1E+07	2.2E+07	4.4E+07	49.1	50.9	36.3
15/11/2014	5.5E+07	4.5E+06	5.9E+07	92.4	7.6	54.3
30/12/2014	6.1E+05	3.9E+05	1.0E+06	60.7	39.3	61.2
28/02/2015	1.1E+06	3.5E+06	4.6E+06	23.6	76.4	37.2
15/11/2015	2.9E+07	4.1E+06	3.3E+07	87.6	12.4	90.8
15/12/2015	2.8E+07	3.7E+06	3.2E+07	88.4	11.6	83.2
14/01/2016	2.3E+07	5.5E+06	2.8E+07	80.3	19.7	100.0
13/02/2016	1.3E+07	9.8E+06	2.3E+07	57.5	42.5	54.0
14/03/2016	1.4E+07	3.0E+07	4.4E+07	32.7	67.3	82.5
30/11/2016	6.8E+07	7.4E+06	7.6E+07	90.2	9.8	95.0
14/01/2017	7.6E+06	1.5E+06	9.1E+06	83.1	16.9	95.4
13/02/2017	1.5E+07	1.3E+07	2.7E+07	53.7	46.3	79.8
28/02/2017	4.1E+06	2.9E+07	3.3E+07	12.6	87.4	66.2
15/12/2017	2.3E+07	2.8E+06	2.5E+07	89.1	10.9	99.9
30/12/2017	1.0E+07	1.4E+06	1.1E+07	87.8	12.2	75.0
15/11/2018	1.1E+06	5.8E+05	1.7E+06	64.9	35.1	33.0
30/12/2018	6.1E+06	1.1E+06	7.2E+06	85.1	14.9	50.7
29/01/2019	4.4E+06	1.2E+06	5.6E+06	78.5	21.5	97.0
28/02/2019	1.4E+06	1.2E+07	1.3E+07	10.1	89.9	75.0

14/03/2020	1.3E+07	1.6E+07	2.9E+07	44.1	55.9	92.0
15/11/2020	5.0E+07	5.9E+06	5.6E+07	89.4	10.6	74.1
30/11/2020	7.5E+06	1.7E+06	9.1E+06	81.7	18.3	72.2

Table C.8: Data for all 15-day products that cover $\geq 20\%$ of the full area of Larsen C Ice Shelf. Columns record the end date for each 15-day product, scaled slush area, scaled ponded water area, scaled total melt area, percentage of the total area that is classified as slush, percentage of the total area that is classified as ponded water, and percentage coverage over the ice shelf area.

End Date	Scaled		Ponded		AOI Coverage (%)
	Scaled Slush Area (m ²)	Water Area (m ²)	Scaled Total Area (m ²)	Ponded Water (%)	
15/11/2013	1.3E+07	9.1E+06	2.2E+07	58.2	39.0
15/12/2013	1.0E+07	2.8E+06	1.3E+07	78.9	39.6
14/01/2014	8.8E+06	6.2E+06	1.5E+07	58.9	42.2
29/01/2014	8.7E+06	6.1E+06	1.5E+07	58.8	24.3
28/02/2014	1.2E+07	4.9E+07	6.1E+07	19.7	46.1
15/11/2014	7.9E+06	6.7E+06	1.5E+07	54.1	64.0
30/11/2014	1.7E+06	2.0E+06	3.7E+06	45.7	33.5
15/12/2014	4.3E+06	3.1E+06	7.4E+06	58.7	75.4
30/12/2014	4.5E+06	2.4E+06	6.9E+06	65.7	76.9
13/02/2015	7.0E+06	1.1E+07	1.8E+07	38.3	36.3
28/02/2015	1.6E+06	7.9E+06	9.5E+06	16.9	23.4
15/11/2015	9.3E+06	2.8E+06	1.2E+07	77.0	50.7
30/11/2015	2.0E+07	2.9E+06	2.3E+07	87.4	24.6
15/12/2015	4.0E+07	7.3E+06	4.8E+07	84.6	46.3
14/01/2016	1.9E+07	1.4E+07	3.3E+07	57.7	98.7
29/01/2016	7.8E+06	7.9E+06	1.6E+07	49.8	74.3
13/02/2016	3.8E+07	4.3E+07	8.1E+07	46.6	50.6

15/11/2016	3.3E+06	8.0E+06	1.1E+07	28.9	71.1	22.2
30/11/2016	2.7E+07	7.0E+06	3.4E+07	79.4	20.6	55.2
15/12/2016	2.3E+07	8.4E+06	3.1E+07	72.9	27.1	37.2
13/02/2017	1.1E+07	2.0E+07	3.2E+07	36.3	63.7	58.7
28/02/2017	5.2E+06	9.8E+06	1.5E+07	34.8	65.2	71.9
15/11/2017	1.2E+07	7.2E+06	1.9E+07	61.6	38.4	79.6
30/11/2017	1.4E+07	1.1E+07	2.4E+07	55.7	44.3	43.8
15/12/2017	1.4E+07	4.3E+06	1.8E+07	76.6	23.4	96.7
30/12/2017	6.3E+06	3.0E+06	9.4E+06	67.6	32.4	55.0
14/01/2018	5.4E+06	3.4E+06	8.8E+06	61.2	38.8	55.4
29/01/2018	6.6E+06	6.7E+06	1.3E+07	49.7	50.3	25.5
28/02/2018	3.9E+06	1.3E+07	1.7E+07	22.8	77.2	27.1
30/11/2018	3.1E+06	4.0E+06	7.1E+06	43.3	56.7	26.1
30/12/2018	7.3E+06	1.7E+06	8.9E+06	81.2	18.8	35.3
29/01/2019	3.9E+06	3.2E+06	7.1E+06	54.5	45.5	78.0
13/02/2019	4.0E+06	1.7E+07	2.1E+07	19.2	80.8	87.0
28/02/2019	4.2E+06	6.8E+07	7.2E+07	5.9	94.1	28.0
30/11/2019	1.4E+07	8.3E+06	2.3E+07	63.3	36.7	25.2
30/12/2019	2.0E+07	7.8E+06	2.7E+07	71.4	28.6	34.1
14/01/2020	2.0E+07	1.1E+07	3.1E+07	63.8	36.2	65.2
29/01/2020	1.9E+07	7.0E+06	2.6E+07	72.7	27.3	62.2
13/02/2020	7.2E+07	9.0E+07	1.6E+08	44.4	55.6	28.0
15/12/2020	3.3E+07	2.3E+07	5.5E+07	59.1	40.9	21.5
30/12/2020	4.9E+06	8.3E+06	1.3E+07	37.2	62.8	37.3
13/02/2021	3.0E+07	7.8E+07	1.1E+08	27.9	72.1	44.0
28/02/2021	1.1E+07	1.8E+07	3.0E+07	37.8	62.2	23.0

Table C.9: Data for all 15-day products that cover $\geq 20\%$ of the full area of Larsen D Ice Shelf. Columns record the end date for each 15-day product, scaled slush area, scaled ponded water area, scaled total melt area, percentage of the total area that is classified as slush, percentage of the total area that is classified as ponded water, and percentage coverage over the ice shelf area.

End Date	Scaled		Scaled Total Area (m²)	Slush (%)	Ponded		AOI Coverage (%)
	Slush Area (m²)	Water Area (m²)			Water (%)	AOI Coverage (%)	
15/11/2013	5.4E+07	2.2E+07	7.6E+07	70.6	29.4	65.3	
30/11/2013	4.2E+07	2.4E+07	6.6E+07	63.9	36.1	76.1	
15/12/2013	3.7E+07	1.2E+07	4.9E+07	76.0	24.0	74.8	
30/12/2013	4.7E+07	1.6E+07	6.3E+07	75.0	25.0	59.0	
14/01/2014	5.2E+07	2.0E+07	7.2E+07	71.9	28.1	67.9	
13/02/2014	1.5E+07	1.9E+07	3.4E+07	44.9	55.1	40.3	
28/02/2014	3.6E+07	7.7E+07	1.1E+08	32.2	67.8	43.6	
15/11/2014	1.8E+07	1.5E+07	3.3E+07	54.8	45.2	46.7	
30/11/2014	1.2E+07	6.1E+06	1.8E+07	65.8	34.2	33.5	
15/12/2014	3.0E+07	1.5E+07	4.5E+07	66.1	33.9	64.1	
30/12/2014	3.9E+07	1.4E+07	5.2E+07	74.1	25.9	46.1	
14/01/2015	3.6E+07	1.8E+07	5.4E+07	67.3	32.7	42.7	
29/01/2015	1.7E+07	2.2E+07	3.9E+07	43.1	56.9	53.4	
13/02/2015	1.3E+07	2.9E+07	4.2E+07	31.0	69.0	30.0	
15/11/2015	1.2E+07	8.1E+06	2.0E+07	59.6	40.4	20.3	
30/11/2015	1.9E+07	1.3E+07	3.2E+07	59.5	40.5	37.7	
15/12/2015	7.2E+07	2.4E+07	9.6E+07	75.2	24.8	62.0	
30/12/2015	4.0E+07	1.7E+07	5.7E+07	69.8	30.2	64.4	
14/01/2016	4.3E+07	4.8E+07	9.1E+07	47.4	52.6	43.5	
29/01/2016	4.3E+07	3.3E+07	7.6E+07	56.2	43.8	80.6	
13/02/2016	2.6E+07	3.3E+07	5.9E+07	44.0	56.0	85.2	
28/02/2016	3.0E+07	7.2E+07	1.0E+08	29.3	70.7	24.2	
15/11/2016	9.0E+07	3.5E+07	1.2E+08	72.3	27.7	83.3	
30/11/2016	1.1E+08	2.6E+07	1.3E+08	80.0	20.0	31.7	
15/12/2016	5.1E+07	3.8E+07	8.8E+07	57.3	42.7	47.0	
30/12/2016	5.4E+07	3.2E+07	8.5E+07	62.8	37.2	30.2	
14/01/2017	8.9E+07	5.2E+07	1.4E+08	62.9	37.1	39.2	
13/02/2017	2.0E+07	3.3E+07	5.3E+07	37.8	62.2	53.0	

28/02/2017	3.6E+07	6.5E+07	1.0E+08	35.3	64.7	67.6
15/11/2017	6.5E+07	3.5E+07	1.0E+08	64.9	35.1	62.8
30/11/2017	5.9E+07	2.1E+07	8.0E+07	73.5	26.5	96.5
15/12/2017	2.5E+07	6.4E+06	3.2E+07	79.8	20.2	26.0
14/01/2018	5.0E+07	2.0E+07	7.0E+07	71.9	28.1	34.8
29/01/2018	2.2E+07	8.0E+06	3.0E+07	73.5	26.5	51.9
13/02/2018	3.2E+07	7.2E+07	1.0E+08	31.1	68.9	37.6
15/11/2018	1.0E+07	1.7E+07	2.7E+07	37.5	62.5	35.2
15/12/2018	2.8E+07	2.5E+07	5.4E+07	52.6	47.4	57.9
14/01/2019	5.9E+07	2.7E+07	8.5E+07	68.5	31.5	50.2
29/01/2019	2.5E+07	2.1E+07	4.7E+07	54.2	45.8	58.5
13/02/2019	1.4E+07	2.9E+07	4.2E+07	32.7	67.3	52.4
28/02/2019	6.8E+06	6.3E+07	6.9E+07	9.8	90.2	24.8
15/11/2019	5.8E+07	2.4E+07	8.2E+07	70.5	29.5	52.4
30/11/2019	6.3E+07	4.2E+07	1.1E+08	59.9	40.1	46.8
15/12/2019	6.6E+07	3.1E+07	9.6E+07	68.0	32.0	56.8
30/12/2019	4.9E+07	1.7E+07	6.6E+07	74.4	25.6	55.7
14/01/2020	2.2E+07	3.2E+07	5.4E+07	40.4	59.6	21.5
29/01/2020	4.7E+07	4.0E+07	8.7E+07	54.1	45.9	65.0
13/02/2020	5.7E+06	2.9E+06	8.6E+06	66.4	33.6	20.7
28/02/2020	4.5E+07	7.6E+07	1.2E+08	36.9	63.1	22.2
30/11/2020	8.8E+06	7.1E+06	1.6E+07	55.3	44.7	57.2
15/12/2020	1.2E+07	9.6E+06	2.1E+07	55.1	44.9	41.3
30/12/2020	1.3E+07	6.0E+06	1.9E+07	67.9	32.1	38.4
14/01/2021	9.8E+07	2.6E+07	1.2E+08	79.0	21.0	30.4
13/02/2021	2.4E+07	3.4E+07	5.8E+07	41.8	58.2	52.3
28/02/2021	1.7E+07	3.3E+07	4.9E+07	33.6	66.4	27.7